Quantum Dynamics in Condensed Phases: Charge Carrier Mobility, Decoherence, and Excitation Energy Transfer

by

Yuan-Chung Cheng

B.S., National Taiwan University, Taiwan (1995)
M.S., National Taiwan University, Taiwan (1997)

Submitted to the Department of Chemistry
in partial fulfillment of the requirements for the degree of

Doctor of Philosophy

at the

MASSACHUSETTS INSTITUTE OF TECHNOLOGY

February 2006

Author .....
Department of Chemistry
January 26, 2006

Certified by .....
Robert J. Silbey
Dean of Science & Class of '42 Professor of Chemistry
Thesis Supervisor

Accepted by .....
Robert W. Field
Chairman, Department Committee on Graduate Students

This doctoral thesis has been examined by a Committee of the Department of Chemistry as follows:

Professor Jianshu Cao .....

Chairman

Professor Robert J. Silbey .....

Thesis Supervisor

Professor Robert W. Field .....

Quantum Dynamics in Condensed Phases: Charge Carrier Mobility, Decoherence, and Excitation Energy Transfer

by

Yuan-Chung Cheng

Submitted to the Department of Chemistry
on January 26, 2006, in partial fulfillment of the
requirements for the degree of
Doctor of Philosophy

Abstract

In this thesis, we develop analytical models for quantum systems and perform theoretical investigations on several dynamical processes in condensed phases. First, we study charge-carrier mobilities in organic molecular crystals, and develop a microscopic theory that describes both the coherent band-like and incoherent hopping transport observed in organic crystals. We investigate the structures of polaron states using a variational scheme, and calculate both band-like and hopping mobilities at a broad range of parameters. Our mobility calculations in 1-D nearest-neighbor systems predict universal band-like to hopping transitions, in agreement with experiments. Second, motivated by recent developments in quantum computing with solid-state systems, we propose an effective Hamiltonian approach to describe quantum dissipation and decoherence. We then applied this method to study the effect of noise in a number of quantum algorithms and calculate noise threshold for fault-tolerant quantum error corrections (QEC). In addition, we perform a systematic investigation on several variables that can affect the efficiency of the fault-tolerant QEC scheme, aiming to generate a generic picture on how to search for optimal circuit design for real physical implementations. Third, we investigate the quantum coherence in the B800 ring of of the purple bacterium *Rps. acidophila* and how it affects the dynamics of excitation energy transfer in a single LH2 complex. Our calculations suggest that the coherence in the B800 ring plays a significant role in both spectral and dynamical properties. Finally, we discussed the validity of Markovian master equations, and propose a concatenation scheme for applying Markovian master equations that absorbs the non-Markovian effects at short times in a natural manner. Applications of the concatenation scheme on the spin-boson problem show excellent agreements with the results obtained from the non-Markovian master equation at all parameter range studied.

Thesis Supervisor: Robert J. Silbey
Title: Dean of Science & Class of '42 Professor of Chemistry

Acknowledgments

I am grateful for this opportunity to express my gratitude to those who made this thesis possible. First and foremost, I would like to thank my advisor, Prof. Robert J. Silbey, for his excellent guidance and inspiration throughout my stay at MIT. Few students can have been as fortunate as I have been to work with a supervisor of his caliber. I am especially grateful to him for his openness to new research ideas and for allowing me personal and intellectual freedoms, which truly helped my own professional development. It has been a wonderful experience to work with him.

Profs. Jianshu Cao and Robert W. Field are greatly acknowledged for valuable comments they made as the committee members. In addition, my thanks go to Profs. Peter Shor and Isaac L. Chuang for their excellent quantum computing classes, as well as Prof. Edward H. Farhi for inviting me to join their QIP group meetings. The chapter regarding quantum computing in this thesis would not be possible without the knowledge I learned from them.

I am indebted to my former advisors at National Taiwan University, Profs. Jwu-Ting Chen and Bih-Yaw Jin, for their valuable advices and encouragement. Without their help, I would not be able to begin this journey.

During my stay at MIT, many colleagues in the theory group offered support and encouragement that I value greatly. Thanks to Shilong Yang, Eli Barkai, Jianlan Wu, and Jaeyoung Sung for many fruitful discussions and ideas, which I benefited a lot. I am also grateful to other former and current fellow "zoo-mates", Seogjoo Jang, YounJoon Jung, Jim Witkoskie, Serhan Altunata, Xiang Xia, Steve Presse, Chiao-Lun Cheng, and Xiaogeng Song; their friendships have made my stay at room 6-228 a positive and enjoyable experience to say the least.

I am also grateful to many fellow Taiwanese graduate students. Thanks to Bruce Yu, Jhih-Wei Chu, Kan-Nian Hu, Nai-Yuan Chang, Patty Sun, and Chi-Wang Lin. Their friendships played an important role in keeping my sanity intact, and I would certainly miss those enlightening discussions during lunch times. I also want to thank my friends in Taiwan for their support. Through the Internet, we maintained com-

munications and exchanged ideas. In particular, thanks to Jason Chang, Seventeen Chen, Jing-Jong Shyue, and Enid Liao for the computing resources they provided, and more importantly, for the many lighthearted moments that we enjoyed together.

Last but not least, I would like to thank my family for their love and support. The unconditional support and love from my parents gave me the strength to persevere while studying abroad, and will always be appreciated. My sister and brother have been taking care of my parents since I was away form home, which I am deeply indebted. Finally, I would like to thank my wonderful wife, Meng-Chuan Cheng. Her encouragement and caring through the years have made everything possible, and I am sure she will continue to be there as we start a new chapter of our life together.

Contents

List of Figures

List of Tables

Chapter 1

Prologue

1.1 Introduction

Quantum dynamics in condensed-phase systems are difficult to deal with theoretically. In contrast to gas-phase systems that can usually be modeled adequately as isolated systems with well defined Hamiltonians and a limited number of degrees of freedom, a quantum system in condensed phases is inevitably coupled to a vast number of degrees of freedom in its surroundings; consequently, a dynamical process in condensed phases typically involves a large number of degrees of freedom, and a complete theoretical description of the process requires the inclusion of the complex condensed-phase environment as well, which makes the theoretical description of quantum dynamics in condensed-phase systems a formidable task.

In principle, it is possible to build an approximate model for a condensed-phase system by truncating the size of the full system. By considering an increasing number of molecules in the model, the properties of the truncated model will eventually approach the bulk properties. In fact, recent advancements in computing power has motivated much interest along this direction. Methods based on density functional theories and molecular-orbital theories have been developed for *ab initio* molecular dynamics simulations of many-body systems, and these numerical simulations have been proved useful in the understanding of ground state properties and dynamics in condensed phases. However, despite ever increasing computing power, the size of

systems and time scales tractable by computer simulations are still restricted, and to include all physically relevant degrees of freedom quantum mechanically in simulations is still prohibitive. Note that even if a complete atomistic simulation of quantum dynamics in condensed phases is possible, it is usually difficult to critically access key aspects of the dynamics from the results of numerical simulations. Therefore, it is desirable to develop analytical models that describe quantum dynamics in condensed-phase systems.

In most physical applications, one is only interested in properties that are determined by a subsystem with only a few relevant degrees of freedom. This allows one to partition the global system into a relevant part (system) and an irrelevant part (bath), and concern only on the dynamics of the system part. The system-plus-bath model has become the standard theoretical framework for condensed phase dynamics. After averaging out the bath degrees of freedoms by a coarse-graining procedure, one obtains the reduced description of the dynamics. The reduced dynamics description allows one to study dynamical processes in condensed phases.

The quantum master equation approach is a well known technique based on the system-plus-bath model. By using projection operator or cumulant expansion techniques, one can reformulate the exact quantum Liouville equation and perform a mathematically rigorous expansion in the limit of weak system-bath coupling to derive a quantum master equation for the reduced dynamics of the system. Moreover, Markovian approximation that assumes short bath relaxation time is often applied. The resulting equation, usually called the Redfield equation, has found broad applications in chemical physics. Adequate results for quantum dynamics can be obtained in the weak system-bath coupling regime, although such conditions are usually difficult to verify for generally systems.

It is also possible to avoid treating the bath degrees of freedom explicitly and still yield adequate descriptions for dynamical processes in condensed phase systems. By including stochastic fluctuations in the effective Hamiltonian of the system, one can mimic the influence of the bath for a system embedded in condensed-phase environments. This kind of approach usually leads to a stochastic Liouville equation, and the

statistical average of the stochastic processes results in decoherence and relaxation of the system. If applicable, the effective Hamiltonian approach provides an efficient method to describe condensed phase dynamics. However, extra care must be taken to justify the applicability of these models.

Quantum dynamical processes in condensed phases are often governed by the interplay of the couplings between quantum states in the system (coherence) and the system-bath couplings between the system and the environment (fluctuations). When the couplings in the system dominate the interactions, the dynamics is characterized by coherence evolution within the system states; in contrast, when the system-bath couplings dominate the interactions, the dynamics is characterized by incoherent relaxation towards the thermal equilibrium. The intermediate regime in which the strengths of different types of interactions are comparable usually presents a greater difficulty for theoretical descriptions. Furthermore, the condensed phase dynamics is also influenced by the time scales of the bath dynamics. Generally speaking, adequate and consistent descriptions of condensed phase dynamics can be obtained in some limiting cases, but a general theory is difficult to formulate.

1.2 Motivation

Recent developments in preparing novel materials and manufacturing nanoscale devices operating according to quantum mechanical principles have not only allowed us to achieve new technologies, but also revealed interesting physics regarding the dynamical properties of condensed-phase systems. These new experiments also necessitate the developments of theoretical models that can capture the underlying physical principles of the observed phenomena. In particular, the theoretical work presented in this thesis was motivated by recent advancements in the applications of organic materials in electronic devices, solid-state implementations of quantum computers, and single-molecule measurements on optical properties of nanoscale molecular aggregates.

Recently, advancements in preparing ultra-pure single crystals of organic molec-

ular materials have opened a whole new research area for material scientists. Novel electronic devices based on organic materials, such as organic light-emitting diodes, organic solar cells, and organic field-effect transistors, have been realized and proved to offer as potential substitutes for their inorganic counterparts [1, 2, 3]. Crystals or thin films of some organic compounds might just be the keys to the revolution toward the next generation of electronic devices. In addition, these new experimental results have renewed the interest in developing theoretical models to better understand the intrinsic charge transport mechanisms in organic molecular crystals. The temperature dependence of charge-carrier mobilities in organic molecular crystals universally exhibits a power-law behavior (resembling the band transport found in conventional silicon-based semiconductors) at low temperatures, and an almost temperature independent or slightly thermal activated behavior (resembling the hopping transport found in disordered materials) at high temperatures. The universal crossover from band-like to hopping transport in the intrinsic mobilities of ultrapure organic aromatic molecular crystals occurs at about room temperature [4, 5, 6, 7, 2, 8]. Because having high mobilities is essential for the efficiencies and fast response times of electronic devices, finding organic materials with high intrinsic charge mobilities at room temperature has been the focus of recent developments in optimizing the performance of organic-based devices. In order to describe the experimental temperature dependence of charge mobilities and devise design rules that facilitate the development of organic electron devices, a theoretical model that describes both the band-like regime and the hopping regime of charge mobilities in organic crystals is essential.

We are also interested by recent developments in quantum information processing. Since the discovery of the quantum factoring algorithm by Peter Shor in 1994 [9], quantum information theory has rapidly grown into an active interdisciplinary field involving physics, computer science, and mathematics [10, 11, 12]. In principle, a quantum computer can outperform its classical counterpart and provide efficient ways to solve many important problems. In fact, the most early motivation to exploit the principle of quantum mechanics to achieve a greater computing power is to simulate many-body quantum systems. In a seminal work titled "Simulating physics with

computers", Richard Feynman first mentioned about building a quantum computer in 1982 [13]:

> "*[...] the full description of quantum mechanics for large systems with R particles [...] has too many variables, it cannot be simulated with a normal computer with a number of elements proportional to R [...] how can we simulate the quantum mechanics? [...] Let the computer itself be built of quantum mechanical elements which obey the quantum mechanical laws.*"
> - *Richard P. Feynman, 1982.*

Recent realizations of quantum algorithms using nuclear magnetic resonance (NMR) [14, 15, 16, 17] and ion-trap [18] techniques have clearly demonstrated that quantum computing is realizable in principle; however, it is also clear that NMR and ion-trap techniques are limited in their applications, because the number of spins that can be implemented in these systems is restricted. As a result, more recent efforts for building quantum computers have focused on techniques based on solid-state devices that are considered to be more scalable. However, the extra degrees of freedom and the inherent system-bath interactions in a solid-state system pose a great challenge for quantum computing with such devices. The inevitable interactions between the solid-state device and its surroundings introduce noise into the quantum system, resulting in the degradation of the quantum superposition state (decoherence). As such, the decoherence problem is the main obstacle towards the realization of a scalable quantum computer. Because the ability to compute and predict the behavior of a quantum computer under the influence of noise is crucial, a theoretical framework that describes decoherence according to realistic device conditions could be extremely useful in the study of quantum error-correcting and error-preventing schemes, as well as provide informative guidelines for the design of quantum computers [19, 20, 21, 22].

In another area, the developments in ultrafast laser spectroscopy and single molecule spectroscopy have allowed us to reveal detailed information of optical processes in nanoscale molecular aggregate systems, which have drawn considerable attention due to their important role in biological processes and synthetic molecular devices. The

photo-synthetic unit of purple bacteria is certainly one of the most studied molecular assemblies [23, 24, 25]. Recent spectroscopic studies, especially single molecule experiments, have significantly advanced our knowledge about the processes of excitation energy transfer in the bacterio photo-synthetic unit; however, a detailed understanding is still not at hand, mainly due to the difficulty of characterizing the quasi-static disorder due to the slow fluctuations of local protein environments and pigment structures. Dynamical processes in these systems are complicated by the competition between electronic coherence and quasi-static disorder in the system. Thus, in order to describe experimental results in a consistent framework, a theoretical model that treats electronic coherence and static disorder in the same footing is required. A molecular-level description for the dynamics of excitation energy transfer in the photo-synthetic unit may also prove useful for understanding other nanoscale molecular assemblies and designing efficient nanoscale optical devices.

A sound microscopic molecular-level description for each of the system mentioned above will answer many long-standing questions and may also help developing novel materials and new devices.

1.3 Overview

In response to questions raised by new experiments mentioned in the previous section, we develop theoretical models and perform investigations on the dynamical processes regarding the charge-carrier mobilities in organic molecular crystals (Chapter 2 and 3), effect of quantum decoherence in quantum computations (Chapter 4 and 5), and excitation energy transfer in the light-harvesting system of purple bacteria (Chapter 6). Note that each of the system presents a distinct challenge to a sound theoretical description. In the following, we present an overview of the chapters in this thesis.

In Chapter 2, quantum-chemical calculations coupled with a tight binding model are used to examine the applicability of the wide-band theory on the charge carrier mobilities in oligoacene crystals. In particular, the transfer integrals for all non-zero interactions in four crystalline oligoacenes (naphthalene, anthracene, tetracene

and pentacene) are calculated, and then used to construct the excess electron and hole band structures of all four oligoacene crystals in the tight binding approximation. From these band structures, thermal-averaged velocity-velocity tensors in the constant-free-time and the constant-free-path approximations for all four materials are calculated at temperatures ranging from 2-500 K. Comparison of the thermal-averaged velocity-velocity tensors with the experimental mobility data indicates that the simple band model is applicable for temperatures only up to about 150 K.

To characterize the crossover from band-like transport to hopping transport in molecular crystals, we study a microscopic model that treats electron-phonon interactions explicitly in Chapter 3. In order to describe the intermediate electron-phonon coupling regime that is relevant for charge-carrier mobilities in organic crystals, we develop a finite-temperature variational method combining Merrifield's transformation with Bogoliubov's theorem to obtain the optimal basis for an interacting electron-phonon system, and then based on the optimal basis to calculate the band-like and hopping mobilities for charge-carriers. Our calculations on the 1-D Holstein model at T=0K and finite temperatures suggest that the variational-perturbation method gives results that compared favorably to other analytical methods. We also study the structures of polaron states at a broad range of parameters including different temperatures. In addition, we calculate the band-like and hopping mobilities of the 1-D Holstein model in different parameters and showed that our theory predicts universal power-law decay at low temperatures and an almost temperature independent behavior at higher temperatures, in agreement with experimental observations. Our result also indicates that the self-trapping transition studied in conventional polaron theories does not necessary correspond to the crossover from band-like to hopping transport in the transport properties in organic crystals. A comparison of our 1-D results with experiments on ultrapure naphthalene crystals suggests that our method can describe the charge-carrier mobilities quantitatively across the whole experimental temperature range. Thus, we develop a unified theory that describes both coherent and incoherent transport in the Holstein Hamiltonian and can quantitatively describe the temperature dependence of the charge-carrier mobilities in organic molecular crys-

tals.

In Chapter 4, we propose a model based on a generalized effective Hamiltonian for studying the effect of noise in quantum computations. The system-environment interactions are taken into account by including stochastic fluctuating terms in the system Hamiltonian. Treating these fluctuations as Gaussian Markov processes with zero mean and delta function correlation times, we derive an exact equation of motion describing the dissipative dynamics for a system of n two-level systems (qubits). The limitations and possible extensions of this stochastic noise model is also discussed. In Chapter 5, we then apply this model to study the effect of noise on a number of quantum algorithms. We first investigate the effect of noise in the quantum channels on the quantum teleportation and derive analytical equations for the fidelity of teleportation. The effect of collective decoherence is also studied for different two-qubit entangled states. We then study the effect of noise on a set of one- and two-qubit quantum gates, and show that the results can be assembled together to investigate the quality of a quantum controlled-NOT gate operation. We compute the averaged gate fidelity and gate purity for the quantum controlled-NOT gate, and investigate phase, bit-flip, and flip-flop errors during the gate operation. The effects of direct inter-qubit coupling and fluctuations on the control fields are also studied. We find that the quality of the controlled-NOT gate operation is sensitive to the strengths of the control fields and the strengths of the noise, and the effect of noise is additive regardless of its origin.

In addition, quantum circuits implementing fault-tolerant quantum error correction (QEC) for the three qubit bit-flip code and five-qubit code are studied using the generalized effective Hamiltonian approach. We investigate the effect of noise in QEC circuits under realistic device conditions and avoid strong assumptions such as maximal parallelism and weak storage errors. Noise thresholds of the QEC codes are calculated. In addition, the effects of imprecision in projective measurements, collective bath, fault-tolerant repetition protocols, and level of parallelism in circuit constructions on the threshold values are also studied with emphasis on determining the optimal design for the fault-tolerant QEC circuit. These results provide insights

into the fault-tolerant QEC process as well as useful information for designing the optimal fault-tolerant QEC circuit for particular physical implementation of quantum computer.

In Chapter 6, we study the quantum coherence in the B800 ring of the light-harvesting system form purple bacteria and how the coherence affects the dynamics of excitation energy transfer in photosynthetic light-harvesting systems. To include the effect of slow fluctuations in the environment, we consider static disorder described by Gaussian random variables and employ Monte-Carlo simulations to perform sampling and calculate ensemble properties for the system. From an analysis of the ensemble absorption spectrum, we determine the disorder parameters for the B800 ring and show that the relatively weak electronic coupling between B800 pigments subtly changes the dynamics of excitation energy transfer and improves the uniformity and robustness of B800→B850 excitation energy transfer at room temperature, an example of how a multi-chromophoric assembly can exploit coherence to optimize the efficiency of photosynthesis.

Finally, we discuss an issue that has been left out in all previous chapters, namely the validity of the Markovian approximation in the Markovian master equations (Redfield equations). We argue that for a bath described by a spectral function $J(\omega)$ that is dense and smoothly spread out over a wide frequency range, a bath relaxation time τ_b can be defined; for times $t > \tau_b$, the Markovian approximation is applicable. In addition, if $J(\omega)$ decays to zero reasonably fast in both $\omega \to 0$ and $\omega \to \infty$ limit, then the bath relaxation time is determined by the width of the spectral function, and is only weakly dependent on the temperature of the bath. Based on this criterion of τ_b, a scheme to incorporate transient memory effects in the Markovian master equation is suggested. We propose a concatenation scheme that uses the second order perturbation theory for short time dynamics and the Markovian master equation at long times. Application of this concatenation scheme to the spin-boson model shows that it reproduces the reduced dynamics obtained from the non-Markovian master equation for all parameters studied.

Bibliography

[1] Martin Pope and Charles E. Swenberg. *Electronic Processes in Organic Crystals.* Oxford University Press, New York, 1982.

[2] N. Karl. Fast electronic transport in organic molecular solids? *J. Vac. Sci. Technol. A*, 17(4):2318, 1999.

[3] R. Farchioni and G. Grosso, editors. *Organic Electronic Materials:Conjugated Polymers And Low Molecular Weight Organic Solids.* Springer, New York, 2001.

[4] N. Karl. *Organic Semiconductors*, volume 17 of *Landolt Börnstein/New Series Group III.* Springer, Berlin, subvol. 17i, pp. 106-218 edition, 1985.

[5] N. Karl. Studies of organic semiconductors for 40 years .3. *Mol. Cryst. Liq. Cryst.*, 171:31 – 51, 1989.

[6] N. Karl. Growth and electrical-properties of high-purity organic molecular-crystals. *J. Cryst. Growth*, 99(1-4):1009 – 1016, 1990.

[7] C. E Swenberg and M. Pope. an observation on the mobility and the carrier effective mass in naphthalene. *Chem. Phys. Lett.*, 287:535, 1998.

[8] Edgar A. Silinsh and Vladislav Čápek. *Organic Molecular Crystals: Interaction, Localization, and Transport Phenomena.* AIP Press, Woodbury, NY, 1994.

[9] P. W. Shor. Algorithms for quantum computation: Discrete logarithms and factoring. In *Proceedings of the Symposium on the Foundations of Computer Science, 1994, Los Alamitos, California*, pages 124 – 134. IEEE Computer Society Press, New York, 1994.

[10] M. A. Nielsen and I. L. Chuang. *Quantum Computation and Quantum Information.* Cambridge University Press, 2000.

[11] M. Hirvensalo. *Quantum Computing.* Springer-Verlag, Berlin; New York, 2004.

[12] D. Bouwmeester, Ekert. A., and A. Zeilinger. *The Physics of Quantum Information : Quantum Cryptography, Quantum Teleportation, Quantum Computation.* Springer-Verlag, Berlin; New York, 2000.

[13] R. P. Feynman. Simulating physics with computers. *Int. J. Theor. Phys.*, 21:467 – 488, 1982.

[14] I. L. Chuang, L. M. K. Vandersypen, X. L. Zhou, D. W. Leung, and S. Lloyd. Experimental realization of a quantum algorithm. *Nature*, 393(6681):143 – 146, 1998.

[15] I. L. Chuang, N. Gershenfeld, and M. Kubinec. Experimental implementation of fast quantum searching. *Phys. Rev. Lett.*, 80(15):3408 – 3411, 1998.

[16] L. M. K. Vandersypen, M. Steffen, G. Breyta, C. S. Yannoni, R. Cleve, and I. L. Chuang. Experimental realization of an order-finding algorithm with an NMR quantum computer. *Phys. Rev. Lett.*, 85(25):5452 – 5455, 2000.

[17] L. M. K. Vandersypen, M. Steffen, G. Breyta, C. S. Yannoni, M. H. Sherwood, and I. L. Chuang. Experimental realization of Shor's quantum factoring algorithm using nuclear magnetic resonance. *Nature*, 414(6866):883 – 887, 2001.

[18] S. Gulde, M. Riebe, G. P. T. Lancaster, C. Becher, J. Eschner, H. Haffner, F. Schmidt-Kaler, I. L. Chuang, and R. Blatt. Implementation of the Deutsch-Jozsa algorithm on an ion-trap quantum computer. *Nature*, 421(6918):48 – 50, 2003.

[19] W. G. Unruh. Maintaining coherence in quantum computers. *Phys. Rev. A*, 51(2):992 – 997, 1995.

[20] G. M. Palma, K.-A. Suominen, and A. K. Ekert. Quantum computers and dissipation. *Proc. R. Soc. Lond. A.*, 452:567, 1996.

[21] H. E. Brandt. Qubit devices and the issue of quantum decoherence. *Prog. Quantum Electron.*, 22(5-6):257 – 370, 1998.

[22] G. G. Carlo, G. Benenti, G. Casati, and C. Mejia-Monasterio. Simulating noisy quantum protocols with quantum trajectories. *Phys. Rev. A*, 69(6), 2004.

[23] V. Sundstrom, T. Pullerits, and R. van Grondelle. Photosynthetic light-harvesting: Reconciling dynamics and structure of purple bacterial LH2 reveals function of photosynthetic unit. *J. Phys. Chem. B*, 103(13):2327 – 2346, 1999.

[24] T. Renger, V. May, and O. Kuhn. Ultrafast excitation energy transfer dynamics in photosynthetic pigment-protein complexes. *Phys. Rep.*, 343(3):138 – 254, 2001.

[25] X. C. Hu, T. Ritz, A. Damjanovic, F. Autenrieth, and K. Schulten. Photosynthetic apparatus of purple bacteria. *Quart. Rev. Biophys.*, 35(1):1 – 62, 2002.

Chapter 2

Band Structure and Band-Like Mobility in Oligoacene Single Crystals

Part of the content in this chapter has been published in the following paper:
Y.C. Cheng, R.J. Silbey, D.A. da Silva Filho, J.P. Calbert, J. Cornil, and J.L. Brédas. Three-Dimensional Band Structure and Band-Like Mobility in Oligoacene Single Crystals: A Theoretical Investigation. *Journal of Chemical Physics*, 118:3764-3774, 2003.

2.1 Introduction

The study of charge-carrier mobilities in organic molecular crystals has continued for more then 30 years [1, 2, 3], but the problem of the best way to describe the motion of charge carriers in the crystal has still not been fully resolved [4, 5, 6]. Recently, the realization of electronic devices based on crystalline organic materials has renewed the interest in developing new theoretical models to better understand this problem [6, 7, 8], and new techniques developed for preparing ultra-pure single crystals of these organic materials have enabled the study of intrinsic charge transport mechanisms [9, 10, 11, 12]. Because the mobility is an important factor for potential

electronic applications, it is of importance that we develop a theoretical model capable of describing the charge transport mechanism in organic molecular crystals.

The measured intrinsic mobilities of oligoacene single crystals show a band to hopping transition occurs at about room temperature [13, 14, 5], which enables us to characterize the charge-transport mechanism in two different regimes, band-like mechanism at low temperature, and hopping mechanism at high temperature. Although it is widely accepted that this transition occurs because of the effect of electron-phonon coupling and the polaron model has been applied to earlier studies on naphthalene with some success [13, 15, 16, 17], a quantitative theory that can describe the charge-carrier behavior in both regimes is still missing, especially for the wider band materials, tetracene and pentacene. In this chapter, we will focus on the study of the band-like mobilities of oligoacene crystals. A microscopic theory that describes the temperature dependent transition from band-like regime to hopping regime will be presented in the next chapter.

The charge transport in the band-like regime of oligoacene crystals is of particular interest, because relatively high charge carrier mobilities, ranging from 1-10 $cm^2/V \cdot s$ at room temperature to more than 10^2 $cm^2/V \cdot s$ at low temperature, have been achieved in well ordered materials [9, 18, 11, 7]. In addition, the measured mobilities follow the power law temperature dependence $\mu \sim T^{-n}$ with $n \approx 1.5 - 3.0$ in a broad temperature range. This power law dependence suggests a wide-band theory may be applicable in highly purified aromatic molecular single crystals, but so far all theoretical calculations have failed to provide the correct magnitudes and temperature dependences of the charge-carrier mobilities in organic molecular crystal systems [19, 3, 5]. Karl *et al.* have used a standard wide-band theory to describe the high, field-dependent hole mobilities observed in naphthalene at low temperature, and obtained a reasonable fit to their field-dependent results [9]. They concluded that a classical band-type transport model with combined acoustic- and optical-phonon scattering in nonparabolic bands is suitable for describing the mobilities in naphthalene at low temperature. However, because of the lack of reliable information on the band structure of the system, an important problem about the consistency of

the band picture was left unanswered in their paper. Due to the advances of modern quantum-chemical techniques, it is now possible to compute the band structure and examine the wide-band model theoretically. Therefore, an investigation based on purely theoretical parameters and modeling is essential to interpret new experimental developments and better understand the underlying transport mechanism.

In this chapter, a band model coupled with quantum-chemistry calculations is used to study the charge carrier mobilities in oligoacene crystals. Recently, Cornil *et al.* developed a semi-empirical Hartree-Fock INDO (Intermediate Neglect of Differential Overlap) method which can be used to obtain good estimates of the transfer integrals in van der Waals bonded crystals [20, 21, 22]. Here we adopt this method to calculate transfer integrals for all non-zero interactions in naphthalene, anthracene, tetracene and pentacene crystals, and then use these parameters to obtain the band structures and the mobility tensors for these crystals. A tight binding method is used to construct the band structure of these oligoacene crystals, and the velocity-velocity tensor products averaging over the Boltzmann distribution among the energy bands are used to estimate the value of band-like mobilities. In addition, in order to account for the effect of electron-phonon coupling under the framework of a basic band model, we discuss the polaron band theory and its applicability. Throughout this work, we focus on the behavior of charge carriers in the low temperature band-like regime, and neglect the hopping regime. The goal of this investigation is to re-examine the standard wide-band description of the mobility in oligoacene compounds based on the new parameters, and provide information about the applicability of the simple wide-band model. A unified theory that describes the band-like to hopping transition will be presented in the next chapter.

2.2 Method

2.2.1 Theoretical Background

The model adopted here for calculating the band structure and the mobility tensors for organic molecular crystals was first proposed by LeBlanc [2] and then extended by Katz *et al.* [23] in the early 1960s. Note that since all the compounds investigated here have a crystal structure containing two molecules (say, type α and type β) in a unit cell, there are two bands arising from the symmetric and antisymmetric combinations of molecular wavefunctions in a cell for both excess-electron and excess-hole. Assuming the concentration of charge carriers is very small so that one-particle formalism is applicable, and the excess electron or hole does not significantly change the wavefunction of the molecule, the lowest unoccupied molecular orbital (LUMO) of a molecule can be used as a basis for crystal electron wavefunctions, and the highest occupied orbital (HOMO) can be used for hole wavefunctions. In the tight binding approximation, the energies of the two excess-electron (excess-hole) bands, $E_+(\mathbf{k})$ and $E_-(\mathbf{k})$, can be expressed in terms of the transfer integrals between molecular LUMOs (HOMOs) [23]:

$$E_{\pm}(\mathbf{k}) = \left(\frac{T_\alpha + T_\beta}{2}\right) \pm \sqrt{\left(\frac{T_\alpha - T_\beta}{2}\right)^2 + V(\mathbf{k})^2}. \tag{2.1}$$

For crystals with inversion symmetry:

$$T_\alpha = E_\alpha - 2 \cdot \sum_i t_i^\alpha \cdot \cos(\mathbf{k} \cdot \mathbf{r}_i^\alpha), \tag{2.2}$$

$$T_\beta = E_\beta - 2 \cdot \sum_i t_i^\beta \cdot \cos(\mathbf{k} \cdot \mathbf{r}_i^\beta), \tag{2.3}$$

$$V(\mathbf{k}) = -2 \cdot \sum_i t_i^{\alpha\beta} \cdot \cos(\mathbf{k} \cdot \mathbf{r}_i^{\alpha\beta}), \tag{2.4}$$

where $\mathbf{k}$ is the wavevector; T_α and T_β represent the interactions between *translationally equivalent* molecules, E_α and E_β are the corresponding molecular orbital energy

on monomer type α and β, respectively; the summation in T_α (T_β) is taken over all interacting *translationally equivalent* molecules; t_i^α (t_i^β) is the intermolecular transfer integral between the central type α (β) molecule and the type α (β) molecule at the i-th unit cell. For crystals with a unit cell containing two equivalent molecules, $E_\alpha = E_\beta$ and $t_i^\alpha = t_i^\beta$; $\mathbf{r}_i^\alpha$ ($\mathbf{r}_i^\beta$) is the vector from the center type α (β) molecule to the type α (β) molecule at the i-th unit cell; $V(\mathbf{k})$ represents the interaction between type α and β molecules, and the summation is over all interacting *translationally inequivalent* molecules; $t_i^{\alpha\beta}$ is the intermolecular transfer integral between the central molecule and the *translationally inequivalent* molecule at the i-th unit cell, and $\mathbf{r}_i^{\alpha\beta}$ is the vector connecting these two molecules.

Eq. 2.1 to Eq. 2.4 are the necessary analytical equations for constructing the energy band structure for an excess electron or an excess hole in a crystal with two molecules in a unit cell, regardless of the details of crystal structure and intermolecular interactions. In addition, the velocity of charge carriers can be calculated from the band structure. In a standard band-theory model, the group velocity $\mathbf{v}(\mathbf{k})$ of the delocalized electron waves or hole waves is given by the gradient of the band energy in k-space:

$$\mathbf{v}(\mathbf{k}) = (1/\hbar) \cdot \nabla_k E(\mathbf{k}). \tag{2.5}$$

Although it is not possible to directly calculate the value of the mobility tensor using a band model, we can use two simplified models for the relaxation time to evaluate important parameters related to the mobility tensors [2, 23, 24]. Given a constant isotropic relaxation time τ_0 (constant-free-time approximation) or a constant isotropic free path λ (constant-free-path) for the motion of the charge carriers in the crystal, the components of the mobility tensor are

$$\mu_{ij} = e\tau_0 \langle v_i v_j \rangle / kT, \tag{2.6}$$

and

$$\mu_{ij} = (e\lambda/kT)\langle v_i v_j/|\mathbf{v}(\mathbf{k})|\rangle, \tag{2.7}$$

in the constant-free-time and constant-free-path approximations, respectively. Here v_i is the i-th component of the group velocity, $\mathbf{v}(\mathbf{k})$, and the bracket in the equation means an average over the Boltzmann distribution of a charge carrier in the energy bands:

$$\langle v_i v_j \rangle = \frac{\int \{ \frac{\partial E_+}{\partial k_i} \frac{\partial E_+}{\partial k_j} e^{-\beta E_+(\mathbf{k})} + \frac{\partial E_-}{\partial k_i} \frac{\partial E_-}{\partial k_j} e^{-\beta E_-(\mathbf{k})} \} d\mathbf{k}}{\hbar^2 \int \{ e^{-\beta E_+(\mathbf{k})} + e^{-\beta E_-(\mathbf{k})} \} d\mathbf{k}}, \tag{2.8}$$

where $E_+(\mathbf{k})$ is the energy of the upper band, and $E_-(\mathbf{k})$ is the energy of the lower band, as described in Eq. 2.1. Integrals in Eq. 2.8 can be evaluated numerically to obtain the values of thermal-averaged velocity-velocity tensor products $\langle v_i v_j \rangle$ and $\langle v_i v_j/|\mathbf{v}(\mathbf{k})|\rangle$. The two terms, $\langle v_i v_j \rangle$ and $\langle v_i v_j/|\mathbf{v}(\mathbf{k})|\rangle$, are the main quantities of concern here, because they can serve as estimates of the values of the real mobility tensors under the constant-free-time or constant-free-path approximations.

2.2.2 Models and Numerical Calculations

Values of important parameters in the band equations (Eq. 2.1 to Eq. 2.4) can be evaluated using numerical methods. In this investigation, the values of site energy and transfer integrals were calculated using the INDO semi-empirical quantum-chemical method [25, 21, 22]. Four oligoacene compounds, namely naphthalene, anthracene, tetracene, and pentacene, are studied. Figure 2-1 shows the molecular structure of these model compounds. Using crystal structures taken from the Cambridge database, parameters for these model compounds (naphthalene [26], anthracene [27], tetracene, and pentacene [28]) were calculated by performing ZINDO [20, 29] calculations on all molecular dimers within the third nearest-neighbor shells for each crystal. The crystal data used in our calculations are listed in Table 2.1. Because it is highly unlikely that molecules located outside the third shell will interact with the central molecule, we expect that all non-zero interactions are included in our calculations. Note that special attention needs to be paid to the phase of the macromolecule wavefunctions

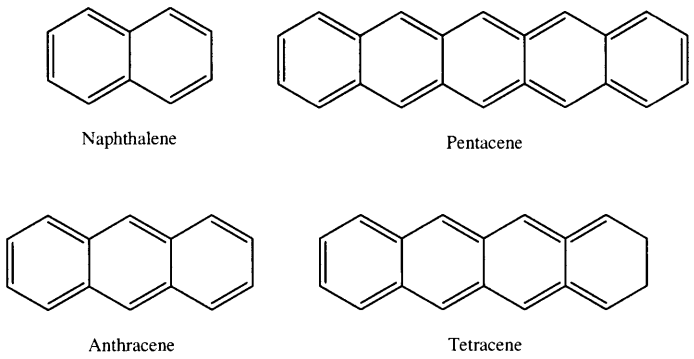

Figure 2-1: Molecular structures of the four oligoacenes studied in this work.

Table 2.1: Crystal constants and structures of oligoacenes

	Naphthalene	Anthracene	Tetracene	Pentacene
Crystal Constants	Monoclinic	Monoclinic	Triclinic	Triclinic
a[a]	8.0980	8.4144	6.057	6.275
b	5.9530	5.9903	7.838	7.714
c	8.6520	11.0953	13.010	14.442
α^b	90.000	90.000	77.13	76.75
β	124.400	125.293	72.12	88.01
γ	90.000	90.000	85.79	84.52

a : units: Å. b : units: degree

to determine the correct signs of the transfer integrals. Once we have the site energy and transfer integrals, analytical expressions of the energy bands as a function of the wavevector, k, can be obtained using Eq. 2.1 to Eq. 2.4. In addition, the 3-D total density of states (DOS) can be calculated by performing a primitive histogram calculation inside the first Brillouin zone.

The group velocity across the band can be obtained using Eq. 2.4. Note that because the unit cell vectors **a**, **b** and **c** are not orthogonal to each other for the crystals investigated here, a new Cartesian coordinate system was used to perform the group velocity calculations. The new coordinate system is chosen as follows: the new x-axis is parallel to the **a** direction, the y-axis is in the **ab** plane and points to the positive **b** direction, and the new z-axis is parallel to the interlayer **c**′ direction which

is perpendicular to the **ab** plane. The group velocity of charge carriers in the energy band was calculated in the new coordinate system, and projected back to each unit cell direction to evaluate the velocity vector in the real space. The thermal-averaged integral (Eq. 2.8) was evaluated numerically by applying an adaptive Gaussian integration method using a 51-point Gauss-Kronrod rule over the first Brillouin zone with more than 102x102x102 points. The estimated absolute error is less than 10^{-6} in all numerical integrations performed. Values of the thermal-averaged velocity-velocity tensor products were calculated at temperatures ranging from 1.7 K to 500 K.

2.3 Results and Discussion

2.3.1 Transfer Integrals

The calculated site energies and transfer integrals for all four oligoacenes are listed in Table 2.2. The calculated site energies for type α and type β molecules in naphthalene and anthracene crystals are the same because of their monoclinic $\mathbf{P}_{21/a}$ symmetry. However, in tetracene and pentacene crystals, which have a triclinic $\mathbf{P}_{1/2}$ symmetry, an energy difference is found between type α and type β molecules. This energy difference is due to a slight geometry difference between type α and type β molecules, and leads to a significant difference in the band structures, as we will see in the next section.

For all compounds investigated here, calculated intra-layer interactions are significantly larger than inter-layer interactions. The important in-plane interactions found are those along the nearest-neighbor directions, d_1 (1/2, 1/2, and 0 along the a, b, and c directions) and d_2 (-1/2, 1/2, and 0 along the a, b, and c directions), and short crystal axis (b for naphthalene and anthracene, a for tetracene and pentacene); these results are in agreement with previous calculations for oligoacene crystals [22, 24, 30] and mobility measurements pointing to two-dimensional transport in oligoacene crystals [31, 32, 12].

The evolution of the size of transfer integrals with respect to the size of oligoacene

Table 2.2: Calculated site energy and transfer integrals (units: meV)

			Naphthalene		Anthracene		Tetracene		Pentacene	
			HOMO	LUMO	HOMO	LUMO	HOMO	LUMO	HOMO	LUMO
	ΔE^a		0	0	0	0	48	-52	0.0	-2
a[b]	b	c								
1	0	0	0.00	0.00	0.00	0.00	-29.25	33.33	49.93	48.30
0	1	0	38.50	11.15	48.30	29.93	0.00	0.00	0.00	0.00
-1/2	1/2	0	36.59	-41.49	-47.89	-56.05	-68.88	-70.80	-97.82	-81.08
1/2	1/2	0	36.59	-41.49	-47.89	-56.05	-61.92	-47.42	-72.65	-81.62
-3/2	1/2	0	0.00	0.00	0.00	0.00	0.00	15.88	-4.61	-5.74
3/2	1/2	0	0.00	0.00	0.00	0.00	-14.56	0.0	-4.75	-3.22
-1/2	3/2	0	-2.99	-2.99	-3.40	-3.26	0.00	0.00	0.00	0.00
1/2	3/2	0	-2.99	-2.99	-3.40	-3.26	0.00	0.00	0.00	0.00
0	-1	1	-1.49	-4.08	0.0	-2.31	1.08	-3.53	3.12	0.0
1/2	1/2	1	-13.60	-4.21	-13.87	-3.80	0.00	0.00	0.00	0.00
1/2	-1/2	1	-13.60	-4.21	-13.74	-3.80	6.82	0.00	-2.43	0.00
-1/2	-1/2	1	0.00	0.00	0.00	0.00	-12.63	0.0	-2.29	-5.33
-1/2	-3/2	1	0.00	0.00	0.00	0.00	0.00	-7.58	0.00	-1.21
1/2	-3/2	1	-1.22	1.08	1.22	-1.22	0.00	0.00	0.00	-2.04
1/2	3/2	1	-1.22	1.08	1.22	-1.22	0.00	0.00	0.00	0.00
-3/2	-1/2	1	0.00	0.00	0.00	0.00	0.00	-9.33	0.0	-1.72
3/2	-1/2	1	1.63	1.63	1.63	1.49	0.00	0.00	0.00	0.00
3/2	3/2	1	1.63	1.63	1.63	1.49	0.00	0.00	0.00	0.00
-3/2	-3/2	1	0.00	0.00	0.00	0.00	-5.13	0.00	0.00	0.00

[a] Relative on-site energy, $E_\beta - E_\alpha$.

[b] Unit vectors being the lattice vectors.

molecules, from two rings in naphthalene to five rings in pentacene, indicates that the size of the conjugated π system and the structure of the crystal are both important factors determining the strength of the interactions [33]. We find that as the size of the molecule increases, the calculated interactions for both holes and electrons along d_1 and d_2 increase; this contrasts with the situation observed in cofacial dimers (where the HOMO splitting decrease with increasing chain size), thus pointing to the subtle interplay between crystal packing and calculated transfer integrals [33]. Interestingly, interactions between molecules located in adjacent layers (along the c direction) decrease as the size of the molecule increases. This result can be attributed to the longer distance between layers in larger molecules. As the distances between the adjacent layers increase, the weak $\pi-\pi$ interactions along the c direction decrease.

2.3.2 Band Structure and Density of States

The DOS spectra and band structures along different unit cell vectors are displayed in Figs. 2-2 to 2-5 for naphthalene, anthracene, tetracene and pentacene, respectively. Shapes of LUMO and HOMO bands along the k_a , k_b , k_c , k_{d1} and k_{d2} directions are plotted. Note that the values of the k vectors are scaled such that the value at the first Brillouin zone edge is unity. The band structures of tetracene and pentacene are slightly different from those of naphthalene and anthracene, which can be ascribed to the different crystal structures and the significant energy differences between type α and type β molecules in the tetracene crystal. For monoclinic naphthalene and anthracene crystals, the degeneracy at the Brillouin zone edge on the **ab** plane due to the crystal $\mathbf{P}_{1/2}$ symmetry can be clearly seen in the graph, as well as the Van Hove singularities around the band edges. Because no such symmetry exists in triclinic crystals, there is no degeneracy at the zone edge in the results for tetracene and pentacene crystals. The largest contribution to the energy splitting at the zone edge is from the difference between $\alpha - \beta$ site energies, so that the size of the splitting is approximately twice the size of the site energy difference. In all cases, the dispersion along the c direction is much smaller than those along the other directions, and a large gap is found between upper and lower bands along the c direction. This is

clearly due to smaller interactions between molecules located in adjacent layers, and is a well known result for this kind of herringbone packing material [23, 24, 22]. As a result, we expect the charge carrier mobilities along the c direction to be smaller than those along other directions.

The bandwidth values for all oligoacenes are summarized in Table 2.3. Bandwidths along the $\mathbf{a}$, $\mathbf{b}$, $\mathbf{c}$, $\mathbf{d}_1$, $\mathbf{d}_2$ directions and the 3-D total bandwidths calculated from the widths of the continuous region in the DOS spectrum are listed in Table 2.3, as well as values of the gaps between the upper and lower bands in each direction. All four compounds investigated here have a continuous band with widths from 400 meV to 700 meV, in agreement with recent experimental and theoretical results [9, 12, 22, 34]. In addition, comparing the total bandwidth for different oligoacenes, we find that the bandwidth increases when the size of the molecule increases, as we expect for herringbone structures [33].

When the thermal populations of the charge carriers are taken into account, a parameter other than total bandwidth should be adopted for comparing intrinsic transport properties. For all the compounds investigated here, the bandwidths are significantly larger than the thermal energy, i.e. $W \gg kT$. This result implies that a wide band limit can be used to describe the transport of excess holes or excess electrons, and at normal temperatures, only the states around the energy minima of the band are populated. Note that due to the nature of the excess charge carriers, the energy of an excess electron is measured upward from the bottom of the lower band, while the energy of an excess hole is measured downward from the top of the upper band. That is, within this two-band model, the motion of the excess electrons in the crystal are governed by the lower LUMO band, while the motion of the excess holes are governed by the upper HOMO band.

Previous theoretical investigations have often used total bandwidths as criteria for comparing intrinsic excess electron and excess hole mobilities, but comparing values of total bandwidths can be misleading. For example, in a pentacene crystal, the total bandwidths of HOMO and LUMO bands along the d_1 direction (which is the direction with the strongest interaction) are approximately the same (738 meV and

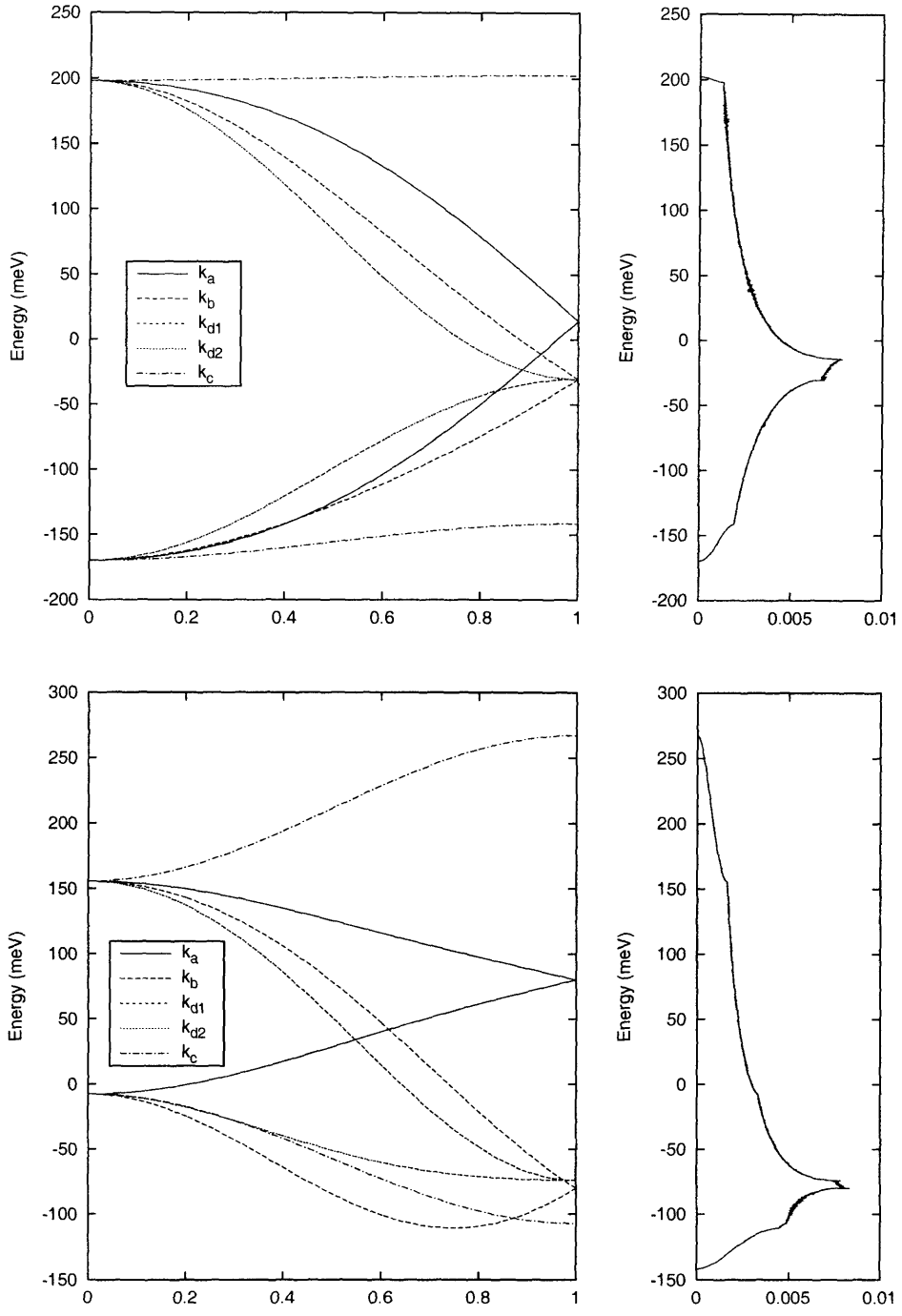

Figure 2-2: Shape of the LUMO band (upper panel) and the HOMO band (lower panel) of Naphthalene in the major crystal directions; the right panel is the corresponding Density of States.

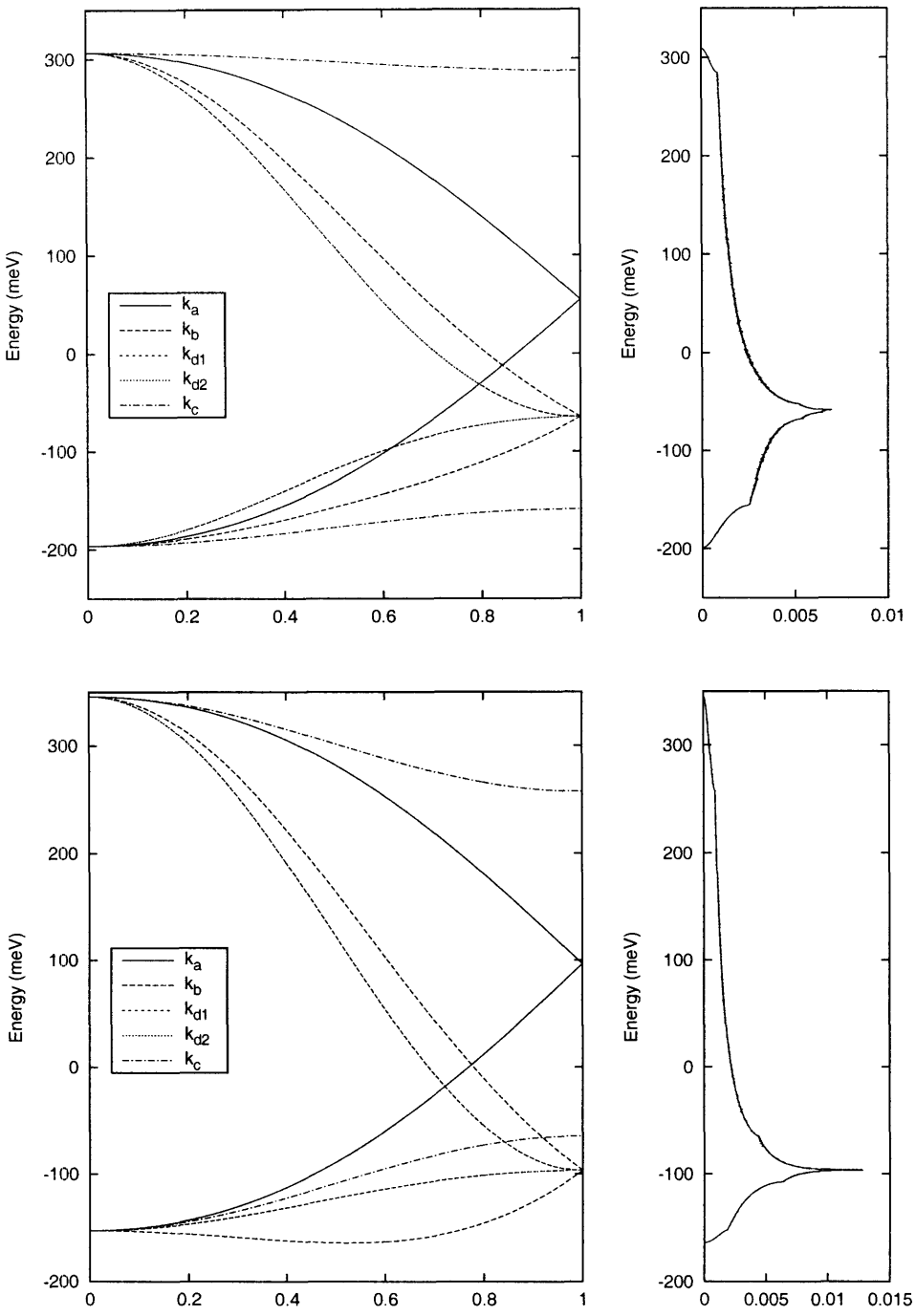

Figure 2-3: Shape of the LUMO band (upper panel) and the HOMO band (lower panel) of Anthracene in the major crystal directions; the right panel is the corresponding Density of States.

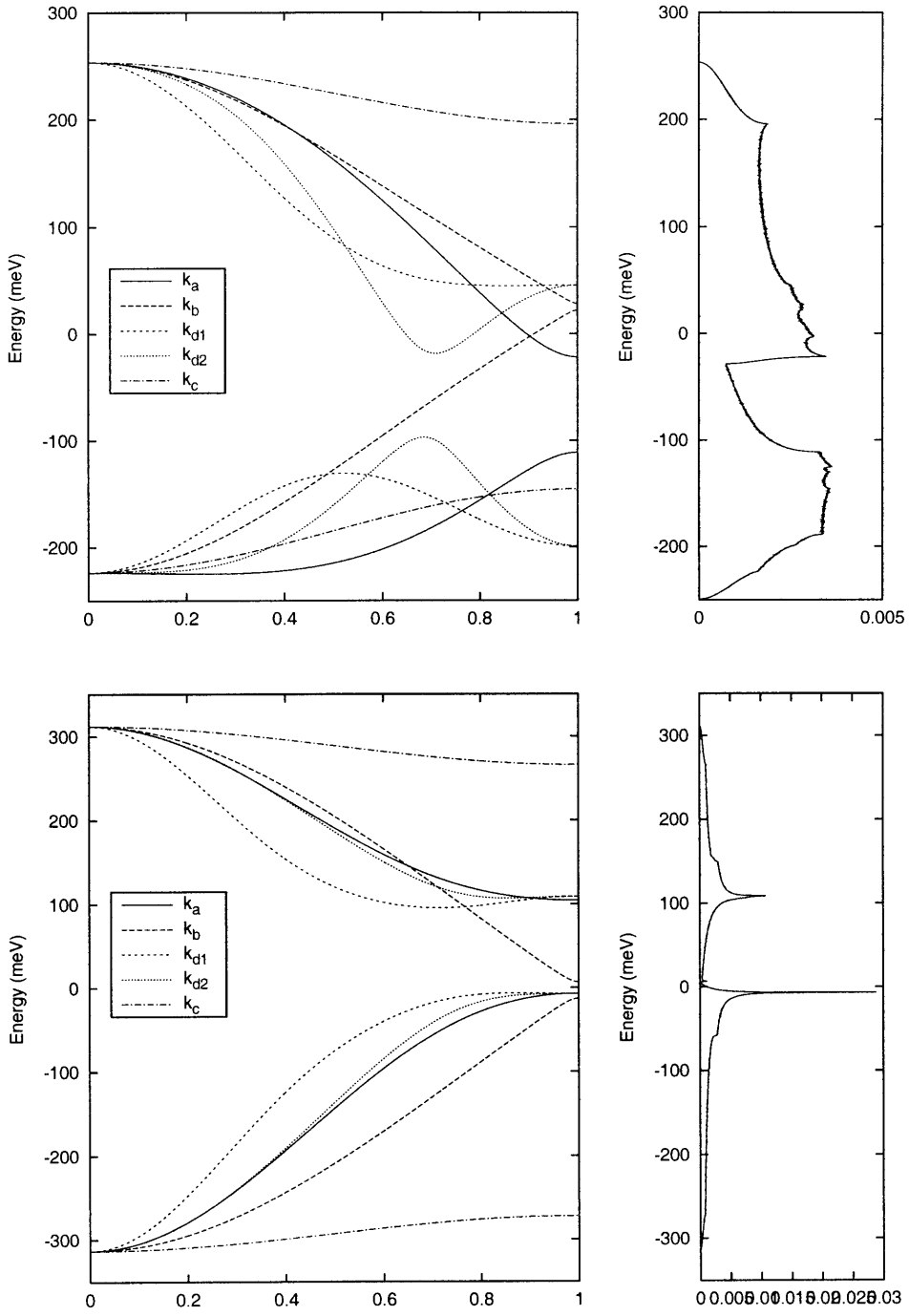

Figure 2-4: Shape of the LUMO band (upper panel) and the HOMO band (lower panel) of Tetracene in the major crystal directions; the right panel is the corresponding Density of States.

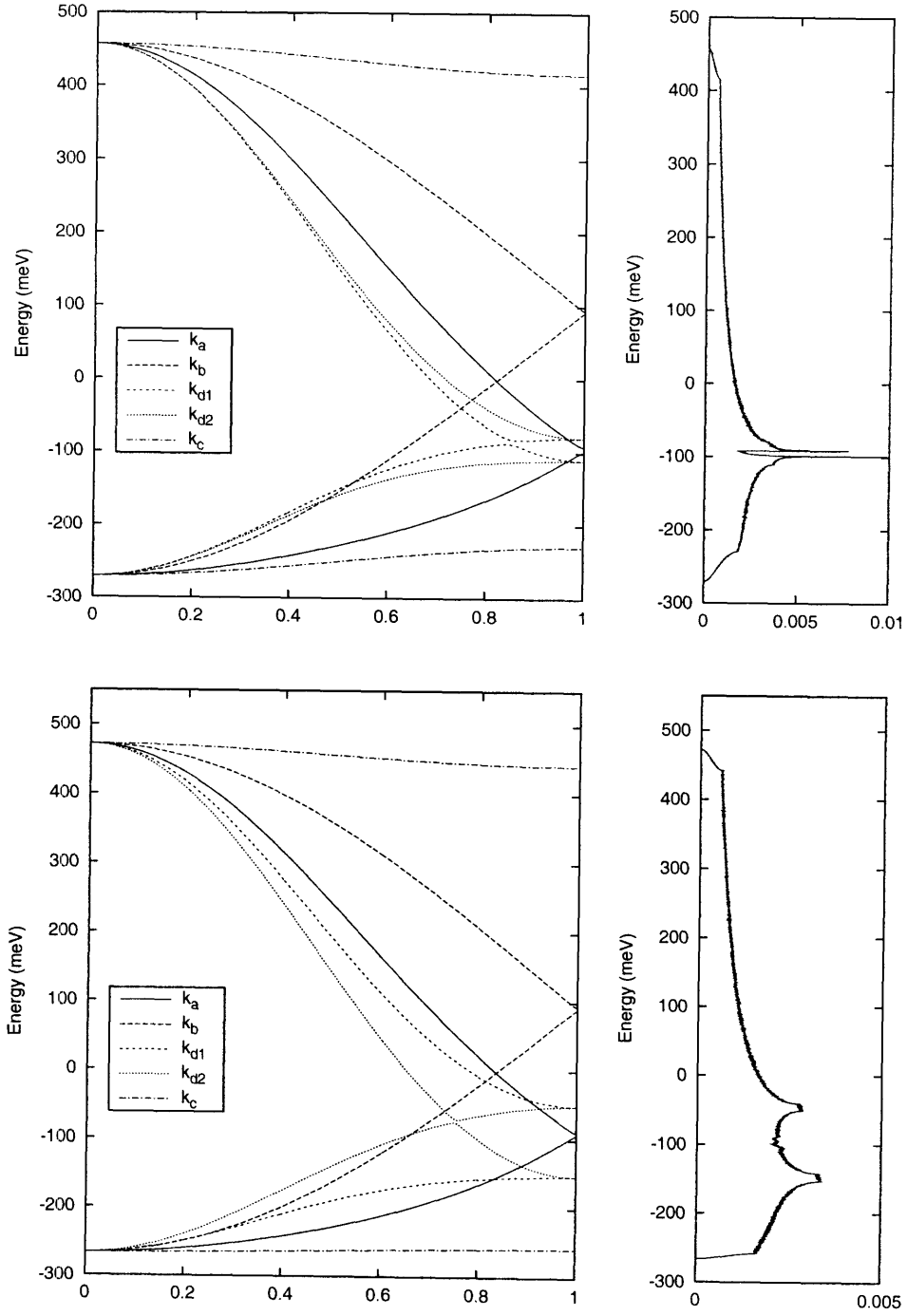

Figure 2-5: Shape of the LUMO band (upper panel) and the HOMO band (lower panel) of Pentacene in the major crystal directions; the right panel is the corresponding Density of States.

Table 2.3: Widths of excess electron and hole bands (units: meV).

	Naphthalene		Anthracene		Tetracene		Pentacene	
Direction	HOMO	LUMO	HOMO	LUMO	HOMO	LUMO	HOMO	LUMO
a^{+}[a]	75.65	183.95	249.26	251.44	207.71	275.22	560.89	548.77
a^{-}[b]	87.62	183.95	249.26	251.44	306.76	113.59	173.40	172.16
a_{gap}[c]	0.00	0.00	0.00	0.00	111.02	89.53	4.08	7.08
a_{width}[d]	163.27	367.90	498.52	502.87	625.49	478.34	738.37	728.00
b^{+}	235.65	228.58	442.46	371.17	305.13	225.15	377.76	362.64
b^{-}	103.11	139.32	67.43	131.70	300.77	245.83	355.44	362.64
b_{gap}	0.00	0.00	0.00	0.00	19.59	6.26	5.17	2.72
b_{width}	266.38	367.90	509.89	502.87	625.49	477.24	738.37	728.00
c^{+}	111.57	4.35	88.17	19.05	45.89	57.38	30.09	41.27
c^{-}	99.59	28.30	88.17	37.55	41.54	78.06	7.78	41.27
c_{gap}	163.27	339.60	322.19	446.27	538.06	341.80	700.50	645.47
c_{width}	374.43	372.25	498.52	502.87	625.49	477.24	738.37	728.00
$d_1{}^{+}$	229.67	228.58	442.46	371.17	216.50	208.50	523.09	539.88
$d_1{}^{-}$	66.40	139.32	56.06	131.70	307.19	93.08	113.28	183.12
$d_{1_{gap}}$	0.00	0.00	0.00	0.00	101.79	175.66	102.00	5.00
$d_{1_{width}}$	229.67	367.90	498.52	502.87	625.49	477.24	738.37	728.00
$d_2{}^{+}$	229.67	228.58	442.46	371.17	205.12	271.79	542.88	536.89
$d_2{}^{-}$	66.40	139.32	56.06	131.70	306.43	93.08	191.58	160.28
$d_{2_{gap}}$	0.00	0.00	0.00	0.00	101.79	175.66	3.91	30.82
$d_{2_{width}}$	229.67	367.90	498.52	502.87	625.49	477.24	738.37	728.00
Total[e]	409.00	372.30	509.40	508.30	625.50	502.70	738.40	728.00

[a] Widths of the upper bands. [b] Widths of the lower bands. [c] Widths of the gaps between the upper and lower bands. [d] Total bandwidth along this direction. [e] 3-D total bandwidths are calculated from the widths of the continuous region in the DOS spectrum.

728 meV, respectively); this could easily lead to the conclusion that the electrons can be as mobile as holes in pentacene crystals. However, if we consider the thermal population and compare mobilities according to the width of the upper HOMO band for excess hole and the lower LUMO band for excess electron (523 meV and 183 meV, respectively), the intrinsic excess hole mobility is predicted to be significantly larger than the intrinsic excess electron mobility in a pentacene crystal. Therefore, the width of the upper HOMO band appears to be a better parameter for estimating excess hole mobility, and the width of the lower LUMO band is a better parameter for estimating excess electron mobility. According to these two criteria, we predict all oligoacenes investigated here to have higher excess hole mobilities, in agreement with experimental results [31, 12].

2.3.3 Thermal Averaged Velocity-Velocity Tensor

The calculated thermal-averaged velocity-velocity tensor products in constant-free-time and constant-free-path approximations for naphthalene in the temperature range from 1.7 K to 300 K are presented in Fig. 2-6. Data for all other oligoacene crystals have a similar temperature dependence and are therefore not presented here. For all four crystals studied here, the components $\langle V_a V_a \rangle$ and $\langle V_b V_b \rangle$ show a linear temperature dependence at temperatures higher than 10 K, which can be ascribed to the increasing thermal population of higher energy states. The component $\langle V_{c'} V_{c'} \rangle$ behaves differently and saturates quickly at about 100 K, which can be easily understood by considering the small bandwidth ($\sim$ 30 meV) and the band gap along the $\mathbf{c}'$ direction. Because of the small bandwidth along this direction, charge carriers quickly populate the nonparabolic part of the band as temperature increases, resulting in the saturation of the group velocity of charge carriers. To test the result, we calculated values of the other two diagonal components at higher temperatures, no saturation behavior can be observed in $\langle V_a V_a \rangle$ and $\langle V_b V_b \rangle$ up to 1000 K, in agreement with the larger values of bandwidths along these directions.

The amplitude of $\langle V_{c'} V_{c'} \rangle$ at low temperatures is comparable to or even larger than the components along the **a** and **b** directions. This result seems to be contrary to the

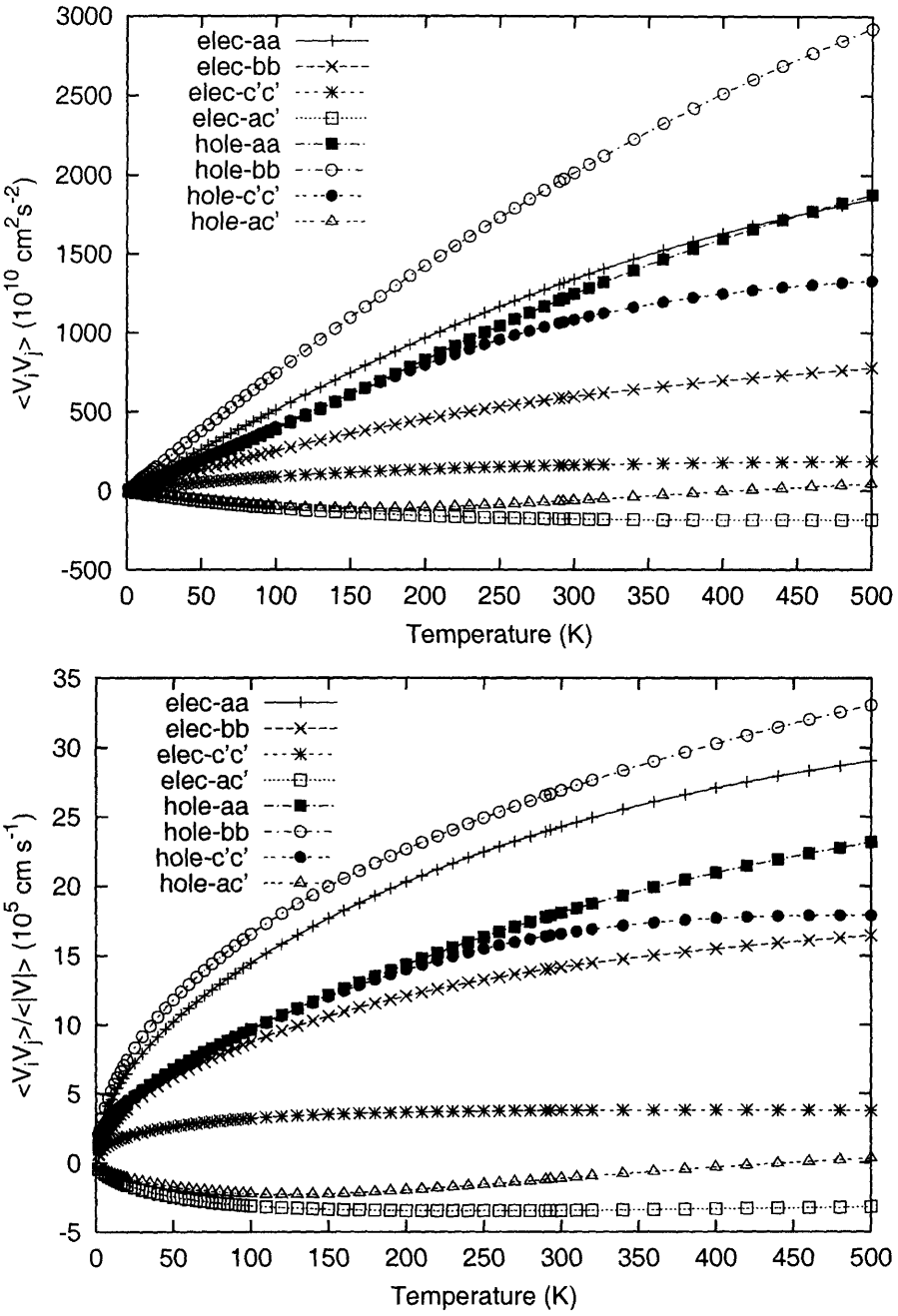

Figure 2-6: Temperature dependence of naphthalene velocity-velocity tensor under constant-free-time approximation (upper panel) and constant-free-path approximation (lower panel).

general belief that the in-plane mobilities are significant higher than the perpendicular ones in oligoacene single crystals, and the result that the transfer integral along the $\mathbf{c}'$ direction is much smaller than transfer integrals on the plane. However, on closer inspection, the unexpected large value of $\langle V_{c'} V_{c'} \rangle$ can be explained by considering the thermal population of the electronic states. The states at the bottom of the band have zero velocities. Therefore, in order to obtain any non-zero velocity, states with higher energy have to be populated. If the band is narrow, states with higher velocity can be populated at lower temperature; if the band is broad, then only states with low velocity are populated at low temperature. As a result, the value of $\langle V^2 \rangle$ is a trade-off between the width of the band and the population of states with higher velocity (which is easier to achieve for narrower bands).

Table 2.4 lists values of six tensor components for all four oligoacene crystals at 50 K. Note that for crystals with monoclinic unit cells, such as naphthalene and anthracene, the $\mathbf{b}$ direction is one of the three principal axes, so that there are only four nonzero mobility components. However, the orientations of the three principal axes for the triclinic unit cells are not unique, and in general all six mobility tensor components for tetracene and pentacene crystals are nonzero. Given the approximations in our model, these velocity-velocity tensor products contain the contribution to the charge carrier mobility from the potential energy field applied to the charge carrier. Therefore, diagonal components of these products can be seen as the theoretical upper bound of the charge carrier mobilities when scattering processes are omitted. Values of these tensor components again suggest that the excess hole mobility is higher than the excess electron mobility in oligoacene crystals, and that the mobilities increase with chain length in agreement with the previous considerations. Furthermore, great variations between values of components along different directions indicate highly anisotropic crystal environments in these crystals.

2.3.4 Self-Consistency Check on the Band Model

The use of a band representation to describe the motion of the charge carriers in the crystal can be justified only when both the mean free path exceeds many intermolec-

Table 2.4: Components of thermal averaged velocity-velocity tensor product in constant-free-time and constant-free-path approximations at 50 K.

	Naphthalene		Anthracene		Tetracene		Pentacene	
	Hole	Elec.	Hole	Elec.	Hole	Elec.	Hole	Elec.
$\langle V_a^2 \rangle^a$	191.19	261.19	376.12	435.62	358.76	556.63	852.48	137.47
$\langle V_b^2 \rangle^a$	380.04	131.95	618.32	122.26	537.92	365.56	532.15	528.47
$\langle V_{c'}^2 \rangle^a$	199.08	52.88	351.97	158.08	312.27	416.25	251.48	355.19
$\langle V_a V_{c'} \rangle^a$	-57.40	-64.92	-111.80	-58.62	-140.79	-95.96	0.98	-75.27
$\langle V_a V_b \rangle^a$	0	0	0	0	197.94	-48.06	72.68	46.81
$\langle V_b V_{c'} \rangle^a$	0	0	0	0	-134.86	-160.37	-32.92	-79.35
$\langle V_a^2/\mid \mathrm{V}\mid \rangle^b$	6.75	10.21	9.85	13.32	9.56	13.12	17.82	4.72
$\langle V_b^2/\mid \mathrm{V}\mid \rangle^b$	11.81	6.20	14.57	4.96	13.49	9.54	12.30	13.99
$\langle V_{c'}^2/\mid \mathrm{V}\mid \rangle^b$	6.72	2.61	9.38	6.25	8.82	10.76	6.93	10.60
$\langle V_a V_{c'}/\mid \mathrm{V}\mid \rangle^b$	-1.74	-2.46	-2.31	-1.46	-3.22	-2.07	0.01	-1.99
$\langle V_a V_b/\mid \mathrm{V}\mid \rangle^b$	0	0	0	0	4.29	-0.80	1.55	1.18
$\langle V_b V_{c'}/\mid \mathrm{V}\mid \rangle^b$	0	0	0	0	-2.81	-3.53	-0.69	-1.79

[a] Constant free-time approximation; units: $10^{10} cm^2 \cdot sec^{-2}$.

[b] Constant free-path approximation; units: $10^5 cm \cdot sec^{-1}$.

ular distances and the uncertainty in the energy of the scattered carriers does not exceed the bandwidth:

$$\lambda \gg a_0$$
$$W \gg \hbar/\tau_0.$$

For the crystals studied here $a_0 \approx 5$ Å and $W \approx 0.5$ eV, therefore the criteria for band theory to be applicable are λ longer than 5 Å and τ_0 larger than 10^{-15} s. To examine the applicability of the band model used in our calculations, the temperature dependent mean free time and mean free path were calculated by fitting the available experimental mobility data [19, 12] to our theoretical thermal-averaged velocity-velocity tensor products using Eq. 2.6 and Eq. 2.7. The results in the temperature range from 30 K to 300 K for excess hole in naphthalene crystal are presented in Fig. 2-7.

From Fig. 2-7, it can be clearly seen that the above criteria are fulfilled only

at temperature lower than 150 K, and any application of this simple band model to temperatures higher than 150 K is open to criticism. In addition, the calculated results along different directions are significantly different, which implies that the scattering processes are highly anisotropic.

Because of possible highly anisotropic scattering processes, the use of constant-free-path or constant-free-time approximations should be treated with care, and a better approach would be to consider the free time or free path as a temperature dependent tensor property of the crystal. Basically, the present model keeps the mobility anisotropy originating from the energy band structure in the averaged velocity-velocity tensor, and puts dynamic effects related to the scattering processes into the constant-free-path or constant-free-time terms. Using only averaged free time or free path to describe the scattering processes can only be justified when the following conditions are all fulfilled: (i) The scattering processes along the three different crystal directions are the same. (ii) Coupling between charge carriers and crystal phonons is small. (iii) Molecular motions have only a small effect on the electronic structure of the crystal. Note that the constant-free-time and constant-free-path approximations are very crude especially for organic molecular crystal systems, because the highly anisotropic crystal environments and somewhat small (compared to traditional inorganic semiconductors) intermolecular interactions contradict the basic assumptions behind these approximations. Early investigations related to band-like mobility calculations tried to compare the predicted mobility anisotropy to the experimental data in order to verify the theory [2, 23, 24]; this should be taken with much caution because of the possible differences of scattering processes along different crystal directions, and considering the band structure effect alone is unlikely to account for the real anisotropy in mobilities.

2.4 Polaronic Effects

In order to understand the temperature dependence of the mobilities, one should include the possibility of the formation of polaron bands [17]. Especially, in the case

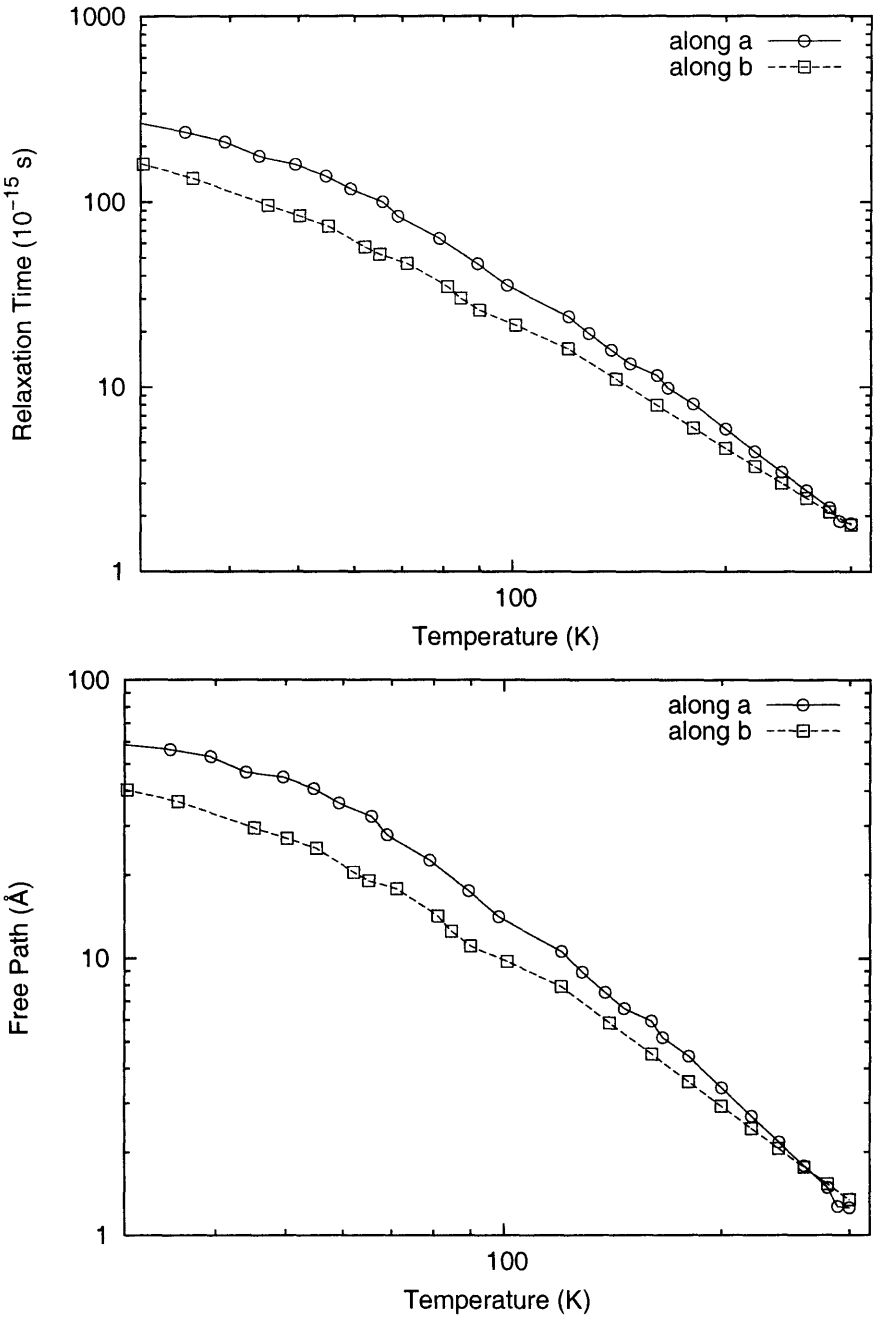

Figure 2-7: Temperature dependence of calculated hole relaxation time (upper panel) and hole free path (lower panel) for naphthalene crystal. Results along the crystal $\vec{a}$ direction (open circle) and $\vec{b}$ direction (open square) are presented.

of the oligoacene crystals where low frequency optical modes exist, excitation of these optical modes can renormalize the transfer matrix elements significantly, because the transfer matrix elements are strongly dependent on orbital overlap in these systems [33]. In addition, there are low lying librational modes in the oligoacene crystals, these modes will be moderately to strongly coupled to the transfer matrix elements [35, 36]. A theoretical description of the effect of a strongly coupled optical mode on the diffusion or mobility of an electron or hole in a molecular crystal was first given by Holstein [37, 38] and discussed further by many other authors [39, 40, 41, 17]. Here we will only use the results of these theoretical investigations.

We assume that at least one optical mode is coupled moderately or strongly to the transfer matrix elements and that the band width of this mode is much smaller than its frequency, so that we can approximate the optical mode as a local mode. We also assume that the coupling constant of that local mode to the transfer matrix elements is approximately independent of the sites involved in the transfer matrix element. Finally we assume that the coupling is not strong enough to localize the electron or hole, so that the correct description of the transport is that of a polaron band model (i.e. that hopping transport, although described by the same Hamiltonian, is a small term in the temperature range of interest). Under these circumstances, the effect of the electron-optical phonon coupling is to renormalize the effective transfer matrix elements and make the effective bandwidth temperature dependent. As the temperature increases, the effective bandwidth decreases.

In the small polaron theory, the standard form to describe the temperature dependence of the effective transfer matrix elements is

$$t_{eff} = \bar{t} \exp(-g^2 \coth(\beta\omega/2)), \tag{2.9}$$

where g is the electron-optical phonon coupling constant, ω is the optical phonon frequency, and β is $1/k_bT$. As a simple test, we use Eq. 2.9 to calculate the effective transfer matrix elements at different temperatures, and then use the results to construct the polaron band structure and calculate velocity-velocity tensors according to

the procedure described in section 2.2. Several different values of both g and ω are used to perform the calculation, and we found that only a large ω and small g can produce a reasonable fit to the experimental power law results. However, the exponential band-narrowing effect described in Eq. 2.9 results in a exponential decrease of mobility when $k_bT > \omega$, contradicting the power law results observed in experiments. Therefore, a full-dressed small polaron band theory is inadequate for describing the charge-carrier mobilities in oligoacene single crystals. Similar results appear to have been obtained by Giuggioli *et al.* independently to the present work [42]. Given that in organic crystals, the electron-phonon coupling constant is believed to be small to intermediate in value and the bare bandwidth is large, it is possible that the polaron band narrowing effect does not obey a simple exponential form as in Eq. 2.9. A polaron-band theory that includes the correct band narrowing effect is necessary to adequately describe charge-carrier mobilities in the band-like regime.

The complicated anisotropic environment as well as the subtle interplay between crystal packing and transfer integrals make the charge-carrier transport in molecular crystals a complicated phenomena. The phonon modes in molecular crystals have different frequency and bandwidth, and also couple to the electronic states with different mechanism and strength. Kenkre *et al.* have used a band model with both acoustic and optical phonon scattering to obtain a reasonable fit to the pentacene experimental data in the band-transportation regime [43]. Their study suggests that in order to describe the experimental data using a polaron band theory, at least two-phonon modes, one moderately to strongly coupled and the other weakly coupled to the electron, are necessary. The strongly coupled mode (most likely an intermolecular optical mode) *dresses* the carrier and produces a polaron band, and the weakly coupled mode (most likely an acoustic mode) does the scattering among the polaron band states. As a result, the temperature dependence of mobilities is due to both the temperature dependent polaron bandwidth and the temperature dependent scattering rate.

2.5 Conclusion

In this chapter, transfer integrals for four oligoacene single crystals are calculated using the INDO semi-empirical method, and then used to construct the excess electron and hole band structures in the tight-binding approximation. The band structure results suggest that a two-band model is necessary to understand the trend of mobilities in different oligoacene crystals, and the width of the upper HOMO band or the width of the lower LUMO band is a better parameter for estimating the mobility for excess holes or electrons, respectively. Our theoretical model can be used to explain the experimental results that the hole mobility is higher than the electron mobility in oligoacene single crystals and that compounds with a longer conjugation length tend to have higher mobility values.

From these band structures, thermal-averaged velocity-velocity tensors are evaluated using a standard semiconductor mobility theory. We have compared these tensors to recent experimental data. We conclude that a simple band model is unable to explain the temperature dependence of the charge carrier mobility in oligoacene crystal systems for temperatures higher than 150 K, and that the approximations that constant-free-time and constant-free-path are isotropic are open to criticism. In conclusion, a simple wide-band theory is insufficient for describing charge-carrier mobilities of oligoacene single crystals even in the band-like regime.

A closer study of the polaron effect using the standard small polaron narrowing model shows that a fully-dressed small polaron band theory is also inadequate for describing the charge-carrier mobilities in oligoacene single crystals. This result suggests that the next step beyond the simple band model will be to develop a model that can explicitly include the polaronic effects. The key issue is to obtain the correct form for the polaron band narrowing effect. By means of a microscopic model Hamiltonian and a variational-perturbational technique, we will develop a unified theory in the next chapter of this Thesis that considers explicitly the electron-phonon interactions and describes the polaron band-narrowing effect.

Bibliography

[1] R. G. Kepler. Charge carrier production and mobility in anthracene crystals. *Phys. Rev.*, 119(4):1226, 1960.

[2] Oliver H. LeBlanc. Band structure and transport of holes and electrons in anthracene. *J. Chem. Phys.*, 35(4):1275, 1961.

[3] N. Karl. Studies of organic semiconductors for 40 years .3. *Mol. Cryst. Liq. Cryst.*, 171:31 – 51, 1989.

[4] Martin Pope and Charles E. Swenberg. *Electronic Processes in Organic Crystals.* Oxford University Press, New York, 1982.

[5] Edgar A. Silinsh and Vladislav Čápek. *Organic Molecular Crystals: Interaction, Localization, and Transport Phenomena.* AIP Press, Woodbury, NY, 1994.

[6] R. Farchioni and G. Grosso, editors. *Organic Electronic Materials:Conjugated Polymers And Low Molecular Weight Organic Solids.* Springer, New York, 2001.

[7] C. D. Dimitrakopoulos and D. J. Mascaro. Organic thin-film transistors: A review of recent advances. *IBM J. Res. & Dev.*, 45(1):11, 2001.

[8] H. Klauk, D. J. Gundlach, J. A. Nichols, and T. N. Jackson. Pentacene organic thin-film transistors for circuit and display applications. *IEEE Trans. Electron Devices*, 46(6):1258 – 1263, 1999.

[9] Wilhelm Warta and Norbert Karl. Hot holes in naphthalene: High, electric-field-dependent mobilities. *Phys. Rev. B.*, 32(2):1172, 1985.

[10] D. J. Gundlach, Y. Y. Lin, T. N. Jackson, S. F. Nelson, and D. G. Schlom. Pentacene organic thin-film transistors - Molecular ordering and mobility. *IEEE Electron Dev. Lett.*, 18(3):87 – 89, 1997.

[11] N. Karl. Fast electronic transport in organic molecular solids? *J. Vac. Sci. Technol. A*, 17(4):2318, 1999.

[12] N. Karl and J. Marktanner. Electron and hole mobilities in high purity anthracene single crystals. *Mol. Cryst. Liquid Cryst.*, 355:149 – 173, 2001.

[13] L. B. Schein, C. B. Duke, and A. R. McGhie. Observation of the band-hopping transition for electrons in naphthalene. *Phys. Rev. Lett.*, 40:197, 1978.

[14] L. B. Schein, W. Warta, A. R. McGhie, and N. Karl. Mobilities of electrons and holes in naphthalene and perdeuterated naphthalene. *Chem. Phys. Lett.*, 100(1):34 – 36, 1983.

[15] C. B. Duke, A. Paton, W. R. Salaneck, H. R. Thomas, E. W. Plummer, A. J. Heeger, and A. G. MacDiarmid. Electronic-structure of polyenes and polyacetylene. *Chem. Phys. Lett.*, 59(1):146 – 150, 1978.

[16] J. D. Andersen, C. B. Duke, and V. M. Kenkre. Injected electrons in naphthalene: Band motion at low temperatures. *Phys. Rev. Lett.*, 51(24):2202, 1983.

[17] V. M. Kenkre, John D. Andersen, D. H. Dunlap, and C. B. Duke. Unified theory of the mobilities of photoinjected electrons in naphthalene. *Phys. Rev. Lett.*, 62(10):1165, 1989.

[18] S. F. Nelson, Y. Y. Lin, D. J. Gundlach, and T. N. Jackson. Temperature-independent transport in high-mobility pentacene transistors. *Appl. Phys. Lett.*, 72(15):1854 – 1856, 1998.

[19] N. Karl. *Organic Semiconductors*, volume 17 of *Landolt Börnstein/New Series Group III.* Springer, Berlin, subvol. 17i, pp. 106-218 edition, 1985.

[20] J. Ridley and M. C. Zerner. An intermediate neglect of differential overlap technique for spectroscopy: Pyrrole and the azines. *Theor. Chim. Acta.*, 32:111, 1973.

[21] J. Cornil, J. Ph. Calbert, D. Beljonne, R. Silbey, and J. L. Brédas. Charge transport versus optical properties in semiconducting crystalline organic thin films. *Adv. Mater.*, 12(13):978, 2000.

[22] J. Cornil, J. Ph. Calbert, and J. L. Brédas. Electronic structure of the pentacene single crystal: Relation to transport properties. *J. Am. Chem. Soc.*, 123(6):1250, 2001.

[23] J. I. Katz, S. A. Rice, S. Choi, and Joshua Jortner. On the excess electron and hole band structure and carrier mobility in naphthalene, anthracene, and several polyphenyls. *J. Chem. Phys.*, 39:1683, 1963.

[24] R. J. Silbey, J. Jortner, S. A. Rice, and Martin T. Vala. Exchange effects on the electron and hole mobility in crystalline anthracene and naphthalene. *J. Chem. Phys.*, 42(2):733, 1965.

[25] D. Beljonne, J. Cornil, R. Silbey, P. Millie, and J. L. Bredas. Interchain interactions in conjugated materials: The exciton model versus the supermolecular approach. *J. Chem. Phys.*, 112(10):4749 – 4758, 2000.

[26] V. I. Ponomarev, O. S. Filipenko, and L. O. Atovmyan. Structure and vibrational spectrum of some polycyclic aromatic compounds studied by density functional theory. i. naphthalene, azulene, phenanthrene, and anthracene. *Kristallografiya*, 21:392, 1976.

[27] C. P. Brock and J. D. Dunitz. Temperature dependence of thermal motion in crystalline anthracene. *Acta. Crystallogr. Sect. B (Str. Sci.)*, 46:795, 1990.

[28] D. Holmes, S. Kumaraswamy, A. J. Matzger, and K. P. C. Vollhardt. On the nature of nonplanarity in the [N]phenylenes. *Chem.-Eur. J.*, 5(11):3399 – 3412, 1999.

[29] M. C. Zerner, G. H. Loew, R. F. Kichner, and U. T. Mueller-Westerhoff. Intermediate neglect of differential-overlap technique for spectroscopy of transition-metal complexes - ferrocene. *J. Am. Chem. Soc.*, 102:589, 1980.

[30] R. M. Glaeser and R. Stephen Berry. Mobilities of electrons and holes in organic molecular solids. comparison of band and hopping models. *J. Chem. Phys.*, 44(10):3797, 1966.

[31] W. Warta, R. Stehle, and N. Karl. Ultrapure, high mobility organic photoconductors. *Appl. Phys. A*, 36:163, 1985.

[32] N. Karl. Growth and electrical-properties of high-purity organic molecular-crystals. *J. Cryst. Growth*, 99(1-4):1009 – 1016, 1990.

[33] J. L. Brédas, J. P. Calbert, D. A. da Silva, and J. Cornil. Organic semiconductors: A theoretical characterization of the basic parameters governing charge transport. *Proc. Natl. Acad. Sci. U. S. A.*, 99(9):5804 – 5809, 2002.

[34] R. C. Haddon, X. Chi, M. E. Itkis, J. E. Anthony, D. L. Eaton, T. Siegrist, C. C. Mattheus, and T. T. M. Palstra. Band electronic structure of one- and two-dimensional pentacene molecular crystals. *J. Phys. Chem. B*, 106(33):8288 – 8292, 2002.

[35] H. Sumi. Exciton-lattice interaction and line-shape of exciton absorption in molecular-crystals. *J. Chem. Phys.*, 67(7):2943 – 2954, 1977.

[36] H. Sumi. Theory of electrical-conduction in organic molecular-crystals - temperature-independent mobilities. *J. Chem. Phys.*, 70(8):3775 – 3785, 1979.

[37] T. Holstein. Studies of polaron motion, part 1. the molecular-crystal model. *Ann. Phys. (N. Y.)*, 8:325, 1959.

[38] T. Holstein. Studies of polaron motion, part 2. the "small" polaron. *Ann. Phys. (N. Y.)*, 8:343, 1959.

[39] R. J. Silbey and R. W. Munn. General theory of electronic transport in molecular crystals. I. local linear electron-phonon coupling. *J. Chem. Phys.*, 72(4):2763, 1980.

[40] D. R. Yarkony and R. J. Silbey. Variational approach to exciton transport in molecular crystals. *J. Chem. Phys.*, 67(12):5818, 1977.

[41] D. Emin. On the existence of free and self-trapped carriers in insulators: An abrupt temperature-dependent conductivity transition. *Adv. Phys.*, 22:57, 1973.

[42] L. Giuggioli, J. D. Andersen, and V. M. Kenkre. preprint.

[43] P. E. Parris and V. M. Kenkre. Variational considerations in the study of carrier transport in organic crystals. *Phys. Rev. B*, 70(6):064304, 2004.

Chapter 3

A Unified Theory for Charge Transport in Molecular Crystals

3.1 Introduction

In the previous chapter, we have calculated electronic structures for 3-D polyacene crystals, and showed that simple wide-band model is insufficient for the description of experimental charge-carrier mobilities. We also argued that the polaronic effect is important for a sound description of the charge-carrier mobilities in these systems [1, 2]. In this chapter, we study a microscopic model that treats electron-phonon interactions explicitly, and focus on the problem regarding the coherent band-like versus incoherent hopping transport in molecular crystals. Despite numerous studies concerning the puzzling band-like to hopping transition, a quantitative theory that can describe the charge-carrier behavior in both regimes is still not at hand. Our work in this chapter aims at filling this gap.

It is well known that electron-phonon interactions play a central role in the intrinsic transport properties of organic molecular crystals (OMC), however, the large number of parameters governing the system makes the problem extremely complicated. To name a few, the exciton and charge-carrier transport in OMC is governed by: (1) the width of the electronic band (Δ, determined by resonance transfer integrals between electronic states), (2) the mechanisms and strength of electron-phonon

couplings (g), (3) the characteristics of the phonon bands (e.g. phonon frequency ω_0 and widths of phonon bands), and (4) temperature (T). In addition, the complexity of the vibrations and the absence of any clear ordering of the parameters make the description of charge-carrier transport in OMC a formidable problem. The situation is more complex for wide-band materials because the effective bandwidth Δ of the charge-carriers can crossover from $\Delta \gg \omega_0$ at low temperatures to $\Delta \ll \omega_0$ at high temperatures due to the polaronic band narrowing effect. The development of wide-band materials have necessitated the development of a unified theory that is applicable in all parameter regimes.

Theories constructed for a particular picture of transport have been successful in specific regimes of electron-phonon coupling strengths; however, a general description that is applicable in all parameter regimes is still unavailable. Early phenomenological transport theories, including band theory [3], stochastic Liouville equation model [4, 5, 6, 7], and polaron effective mass model [2], have been successfully applied to many related problems, but all of them were restricted in scope and failed to provide a complete description in the light of the recent discoveries in experiments on ultrapure crystals [8, 9, 2].

Microscopic models that explicitly include the electron-phonon interactions in the Hamiltonian seem to offer more promising results. In particular, a microscopic model first given by Holstein [10] has been used to study the effect of a moderately to strongly coupled optical mode on the diffusion or mobility of an electron or hole in a molecular crystal. The Holstein Hamiltonian has been examined extensively by many authors to describe charge-carrier and exciton transport [11, 12, 13, 14, 15], and to consider energy transfer between molecules embedded in a lattice [16]. These models are capable of reproducing both weak-coupling and strong-coupling results, but their applicability in the intermediate coupling regime is still not clear. Generally speaking, all theoretical calculations have so far failed to provide the correct magnitudes and temperature dependences of the charge-carrier mobilities in organic molecular crystal systems [17, 18, 2].

Yarkony and Silbey's variational approach [19, 12] to exciton transport in molec-

ular crystals offered a promising direction to the solution of the problem, because in principle the variational method can provide the optimal partition between the zeroth-order Hamiltonian and the perturbation, hence making the perturbation expansion in the intermediate coupling regime justified. Recently, Parris and Kenkere have extended Yarkony and Silbey's variational method to treat two phonon bands in three spatial dimensions [20]. They argued that two phonon bands, one that narrows the band while the other scatters the electron, are required to describe the temperature dependence of charge-carrier mobilities in OMC. However, the variational ansatz used by Yarkony and Silbey contains only one variational variable, and is known to suffer from a lack of flexibility [21]. Therefore, a more flexible ansatz is necessary to obtain the correct temperature dependence of mobilities.

In this chapter, we develop a microscopic model that describes quantitatively the crossover from the coherent band-like regime to the incoherent hopping regime in a single unified theory. In Section 3.2, we will describe the finite-temperature variational method and the model Hamiltonian used in this study, and derive expressions that are necessary for calculating the charge-carrier mobilities in OMC. In essence, our variational approach extends the scope of applicability of Yarkony's method by using a more flexible ansatz. To demonstrate the improvement that a variational basis provides, in Section 3.3, we will employ a simplified version of the variational method and time-independent second-order perturbation theory to study the polaron problem at zero K in one dimension, and compare our results to results from previous studies by other groups. In Section 3.4, we will apply the variational approach to a one dimension interacting electron-phonon system to examine the nature of polaron states in different parameter regimes and study the temperature dependence of both band-like and hopping transport. Most importantly, we will show that when the temperature increases, the hopping transport can become dominate even before the polaron state changes its character. Thus, our result indicates that the self-trapping transition studied in conventional polaron theories does not necessary correspond to the band-like to hopping transition in the transport properties in OMC. Then, in Section 3.5, we compare our results to experiments on the temperature dependent

charge-carrier mobilities in ultrapure naphthalene crystals to show that our theoretical description provides quantitative agreement for both hole and electron mobilities in naphthalene crystals. Finally, in Section 3.6 we briefly summarize our conclusions and remarks.

3.2 Theoretical Models

In this section, we present the theoretical model that is developed to describe the charge transport in molecular crystals. We first show that the Bogoliubov's theorem on the upper bound on the free-energy of a quantum system can be used as the foundation of a variational method, and describe the Holstein Hamiltonian and Merrifield's transformation that we used to model an excess charge-carrier in molecular crystals. We then combine the Bogoliubov's Bound and Merrifield's transformation to derive a finite-temperature variational method that can be used to obtain the optimal polaronic state for an interacting electron-phonon system. In the end of this section, we consider a formula for charge-carrier mobilities that describes both band-like and hopping transport, and derive expressions that can be used to compute mobilities based on the optimal polaronic state obtained from the variational method.

3.2.1 Bogoliubov's Bound on the Free Energy

We first describe our formulation for an upper bound on the free energy of a general electron-phonon system. The Helmholtz free energy A for a system defined by a Hamiltonian H at temperature T is given by

$$A_H = -\beta^{-1} \ln \mathrm{Tr} e^{-\beta H}. \tag{3.1}$$

where $\beta = k_B T$. For general interacting electron-phonon systems, explicit calculation of the free energy is a formidable task. Fortunately, the following inequality exists as a consequence of the convexity of the exponential function:

Bogoliubov's theorem: If H and H' are two self-adjoint operators with the prop-

erty that the traces $\mathbf{Tr}\{\exp(-\beta H)\}$ and $\mathbf{Tr}\{\exp(-\beta H')\}$ are finite for all $\beta > 0$, then one has, for all $\beta > 0$,

$$-\beta^{-1} \ln \mathbf{Tr} e^{-\beta H} \leq -\beta^{-1} \ln \mathbf{Tr} e^{-\beta H'} + \langle H - H' \rangle_{H'} \equiv A_H^B(H')$$

where the bracket $\langle ... \rangle_{H'}$ denotes average according to the trial Hamiltonian H'

$$\langle H - H' \rangle_{H'} = \frac{\mathbf{Tr}\{(H - H')e^{-\beta H'}\}}{\mathbf{Tr} e^{-\beta H'}}.$$

Bogoliubov's theorem provides us with a convenient method to calculate an upper bound $A_H^B(H')$ on the free energy using a trial Hamiltonian H'. Generally, we can partition the full Hamiltonian H into a zeroth order Hamiltonian H_0 whose eigenstates are well defined, and a perturbation part V, so that $H = H_0 + V$. Using H_0 as the trial Hamiltonian enables us to evaluate a upper bound on the free energy. Note that the Bogoliubov's theorem is equivalent to saying that first-order thermodynamic perturbation theory always yields an upper bound. In addition, we can use a trial Hamiltonian that contains adjustable variational parameters, and by minimizing the Bogoliubov's bound with respect to these variational parameters, we can obtain the optimal choice for the partition of the Hamiltonian into a zeroth order part and a perturbation part. Thus, based on the Bogoliubov's theorem, we can construct a finite-temperature variational theory that provides temperature dependent optimal zeroth order Hamiltonian for the general electron-phonon system.

Since the free energy is invariant under unitary transformations, a systematic way to introduce the trial Hamilton is to apply a unitary transformation that contains variational parameters on the Hamiltonian, and use part of the transformed Hamiltonian as the trial Hamiltonian to calculate the Bogoliubov's bound. Suppose a unitary transformation U ($U^\dagger U = 1$) is applied on H so that

$$\begin{aligned} \tilde{H} &= U^\dagger H U \\ &\equiv \tilde{H}_0 + \tilde{V}, \end{aligned}$$

where $\tilde{H}_0$ is the zeroth order part whose exponential $e^{-\beta\tilde{H}_0}$ can be evaluated, the Bogoliubov's bound becomes

$$A_H^B(\tilde{H}_0) = -\beta^{-1} \ln \mathbf{Tr} e^{-\beta\tilde{H}_0} + \langle \tilde{V} \rangle_{\tilde{H}_0}. \tag{3.2}$$

In the following, this expression will be used to compute the upper bound on the free energy of an interacting electron-phonon system.

3.2.2 The Hamiltonian and Merrifield's Transformation

We investigate the Holstein molecular crystal model (Eq. 3.3) using a variational approach. The Holstein model [10, 22] is widely used to describe the transport properties of organic molecular crystals, and believed to contain the essential interactions that determine the behaviors of charge-carriers. The Hamiltonian includes a band of electronic excitation (electron or hole) in a perfect crystal coupled linearly to the coordinate of harmonic oscillators located at each site. For simplicity, we consider one molecule per unit cell and a narrow phonon band, i.e. Einstein's model of dispersionless phonons, which is a good description for the optical intramolecular modes in molecular crystals. The second quantized form of the Hamiltonian in the direct space representation (site representation) is given by ($\hbar = 1$)

$$H = H_e + H_{ph} + H_{int} \tag{3.3}$$

where

$$\begin{aligned} H_e &= \textstyle\sum_{n,m} J_{nm} a_n^\dagger a_m, \\ H_{ph} &= \omega_0 \textstyle\sum b_n^\dagger b_n, \end{aligned} \tag{3.4}$$

and

$$H_{int} = g\omega_0 \sum_n a_n^\dagger a_n \cdot (b_n^\dagger + b_n). \tag{3.5}$$

Here $a_n^\dagger$ (a_n) is the creation (annihilation) operator of the electronic excitation (electron or hole) at site n, ω_0 is the phonon frequency, and $b_n^\dagger$ (b_n) is the creation (annihilation) operator of the localized phonon state at site n. Throughout this work, we assume the position n and wavevectors are measured relative to the lattice constants, therefore the lattice constant and lattice structure of the crystal do not appear explicitly in our formulas. Hereafter we will call the electronic excitation as "electron", but it is actually general and can be readily translate to other charge-carriers or excitons. In addition, we assume the concentration of charge-carriers are small, so that we can work exclusively in the one particle subspace. The quantity J_{nm} is the transfer integral between localized electronic states at site n and site m. Because of the translational symmetry, J_{nm} is a function of $n-m$ only, i.e. $J_{nm} \equiv J_{n-m}$. The last term [Eq. (3.5)] is the electron-phonon coupling term, of magnitude determined by the dimensionless electron-phonon coupling constant g. Note that we assume the electron interacts linearly and locally to the phonon states. The Holstein Hamiltonian captures the interplay between the electronic couplings and the electron-phonon coupling, which is a repeating theme in quantum dynamics.

The electron-phonon Hamiltonian in Eqs. (3.3)-(3.5) has well-known exact solutions in two limiting cases. When the strength of electron-phonon coupling is set to zero, $g = 0$, H is diagonal in the k-space of the lattice; using the delocalized basis $a_k^\dagger = N^{-1/2}\sum_n e^{-ikn}a_n^\dagger$ and $b_q^\dagger = N^{-1/2}\sum_n e^{-iqn}b_n^\dagger$, the Hamiltonian at $g = 0$ can be diagonalized,

$$H = \sum_k E(k)a_k^\dagger a_k + \omega_0 \sum_q b_q^\dagger b_q,$$

with band energy given by

$$E(k) = \sum_{n' \neq 0} J_{n'} e^{ikn'}.$$

This representation corresponds to the free electron state, and is a good zeroth order basis in the weak-coupling regime in which the electronic couplings are stronger than

electron-phonon couplings ($|J| \gg g^2\omega_0$). Therefore, when g is small, a perturbation expansion in terms of g in the k-representation is justified; this kind of approach is usually called a weak-coupling perturbation theory (WCPT), and has been widely used to describe covalent bonded or ionic solid-state systems in which electronic interactions are strong. The wide-band model we applied in the previous chapter is an example of such a WCPT approach.

In the other limit where the resonance transfer integrals are set to zero ($J = 0$), the Hamiltonian can be diagonalized by the small polaron transformation:

$$U_S = e^{\frac{1}{\sqrt{N}} \sum_{n,q} g e^{iqn} a_n^\dagger a_n (b_{-q}^\dagger - b_q)}$$

Applying U_S onto the bare electronic operator yields a dressed "small polaron state":

$$A_n^\dagger = U_S a_n^\dagger U_S^\dagger = a_n^\dagger e^{-g(b_n - b_n^\dagger)}.$$

The operator $A_n^\dagger$ now not only creates an electron at site n, but also displaces the phonon mode at site n. The electron is now "dressed" because of the phonon cloud associated with it, and it is called the small polaron because the displacement of the phonon field is local. Applying U_S onto the Holstein Hamiltonian with $J = 0$, we obtain

$$U_S H U_S^\dagger = -g^2\omega_0 \sum_n a_n^\dagger a_n + \omega_0 \sum_q b_q^\dagger b_q.$$

The result is a transformed Hamiltonian diagonalized in the site representation; i.e. the Hamiltonian with $J = 0$ is diagonal in the small polaron basis. Therefore, the small polaron basis is a good zeroth-order representation when the electron-phonon coupling is stronger than the resonance transfer integrals of the electronic states ($|J| \ll g^2\omega_0$). This representation is referred to as the small polaron representation and is widely applied to study the electron-phonon Hamiltonian in the strong-coupling regime, in which a perturbation expansion in terms of renormalized J in the small

polaron representation is justified. This kind of approach is usually called a strong-coupling perturbation theory (SCPT).

Thus, well justified perturbation theories in both the weak-coupling and strong-coupling regimes are available and accurate. However, for intermediate coupling regime, there is no clear small parameters on which we can perform a perturbation expansion. It has been argued by many authors that in the intermediate coupling regime, a variational approach is required in order to provide adequate zero-order description of the electron-phonon system. To obtain a reasonable zeroth order representation in the intermediate coupling regime, we apply Merrifield's transformation [23, 24]:

$$U = e^{\left\{\sum_n a_n^\dagger a_n \sum_m f_m (b_{n+m} - b_{n+m}^\dagger)\right\}} \tag{3.6}$$

where $\{f_m\}$ are real parameters to be determined variationally. Note that m labels the relative lattice site, and f_m is the amplitude of the displacement to the equilibrium oscillator position at site $n+m$. For crystal structures with inverse symmetry, $f_m = f_{-m}$. The optimal transformation defined by $\{f_m\}$ may be temperature dependent because of the variational procedure. Note that when $f_m = \delta_m \cdot f$, the transformation is local and we recover Yarkony and Silbey's one-parameter unitary transformation ansatz. When $f_m = \delta_m \cdot g$, we recover Holstein's small polaron transformation, and the well know small polaron results. Therefore, Merrifield's transformation can be regarded as a generalization of the small polaron transformation to include nonlocal displacement of the phonon modes around the electronic excitation.

Merrifield's transformation takes a localized electron operator to a partially dressed state that includes a phonon cloud (deformation of lattice) surrounding the electron

$$\begin{aligned} A_n^\dagger &= U^\dagger a_n^\dagger U \\ &= a_n^\dagger e^{-\sum_m f_m (b_{n+m} - b_{n+m}^\dagger)} . \end{aligned}$$

This transformed basis can be seen as dressed states which contain electrons and

their tightly bound phonon cloud. Physically, Merrifield's transformation contains non-local displacement of the lattice surrounding the electron and the values of f_m correspond to the amplitude of displacement from the equilibrium phonon position. Thus, the set of variational parameters $\{f_m\}$ represents the degree of dressing. For the boson operators, we obtain

$$\begin{aligned} B_n^\dagger &= U^\dagger b_n^\dagger U = b_n^\dagger - \sum_m f_{n-m} \cdot a_m^\dagger a_m, \\ B_n &= U^\dagger b_n U = b_n - \sum_m f_{n-m} \cdot a_m^\dagger a_m. \end{aligned}$$

Substitution of these expressions into the Holstein Hamiltonian gives the transformed Hamiltonian:

$$\tilde{H} = U^\dagger H U = \tilde{H}_0 + \tilde{V}'.$$

The zeroth-order Hamiltonian $\tilde{H}_0$ is diagonal in the k-representation

$$\widetilde{\mathbf{H}}_0 = \sum_k \left[\omega_0 \cdot (\sum_m f_m^2 - 2g f_0) + \widetilde{J}_k \right] a_k^\dagger a_k + \omega_0 \sum_q b_q^\dagger b_q \equiv \tilde{H}_e + \tilde{H}_{ph}, \tag{3.7}$$

where the energy band $\widetilde{J}_k$ is given by renormalized resonance transfer integrals:

$$\widetilde{J}_k = \textstyle\sum_{n,m} e^{ik(n-m)} J_{nm} \cdot \langle \theta_n^\dagger \theta_m \rangle_0 \ ,$$

with the renormalization factors at finite temperatures given by

$$\langle \theta_n^\dagger \theta_m \rangle_0 = e^{-\frac{1}{2}\sum_{m'} (f_{m'-m} - f_{m'-n})^2 \cdot \coth(\beta\omega_0/2)}.$$

The transformed interacting term $\tilde{V}'$ has a complicated form

$$\begin{aligned}\widetilde{V}' &= \frac{1}{N}\sum_{k_1,k_2}\sum_{n,m} e^{-ik_1 n}e^{ik_2 m}\cdot J_{n,m}\cdot(\theta_n^\dagger\theta_m - \langle\theta_n^\dagger\theta_m\rangle_0)a_{k_1}^\dagger a_{k_2} \\ &+\frac{\omega_0}{\sqrt{N}}\sum_{k,q}(g-f_q)\cdot a_{k+q}^\dagger a_k\cdot(b_q+b_{-q}^\dagger),\end{aligned} \tag{3.8}$$

where the angle brackets $\langle ...\rangle_0$ denotes thermal average over phonon states, and we have defined $f_q = \sum_m e^{iqm}f_m$, $\theta_n = e^{\sum_m f_{|n-m|}(b_m - b_m^\dagger)}$. Note that we have partitioned the transformed Hamiltonian into a pure electronic part $\tilde{H}_e$, a pure phonon part $\tilde{H}_{ph}$, and the perturbation part $\tilde{V}'$. In addition, we have intentionally included the $\widetilde{J}_k$ term in the zeroth-order Hamiltonian to make the average of the interactions identically zero, $\langle\widetilde{V}'\rangle_0 = 0$.

By construction $\langle\widetilde{V}'\rangle_0 = 0$, therefore the Bogoliubov's bound is simply $A \leq -\beta\mathbf{Tr}\exp(-\beta\tilde{H}_0) \equiv A_0$. Since the zeroth order Hamiltonian $\tilde{H}_0 = \tilde{H}_e + \tilde{H}_{ph}$ is diagonal, the Bogoliubov's bound is readily available

$$\begin{aligned}A_0 &= -\beta^{-1}\ln\mathbf{Tr}e^{-\beta\tilde{H}_0} \\ &= -\beta^{-1}\ln\mathbf{Tr}e^{-\beta\tilde{H}_e} - \beta^{-1}\ln\mathbf{Tr}e^{-\beta\tilde{H}_{ph}}.\end{aligned}$$

We can further ignore the non-interesting phonon part and focus on the contribution from the dressed electronic states

$$A_0^e = -\beta^{-1}\ln\mathbf{Tr}e^{-\beta\tilde{H}_e} = -\beta^{-1}\ln\sum_k e^{-\beta\varepsilon_k}, \tag{3.9}$$

where the electronic band energy is given by

$$\varepsilon_k = \omega_0\cdot(\sum_m f_m^2 - 2gf_0) + \widetilde{J}_k \tag{3.10}$$

Note that the energy band of the dressed particle is temperature dependent. The temperature dependence comes into play through the temperature dependent variational parameters $\{f_m\}$ and the average effective transfer integral factor $\langle\theta_n^\dagger\theta_m\rangle_0$, and can be very complicated. For a system defined by a given set of parameters (J_0, ω_0, g, T), minimizing the quantity A_0^e defined in Eq. (3.9) by adjusting $\{f_m\}$ enables us to find the optimal set of the dressing coefficients $\{f_m\}$ that describes the system,

i.e. the optimal partially-dressed polaron state. In addition, it is easy to check that minimizing A_0^e reproduces strong-coupling result ($\sim e^{-g^2 \coth(\beta\omega/2)}$) and weak-coupling result at finite temperature in large g and small g limits, respectively.

Note that we minimize the free energy contributed by the electronic subsystem, while in Yarkony and Silbey's original treatment, the free energy of a subsystem with total (electron plus phonon) crystal wavevector K was minimized. Compared to their treatment, our approach is more straightforward and our expression in Eq. (3.9) is easier to evaluate. In addition, at non-zero temperatures, the quantity minimized in Yarkony and Silbey's treatment is swamped by phonon free energies. Because uninteresting phonon free energy overwhelms the electronic free energy, it is difficult to implement a numerical scheme that minimizes the free energy functional accurately in Yarkony and Silbey's theory. Generally speaking, we have extended Yarkony and Silbey's approach by using a more general variational ansatz and providing a more straightforward variational scheme that results in clean partition of the electronic free energy and phonon free energy.

3.2.3 Mobility

In the late 70s, Yarkony and Silbey derived a general expression for exciton mobilities in molecular crystals that describes both band-like and hopping transport [12, 14]. We use their expression to perform mobility calculations. In the following, we will summarize their deviation and the resulting mobility formula when the transformed Hamiltonian in Eq. (3.7)-(3.8) is used.

Yarkony and Silbey considered a general electron-phonon Hamiltonian

$$\begin{aligned} H &= H_e + H_{ph} + V \\ &= \sum_k E_k a_k^\dagger a_k + \sum_q \omega_q b_q^\dagger b_q + \frac{1}{\sqrt{N}} \sum_{k_1,k_2} a_{k_1}^\dagger a_{k_2} V_{k_1 k_2}, \end{aligned} \tag{3.11}$$

where $V_{k_1 k_2}$ are operators that act on phonon degrees of freedom. Using a quantum master equation approach in a approximation equivalent to second-order time-dependent perturbation theory in the exciton-phonon coupling V, they find the equa-

tion of motion for the reduced density matrix of the exciton[1]

$$\dot{\sigma}_{kk'}(t) = -i(E_k - E_{k'})\sigma_{kk'}(t) - \Gamma_{kk'}\sigma_{kk'}(t) + \sum_{q,s} W_{kk';qs}\sigma_{qs}(\tau), \tag{3.12}$$

where E_k is the energy of the state k, the relaxation tensor $W_{kk';qq'}$ is defined using phonon correlation functions

$$W_{kk';qq'} = \int_0^\infty d\tau \left\{ \langle V_{q'k'} V_{kq}(\tau) \rangle_0 e^{-i(E_{q'} - E_{k'})\tau} + \langle V_{q'k'}(\tau) V_{kq} \rangle_0 e^{-i(E_k - E_q)\tau} \right\}, \tag{3.13}$$

and the quantities $\Gamma_{kk'}$ is given by

$$\Gamma_{kk'} = \frac{1}{2} \sum_q \left(W_{qq;kk} + W_{qq;k'k'} \right).$$

Note that the diffusion coefficient D of a non-equilibrium distribution of electronic states can be related to the mean-square displacement of a particle $\langle R^2(t) \rangle$ using the following expression

$$D = \frac{1}{2d} \lim_{t \to \infty} \frac{d}{dt} \langle R^2(t) \rangle,$$

where d is the dimensionality of the system (assuming an isotropic system). The mean-square displacement of a particle is related to the diagonal density matrix elements of the system in the site-representation, $\langle R^2(t) \rangle = \sum_n n^2 \sigma_{nn}(t)$. In the k-representation, the diffusion coefficient is given by

$$D = \frac{1}{2d} \lim_{t \to \infty} \sum_k \nabla_K^2 \dot{\sigma}_{k,k+K}(t) \big|_{K=0}. \tag{3.14}$$

Substitution of the quantum master equation in Eq. (3.12) into this equation in the limit of $t \to \infty$ yields a complicated equation that gives the diffusion coefficient of the electron. After neglecting small terms, an approximate formula for the mobility

[1]Equation (3.12) can be derived using the projection operator technique. The procedure used to derive the quantum master equation will be described in detail in Chapter 7.

of the electron that consists of a band-like term and a hopping term is obtained

$$\mu = e\beta D = \mu_B + \mu_H, \tag{3.15}$$

where the band-like mobility is given by

$$\mu_B = e\beta \sum_k \sigma_{kk}^{eq} \cdot \frac{v_k^2}{\gamma_0 + \Gamma_{kk}}, \tag{3.16}$$

where e is the electron charge, $\sigma_{kk}^{eq} = e^{-\beta E_k} / \sum_q e^{-\beta E_q}$ is the thermal population of state k, $v_k = \nabla_k E_k$ is the electron group velocity in state k, Γ_{kk} is the rate of scattering out of state k,

$$\Gamma_{kk} = \sum_q W_{qq;kk},$$

and γ_0 is an extra term inserted to represent the contribution to the scattering rate from mechanisms not considered in the Hamiltonian (e.g. scattering due to quadratic electron-phonon couplings and impurities). Notice that Eq. (3.16) is the expression that we have used in the previous chapter to calculate the mobility of excess charge-carriers in a wide-band theory using the mean-scattering-time approximation.

The hopping term is given by

$$\mu_H = e\beta \sum_k \sigma_{kk}^{eq} \cdot \gamma_{kk}, \tag{3.17}$$

where γ_{kk} is a complicated function defined using the relaxation tensor W

$$\gamma_{kk} = -Re \sum_q \left. \frac{d^2 W_{q,q+K;k,k+K}}{dK^2} \right|_{K=0} + \frac{1}{2} \frac{d^2 \Gamma_{kk}}{dk^2}. \tag{3.18}$$

Equations (3.15)-(3.18) are the main results derived by Yarkony and Silbey. We will adopt their expression to calculate the mobility of a partially dressed electron governed by the transformed Hamiltonian in Eq. (3.7).

We first evaluate the phonon correlation functions $\langle V_{q'k'} V_{kq}(\tau) \rangle_0$. Reorganizing the interaction term of the transformed Hamiltonian in Eq. (3.8) and comparing the result

to Eq. (3.11), we obtain the corresponding phonon operators for the Hamiltonian after Merrifield's transformation,

$$\begin{aligned} V_{k_1k_2} &= \frac{1}{N}\sum_{n,m} e^{-ik_1n}e^{ik_2m}\cdot J_{n,m}\cdot(\theta_n^\dagger\theta_m - \langle\theta_n^\dagger\theta_m\rangle_0) \\ &\quad +\omega_0(g-f_{k_1-k_2})\cdot(b_{k_1-k_2}+b_{k_2-k_1}^\dagger), \end{aligned} \tag{3.19}$$

This expression for phonon operators is used to compute the phonon correlation functions $\langle V_{q'k'}V_{kq}(\tau)\rangle_0$. Due to the complex form of $V_{k_1k_2}$, the expression for $\langle V_{q'k'}V_{kq}(\tau)\rangle_0$ is quite involved; to avoid confusion, the result is given in Appendix 3.A.

Our mobility calculations depend on the evaluation of the following relaxation tensor elements

$$\begin{aligned} W_{q,q+K;k,k+K} &= \int_0^\infty d\tau\left\{\langle V_{k+K,q+K}V_{qk}(\tau)\rangle_0 e^{-i(E_{k+K}-E_{q+K})\tau}\right. \\ &\quad \left.+\langle V_{k+K,q+K}(\tau)V_{qk}\rangle_0 e^{-i(E_q-E_k)\tau}\right\}. \end{aligned}$$

In order to evaluate the integral over τ while avoiding singularities introduced by δ functions, we assume a phonon bandwidth α (inverse relaxation time of phonons) and treat integral of the form $\int d\tau e^{iF\tau}$ as

$$\int_0^\infty d\tau e^{iF\tau}\cdot e^{-\alpha\tau} = \frac{\alpha}{\alpha^2+F^2}.$$

The result for $W_{q,q+K;k,k+K}$ is

$$\begin{aligned} W_{q,q+K;k,k+K} &= n_0\omega_0^2(g^2-f_{k-q}^2)\left[\frac{\alpha}{\alpha^2+(\varepsilon_q-\varepsilon_k-\omega_0)^2}+\frac{\alpha}{\alpha^2+(\varepsilon_{q+K}-\varepsilon_{k+K}-\omega_0)^2}\right] \\ &\quad +(n_0+1)\omega_0^2(g^2-f_{k-q}^2)\left[\frac{\alpha}{\alpha^2+(\varepsilon_q-\varepsilon_k+\omega_0)^2}+\frac{\alpha}{\alpha^2+(\varepsilon_{q+K}-\varepsilon_{k+K}+\omega_0)^2}\right] \\ &\quad +\frac{1}{N}\sum_{n_1,m_1}\sum_{n_2,m_2} e^{-ik(n_1-m_2)}e^{-iq(n_2-m_1)}\tilde{J}_{n_1m_1}\tilde{J}_{n_2m_2}\times\sum_{n=1}^{\infty}\sum_{m=0}^{n}\frac{A^mB^{n-m}}{m!(n-m)!} \\ &\quad \times\left\{\frac{\alpha}{\alpha^2+[\varepsilon_q-\varepsilon_k+(2m-n)\omega_0]^2}\right. \end{aligned}$$

$$+\frac{\alpha}{\alpha^2+[\varepsilon_{q+K}-\varepsilon_{k+K}+(2m-n)\omega_0]^2}\Bigg\}, \tag{3.20}$$

where we have defined thermal population number of phonon modes $n_0 = 1/(e^{-\beta\omega_0} - 1)$, phonon renormalized resonance transfer integrals $\tilde{J}_{nm} = J_{nm}\langle\theta_n^\dagger\theta_m\rangle_0$, and functions

$$\begin{aligned} A &= \frac{-1}{2}\sum_{q'} X_{q'}^{n_1m_1}\bar{X}_{q'}^{n_2m_2}\cdot(n_0+1), \\ B &= \frac{-1}{2}\sum_{q'} \bar{X}_{q'}^{n_1m_1}X_{q'}^{n_2m_2}\cdot n_0, \end{aligned}$$

with $X_q^{nm} = \frac{1}{\sqrt{N}}f_q(e^{iqm} - e^{iqn})$ and $\bar{X}_q^{nm} = \frac{1}{\sqrt{N}}f_q^*(e^{-iqm} - e^{-iqn})$. Note that for narrow phonon bands, the value for αshould be small ($0 < \alpha \ll 1$), and when $\alpha \to 0$ we obtain δ functions in the expression.

The three terms in Eq. (3.20) have simple physical interpretations. In Eq. (3.20), the first term represents a process in which an electron absorbs one phonon and is scattered upward to a higher energy state, the second term is a process that emits a phonon and scatters the electron downward to a lower energy state, and the third term represents multi-phonon processes in which multiple phonons are exchanged. For very narrow-band materials whose electronic bandwidth is smaller than the phonon frequency ω_0, only the multi-phonon term contributes to the scattering of electrons. In addition, for systems with strong electron-phonon coupling g, it is possible that at high temperatures, the polaronic narrowing effect will result in a narrow polaron band such that $\tilde{J} \ll \omega$, and again the single phonon processes (the first and second terms) do not contribute. Note that at low temperatures ($n_0 \ll 1$) or when the electron is only weakly dressed ($f_m \ll 1$), the prefactor $A^m B^{n-m} \ll 1$, and the multi-phonon processes are negligible. On the other hand, when temperature increases, the thermal population of phonon modes n_0 as well as the dressing coefficients $\{f_m\}$ increase, and the contribution of the multi-phonon term would increase. Eventually, multi-phonon term dominates the scattering of electrons at high temperatures.

The expression for $W_{q,q+K;k,k+K}$ in Eq. (3.20) can be used to calculate the band-like mobility μ_B and the hopping mobility μ_H. The calculation of the band-like contribution to the electron mobility [Eq. (3.16)] is more straightforward. The group velocity $v_k = \nabla_k \varepsilon_k$ and the equilibrium density matrix $\sigma_{kk}^{eq} = e^{-\beta\varepsilon_k} / \sum_q e^{-\beta\varepsilon_q}$ can be easily obtained by recalling the formula for ε_k:

$$\varepsilon_k = \omega_0 \cdot (\sum_m f_m^2 - 2gf_0) + \sum_{n,m} e^{ik(n-m)} J_{nm} \cdot e^{-\frac{1}{2}\sum_{m'}(f_{m'-m} - f_{m'-n})^2 \cdot \coth(\beta\omega_0/2)}.$$

The rate of scattering out of state k can be calculated from $W_{q,q+K;k,k+K}$ using

$$\Gamma_{kk} = \sum_q W_{q,q+K;k,k+K}|_{K=0,\alpha\to 0}.$$

Note that because of the δ functions in the limit of $\alpha \to 0$, the summation over q can be replaced by summing $W_{q,q;k,k}$ over q points that satisfy the energy conservation conditions required by the δ functions. In general, when the energy band ε_k is obtained, the quantities Γ_{kk} can be evaluated and the band-like mobility can be calculated according to Eq. (3.16).

In contrast, the hopping contribution to the electron mobility [Eq. (3.17)-(3.18)] is extremely difficult to evaluate. An analytical expression for γ_{kk} is unavailable even for the simplest one dimensional system. Nevertheless, with finite but small α ($0 < \alpha \ll 1$), the expression for the second derivative of $W_{q,q+K;k,k+K}$, $\frac{d^2}{dK^2} W_{q,q+K;k,k+K}|_{K=0}$, can be obtained using a computational algebraic software such as Maple or Mathematica, and the result can be numerically integrated to obtain the hopping mobility according to Eq. (3.17) and (3.18).

The expressions for the upper bound on the electronic free energy A_0^e in Eq. (3.9) and the relaxation tensor $W_{q,q+K;k,k+K}$ in Eq. (3.20) are the main results of the present work. Minimizing A_0^e with respect to the dressing coefficients $\{f_m\}$ gives the optimal polaron state, and the optimal set of $\{f_m\}$ can then be used to compute $W_{q,q+K;k,k+K}$ and electron mobilities according to Equations (3.15)-(3.18). To demonstrate our variational-perturbation approach, we will apply this method to study the properties

of a simple electron-phonon system in one spatial dimension in the following sections.

3.3 Polaron States at 0K

In this section, we examine the properties of polaron states at zero K. We use a variation method to obtain the optimal dressed state, and apply standard second-order time-independent perturbation theory to calculate the ground state energy and the polaron effective mass of the Holstein model at zero K. Numerous variational methods have been applied to study the Holstein Hamiltonian in the context of polaron problem [23, 25, 26, 27, 28]. In particular, Lindenberg *et al.* have performed extensive investigations on several variational ansatzs and found that variational methods can produce results comparable to computationally much more demanding methods such as quantum Monte Carlo (QMC) [29, 30], density-matrix renormalization group (DMRG), and cluster diagonalization methods [31]. Although variational treatments of the Holstein Hamiltonian have been carried out extensively, most existing works are restricted in the ground state and focused on problems such as polaron localization and spectra properties. Treatments of the Holstein Hamilton at finite-temperature or regarding dynamical properties are limited [32, 33, 34]. Therefore, before we proceed to study the dynamics of the Holstein Hamilton at finite temperatures, we first examine the variation method at zero temperature and compare our calculations to previous results in the polaron theory. The objective is to test the applicability of our method. We will show that our variational approach combined with second-order perturbation theory produce results that are in good agreement with calculations employing more complicated methods.

We consider a 1-D system with only nearest-neighbor resonance transfer integrals described by the following Hamiltonian

$$H = J_0 \sum_n (a_n^\dagger a_{n+1} + a_{n+1}^\dagger a_n) + \omega_0 \sum_n b_n^\dagger b_n + g\omega_0 \sum_n a_n^\dagger a_n \cdot (b_n^\dagger + b_n).$$

To further simplify the problem, we use Merrifield's transformation [Eq. (3.6)] with

a single dressing coefficient $f_m = f \cdot \delta_m$, i.e. we consider only one variation parameter f. Applying the simplified unitary transformation to the 1-D Hamiltonian, we obtain the transformed Hamiltonian $\tilde{H} = \tilde{H}_0 + \tilde{V}'$ where

$$\tilde{H}_0 = \sum_k \left[\omega_0 \cdot (f^2 - 2gf) - 2J_0 e^{-f^2} \cos k\right] a_k^\dagger a_k + \omega_0 \sum_q b_q^\dagger b_q,$$

and

$$\begin{aligned}\tilde{V}' &= \frac{1}{N}\sum_{k_1,k_2}\sum_{n,m} e^{-ik_1 n + ik_2 m} J_0 \delta_{1,|n-m|} \left[e^{-f(b_n - b_n^\dagger)} e^{f(b_m - b_m^\dagger)} - e^{-f^2}\right] a_{k_1}^\dagger a_{k_2} \\ &\quad + \frac{\omega_0(g-f)}{\sqrt{N}} \sum_{k,q} a_{k+q}^\dagger a_k (b_q + b_{-q}^\dagger).\end{aligned}$$

Therefore, the zeroth-order band structure of the 1-D system can be written as

$$E^{(0)}(k) = \omega_0 \cdot (f^2 - 2gf) - 2J_0 e^{-f^2} \cos k. \tag{3.21}$$

At T=0K, the Bogoliubov's bound in Eq. (3.30) is an upper bound on the energy of the ground state. For the 1-D nearest-neighbor coupling system at T=0K, the optimal f satisfies

$$\frac{d}{df} E^{(0)}(k=0)\Big|_{f=f_{opt}} = 0,$$

and we have the following self-consistent equation for the optimal f

$$f_{opt} = \frac{g\omega_0}{\omega_0 + 2J_0 e^{-f_{opt}^2}}. \tag{3.22}$$

Given g, J_0, and ω_0, the optimal f_{opt} can be obtained by solving Eq. (3.22) iteratively. Note that the ground state energy $E^{(0)}(k=0)$ as a function of f can have more than one minima, therefore, when an iterative scheme is used to calculate f_{opt}, multiple initial guesses must be applied and then the resulting energy values compared to locate the true optimal f_{opt}.

We now calculate the second-order energy correction to the energy band structure based on the partially dressed basis defined by f_{opt}. In the $|k;\vec{n}\rangle$ basis set, where k denotes the k state of the electron and the vector $\vec{n}$ denotes the states of all phonon modes in the system, the energy band structure calculated from second-order time-independent perturbation theory is

$$\begin{aligned} E(k) &= E^{(0)}(k) + E^{(2)}(k) \\ &= \omega_0 \cdot (f_{opt}^2 - 2g f_{opt}) - 2J_0 e^{-f_{opt}^2} \cos k \\ &\quad - \sum_{n_T \geq 0} \sum_{k'} \frac{\sum_{\vec{n}_i} |\langle k';\vec{n}_i|\tilde{V}'|k;0\rangle|^2}{\varepsilon_k - \varepsilon_{k'} - n_T\omega_0}, \end{aligned} \tag{3.23}$$

where $n_T = 0, 1, 2, ..., \infty$ is the total number of phonon quanta, $\vec{n}_i$ is a vector representing the distribution of n_T phonon quanta in all phonon modes, and the summation over $\vec{n}_i$ means summing over all phonon configurations that contains totally n_T quanta of phonons. The $E^{(2)}(k)$ term can be evaluated analytically, and the explicit expression is given in Appendix 3.B. In the following we will calculate ground state energy and polaron effective mass using Eq. (3.21) and Eq. (3.23), and compare the results to other methodologies in the literatures to measure the adequacy of the variational-perturbation method.

3.3.0.1 Ground state energy

The groundstate properties of the 1-D Holstein Hamiltonian have been investigated extensively, and accurate results regarding the ground state energy of the 1-D Holstein Hamiltonian are available [31]. Therefore, we first compare our result to these calculations at zero temperature. In Table 3.1, we compare the ground state energy from our method to a number of previous calculations for a set of system parameters in the intermediate coupling regime ($J_0/\omega_0 = 1$ and $g = 1$). The zeroth-order ground state energy $E^{(0)}(0)$ [Eq. (3.21)] and the second-order result $E(0) = E^{(0)}(0) + E^{(2)}(0)$ [3.23] are listed along with results from several other methods. Among the methodologies listed in Table 3.1, the $E^{(0)}(0)$, Merrifield [23, 24], Toyozawa [25, 35], and Global-Local [26] methods are variational methods, therefore, these numbers are up-

Table 3.1: A comparison of ground state energy from different methods

$J_0/\omega_0 = 1,\ g = 1$		
Value	Method	Reference
-2.3473	$E^{(0)}(0)$	This work, Eq. (3.21)
-2.4472	2^{nd}-order WCPT	This work, Eq. (3.24)
-2.4561	Merrifield variation	Ref. [23, 24]
-2.4687	Toyozawa variation	Ref. [25, 35]
-2.4693	Global-Local variation	Ref. [26]
-2.4697	DMRG $N = 32$	Ref. [36]
	Exact value	
-2.471	Cluster diag. $N = 6$	Ref. [37, 33]
-2.4826	$E(0)$	This work, Eq. (3.23)
-2.5679	GS 2^{nd}-order SCPT	This work, Eq. (3.25)
-3.0896	Marsiglio's 2^{nd}-order SCPT	Ref. [38, 39], Eq. (3.26)

per bounds to the true ground state energy. Note that the true bulk ground state energy is believed to lie between the $N = 32$ DMRG [36] and the $N = 6$ cluster diagonalization [37, 33] values, both of them are computationally demanding numerical methods. At this particular set of parameters, the value given by $E^{(0)}(0)$ (Yarkony and Silbey's ansatz) significantly overestimates the ground state energy, while the other three variational methods give values that are within 1% range of the exact value. The less satisfactory result given by $E^{(0)}(0)$ is clearly due to the restricted form containing only one variational parameter in the variational ansatz, and the inclusion of nonlocal deformation of the lattice in Merrifield's method significantly improves the value for ground state energy. While the second-order correction is applied, the variational-perturbation result $E(0)$ gives a value that is within 1% range of the exact value at $J_0/\omega_0 = 1$ and $g = 1$. This significantly improvement compared to $E^{(0)}(0)$ indicates that the perturbation expansion based on the optimal polaron basis is justified in the intermediate coupling regime.

To compare our variational-perturbation method to other analytical theories, some approximate perturbation results are also listed in Table 3.1. The second-order weak-coupling perturbation theory (WCPT) based on the free electron states is a limiting

case of our method. By setting $f = 0$ in Eq. (3.23), the band structure from the second-order WCPT is obtained

$$E^{WCPT}(k) = -2J_0 \cos k - g^2\omega_0^2 \frac{1}{N} \sum_{k'} \frac{1}{2J_0 \cos k' - 2J_0 \cos k - \omega_0}.$$

Near the bottom of the band where $k \sim 0$ and $\cos k \sim 1$, the integral over k' can be evaluated explicitly to give

$$E_{k\sim 0}^{WCPT}(k) = -2J_0 \cos k - \frac{g^2\omega_0^2}{2J_0} \times \frac{1}{\sqrt{(\cos k + \omega_0/2J_0)^2 - 1}}. \tag{3.24}$$

The Grover and Silbey's second-order strong-coupling perturbation theory (GS SCPT) is the formalism first used by Grover and Silbey to study exciton transport in OMC [40, 41]. The present method also contains the GS SCPT theory in the limit of $f = g$, and the resulting band structure around the bottom of the band is

$$\begin{aligned} E_{k\sim 0}^{GS}(k) &= -g^2\omega_0 - 2J_0 e^{-g^2} \cos k \\ &\quad -2J_0 e^{-g^2} \sum_{n_T=1}^{\infty} \frac{f_{opt}^{2n_T}}{n_T!} \times \frac{A\sqrt{A^2-1} - AB + B\sqrt{A^2-1} - A^2 - C}{\sqrt{A^2-1}} \qquad (3.25) \\ A &= \cos k + n_T\omega_0/2J_0 e^{-g^2}, \\ B &= \frac{1}{2}\left[2(-1)^{n_T} + (-2)^{n_T}\right]\cos k, \\ C &= \frac{1}{2}\left[2^{n_T} + \cos 2k - 1\right]. \end{aligned}$$

Finally, the result from a second-order strong-coupling perturbation theory due to Marsiglio (Marsiglio SCPT) is also listed [38]. Similar to Grover and Silbey's approach, Marsiglio's theory is also based on the small polaron transformation and treats the renormalized electronic coupling term as the perturbation. However, Marsiglio used the transformed coupling term directly and did not absorb the first order correction into the zeroth-order Hamiltonian. Thus, the first-order energy correction is nonzero in Marsiglio's theory, i.e. $\langle V \rangle_0 \neq 0$. The band structure up to the second-order in J_0 from Marsiglio's SCPT is given by

$$
\begin{aligned}
E^M(k) &= -g^2\omega_0 - 2J_0 e^{-g^2}\cos k - 2h(g^2)\cos(2k) - 2h(2g^2), \qquad (3.26)\\
h(x) &= \frac{J_0^2 e^{-2g^2}}{\omega_0}\left[Ei(x) - \gamma - \ln x\right],
\end{aligned}
$$

where $Ei(x)$ is the exponential integral, and γ is Euler's constant. The Marsiglio's theory is widely used in studies of the Holstein polaron problem.

From Table 3.1, we clearly see that all these simple perturbation theories fail badly in the intermediate coupling regime. In contrast, the present method using perturbation expansion based on a variational zeroth-order Hamiltonian successfully reproduces the ground state energy of the 1-D Holstein model within a reasonable error range. Note that Table 3.1 aims at demonstrating the improvement gained by using a variational zeroth-order Hamiltonian in the intermediate coupling regime; because we only compare the results in a single point of $J_0/\omega_0 = 1$ and $g = 1$, the trend shown in Table 3.1 is in no means representative for the quality of results from different theories.

3.3.0.2 Polaron effective mass

In addition to the ground state energies, we also compare polaron effective masses calculated from a number of different methods. The effective mass of a polaron band m^* can be calculated using the following formula:

$$
\frac{m^*}{m_0} = \frac{2J_0}{\left.\frac{\partial^2 E(k)}{\partial k^2}\right|_{k=0}}.
$$

Note that for the convenience of comparison, we scale the polaron effective mass by the effective mass of a free electron band $m_0 = 2J_0$. In Fig. 3-1, we show the inverse effective mass as a function of electron-phonon coupling constant g at $J_0/\omega_0 = 1/2$. Curve calculated from the present variational-perturbation method are shown along with results from three other second-order perturbation theories. In addition, values calculated numerically using Toyozawa's variational method are also

displayed. Toyozawa's method is known to produce fairly accurate results in this parameter regime [35], therefore, values from Toyozawa's method can serve as the guideline for our comparison. More details about Toyozawa's method can be found in Appendix 3.C. Our variational-perturbation method gives results that are in excellent agreement to Toyozawa's variational method for this system. In the small coupling (g) regime, the effective mass of the polaron state resembles that of a free electron, $m^*/m_0 \sim 1$; as the strength of the electron-phonon coupling increases, the polaron effective mass grows monotonically, and eventually follows the e^{-g^2} behavior predicted by SCPT theories at strong couplings ($g \gg 1$). Note that in the intermediate coupling regime, the effective mass grows rapidly, indicating a change in the character of the polaron state from a weakly dressed state to a fully dressed state. We will discuss about this transition in more details later, and focus solely on the comparison of different theoretical methods in this subsection.

The applicability of the second-order WCPT and Marsiglio's second-order SCPT methods are clearly restricted to the weak-coupling and strong-coupling regimes, respectively; in particular, both of them fail badly in the intermediate coupling regime. Note that at small g, Marsiglio's strong-coupling theory results in effective masses that are smaller than m_0, $m^*_{M-SCPT} < m_0$, which is unphysical. In contrast to Marsiglio's theory, Grover and Silbey's second-order strong-coupling perturbation theory (GS-SCPT) describes both strong- and weak-coupling limits adequately and does not suffer the problem of giving unphysical results. In the intermediate regime, the GS-SCPT method gives correct trend, but overestimates the effective mass. A distinct feature in Grover and Silbey's theory (and the present variational-perturbation theory too) is that the average matrix elements of the perturbation term is included in the zeroth order Hamiltonian so that the first order correction is zero. Note that our comparison in Fig. (3-1) clearly indicates the importance of including the first-order correction in the zeroth-order Hamiltonian.

In contrast to all other simple perturbation theories, the present variational-perturbation method is in excellent agreement with Toyozawa's method at $J_0/\omega_0 = 1/2$ in all electron-phonon coupling strengths. In Fig. (3-2), we compare our variational-

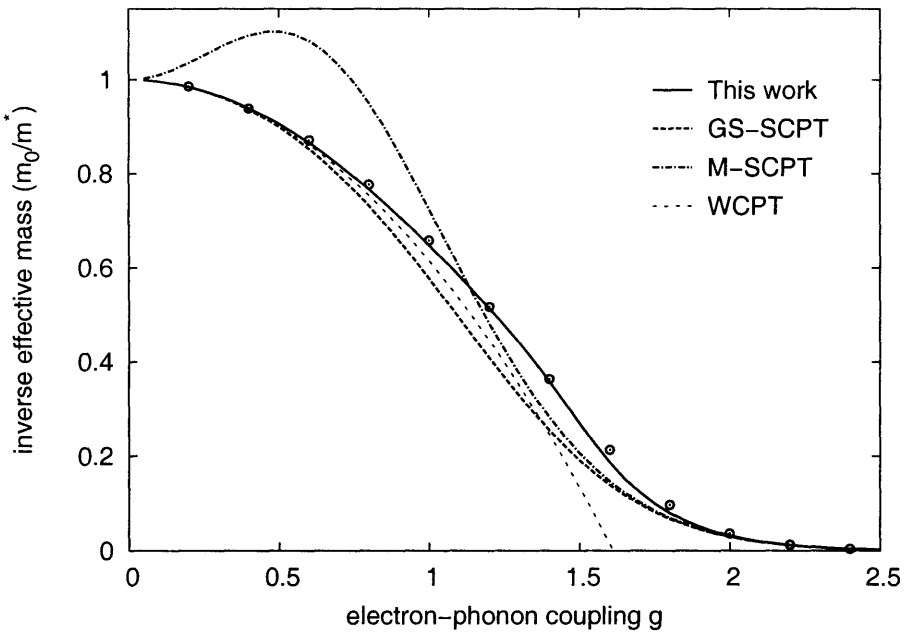

Figure 3-1: Inverse effective mass at T=0K for the 1-D Holstein model at $J_0/\omega_0 = 1/2$ as a function of the electron-phonon coupling g. We show results calculated from five different theories: the variational method using Toyozawa's Ansatz (open circles), the variational-perturbation theory described in this work, a second-order strong-coupling perturbation theory based on Grover and Silbey's formulation (GS-SCPT), the second-order strong-coupling perturbation theory due to Marsiglio (M-SCPT), and second-order weak-coupling perturbation theory (WCPT). Our variational-perturbation method gives result that is in excellent agreement to Toyozawa's variational results.

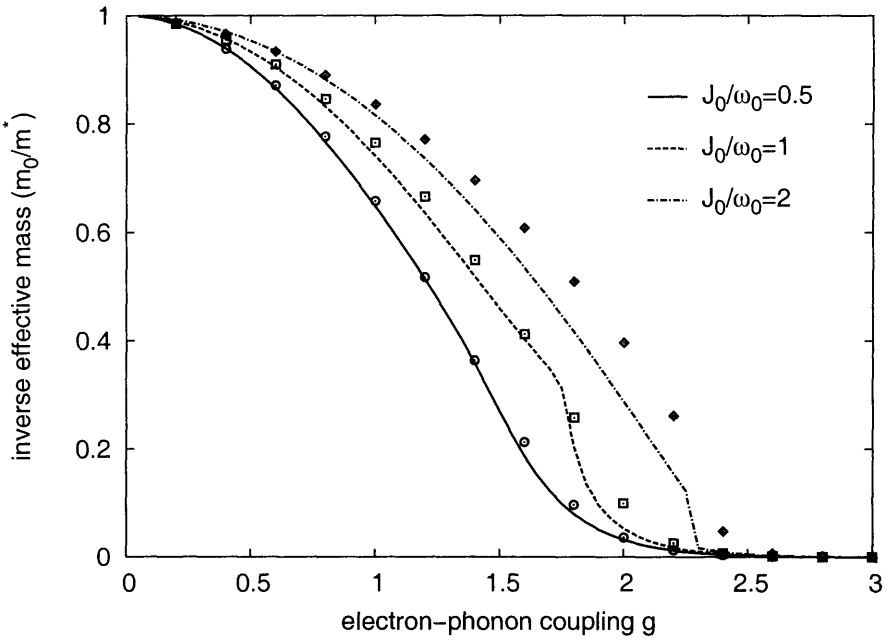

Figure 3-2: Inverse effective mass at T=0K for the 1-D Holstein model as a function of the electron-phonon coupling g. Curves calculated using the present variational-perturbation theory at J_0/ω_0 =1/2, 1, and 2 are shown along with results from Toyozawa's variational method. At smaller J_0, our variational-perturbation method is in excellent agreement to Toyozawa's variational results. At larger $J0$, our variational-perturbation method starts to deviate from Toyozawa's method at intermediate to large g.

perturbation method to Toyozawa's method at J_0/ω_0 =1/2, 1, and 2. At smaller J_0/ω_0, the agreement is excellent, while at larger J_0/ω_0, the agreement is less satisfactory and the variational-perturbation method starts to deviate from Toyozawa's method at intermediate to large g. Nevertheless, the present model describes the effective mass of the 1-D Holstein model quantitatively at smaller J_0/ω_0 and semi-quantitatively at $J_0/\omega_0 > 1$. Note that the present method is less favorable at large J_0/ω_0; we believe it is due to the restricted form of the one-parameter ansatz. For example, at large J_0/ω_0, nonlocal lattice deformation, which is included in more general Merrifield's transformation but not in the current one-parameter ansatz, is expected to be important for a description of the polaron state.

Evidently, the present variational-perturbation method gives favorable results compared to other simple perturbation theories, and is capable of describing the

1-D Holstein model at T=0K in the intermediate coupling regime. Considering that at T=0K, the present analytical method with only one variational parameter is able to give results that are in agreement with much more complicated numerical methods, we believe applying perturbation theory based on a variational optimal basis at finite temperature would also give significantly improved results.

3.4 Interacting Exciton-phonon System in 1-D

In this section, we apply the theoretical methods we developed in Section 3.2 to a simple 1-D system and discuss the implications of the results regarding the mobilities of charge-carriers in organic molecular crystals. We investigate a simplified mode with one spatial dimension and contains only nearest-neighbor transfer integrals:

$$J_{nm} = J_0 \cdot \delta_{n,m\pm1}, \tag{3.27}$$

where J_0 is the bare resonance transfer integral between two nearest-neighbor sites. The phonon-renormalized band structure under Merrifield's transformation is given by

$$\varepsilon_k = \omega_0 \cdot (\sum_m f_m^2 - 2gf_0) + \tilde{J}_k = \omega_0 \cdot (\sum_m f_m^2 - 2gf_0) - 2J_{eff}\cos k, \tag{3.28}$$

where we have defined the effective transfer integral renormalized by the dressing of the phonons

$$J_{eff} = J_0 e^{-\sum_m (f_m^2 - f_m f_{m+1})\coth(\beta\omega_0/2)}. \tag{3.29}$$

Note that J_{eff} is temperature dependent, and the temperature dependence of J_{eff} comes into play through the temperature dependent parameters $\{f_m\}$ and the $\coth(\beta\omega_0/2)$ factor; as a result, the temperature dependence is different from ordinary small pola-

ronic band narrowing factor $e^{-g^2 \coth(\beta\omega_0/2)}$.

The Bogoliubov's bound for the 1-D system is easily obtained from Eq. (3.28):

$$\begin{aligned} A \leq A_0^e &= -\beta^{-1} \ln \sum_k e^{-\beta\varepsilon_k} \\ &= -\beta^{-1} \ln \left\{ e^{-\beta\omega_0(\sum_m f_m^2 - 2gf_0)} \sum_k e^{2J_{eff}\beta\cos k} \right\}, \end{aligned}$$

For a bulk system, we can convert the sum over k into a integral and obtain

$$A_0^e = -\beta^{-1} \ln N + \omega_0(\sum_m f_m^2 - 2gf_0) - \beta^{-1} \ln \{I_0(2\beta J_{eff})\}, \qquad (3.30)$$

where N is the size of the system, and $I_0(x)$ is the Bessel function of the first kind. The extreme values of A_0^e can be found at points where equality $\partial A_0^e/\partial f_m = 0$ is satisfied for all f_m. As a result, we obtain a system of coupled equations

$$f_m - g\delta_m + \frac{J_{eff}}{\omega_0} \times \frac{I_1(2\beta J_{eff})}{I_0(2\beta J_{eff})} \times (2f_m - f_{m+1} - f_{m-1}) \cdot \coth(\beta\omega_0/2) = 0 \qquad (3.31)$$

Equation (3.31) is used to calculate the optimal set of $\{f_m\}$ that minimizes the Bogoliubov's bound on free energy. Note that the effective transfer integral J_{eff} also depends on $\{f_m\}$, therefore, the system of equations must be solved self-consistently. Again, A_0^e as a function of $\{f_m\}$ can have more than one minima, therefore, multiple initial guesses must be applied and then the resulting A_0^e values compared to locate the true optimal set of dressing coefficients. Nevertheless, for given g, ω_0, β, and J_0, it is trivial to obtain accurate solutions and select the optimal solution on a personal computer.

We now check the strong-coupling and the weak-coupling limits in Eq. (3.31). In the limit that $g^2\omega_0 \gg J_0$, we can neglect the last term in the right-hand side of Eq. (3.31) and obtain $f_m = g\delta_m$. The transformation is the small polaron transformation and we recover the conventional strong-coupling results. On the other hand, when

$J_0 \gg g^2\omega$, the first two terms in Eq. (3.31) can be neglected, and the solution to the equation is $f_m = (f_{m+1} + f_{m-1})/2$. Because of the symmetry and boundary conditions required for the 1-D crystal, $f_m = f_{-m}$ and $\lim_{m\to\infty} f_m = 0$, the only physically admissible solution to $\{f_m\}$ is $f_m = 0$. Thus, we also recover the weak-coupling results from Eq. (3.31).

In order to compute the band-like and hopping mobilities using the results in Section 3.2.3, we need to calculate the equilibrium density matrix σ_{kk}^{eq}, the group velocity v_k, and the relaxation tensor elements $W_{q,q+K;k,k+K}$ for the 1-D system. Both σ_{kk}^{eq} and v_k can be evaluated easily from the band structure in Eq. (3.28) to yield

$$\begin{aligned} \sigma_{kk}^{eq} &= \frac{1}{N} \times \frac{e^{2\beta J_{eff}\cos k}}{I_0(2\beta J_{eff})}, \\ v_k &= \frac{d\varepsilon_k}{dk} = 2J_{eff}\sin k. \end{aligned}$$

To compute the relaxation tensor elements $W_{q,q+K;k,k+K}$ for the 1-D system, we insert $J_{nm} = J_0 \cdot \delta_{n,m\pm1}$ into the expression for $W_{q,q+K;k,k+K}$ [Eq. (3.20)] to obtain

$$\begin{aligned} W_{q,q+K;k,k+K}^{1d} &= n_0\omega_0^2(g^2 - f_{k-q}^2)\left[\frac{\alpha}{\alpha^2 + (\varepsilon_q - \varepsilon_k - \omega_0)^2} + \frac{\alpha}{\alpha^2 + (\varepsilon_{q+K} - \varepsilon_{k+K} - \omega_0)^2}\right] \\ &\quad + (n_0+1)\omega_0^2(g^2 - f_{k-q}^2)\left[\frac{\alpha}{\alpha^2 + (\varepsilon_q - \varepsilon_k + \omega_0)^2} + \frac{\alpha}{\alpha^2 + (\varepsilon_{q+K} - \varepsilon_{k+K} + \omega_0)^2}\right] \\ &\quad + 2J_{eff}^2 \times \sum_{n=1}^{\infty}\sum_{m=0}^{n}\sum_{z=-\infty}^{\infty} \frac{A_z^m B_z^{n-m}}{m!(n-m)!}\{\cos[k+q+K+(k-q)z] + (-1)^n\cos[K+(k-q)z]\} \\ &\quad \times \left\{\frac{\alpha}{\alpha^2 + [\varepsilon_q - \varepsilon_k + (2m-n)\omega_0]^2}\right. \\ &\quad \left. + \frac{\alpha}{\alpha^2 + [\varepsilon_{q+K} - \varepsilon_{k+K} + (2m-n)\omega_0]^2}\right\}, \end{aligned} \tag{3.32}$$

where the functions

$$A_z = -(n_0+1)\sum_l [2\cdot f_l f_{l+z} - f_l f_{l+z-1} - f_l f_{l+z+1}],$$

$$B_z = -n_0 \sum_l [2 \cdot f_l f_{l+z} - f_l f_{l+z-1} - f_l f_{l+z+1}] .$$

Once the optimal set of dressing coefficients is obtained, Equation (3.32) is used to evaluate the relaxation tensor elements for the 1-D system, and the result is then integrated numerically according to Eq. (3.16) and Eq. (3.17) to calculate the band-like and hopping mobilities, respectively. In our numerical calculations, we use a constant phonon relaxation rate $\alpha = 0.01\omega_0$. In all parameter range we studied, the result is insensitive to the value of α given that a good numerical algorithm and enough numerical points are applied to evaluate the integrals. In addition, an extra constant scattering rate $\gamma_0 = 0.001\omega_0$ is employed in our calculations for band-like mobilities [Eq. (3.16)]. The additional scattering term γ_0 is used to mimic the scattering channel due to impurities in the crystal, which is known to dominate the band-like transport at low temperature. The amplitude of γ_0 only affects the mobility at extremely low temperature, therefore adding the γ_0 term does not alter the crossover from band-like to hopping transport. In the following, we first study the small polaron transition using the finite-temperature variation method, and then present our results of mobility calculations for the 1-D system.

3.4.1 Small Polaron Transition

In this subsection, we examine the optimal polaron state, defined by the optimal set of $\{f_m\}$, from the finite-temperature Merrifield variational method for the 1-D nearest-neighbor system. The dressing coefficients $\{f_m\}$ in Merrifield's ansatz represent the deformation of the lattice around the electron, and the extend of the deformation characterizes the nature of the polaron state. When the lattice deformation is extended over many lattice sites, the state is usually called a "large polaron" state; on the other hand, when the deformation is restricted to a single site, a "small polaron" state occurs. It is well known that at T=0K, the Holstein Hamiltonian exhibits large polaron states at weak electron-phonon couplings (small g) and small polaron states at strong couplings (large g). The transition from large polaron state to small polaron state, also called the self-trapping transition, is the focus of many theoretical investi-

gations [42, 43, 44, 45, 46, 47]. Our finite-temperature variational method allows us to examine this transition at finite temperatures.

3.4.1.1 Lattice deformation

We first show the structure of polaron states represented by the optimal set of dressing coefficients $\{f_m\}$ at different strengths of electron-phonon couplings (g). In Fig. 3-3, we show the relative amplitude of lattice deformations (f_m/g) surrounding an electron at low temperature ($\beta\omega_0 = 10$) for a system with reduced nearest-neighbor transfer integral $J_0/\omega_0 = 1/2$ at different g. At weak-couplings, the deformation of lattice (polaron profile) is extended over many lattice sites and the relative amplitudes of deformations are small, therefore, the polaron state is only weakly dressed and of the character of a large polaron state. Note that the ansatz used by Yarkony and Silbey contains only a single variational parameter, as a result, their ansatz can not describe these large polaron states adequately. As the strength of electron-phonon coupling g increases, the lattice deformation gradually becomes more localized. At $g > 1.5$, the deformation is complete localized on a single lattice site and $f_0/g \sim 1$, therefore, the polaron state is a fully dressed small polaron state. We emphasize that the "localization" is only relative to the position of an electron in the site-representation, and in no means indicates a localized polaron. The polaron profile shown in Fig. 3-3 should be interpreted as correlations between the position of the electron and the lattice deformation; the eigenstates of the zeroth-order Hamiltonian after Merrifield's transformation are momentum states delocalized over the whole crystal, i.e. the eigenstates form a polaron band.

To also show the effect of varying temperatures, we present polaron profiles for a 1-D system with $J_0/\omega_0 = 1/2$ and $g = 1/2$ at different temperatures in Fig. 3-4. Clearly, the temperature of the system plays a role resembling that of the electron-phonon coupling g. As temperature increases, the deformation of lattice becomes increasingly localized. Thus, increasing temperature also drives the transition from a large polaron state to a small polaron state.

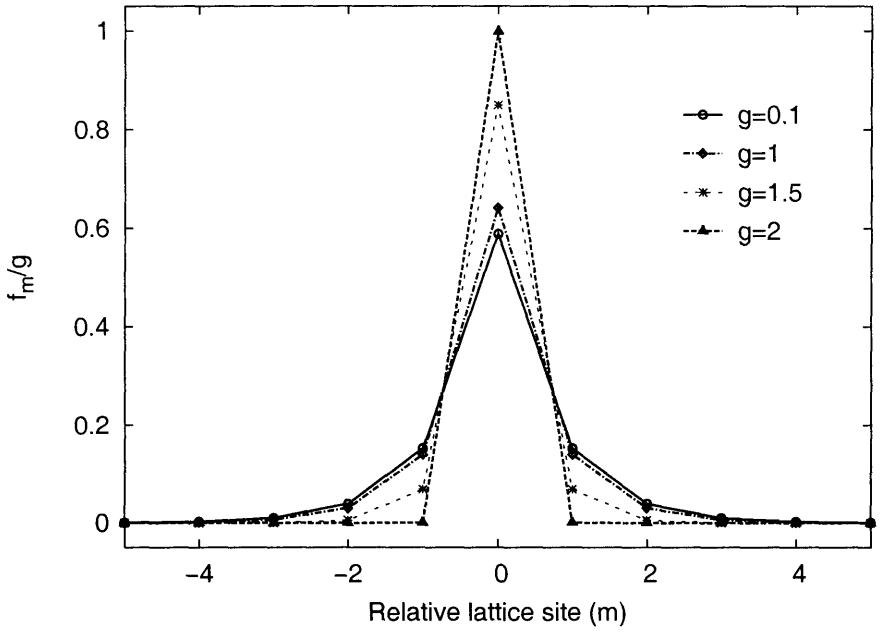

Figure 3-3: Polaron profiles at $\beta\omega_0 = 10$ for a 1-D nearest-neighbor system with $J_0/\omega_0 = 1/2$ at different strengths of electron-phonon couplings g. As g increases, the polaron profile becomes more localized.

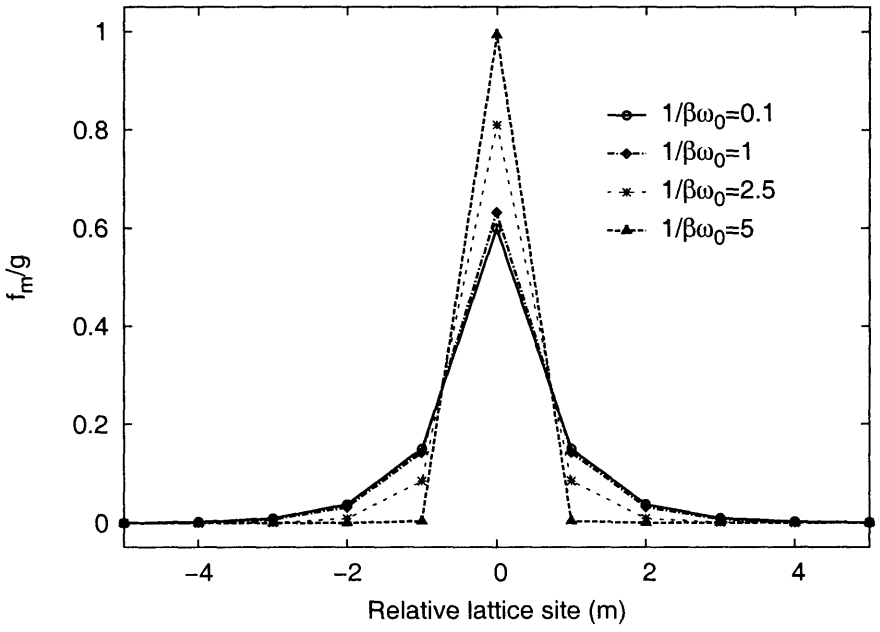

Figure 3-4: Polaron profiles for a 1-D nearest-neighbor system with $J_0/\omega_0 = 1/2$ and $g = 1/2$ at different temperatures. The polaron profile becomes more localized at higher temperatures.

3.4.1.2 Polaronic band-narrowing effect

To further characterize the structure of the polaron states and the polaronic band narrowing effect for the 1-D system, we study the effective transfer integrals J_{eff} [Eq. (3.29)] for optimal polaron states in a broad range of parameters. Note that for the 1-D nearest-neighbor system, the bare bandwidth is $4J_0$ and the polaronic narrowed effective bandwidth is $4J_{eff}$. Hence, J_{eff} is a direct measure of the effective bandwidth of the electrons. In Fig. 3-5, we show relative effective transfer integral J_{eff}/J_0 as a function of electron-phonon coupling g at a low temperature ($\beta\omega_0 = 10$) for 1-D systems with different bare transfer integrals. The transition from a weakly dressed large polaron state at small g ($J_{eff}/J_0 \approx 1$) to a strongly dressed small polaron state at large g ($J_{eff}/J_0 \ll 1$) can be clearly seen. A rapid decrease in J_{eff} occurs in the intermediate coupling regime, signaling the small polaron transition. Note that at small J_0/ω_0, the transition is smooth; however, for systems with sufficiently large J_0/ω_0, the effective bandwidth changes abruptly. The abrupt change is due to the existence of two minima in the free energy functional with respect to the dressing coefficients. When a crossover of the free energies of the two minima occurs, the optimal set of variational parameters abruptly shifted from one minima to the other, resulting in a discontinuous change in the optimal polaron structure. Exact theorems on the ground state of the 1-D Holstein model state that the ground state energy and effective mass are analytical functions of the strength of electron-phonon coupling g [11, 48, 49, 50], and while the character of the polaron state can change sharply in a narrow g range, there is no true phase transition in this system. The abrupt change is considered to be unphysical and an artifact of the variational method [21, 11]. A series of studies by Lindenberg *et al.* comparing a number of variational methods also clearly show that the abrupt change is due to the insufficient flexibility in the variational ansatz [24, 35, 26, 31].

Figure 3-5 also shows that the critical coupling strength where the small polaron transition occurs depends on the reduced bare transfer integral J_0/ω_0. For a narrow-band system whose J_0/ω_0 is small, the small polaron transition occurs at a smaller g,

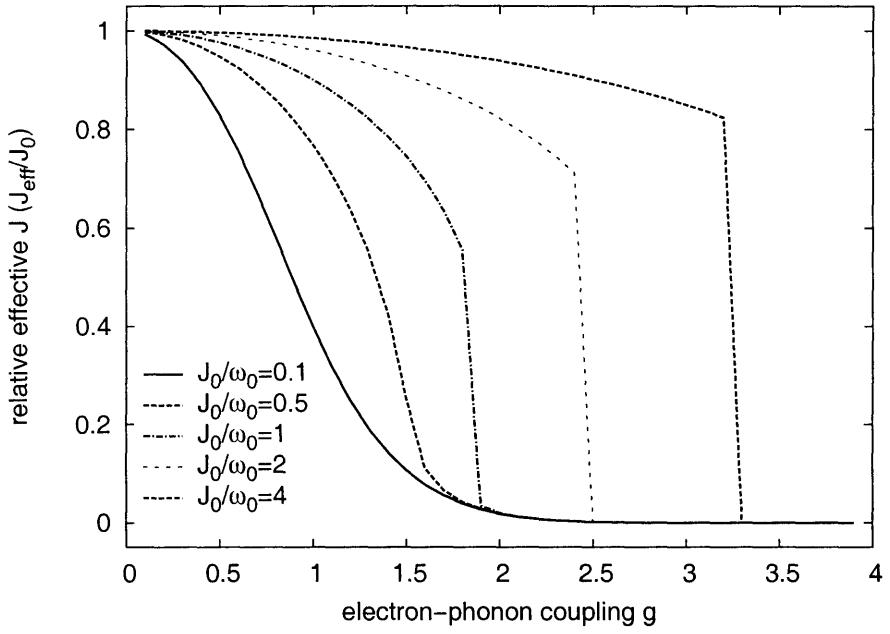

Figure 3-5: Effective transfer integrals as a function of electron-phonon couplings g for systems with different bare transfer integrals J_0/ω_0 at low temperature ($\beta\omega_0 = 10$).

in contrast to wide-band systems with large J_0/ω_0. This trend is the consequence of the competition between electronic coupling J_0 and electron-phonon coupling g. Note that different J_0/ω_0 can also be seen as different ω_0. Given the same J_0 and electron-phonon coupling strength g, our theory predicts that higher frequency phonon modes tend to localize the electron, while the low frequency modes could only dress the electron weakly.

Our finite-temperature variational method allows us to study the temperature dependence of the small polaron transition. To study the effect of varying temperatures, in Fig. 3-6, we compare curves of the relative effective transfer integrals J_{eff}/J_0 at different temperatures for a system with $J_0/\omega_0 = 0.8$. While the asymptotic behaviors of J_{eff} at small $g \ll 1$ and large $g \gg 1$ are not temperature dependent, the transition point where J_{eff} sharply decreases depends on the temperature. At higher temperatures, the small polaron transition occurs at smaller g, and the abrupt change is more pronounced. In addition, Fig. 3-6 also indicates the polaronic band narrowing effect at high temperatures.

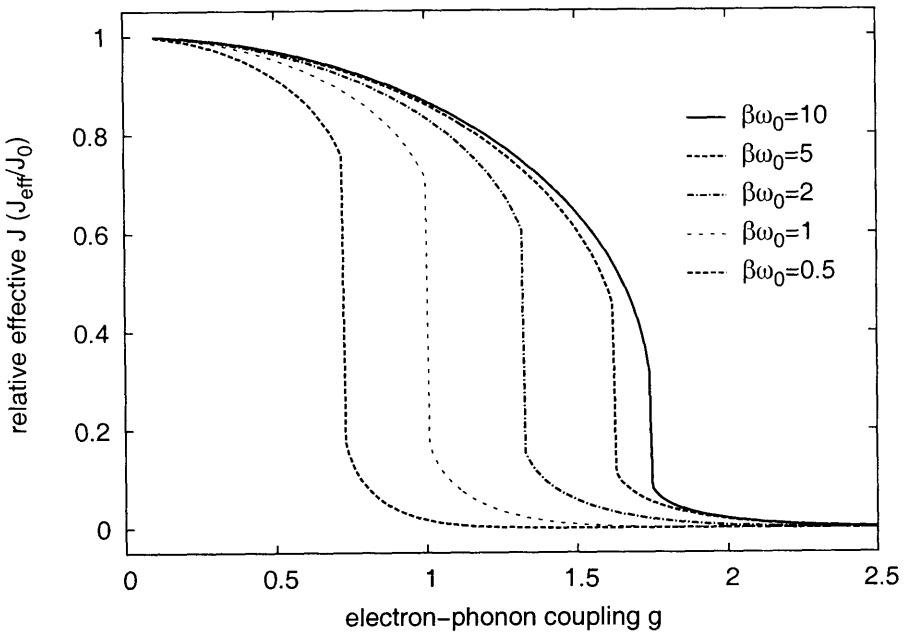

Figure 3-6: Effective transfer integrals as a function of electron-phonon couplings g for a system with $J_0/\omega_0 = 0.8$ at different temperatures.

Figure 3-7 shows the relative effective transfer integrals J_{eff}/J_0 as a function of the reduced temperature $1/\beta\omega_0$ for systems with $g = 1$ and different bare transfer integrals. Clearly, the small polaron band narrowing factor $e^{-g^2 \coth(\beta\omega_0/2)}$ does not describe the temperature dependence in these intermediate coupling systems. The effective transfer integral J_{eff} is a complicated function of temperature because of the variational parameters $\{f_m\}$ are also temperature dependent. Note that again a system with a larger bare transfer integral exhibits small polaron transition at a higher temperature. In the temperature range that we have shown in Fig. 3-7, the small polaron transition occurs smoothly at low temperatures for narrow-band materials whose reduced bare transfer integrals J_0/ω_0 are small. For a system with intermediate $J_0/\omega_0 = 1$, J_{eff} varies slowly at low temperature, and then drops suddenly at $1/\beta\omega_0 \sim 1.4$, indicating the appearance of an abrupt small polaron transition. For wide-bane materials with large J_0/ω_0, the effective transfer integrals J_{eff} are relatively temperature independent in the temperature range shown in Fig. 3-7; the abrupt transition to small polaron states for systems with $J_0/\omega_0 > 1.5$ occur

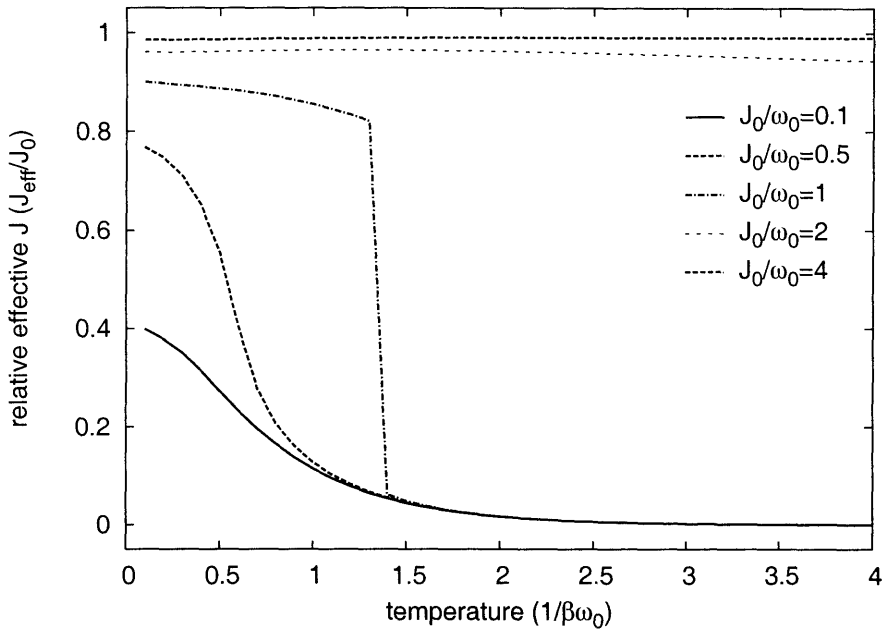

Figure 3-7: Effective transfer integrals as a function of temperature for systems with $g = 1$ and different bare transfer integrals. The small polaron transition signaled by a drop in J_{eff} is more dramatic for wide-band materials.

at higher temperatures not shown in the figure.

3.4.1.3 Phase diagrams

We summarize our findings about the characters of polaron states in the 1-D Holstein model at different parameters in phase diagrams shown in Fig. 3-8. These phase diagrams map the character of the polaron state as a function of electron-phonon coupling constant g and reduced electronic transfer integral J_0/ω_0 at different temperatures. Regions of different polaron characters are labeled as L, L', S, S': L labels the region of large polaron states, S labels the region of small polaron states, L' labels the region where the free energy functional A_0^e [Eq. (3.30)] exhibits spurious double minima with the lower A_0^e giving by the large polaron state, and S' labels the region where spurious double minima exist and the small polaron state gives the lower A_0^e. In these phase diagrams, the wedge-shaped region includes states that exhibit double minima, and abrupt changes occur across the small polaron transition line separating

the L' region and the S' region. For comparison, we also plotted an empirical self-trapping line that separates the small polaron region and the large polaron region of the 1-D Holstein model at zero temperature [51]:

$$g_{ST} = 1 + \sqrt{J_0/\omega_0}.$$

The self-trapping line is obtained by comparing the ground state energy from second-order WCPT and SCPT theories, and is known to reproduce the critical points predicted by more accurate numerical methods. The excellent agreement between g_{ST} and the transition line predicted by our variational method at low temperatures indicates that our variational approach gives reasonable semi-quantitative results at low temperatures. Although the abrupt transition due to spurious double minima is an artifact of the variational ansatz, it captures the point where the small polaron transition occurs.

Our finite-temperature variational method enables us to study the small polaron transition at finite temperatures and construct phase diagrams at different temperatures (Fig. 3-8). As the temperature increases, the wedge-shaped region expands and the small polaron transition line marking the abrupt transition is shifted towards smaller g, indicating that the transition to small polaron states is assisted by thermal population of the phonon modes.

3.4.2 Band-like and Hopping Mobilities

Figure 3-9 shows the results of our mobility calculations for a 1-D nearest-neighbor system with reduced transfer integral $J_0/\omega_0 = 1$ and different electron-phonon coupling constants. In addition, the results for systems with $J_0/\omega_0 = 2$ and 4 are shown in Fig. 3-10 and Fig. 3-11, respectively. Figure 3-9 to 3-11 display the temperature dependence of mobilities for systems with a broad range of electronic couplings (J_0/ω_0) and electron-phonon couplings (g). Our theoretical results presented in these figures clearly show universal band to hopping transitions in the mobilities, as ob-

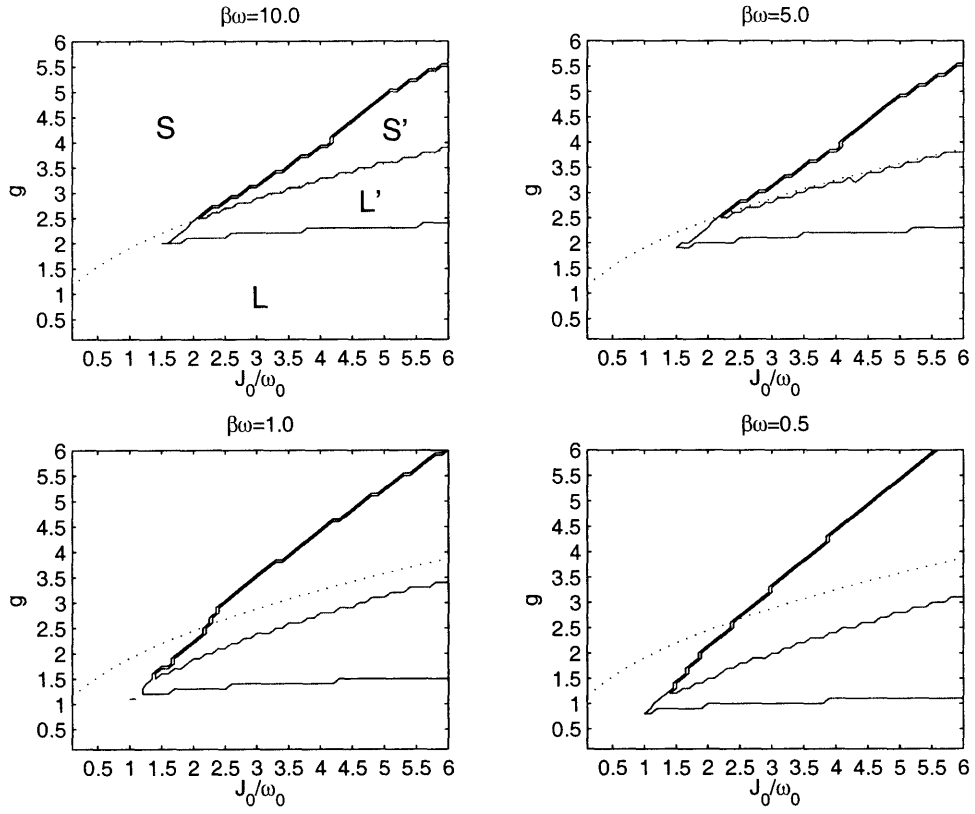

Figure 3-8: Polaron phase diagram determined using the finite-temperature variational method with Merrifield's ansatz at different temperatures. The dotted line is the empirical self-trapping line given by $g_{ST} = 1 + \sqrt{J_0/\omega_0}$.

served in experiments. All theoretical curves exhibit a universal trend. The total mobility is temperature independent in extremely low temperatures because the mobility is determined by the additional scattering channel represented by γ_0. As the temperature increases, the mobility starts to decrease in a power-law fashion. The steep power-law decrease continues over a wide temperature range, during which the mobility decreases by several orders of magnitudes. At intermediate to high temperatures, the mobility cease to decrease and depends only weakly on the temperature. Eventually, an abrupt change in the mobility occurs at a high temperature, which corresponds to the abrupt transition to the small polaron state. Note that beyond this transition point, the polaron state is fully dressed and the polaron bandwidth is narrowed by an exponentially small factor, resulting in very different transport behavior after the transition. As we have mentioned, the abrupt change is unphysical and is an artifact of the Merrifield's ansatz, therefore, mobility results around the discontinuity are questionable. Since the high temperature range in which the abrupt change occurs is usually not accessible in experiments, we disregard mobility points after the small polaron transition, and focus on the transport properties of partially dressed states in this work.

In Fig. 3-9 to 3-11, we also show the band-like contribution to the mobility as well as the hopping contribution. The total mobility is dominated by the band-like term in low temperatures and by the hopping term in high temperatures. At low to intermediate temperatures, the band-like term decreases monotonically, while the hopping term grows as temperature increases. At sufficiently high temperature, the hopping term becomes dominate the mobility even when the electron is only weakly coupled to the phonons. The crossover of the band-like and hopping terms results in the almost temperature independent mobility at the intermediate to high temperature regime. Note that the crossover temperature T_c where the crossover from band-like to hopping transport occurs depends on J_0/ω_0 and g. In general, a weak-coupling (small g) or wide-band (large J_0/ω_0) system has higher T_c.

In a number of previous studies, the small polaron transition in a variational treatment is considered to correspond to the crossover from the band-like to hop-

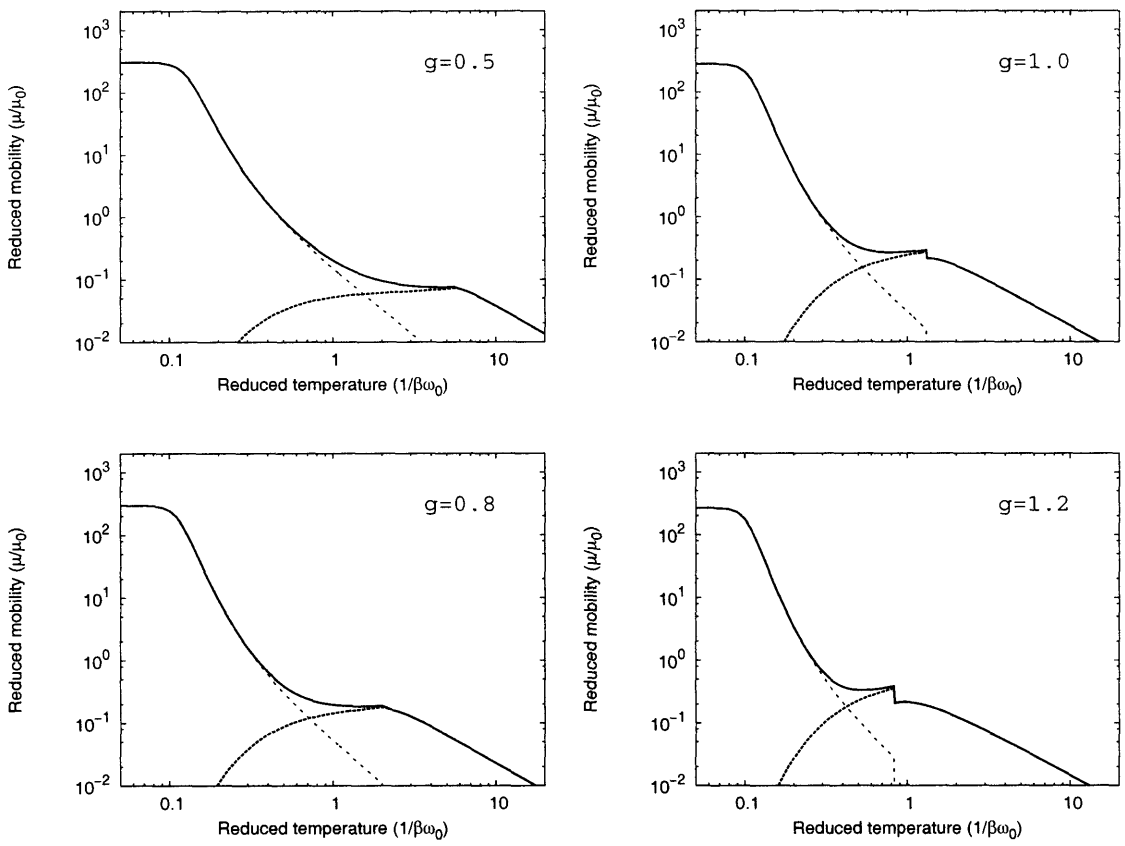

Figure 3-9: Mobilities for a 1-D Holstein system with $J_0/\omega_0 = 1$ at different electron-coupling constant g. We show the total mobility (solid lines), band-like contribution to the mobility (thin dashed lines), and hopping contribution to the mobility (thick dashed lines). $\alpha = 0.01\omega_0$ and $\gamma_0 = 0.001\omega_0$ are employed for these calculations. The unit of the y-axis is $\mu_0 = ea_0^2/\hbar$, where e is the charge of an electron, a_0 is the lattice constant, and $\hbar$ is Planck's constant.

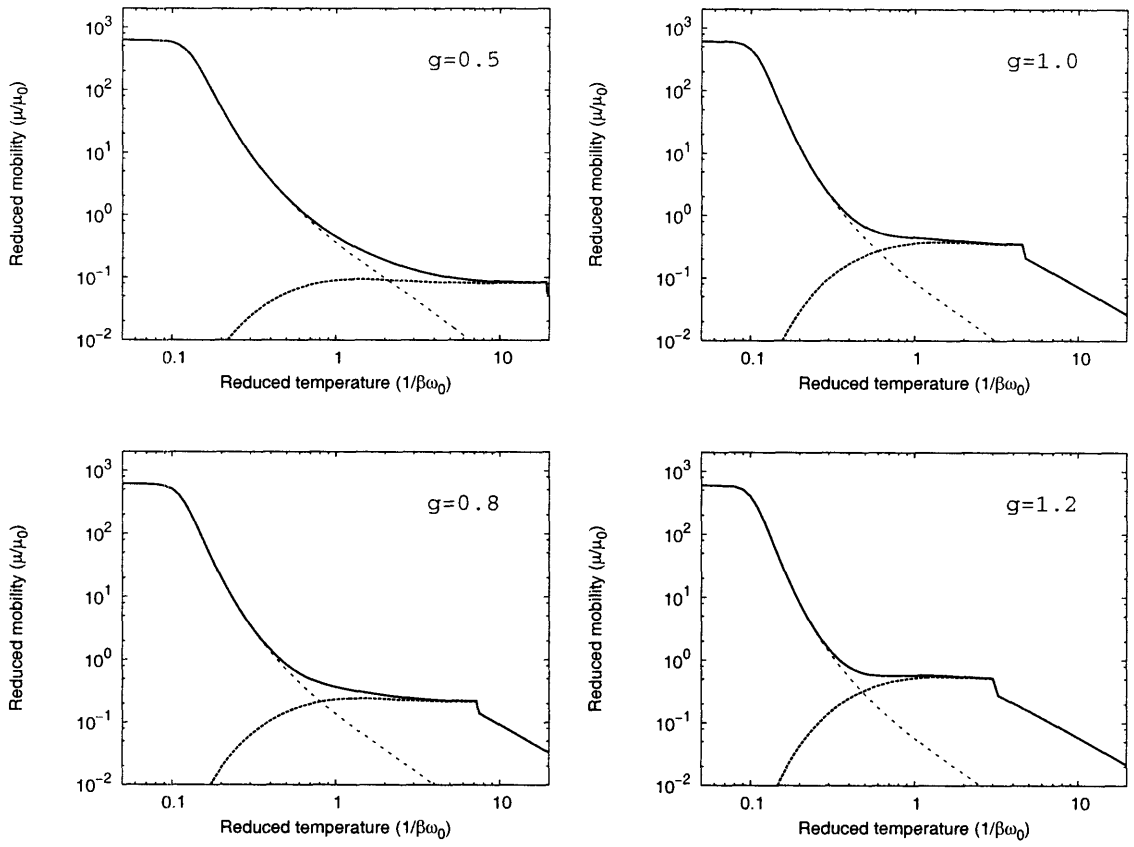

Figure 3-10: Mobilities for a 1-D Holstein system with $J_0/\omega_0 = 2$ at different electron-coupling constant g. We show the total mobility (solid lines), band-like contribution to the mobility (thin dashed lines), and hopping contribution to the mobility (thick dashed lines). $\alpha = 0.01\omega_0$ and $\gamma_0 = 0.001\omega_0$ are employed for these calculations. The unit of the y-axis is $\mu_0 = ea_0^2/\hbar$, where e is the charge of an electron, a_0 is the lattice constant, and $\hbar$ is Planck's constant.

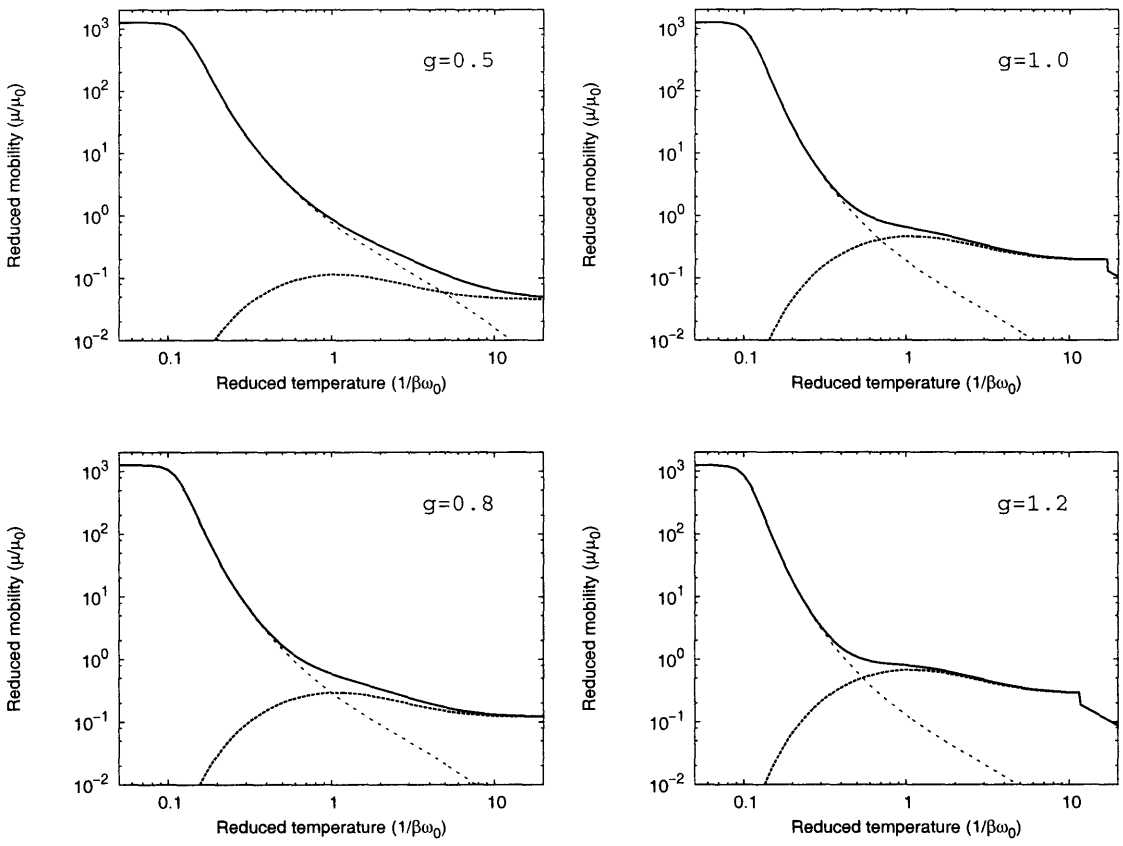

Figure 3-11: Mobilities for a 1-D Holstein system with $J_0/\omega_0 = 4$ at different electron-coupling constant g. We show the total mobility (solid lines), band-like contribution to the mobility (thin dashed lines), and hopping contribution to the mobility (thick dashed lines). $\alpha = 0.01\omega_0$ and $\gamma_0 = 0.001\omega_0$ are employed for these calculations. The unit of the y-axis is $\mu_0 = ea_0^2/\hbar$, where e is the charge of an electron, a_0 is the lattice constant, and $\hbar$ is Planck's constant.

ping transport [19, 20]. However, our results suggest that the two phenomena are not directly correlated. The smooth crossover in the transport mechanisms does not correspond to the transition in the structure of the polaron state; in contrast, the crossover from the band-like mechanism to the hopping mechanism occurs at a lower temperature compared to the small polaron transition (the abrupt change in the mobilities). Our results indicate that partially dressed state can give rise to a significant hopping term in a broad parameter range, which may be responsible for the band-like to hopping transition observed in experiments

We summarize key qualitative results that are exhibited by our partially dressed theory: (1) a steep power-law decrease of the mobility exists in the band-like regime, and the $n > 1.5$ behavior can be explained by the contribution from the multi-phonon scattering in the band-like term; (2) all theoretical curves predict smooth band-like to hopping transition in the temperature dependence of charge-carrier mobilities; however, the change in transport mechanism does not correspond to the small polaron transition; (3) almost temperature independent behavior over a wide temperature range exists in some parameter regime; (4) significant thermal-activated mobility at high temperature is not observed in all parameter regimes that we have studied; however, for sufficiently strong electron-phonon couplings, a slightly increase in the mobility can occur after the crossover from the band-like to hopping transport.

To study how the strength of electron-phonon coupling g affects the mobility, we compare the band-like and hopping mobilities for a 1-D Holstein system with $J_0/\omega_0 = 2$ at different electron-coupling constants (Fig. 3-12). The comparison shows that varying the strength of electron-phonon coupling has different effects on the band-like term and the hopping term. Because an increase in g results in more scattering of the polaron state, the hopping mobility (high-T) is enhanced by strong electron-phonon couplings, while the band-like mobility (low-T) is inhibited. Notice that varying g could result in a change of mobility by an amount of several orders of magnitudes. Thus, our results suggest that selecting a material with proper g value is important for optimizing charge-carrier mobilities at different temperatures; given the same reduced transfer integral J_0/ω_0, small g materials are favorable at

low temperatures (higher band-like mobility), while large g materials are favorable at high temperatures (higher hopping mobility).

3.5 Temperature Dependence on the Charge Mobilities in Naphthalene

In this section we compare our mobility calculations to experimental measurements of excess charge-carrier mobilities on the naphthalene crystals. In Fig. 3-13, we compare two theoretical curves from the 1-D model presented in the previous section to excess electron and hole mobilities measured in parallel to the crystalline b direction of the naphthalene crystals [52, 18]. The curves with (g, J_0, ω_0) =(0.4, 20 meV, 200 cm^{-1}) and (0.5, 13 meV, 150 cm^{-1}) are in agreement with experimental excess hole and electron mobilities, respectively. The fitting parameters indicate weak electron-phonon couplings, and are consistent with other spectroscopic experiments[53, 54, 55, 56, 57] and theoretical calculations[58, 59, 60] on naphthalene crystals.

Our simplified 1-D model is hardly adequate for the description of the mobility in naphthalene crystal because of the highly anisotropic and non-cubic structure of the crystal. Using the theoretical model presented in Section 3.2, it is possible to construct a 3-D description that takes into account the real crystal structure; however, such complete simulation would be too demanding and beyond the scope of this work. Figure 3-13 is not meant to provide a fit to the experimental data. Nevertheless, it demonstrates that our approach does capture the temperature dependence of the mobilities, and can provide a quantitative description that covers the whole experimental temperature range and different types of materials in a unified theory.

3.6 Concluding Remarks

In this chapter, we have developed a unified theory that describes both coherent and incoherent transport in the Holstein Hamiltonian and can quantitatively describe the temperature dependence of the charge-carrier mobilities in OMC. Our formalism uses

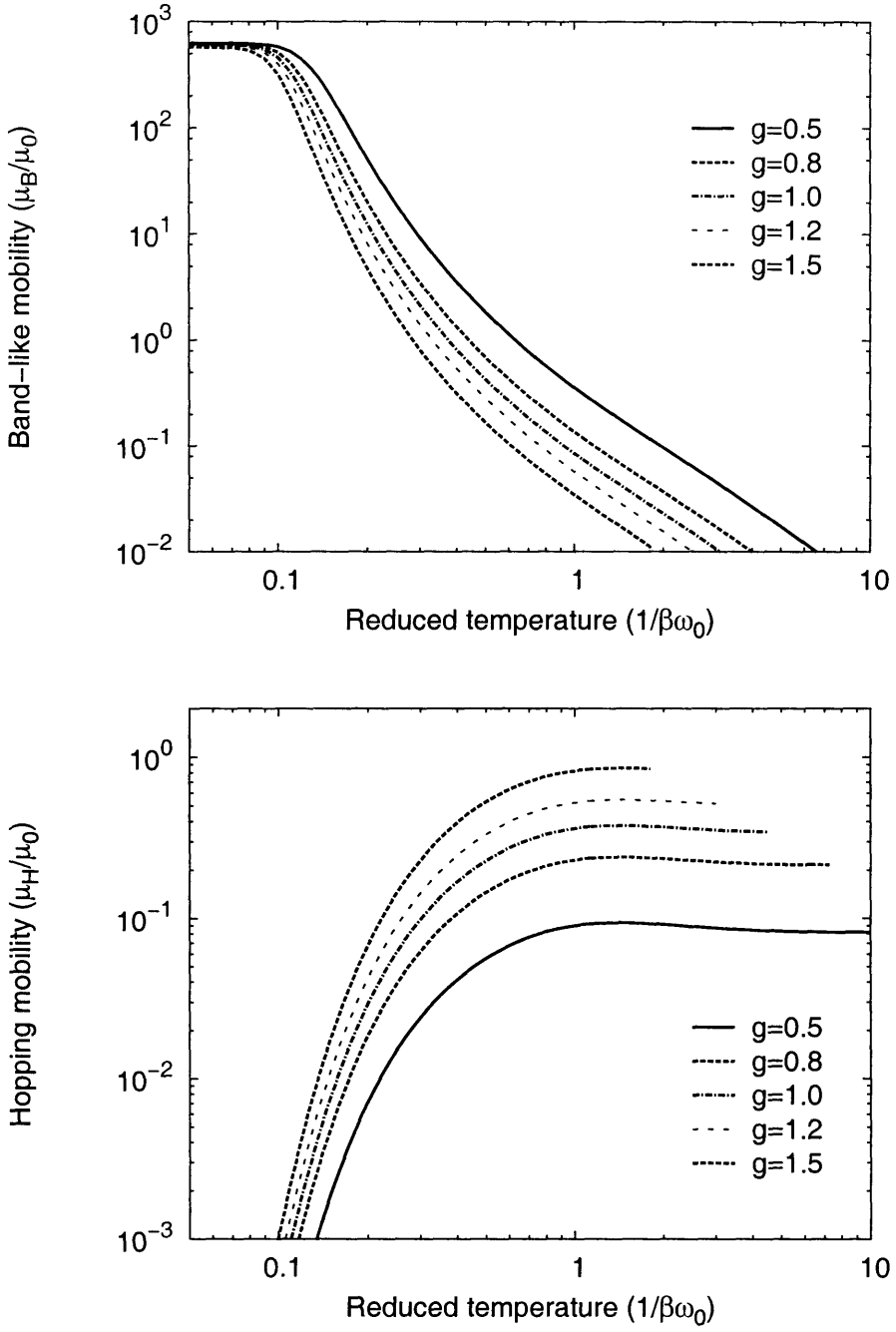

Figure 3-12: A comparison of band-like (upper panel) and hopping (lower panel) mobilities for a 1-D Holstein system with $J_0/\omega_0 = 2$ at different electron-coupling constants.

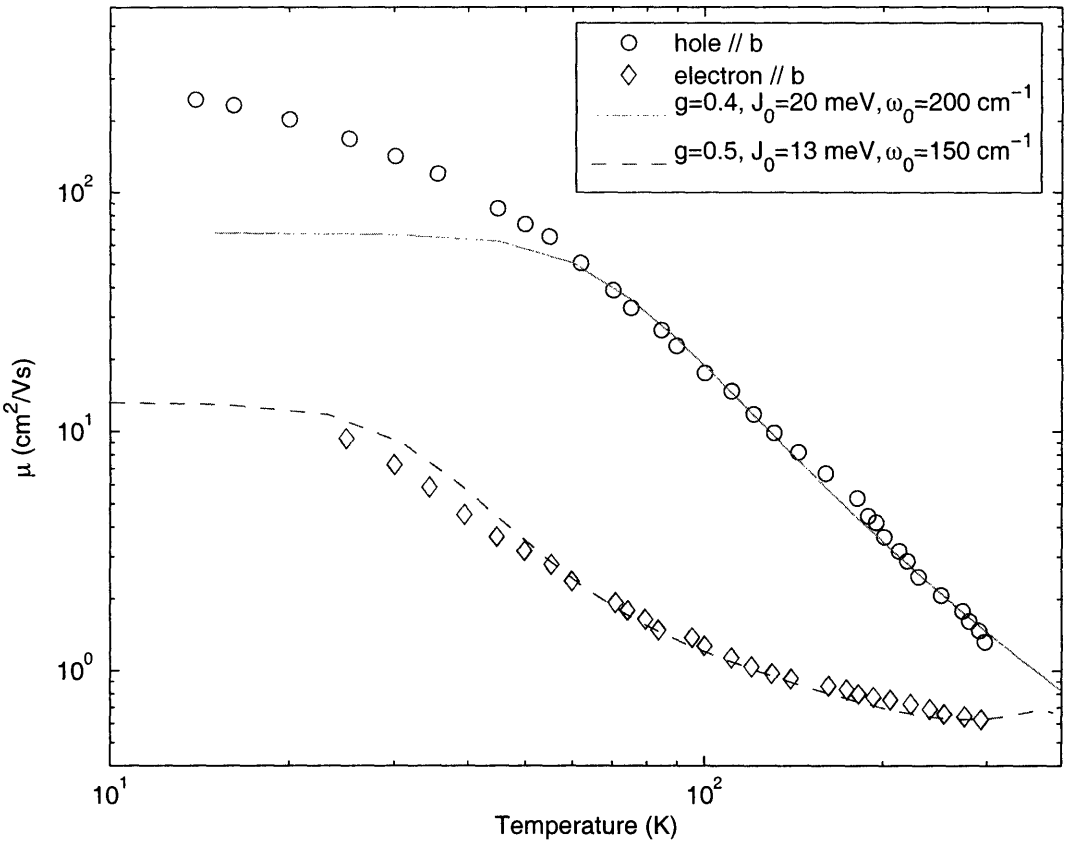

Figure 3-13: A comparison of our results with experimental measurements on ultrapure naphthalene crystals. Both excess electron and hole mobilities measured in parallel to the crystalline b direction of the naphthalene crystals are shown along side with selected 1-D results from our theory presented in the previous section. In addition, $\gamma_0 = 0.025\omega_0$ and $\alpha = 0.05\omega_0$ are employed in the numerical calculations.

a finite-temperature variational method combining Merrifield's transformation with Bogoliubov's theorem to obtain the optimal basis for an interacting electron-phonon system, and then based on the optimal basis to calculate the band-like and hopping mobilities for charge-carriers. Because we use Bogoliubov's theorem to obtain the optimal thermal mean-field description for the interacting electron-phonon system, a time-dependent perturbation expansion based on the variational zeroth-order Hamiltonian is justified in the intermediate coupling regime. Our calculations on the 1-D Holstein model at T=0K and finite temperatures indicate that the variational-perturbation method gives results that are compared favorable to other analytical methods.

We have applied the unified theory to the 1-D Holstein model at finite-temperatures. We studied the structures of polaron states at a broad range of parameters including different temperatures. Our method yields phase diagrams that are in agreement with predictions of more accurate numerical methods at low temperatures. Therefore, the finite-temperature Merrifield's variational method, although contains unphysical double minima on the free energy potential surface, gives reasonable semi-quantitative results for the polaron transition. We also calculated the band-like and hopping mobilities of the 1-D model in different parameters and showed that the temperature dependence of the total mobility predicted by our theory exhibits power-law decay at a wide temperature range, and a almost temperature independent behavior at higher temperatures before an abrupt change occurs. We found that as the temperature increases, the hopping transport can become dominate even before the polaron state changes its characters. Thus, our result indicates that the self-trapping transition studied in conventional polaron theories does not necessary correspond to the crossover from band-like to hopping transport in the transport properties in OMC. Comparing our 1-D results with experiments on ultrapure naphthalene crystals suggests that our method can describe the charge-carrier mobilities in OMC quantitatively across the whole experimental temperature range.

Although our variational method correctly predicts the small polaron transition line at low temperatures, the abrupt transition makes it difficult to access regions

close to or after the transition quantitatively. A more generalized ansatz, such as Toyozawa's ansatz, can greatly improve the applicable range of the current theory. Note that our results suggest that the crossover from bank-like to hopping transport occurs before the self-trapping transition, thus, the deficiency does not affect our main results regarding the charge-carrier mobilities in OMC.

Finally, we note that the mobility expression from Yarkony and Silbey [Eq. (3.15) - Eq. (3.18)] is a approximated expression in which small terms have been dropped. Since we have used numerical integration to evaluate the mobilities, it is straightforward to numerically propagate the reduced density matrix of the system according to the master equation in Eq. (3.12), and then calculate the mobility using Eq. (3.14). The direct propagation scheme is favorable when simulating real 3-D systems because numerical integration of 3-D functions are not efficient. In addition, static disorders and non-equilibrium effect can be easily incorporated into such a numerical scheme, making the approach favorable when modeling disorder materials.

Appendix 3.A Phonon Correlation Functions

The phonon correlation function $\langle V_{q'k'}V_{kq}(\tau)\rangle_0$ for a narrow phonon band with phonon frequency ω_0 is given by

$$\begin{aligned}
\langle V_{q'k'}V_{kq}(\tau)\rangle_0 \;=\; & \frac{1}{N}\sum_{n_1,m_1}\sum_{n_2,m_2} e^{-iq'n_1}e^{ik'm_1}e^{-ikn_2}e^{iqm_2}\tilde{J}_{n_1m_1}\tilde{J}_{n_2m_2} \\
& \times\left\{e^{-\sum_s\left[X_s^{n_1m_1}\bar{X}_s^{n_2m_2}(n_0+1)e^{i\omega_0\tau}+\bar{X}_s^{n_1m_1}X_s^{n_2m_2}n_0e^{-i\omega_0\tau}\right]}-1\right\} \\
& +\frac{\omega_0}{N}(g-f_{k-q})\sum_{n,m}e^{-iq'n}e^{ik'm}\tilde{J}_{nm}\bar{X}_{k-q}^{nm}\left[-n_0e^{-i\omega_0\tau}+(n_0+1)e^{i\omega_0\tau}\right] \\
& +\frac{\omega_0}{N}(g-f_{q'-k'})\sum_{n,m}e^{-ikn}e^{iqm}\tilde{J}_{nm}\bar{X}_{q'-k'}^{nm}\left[n_0e^{-i\omega_0\tau}-(n_0+1)e^{i\omega_0\tau}\right] \\
& +\omega_0^2(g-f_{q'-k'})^2\cdot\left[n_0e^{-i\omega_0\tau}+(n_0+1)e^{i\omega_0\tau}\right]\cdot\delta(q'-k'+k-q),
\end{aligned}$$

where we have defined $\tilde{J}_{nm}=J_{nm}\langle\theta_n^\dagger\theta_m\rangle_0$, $X_q^{nm}=\frac{1}{\sqrt{N}}f_q(e^{iqm}-e^{iqn})$, $\bar{X}_q^{nm}=\frac{1}{\sqrt{N}}f_q^*(e^{-iqm}-e^{-iqn})$, and $n_0=1/(e^{-\beta\omega_0}-1)$. Note that using the symmetry property of quan-

tum correlation functions, we can easily calculate the other correlation function $\langle V_{q'k'}(\tau)V_{kq}\rangle_0$:

$$\langle V_{q'k'}(\tau)V_{kq}\rangle_0 = \langle V_{q'k'}V_{kq}(\tau)\rangle_0^*.$$

Appendix 3.B 2^{nd}-order Correction on the Energy Band at T=0K

The second-order energy correction to the energy band of the polaron state in Eq. (3.23) assumes the following form:

$$\begin{aligned} E^{(2)}(k) &= -2\omega_0 f_{opt}(g-f_{opt}) \\ &\quad -\omega_0^2(g^2-f_{opt}^2)\times\frac{1}{N}\sum_{k'}\frac{1}{2\tilde{J}_0\cos k'-2\tilde{J}_0\cos k-\omega_0} \\ &\quad -2\tilde{J}_0^2\textstyle\sum_{n_T=1}^{\infty}\frac{f_{opt}^{2n_T}}{n_T!} \\ &\quad \times\frac{1}{N}\sum_{k'}\frac{2^{n_T}+\cos 2k+\cos 2k'+2\cdot(-1)^{n_T}\cos(k'-k)+(-2)^{n_T}\cos(k'+k)}{2\tilde{J}_0\cos k'-2\tilde{J}_0\cos k-n_T\omega_0}, \end{aligned}$$

where we have defined $\tilde{J}_0 = J_0 e^{-f_{opt}^2}$. Around the bottom of the band where $k\sim 0$ and $\cos k\sim 1$, the integral over k' can be evaluated explicitly to give

$$\begin{aligned} E^{(2)}_{k\sim 0}(k) &= -2\omega_0 f_{opt}(g-f_{opt}) \\ &\quad -\omega_0^2(g^2-f_{opt}^2)\times\frac{1}{2\tilde{J}_0\sqrt{(\cos k+\omega_0/2\tilde{J}_0)^2-1}} \\ &\quad -2\tilde{J}_0\sum_{n_T=1}^{\infty}\frac{f_{opt}^{2n_T}}{n_T!}\times\frac{A\sqrt{A^2-1}-AB+B\sqrt{A^2-1}-A^2-C}{\sqrt{A^2-1}}, \end{aligned} \tag{3.33}$$

where the auxiliary functions are defined as

$$\begin{aligned} A &= \cos k+n_T\omega_0/2\tilde{J}_0, \\ B &= \frac{1}{2}[2(-1)^{n_T}+(-2)^{n_T}]\cos k, \end{aligned}$$

$$C = \frac{1}{2}\left[2^{n_T} + \cos 2k - 1\right].$$

The expression for $E^{(2)}_{k\sim 0}(k)$ is used to calculated the effective mass of the polaron state at T=0K.

Appendix 3.C Toyozawa Method at 0K

Toyozawa's ansatz can be written as the translationally invariant superposition of localized soliton states. The expression for the trial state with total crystal momentum κ is

$$|\Psi(\kappa)\rangle = \frac{1}{\sqrt{N}} \sum_n e^{i\kappa R_n} |\Psi_n\rangle, \tag{3.34}$$

where $|\Psi_n\rangle$ is the ansatz state localized at site n, and can be written as a direct product of the electron and phonon wavefunctions:

$$|\Psi_n\rangle = \sum_m \phi^\kappa_m a^\dagger_{m+n}|0\rangle_{ex} \otimes \exp[-\frac{g}{\sqrt{N}} \sum_{m,q} f^\kappa_m (e^{iq(R_n+R_m)} b_q - e^{-iq(R_n-R_m)} b^\dagger_{-q})]|0\rangle_{ph}.$$

Here $|0\rangle_{ex}$ and $|0\rangle_{ph}$ denote the electron vacuum state and the phonon vacuum state, respectively. Coefficients $\{\phi^\kappa_m\}$ and $\{f^\kappa_m\}$ are variational variables that must satisfy the symmetry constrain, $\phi^\kappa_m = \phi^\kappa_{-m}$ and $f^\kappa_m = f^\kappa_{-m}$. In addition, $\{\phi^\kappa_m\}$ must satisfy the normalization condition of a single excitation, $\sum_m \phi^\kappa_m = 1$. Toyozawa's ansatz $|\Psi_n\rangle$ has a direct physical interpretation. The set $\{\phi^\kappa_m\}$ represents a pulse-shaped distribution of electron probability amplitudes centered around site n, and $\{f^\kappa_m\}$ represents a lattice deformation around site n. Compared to Merrifield's ansatz used in this chapter, Toyozawa's ansatz can be considered as an extension that adds electronic dispersion to the ansatz state. Note that because of the translational symmetry of the crystal, the final trial state is a Bloch state of these localized states. The trial states $|\Psi(\kappa)\rangle$ are eigenfunctions of the total crystal momentum operator and orthogonal for different κ. Therefore, variational variables for different κ subspace are indepen-

dent, this independence enables us to carry out the variational minimization for each distinct κ subspace.

At zero temperature, the variational upper bound of the ground state polaron energy band can be computed by minimizing the energy function

$$E(\kappa) = \frac{\langle \Psi(\kappa)|H|\Psi(\kappa)\rangle}{\langle \Psi(\kappa)|\Psi(\kappa)\rangle} \tag{3.35}$$

with respect to the variational parameters, $\{\phi_m^\kappa\}$ and $\{f_m^\kappa\}$, under the constrains mentioned above. The polaron band structure and the optimized wave function in different total crystal momentum can be obtained by performing the variational calculation with different κ value. In addition, properties of the polaron state can be evaluated using the optimized wave functions. For example, the polaron effective mass, m^*, often used as an indicator to the polaron structure, can be computed based on the formula

$$\frac{m_{eff}}{m_0} = \frac{2J}{\left.\frac{\partial^2 E(\kappa)}{\partial \kappa^2}\right|_{\kappa=0}}$$

using a parabolic fit to the band around the bottom of the band. In our numerical calculations, we construct the energy band by employing a 31-site lattice with periodic boundary condition. The total number of independent variational parameters are 32. An iterative scheme is adapted to minimize the energy functional and compute the optimal set of $\{\phi_m^\kappa\}$ and $\{f_m^\kappa\}$. We have also compared our results with calculations using a larger ansatz lattice, and the differences are negligible.

Bibliography

[1] Martin Pope and Charles E. Swenberg. *Electronic Processes in Organic Crystals.* Oxford University Press, New York, 1982.

[2] Edgar A. Silinsh and Vladislav Čápek. *Organic Molecular Crystals: Interaction, Localization, and Transport Phenomena.* AIP Press, Woodbury, NY, 1994.

[3] R. M. Glaeser and R. Stephen Berry. Mobilities of electrons and holes in organic molecular solids. comparison of band and hopping models. *J. Chem. Phys.*, 44(10):3797, 1966.

[4] H Haken and G. Strobl. An exactly solvable model for coherent and incoherent exciton motion. *Z. Physik*, 262:135, 1973.

[5] H. Haken and P. Reineker. The coupled coherent and incoherent motion of excitons and its influence on the line shape of optical absorption. *Z. Physik*, 249:253, 1972.

[6] P. Reineker. *Exciton Dynamics in Molecular Crystals and Aggregates.* Springer-Verlag, Berlin, 1982.

[7] V. Čápek. Haken-strobl-reineker model - its limits of validity and a possible extension. *Chem. Phys.*, 171(1-2):79 – 88, 1993.

[8] N. Karl. Studies of organic semiconductors for 40 years .3. *Mol. Cryst. Liq. Cryst.*, 171:31 – 51, 1989.

[9] N. Karl. Fast electronic transport in organic molecular solids? *J. Vac. Sci. Technol. A*, 17(4):2318, 1999.

[10] T. Holstein. Studies of polaron motion, part 1. the molecular-crystal model. *Ann. Phys. (N. Y.)*, 8:325, 1959.

[11] D. Emin. On the existence of free and self-trapped carriers in insulators: An abrupt temperature-dependent conductivity transition. *Adv. Phys.*, 22:57, 1973.

[12] D. R. Yarkony and R. J. Silbey. Variational approach to exciton transport in molecular crystals. *J. Chem. Phys.*, 67(12):5818, 1977.

[13] R. J. Silbey and R. W. Munn. General theory of electronic transport in molecular crystals. I. local linear electron-phonon coupling. *J. Chem. Phys.*, 72(4):2763, 1980.

[14] R. W. Munn and R. Silbey. Remarks on exciton-phonon coupling and exciton transport. *Mol. Cryst. Liq. Cryst.*, 57:131, 1980.

[15] V. M. Kenkre, John D. Andersen, D. H. Dunlap, and C. B. Duke. Unified theory of the mobilities of photoinjected electrons in naphthalene. *Phys. Rev. Lett.*, 62(10):1165, 1989.

[16] S. Rackovsky and R. Silbey. Electronic-energy transfer in impure solids .1. 2 molecules embedded in a lattice. *Mol. Phys.*, 25(1):61, 1973.

[17] J. D. Andersen, C. B. Duke, and V. M. Kenkre. Application of the silbey-munn theory to interpret the temperature-dependence of the mobilities of injected electrons in naphthalene. *Chem. Phys. Lett.*, 110(5):504 – 507, 1984.

[18] N. Karl. *Organic Semiconductors*, volume 17 of *Landolt Börnstein/New Series Group III.* Springer, Berlin, subvol. 17i, pp. 106-218 edition, 1985.

[19] D. R. Yarkony and R. J. Silbey. Comments on exciton phonon couplings: Temperature dependence. *J. Chem. Phys.*, 65(3):1042, 1976.

[20] P. E. Parris and V. M. Kenkre. Variational considerations in the study of carrier transport in organic crystals. *Phys. Rev. B*, 70(6):064304, 2004.

[21] J. W. Allen and R. Silbey. Comments on exciton-phonon coupling .2. variational solutions. *J. Chem. Phys.*, 43(3):341 – 349, 1979.

[22] T. Holstein. Studies of polaron motion, part 2. the "small" polaron. *Ann. Phys. (N. Y.)*, 8:343, 1959.

[23] R. E. Merrifield. Theory of the Vibrational Structure of Molecular Exciton States. *J. Chem. Phys.*, 40:445, 1964.

[24] Y. Zhao, D. W. Brown, and K. Lindenberg. Variational energy band theory for polarons: Mapping polaron structure with the Merrifield method. *J. Chem. Phys.*, 106(13):5622 – 5630, 1997.

[25] Y. Toyozawa. *Prog. Theor. Phys.*, 26:29, 1961.

[26] D. W. Brown, K. Lindenberg, and Y. Zhao. Variational energy band theory for polarons: Mapping polaron structure with the global-local method. *J. Chem. Phys.*, 107(8):3179 – 3195, 1997.

[27] J. Bonca, S. A. Trugman, and I. Batistic. Holstein polaron. *Physical Review B*, 60(3):1633 – 1642, 1999.

[28] L. C. Ku, S. A. Trugman, and J. Bonca. Dimensionality effects on the Holstein polaron. *Physical Review B*, 65(17), 2002.

[29] H. De Raedt and A. Lagendijk. Numerical-calculation of path-integrals - the small-polaron model. *Phys. Rev. B*, 27(10):6097 – 6109, 1983.

[30] H. De Raedt and A. Lagendijk. Numerical study of holsteins molecular-crystal model - adiabatic limit and influence of phonon-dispersion. *Phys. Rev. B*, 30(4):1671 – 1678, 1984.

[31] A. H. Romero, D. W. Brown, and K. Lindenberg. Converging toward a practical solution of the Holstein molecular crystal model. *J. Chem. Phys.*, 109(16):6540 – 6549, 1998.

[32] G. Kopidakis, C. M. Soukoulis, and E. N. Economou. Electron-phonon interaction, localization, and polaron formation in one-dimensional systems. *Phys. Rev. B*, 51(21):15038 – 15052, 1995.

[33] E. V. L. de Mello and J. Ranninger. Dynamical properties of small polarons (vol 55, pg 14 872, 1997). *Phys. Rev. B*, 58(21):14625 – 14625, 1998.

[34] C. L. Zhang, E. Jeckelmann, and S. R. White. Dynamical properties of the one-dimensional Holstein model. *Physical Review B*, 60(20):14092 – 14104, 1999.

[35] Y. Zhao, D. W. Brown, and K. Lindenberg. Variational energy band theory for polarons: Mapping polaron structure with the Toyozawa method. *J. Chem. Phys.*, 107(8):3159 – 3178, 1997.

[36] E. Jeckelmann and S. R. White. Density-matrix renormalization-group study of the polaron problem in the Holstein model. *Physical Review B*, 57(11):6376 – 6385, 1998.

[37] A. S. Alexandrov, V. V. Kabanov, and D. K. Ray. From electron to small polaron - an exact cluster solution. *Phys. Rev. B*, 49(14):9915 – 9923, 1994.

[38] F. Marsiglio. Pairing in the holstein model in the dilute limit. *Physica C*, 244(1-2):21 – 34, 1995.

[39] W. Stephan. Single-polaron band structure of the Holstein model. *Phys. Rev. B*, 54(13):8981 – 8984, 1996.

[40] M. K. Grover and R. Silbey. exciton-phonon interactions in molecular crystals. *J. Chem. Phys.*, 52(4):2099, 1970.

[41] M. Grover and R. Silbey. exciton migration in molecular crystals. *J. Chem. Phys.*, 54(11):4843, 1971.

[42] E. I. Rashba. *Excitons*, page 543. North-Holland, Amsterdam, 1982.

[43] P. O. J. Scherer, E. W. Knapp, and S. F. Fischer. Exciton phonon self-trapping - a continuous transition. *Chem. Phys. Lett.*, 106(3):191 – 196, 1984.

[44] K. S. Song and R. T. Williams. *Self-Trapped Excitons.* Springer-Verlag, Berlin, 1993.

[45] G. Wellein and H. Fehske. Self-trapping problem of electrons or excitons in one dimension. *Physical Review B*, 58(10):6208 – 6218, 1998.

[46] A. H. Romero, D. W. Brown, and K. Lindenberg. The weak, the large, and the empty: bringing order to concepts of spatial coherence in the Holstein polaron. *J. Lumines.*, 83-4:147 – 153, 1999.

[47] D. W. Brown, A. H. Romero, and K. Lindenberg. Franck-Condon factors as spectral probes of polaron structure. *J. Phys. Chem. A*, 103(49):10417 – 10425, 1999.

[48] D. Emin and T. Holstein. Adiabatic theory of an electron in a deformable continuum. *Phys. Rev. Lett.*, 36(6):323, 1976.

[49] H. Löwen. Analytical behavior of the ground-state energy and pinning transitions for a bound polaron. *J. Math. Phys.*, 29:1505, 1988.

[50] B. Gerlach and H. Löwen. Analytical properties of polaron systems or: Do polaronic phase transitions exist or not? *Rev. Mod. Phys.*, 63:63, 1991.

[51] A. H. Romero, D. W. Brown, and K. Lindenberg. Self-trapping line of the Holstein molecular crystal model in one dimension. *Phys. Rev. B*, 60(7):4618 – 4623, 1999.

[52] L. B. Schein, W. Warta, A. R. McGhie, and N. Karl. Mobilities of electrons and holes in naphthalene and perdeuterated naphthalene. *Chem. Phys. Lett.*, 100(1):34 – 36, 1983.

[53] E. L. Bokhenkov, I. Natkanets, and E. F. Sheka. Determination of density of phonon states in a naphthaline crystal on basis of inelastic incoherent neutron-scattering. *Zh. Eksp. Teor. Fiz.*, 70(3):1027 – 1043, 1976.

[54] B. Dorner, E. L. Bokhenkov, E. F. Sheka, S. L. Chaplot, G. S. Pawley, J. Kalus, U. Schmelzer, and I. Natkaniec. Phonon-dispersion curves in the molecular-crystals naphthalene and anthracene measured by inelastic neutron-scattering. *J. Phys. (Paris)*, 42(NC6):602 – 604, 1981.

[55] E. L. Bokhenkov, A. I. Kolesnikov, T. A. Krivenko, E. F. Sheka, V. A. Dementjev, and I. Natkaniec. Neutron spectroscopy of internal phonons of naphthalene and anthracene-crystals. *J. Phys. (Paris)*, 42(NC6):605 – 607, 1981.

[56] N. Sato, H. Inokuchi, B. M. Schmid, and N. Karl. Ultraviolet photoemission spectra of organic single-crystals. *J. Chem. Phys.*, 83(11):5413 – 5419, 1985.

[57] A. L. Motyka, S. A. Wittmeyer, R. J. Babbitt, and M. R. Topp. Weak vibrational couplings in a large van der Waals complex: Fluorescence spectroscopy of perylene/naphthalene. *J. Chem. Phys.*, 89:4586, 1988.

[58] V. Coropceanu, M. Malagoli, D. A. da Silva Filho, N. E. Gruhn, T. G. Bill, and J. L. Brédas. Hole- and Electron-Vibrational Couplings in Oligoacene Crystals: Intramolecular Contributions. *Phys. Rev. Lett.*, 89:275503, 2002.

[59] T. Kato and T. Yamabe. Vibronic interactions and superconductivity in acene anions and cations. *J. Chem. Phys.*, 115:8592, 2001.

[60] T. Kato, M. Kondo, K. Yoshizawa, and T. Yamabe. Superconductivity in acenes. *Synth. Met.*, 126(1):75 – 80, 2002.

Chapter 4

A Stochastic Liouville Equation Approach for Quantum Dissipation and Decoherence

4.1 Introduction

In Chapter 3, a microscopic model that describes interacting electron-phonon systems was developed to study the temperature dependence of the charge-carrier mobilities in organic molecular crystals. Similar microscopic models that explicitly introduce terms in the Hamiltonian to represent the phonon bath and the couplings can be applied to study the dissipation and decoherence of quantum systems [1, 2, 3, 4, 5]. However, due to the complexity caused by including extra bath degrees of freedom in the model, applications of these microscopic methods are usually limited on small systems with only a few quantum states. In this chapter, we will show a stochastic Liouville equation approach that can be solved efficiently to describe the dissipative dynamics of a multi-spin system. The motivation is to develop a theoretical model that can be used to describe the effect of noise in a quantum computer.

The Redfield theory has become the standard relaxation theory for quantum dynamics in condensed phases [6]. The Redfield equations that describe the dynamics

of a quantum system are a set of coupled linear differential equations for the reduced density matrix of the system; the dissipative dynamics of the system is governed by relaxation coefficients that are constructed from bath correlation functions. When the bath is treated explicitly, the evaluation of these relaxation coefficients is a challenging problem. As a result, the application of the Redfield theory with explicit bath is limited to systems with at most a few spins. In order to study the dynamics of a multi-level quantum system, it is usually necessary to adopt phenomenological methods that do not include the bath degree of freedom explicitly. Moreover, the Redfield formalism is also known to violate the complete positivity of the reduced density operator at short times [7, 8, 9]. For some initial conditions, the Redfield equation produces density matrices with negative eigenvalues at short times, which is unphysical. This problem has caused difficulties in applications. For example, to apply the Redfield formalism to study the dissipative dynamics of a quantum computer, non-physical additional time intervals have to be inserted between the switching events [10, 11]. These extra time periods will result in the over-estimation of the degradation of the quantum computer.

It is also possible to totally neglect the bath and use phenomenological relaxation and decoherence rates as the relaxation tensor elements in the Redfield theory. The phenomenological Bloch-Redfield formalism is generally used in studies on NMR spin-dynamics [12, 6, 13], and has been applied to study the dynamics of many-spin systems. However, this formalism, while suitable in NMR systems, is not always applicable in general quantum systems. In addition, the use of simple rate expressions in the eigen-basis of the quantum system is not well justified, and the physical origins of the phenomenological relaxation and decoherence rates are usually not clear. Thus, generally speaking, an efficient method that can be used to calculate the dissipative dynamics of a multi-spin quantum system based on the microscopic parameters of the system is still not available.

In this chapter, we purpose a stochastic Liouville equation approach to describe dissipation and decoherence of quantum systems. The stochastic Liouville equation approach has been widely used to describe the dissipative dynamics of quantum sys-

tems [14, 15]. We follow the approach that originates from the Haken-Strobl-Reineker (HSR) model first proposed by Haken and Strobl and later extended by Reineker in the 1970s to describe charge and energy transfer in organic crystals[16, 17, 18]. It is known that the HSR model captures both the coherent and incoherent dynamics of quantum systems. In the HSR model, the system-bath interactions are taken into account by allowing the site energies and the off-diagonal matrix elements of the system to fluctuate over time. We generalize the idea of Haken and Strobl to describe a system composed of n two-level systems (spins[1]). The resulting stochastic Liouville equation is then solved to obtain the generalized HSR equation of motion, which is a set of linear differential equations describing the dynamics of a general n spin system. We then discuss the limitations and possible extensions of this model. Furthermore, in Appendix 4.A we describe the condition for which the evolution generated by the generalized HSR equation of motion is positive. Thus, the generalized HSR equation of motion, a construction of the Redfield formalism, avoids the positivity problem and is applicable to the study of dissipation and decoherence of multi-spin quantum systems.

4.2 The Stochastic Liouville Equation Approach

Previous work on the study of the population relaxation and decoherence of quantum systems is usually based on the spin-boson Hamiltonian, in which the two-level systems are coupled linearly to the bath degrees of freedom (the environment), and the bath is treated explicitly as a system of harmonic oscillators [3, 19, 20]. Due to the difficulty of applying the spin-boson model to multi-spin systems, we take another approach. Instead of treating the bath explicitly, we substitute the bath with a set of external stochastic noises. Following the stochastic Liouville equation approach of the HSR model, we consider an effective Hamiltonian that treats the effect of the bath as a set of classical fluctuating fields acting on the system [16, 17, 18]. To describe the dynamics of an array of spins under the influence of environmental noise, we consider

[1]In this chapter, the term "spin" refers to a spin-1/2 system, i.e. a two-level system.

a system of n spins (2^n states), and start from a Hamiltonian with time independent and time dependent parts. The general Hamiltonian of the system can be written as

$$\begin{aligned} \mathbf{H}(t) &= \mathbf{H}_0 + \mathbf{h}(t) \\ &= \sum_{i,j=0}^{2^n-1} \left[H_{ij} + h_{ij}(t)\right] c_i^\dagger c_j, \end{aligned} \tag{4.1}$$

where $c_i^\dagger$ and c_i are the creation and annihilation operators for the i-th state of the 2^n basis set. The time independent part $\mathbf{H}_0$ describes the energies and interactions in the spin system, while the time dependent part $\mathbf{h}(t)$ describes the fluctuations of the energies and interactions due to the presence of the system-bath couplings.

The time dependent part of the Hamiltonian describes the stochastic noise due to the fluctuations of the bath. This term may include fluctuations from many different origins, such as the fluctuations of imperfect control fields, the fluctuations induced by nuclear vibrations on the spin excitation energy, the off-diagonal matrix element, and the inter-spin interactions. Following Haken and Strobl [16], we approximate the fluctuations as random Gaussian Markov processes with zero mean and δ-function correlation times:

$$\begin{aligned} \langle h_{ij}(t) \rangle &= 0, \\ \langle h_{ij}(t) h_{kl}(t') \rangle &= R_{ij;kl} \cdot \delta(t - t'). \end{aligned} \tag{4.2}$$

Here the brackets $\langle\rangle$ represents the thermal average over all bath degrees of freedom, and the time independent correlation matrix element $R_{ij;kl}$ is a real number describing the correlations between $h_{ij}(t)$ and $h_{kl}(t')$. All $R_{ij;kl}$ elements form a 2^{2n}-dimensional correlation matrix $\mathbf{R}$. Since we treat the time dependent part of the Hamiltonian $\mathbf{h}(t)$ as classical fields, the matrix elements of $\mathbf{R}$ are classical correlation functions. Therefore, we have the following symmetry properties for $\mathbf{R}$:

$$R_{ij;kl} = R_{ji;kl} = R_{ij;lk} = R_{ji;lk} = R_{kl;ij} \tag{4.3}$$

The value of $R_{ij;kl}$ depends on the strength of the coupling to the environment; therefore, it is a measure of the noisiness of the environment. The δ-function correlation in

time corresponds to the limit of fast bath modulations, which assumes that the correlation time of the bath is much smaller than the characteristic time of the system. Therefore, this model should be valid at the high temperature limit. Also note that although the effect of the temperature can be included by considering temperature dependent correlation matrix elements, there is no explicit temperature dependence in this model. We will discuss the consequences of this assumption and the applicability of this model in more detail in Section 4.4.

The dynamics of the n-spin system is governed by the time independent part of the Hamiltonian $\mathbf{H}_0$ and the correlation matrix $\mathbf{R}$. The values of $\mathbf{H}_0$ and $\mathbf{R}$ depend on the setup of the physical system, the various types of noise considered, and the nature of the bath. Note that in the HSR model, the system is limited to the one exciton subspace, and the correlation matrix $\mathbf{R}$ can be obtained directly. However, in our n-spin system, all 2^n states must be considered, and $\mathbf{H}_0$ and $\mathbf{R}$ have to be determined according to the physical conditions of the quantum system. In the following section, we provide explicit examples of $\mathbf{H}_0$ and $\mathbf{R}$ for a single spin. Generalization of the procedure to determine $\mathbf{H}_0$ and $\mathbf{R}$ for a general n-spin system should be straightforward. Throughout this section we will only use the generic forms of $\mathbf{H}_0$ and $\mathbf{R}$ to derive the equation of motion that describes the time evolution of the n-spin system under the influence of noise.

The Hamiltonian in Eq. (4.1) leads to a stochastic Liouville equation ($\hbar = 1$)

$$\dot{\rho}(t) = -i[\mathbf{H}(t), \rho(t)],$$

where $\rho(t)$ is the density matrix of the system at time t. Using the statistical properties of $\mathbf{h}(t)$ [Eq. (4.2)] and the symmetry property of the correlation functions [Eq. (4.3)], we can compute the exact equation of motion for the averaged density matrix elements of the system by applying the second order generalized cumulant expansion method to average over all fluctuations. The result we obtain is in a simple form:

$$\begin{aligned}\frac{d}{dt}\tilde{\rho}_{\alpha\beta} &= -i\sum_j H_{\alpha j}\tilde{\rho}_{j\beta} + i\sum_j \tilde{\rho}_{\alpha j}H_{j\beta} \\ &\quad -\tfrac{1}{2}\sum_{k,l} R_{lk;k\beta}\tilde{\rho}_{\alpha l} - \tfrac{1}{2}\sum_{k,l} R_{lk;k\alpha}\tilde{\rho}_{l\beta} + \sum_{k,l} R_{\beta l;k\alpha}\tilde{\rho}_{kl},\end{aligned} \tag{4.4}$$

where all the summations are over all 2^n state indices. In addition, we have defined the averaged density matrix of the system, $\tilde{\rho}(t) = \langle\rho(t)\rangle$. We call Eq. (4.4) the generalized HSR equation of motion, and it is the main result of this chapter. In Eq. (4.4), the dynamics of the averaged density matrix can be separated into a coherent part, due to $\mathbf{H}_0$, and a incoherent part, due to $\mathbf{R}$. The dissipation of the system is governed by incoherent dynamics, and is related to the elements of the fluctuation correlation matrix $\mathbf{R}$. Note that the equation of motion described in Eq. (4.4) is exact and does not depend on the perturbation expansion of a small parameter. Because of the δ-function correlations, all cumulants higher than the second order are identically zero. The form of Eq. (4.4) is similar to the form of the widely used Redfield equation, with the relaxation matrix elements given by the corresponding $R_{ij;kl}$ terms in the equation [6]. Nevertheless, Eq. (4.4) provides a convenient starting point to study the dissipative dynamics of a n-spin system, and is derived in an flexible working basis representation, in contrast to the Redfield equation that is usually derived in the eigen-basis representation of the $\mathbf{H}_0$.

Eq. (4.4) forms a system of 2^{2n} linear ordinary differential equations (ODE). Given the values of H_{ij} and $R_{ij;kl}$, the ODE system can be solved efficiently to yield the time dependent averaged density matrix $\tilde{\rho}(t)$. In fact, in most one spin and two spin systems, the equations can be solved analytically, and the analytical formula for $\tilde{\rho}(t)$ can be obtained. In general, we can calculate $\mathbf{H}_0$ and $\mathbf{R}$ from the Hamiltonian of the system and the correlations between fluctuations introduced by the environment. Once we have $\mathbf{H}_0$ and $\mathbf{R}$, the time evolution of the spin system can be obtained by numerically propagating the density matrix of the system $\tilde{\rho}(t)$ using the equations of motion in Eq. (4.4). This procedure is straightforward, and can be used to study the effect of noise in quantum systems with multiple spins. Note that the construction of $\mathbf{H}_0$ and $\mathbf{R}$ depends on the microscopic properties of the quantum system, therefore,

realistic physical conditions of the device can be included in the generalized HSR model. Thus, we provide an efficient and flexible method for the description of the dissipative dynamics of general quantum multi-spin systems. In the next chapter, we will demonstrate the applications of this model to study the effect of noise in quantum computations.

4.3 Relaxation and Decoherence in a Two-level System

To demonstrate the stochastic Liouville equation approach, we apply Eq. (4.4) to study the dissipative dynamics of a two-level system in this section; for a single spin, the model is exactly the same to the two-site HSR model, and is presented here mostly for an illustrative purpose. Applications to multi-spin system, which is the objective for the development of the generalized HSR equation of motion, will be presented in the next chapter.

The HSR model was first proposed by Haken and Strobl and later Reineker in the 60s to describe the charge transport and energy transfer in organic crystals [16, 17, 21]. In this model, the effect of the system-bath interactions is taken into account by allowing the site energy and the hopping matrix element to fluctuate in time. Consider a two-level system with states $|1\rangle$and $|2\rangle$, the Hamiltonian of the system in the form of Eq. (4.1) is

$$\begin{aligned} \mathbf{H}(t) &= \mathbf{H}_0 + \mathbf{h}(t) \\ &= \begin{bmatrix} \varepsilon_0 & J_0 \\ J_0 & -\varepsilon_0 \end{bmatrix} + \begin{bmatrix} \delta\varepsilon_1(t) & \delta J(t) \\ \delta J(t) & \delta\varepsilon_2(t) \end{bmatrix}, \end{aligned} \tag{4.5}$$

where $2\varepsilon_0$ is the energy splitting of the two-level system, J_0 is the average hopping matrix element, $\delta J(t)$ is the fluctuating part of the hopping matrix element, and $\delta\varepsilon_n(t)$ is the fluctuating part of the site-energies. Following Eq. (4.2), we consider the fluctuations $\delta\varepsilon_n(t)$ and $\delta J(t)$ as randomly Gaussian Markov processes with zero mean and δ-function correlation times:

$$
\begin{aligned}
\langle \delta\varepsilon_n(t) \rangle &= \langle \delta J(t) \rangle = 0 \\
\langle \delta\varepsilon_n(t)\delta\varepsilon_m(t') \rangle &= \gamma_0 \cdot \delta_{nm}\delta(t-t') \\
\langle \delta J(t)\delta J(t') \rangle &= \gamma_1 \cdot \delta(t-t') \\
\langle \delta\varepsilon_n(t)\delta J(t') \rangle &= 0
\end{aligned}
\tag{4.6}
$$

Here the strengths of diagonal site energy and off-diagonal hopping matrix element fluctuations are described by γ_0 and γ_1, respectively. In addition, we assume the energy fluctuations on different sites are not correlated, $\langle \delta\varepsilon_n(t)\delta\varepsilon_m(t') \rangle = 0$ for $n \neq m$.

If we define $X(t) = \frac{1}{2}[\rho_{12}(t) - \rho_{21}(t)]$, $Y(t) = -\frac{i}{2}[\rho_{12}(t) - \rho_{21}(t)]$, and $Z(t) = \frac{1}{2}[\rho_{11}(t) - \rho_{22}(t)]$, using the properties in Eq.(4.6), we can derive the HSR equation of motion for X, Y,and Z from Eq. (4.4):

$$
\begin{aligned}
\dot{X}(t) &= -2\varepsilon_0 Y(t) - \gamma_0 X(t), \\
\dot{Y}(t) &= 2\varepsilon_0 X(t) - 2J_0 Z(t) - (\gamma_0 + 2\gamma_1)Y(t) \ , \\
\dot{Z}(t) &= 2J_0 Y(t) - 2\gamma_1 Z(t),
\end{aligned}
\tag{4.7}
$$

and the density matrix of the two-level system at time t is

$$
\begin{aligned}
\rho(t) &= \begin{bmatrix} \rho_{11}(t) & \rho_{12}(t) \\ \rho_{21}(t) & \rho_{22}(t) \end{bmatrix} \\
&= \begin{bmatrix} \frac{1}{2} + Z(t) & X(t) + iY(t) \\ X(t) - iY(t) & \frac{1}{2} - Z(t) \end{bmatrix}
\end{aligned}
$$

In general, when $\varepsilon_0 \neq 0$ and $J_0 \neq 0$, the exact analytical expression for $\rho(t)$ is not available. Nevertheless, the equation of motion in Eq. (4.7) can be solved numerically to obtain the dynamics of the two-level system. In the following, we will study the solutions of Eq. (4.7) in the limit of $\varepsilon_0 = J_0 = 0$ and $\varepsilon_0 = 0$, $J_0 \neq 0$ to demonstrate the physics embedded in the simple HSR model.

4.3.1 The $\varepsilon_0 = J_0 = 0$ limit

In the limit that the two states of the system are degenerate and non-interacting ($\varepsilon_0 = J_0 = 0$), the equation of motion can be solved exactly, and we can clearly understand the physical interpretation for the strengths of the fluctuations (γ_0 and γ_1). For a system initially at the state $|\phi_0\rangle = c_1|1\rangle + c_2|2\rangle$ at time $t = 0$, we obtain the density matrix $\rho(t)$ at time $t > 0$ from Eq. (4.7):

$$\rho(t) = \begin{bmatrix} \frac{1}{2} + \frac{1}{2}(|c_1|^2 - |c_2|^2) \cdot e^{-2\gamma_1 t} & \frac{c_1 c_2^* + c_1^* c_2}{2} \cdot e^{-\gamma_0 t} + \frac{c_1 c_2^* - c_1^* c_2}{2} \cdot e^{-(\gamma_0 + 2\gamma_1)t} \\ \frac{c_1 c_2^* + c_1^* c_2}{2} \cdot e^{-\gamma_0 t} + \frac{c_1^* c_2 - c_1 c_2^*}{2} \cdot e^{-(\gamma_0 + 2\gamma_1)t} & \frac{1}{2} + \frac{1}{2}(|c_2|^2 - |c_1|^2) \cdot e^{-2\gamma_1 t} \end{bmatrix} \tag{4.8}$$

This result describes the decoherence and population relaxation in the two-level system. Note that the dynamics follows strict exponential decay, and the strengths of the fluctuations (γ_0 and γ_1) are related to the decay rates. Thus, the dynamics of the population transfer is described by incoherent motion in this limit. In addition, according to Eq.(4.8), the decay of the real part of the coherence depends on the diagonal fluctuations, while the population relaxation depends on the off-diagonal fluctuations. This is because the diagonal fluctuations $\delta\varepsilon_n(t)$ introduce phase shifts that only affect the coherence of the two-level system, and the off-diagonal fluctuations $\delta J(t)$ introduce coupling between the two states that results in population transfer. Note that the imaginary part of the coherence decays according to both diagonal and off-diagonal fluctuations. In the terminology of quantum computing, phase-shift errors (change in the σ_z component) are caused by the site-energy fluctuations, bit-flip errors (change in the σ_x component) are caused by the hopping matrix element fluctuations, and the change in the σ_y component are due to both types of fluctuations [22]. Also note that the HSR model predicts different decay rate for the real part and the imaginary part of the coherence, which is different from the results of previous study.

4.3.2 The $\varepsilon_0 = 0$, $J_0 \neq 0$ limit

For interacting degenerate two-level systems ($\varepsilon_0 = 0$, $J_0 \neq 0$), the analytical solution to Eq. (4.7) is also available. In this limit, we show that the dynamics of the two-level system exhibits both coherent and incoherent motions, and the transition from the coherent regime to the incoherent regime is controlled by the strength of the diagonal fluctuations.

Consider a system initially at the $|1\rangle$ state at time $t = 0$, the density matrix elements at time $t > 0$ can be calculated easily from Eq. (4.7):

$$\begin{aligned}
\rho_{11}(t) &= \tfrac{1}{2} + \tfrac{1}{2} \cdot e^{-\frac{1}{2}(\gamma_0+4\gamma_1)t} \left[\cosh\left(\tfrac{1}{2}\sqrt{\gamma_0^2 - 16J_0^2} \cdot t\right) + \frac{\gamma_0}{\sqrt{\gamma_0^2-16J_0^2}} \sinh\left(\tfrac{1}{2}\sqrt{\gamma_0^2 - 16J_0^2} \cdot t\right) \right], \\
\rho_{22}(t) &= 1 - \rho_{11}(t), \\
\rho_{12}(t) &= \frac{-2iJ_0}{\sqrt{\gamma_0^2-16J_0^2}} \cdot e^{-\frac{1}{2}(\gamma_0+4\gamma_1)t} \cdot \sinh\left(\tfrac{1}{2}\sqrt{\gamma_0^2 - 16J_0^2} \cdot t\right), \\
\rho_{21}(t) &= \frac{2iJ_0}{\sqrt{\gamma_0^2-16J_0^2}} \cdot e^{-\frac{1}{2}(\gamma_0+4\gamma_1)t} \cdot \sinh\left(\tfrac{1}{2}\sqrt{\gamma_0^2 - 16J_0^2} \cdot t\right).
\end{aligned}$$

The result shows that when $J_0 \neq 0$, the effect of diagonal fluctuations can no longer be clearly distinguished from the effect of off-diagonal fluctuations, both population relaxations and decoherence depend on γ_0 and γ_1. The HSR model takes into account the effects of both types of fluctuations at the same time, which is different from most dissipation models used previously; previous models usually treat only either one of the diagonal or off-diagonal system-bath interactions [20, 23, 24].

To study the the dynamics of population transfer from $|1\rangle \rightarrow |2\rangle$, we investigate the difference of the population in the two states:

$$\begin{aligned}
P_\Delta(t) &= \rho_{11}(t) - \rho_{22}(t) \\
&= e^{-\frac{1}{2}(\gamma_0+4\gamma_1)t} \left[\cosh\left(\frac{1}{2}\sqrt{\gamma_0^2 - 16J_0^2} \cdot t\right) + \frac{\gamma_0}{\sqrt{\gamma_0^2 - 16J_0^2}} \sinh\left(\frac{1}{2}\sqrt{\gamma_0^2 - 16J_0^2} \cdot t\right) \right].
\end{aligned}$$

Clearly, $P_\Delta(t)$ exhibits both coherent and incoherent motions depending on the strength of the diagonal fluctuations γ_0. In the regime where $\gamma_0 < 4|J_0|$, the factor $\sqrt{\gamma_0^2 - 16J_0^2}$

is imaginary and results in oscillatory $P_\Delta(t)$; this indicates that in this regime, the fluctuations are not strong enough to fully destroy the oscillatory nature of the system, and the the dynamics of the population transfer is still coherent. In contrast, in the regime where $\gamma_0 \geq 4|J_0|$, $P_\Delta(t)$ decays monotonically, and the dynamics of population transfer is described by incoherent hopping from $|1\rangle \rightarrow |2\rangle$. Thus, the simple HSR model contains both the coherent and the incoherent limits. The interplay between the coherence in the quantum system (J_0) and the fluctuations due to system-bath couplings (γ_0) is a major issue regarding the dynamics of a open quantum system. The two-site HSR model describes the crossover from the coherent regime at weak fluctuations to the incoherent regime at strong fluctuations. A generalization of the model presented in this section has been successfully applied to describe the dynamics of charge and energy transport in organic molecular crystals, including the transition from band-like regime to hopping regime that we studied in the previous section using a microscopic model with explicit electron-phonon interactions [18].

4.4 Limitations and Possible Extensions

We have shown that the generalized HSR model is efficient and flexible, and can describe both coherent and incoherent motion in the dissipative dynamics of a quantum system. In this section, we will briefly discuss the limitations and possible extensions of this stochastic Liouville equation approach.

A key step in the HSR model is to replace the microscopic system-bath interactions by stochastic processes. This procedure has permitted a full description of the dissipative dynamics of the quantum system and their response to the external fields. At the same time, we introduce phenomenological parameters to describe the strengths of fluctuations (γ_0 and γ_1 in our model). These parameters have to be determined experimentally or computed using a separate microscopic model [17, 25, 26]. Generally, γ_0 and γ_1 should depend on temperature and increase as temperature increases. However, our model lacks explicit temperature dependence for these parameters, thus cannot be used to study the temperature dependence of the quantum dynamics. For-

tunately, these parameters are directly related to physically measurable quantities, and can be easily determined by experiments. In our model, γ_0 and γ_1 correspond to the decoherence rate and population relaxation rate, respectively; both of them can be measured by experiments in the limit that that the two states of the system are degenerate and non-interacting. In addition, recent theoretical studies on the temperature dependence of the quality of quantum gate operations suggest that the temperature dependence of the gate performance is weak [11, 27], which is reasonable in the weak coupling regime and the temperature range relevant to implementations of solid-state quantum computers.

The assumption of the fast modulation of the bath might be a more serious problem for the HSR model. The δ-function correlation time corresponds to an infinite fast decay of the bath correlations, which leads to incorrect short time dynamics and long time equilibrium populations. Palma *et al.* have studied the decoherence of a two-level system and shown that the dynamics exhibits a "quiet" and a "quantum" regime at short times, and a "thermal" regime at long times [20]. The HSR model assumes that the bath relaxes infinitely fast, thus neglects the dynamics of the system before bath relaxation takes place. Although the HSR model cannot predict the short time dynamics correctly, we expect the physics for longer times important for many applications are reasonably well captured. The δ-function correlation can be replaced by an exponential function in time, and the extended model for a dichotomic process has been solved exactly without further assumptions [28, 29, 30, 31].

The white noise assumption in the HSR model also corresponds to a bath with infinite temperature, therefore, the resulting equation of motion does not satisfy detailed balance at finite temperatures. As a consequence, the system always relaxes to equal populations regardless of the energy differences between the states. Extensions of the HSR model to solve this problem has been proposed in Ref. [26]. Note that the motivation to develop the generalized HSR model in this chapter is to study the decoherence problem in quantum computing. In quantum computing, we are mainly concerned about the dynamics of an unbiased quantum system, and even when a bias field is applied to the system to perform gate operations, the time period has to be

short to avoid any population relaxation. Since we will only operate the quantum computer in the time scale that the population relaxation is negligible, we expect the violation of the detailed balance condition will not cause serious problems for applications related to quantum computing.

The stochastic representation for the dynamics of a quantum two-level system has been investigated in Refs. [32] and [33]. The correspondence between the phenomenological parameters describing the stochastic field (γ_0 and γ_1 in this work) and the two-level system microscopic quantities are also studied. The stochastic approximation is found to be able to reproduce the results by Leggett *et al.* for the spin-boson model [3]. Our results presented confirm this observation. In general, the stochastic Liouville equation approach presented in this work is applicable in the weak system-bath interaction limit relevant to quantum computations.

4.5 Conclusion

In this Chapter, we have presented a stochastic Liouville equation approach that provides a simple yet flexible way to calculate the dissipative dynamics of quantum systems with multiple spins. This approach is generalized from the HSR model. Using an effective system Hamiltonian that includes the system-bath interactions as stochastic fluctuating terms with zero mean and delta function correlation times, we derived the exact generalized HSR equation of motion [Eq. (4.4)] that describes the dissipative dynamics for a system of n spins. This generalized HSR equation of motion is similar to the form of the widely used Redfield equation, with the relaxation matrix elements given by the corresponding correlation matrix elements, which can be constructed straightforwardly from the realistic physical conditions of the quantum system.

To demonstrate the use of Eq. (4.4), we have applied the HSR model to study the dissipative dynamics of a two-level system. We showed that the decay rates of the density matrix elements are related to the strengths of fluctuations (γ_0 and γ_1), and the quantum dynamics calculated from the HSR model exhibits coherent regime

in the weak-fluctuation limit and incoherent regime in the strong-fluctuation limit.

We have also discussed the limitations of the HSR type approach. The consequences due to the procedure of replacing the system-bath interactions by classical fluctuating fields and the assumption of the white noise were considered, and the possible extensions were noted. Generally, the application of HSR type model in the weak coupling regime that is relevant to quantum computing is justified.

In conclusion, we have developed an efficient and flexible method that describes the quantum dissipation and decoherence in multi-spin systems. In the next chapter, we will apply the generalized HSR equation of motion [Eq. (4.4)] to study the effect of noise in quantum computations.

Appendix 4.A Positivity of the generalized HSR equation of motion

Because of the product state initial condition implicitly assumed in the Redfield equation, the bath is highly non-equilibrium at the initial time. As a result, a transient time in which the bath relaxes to a new equilibrium exists, and the Markovian approximation is inapplicable within this time scale. The Markovian Redfield equation does not preserve the positivity of the reduced density matrix of the system at short times. The source and a possible slippage scheme to solve this problem has been studied in detail by Suarez, Silbey, and Oppenheim [8]. A closer examination reveals that the violation of positivity condition is due to the Markovian approximation; if a non-Markovian memory kernel is considered, the positivity of the dynamics is always preserved. The positivity problem is due to using improper parameters, naming Markovian memory kernel, to describe the short time dynamics of a reduced quantum system[34, 35]. In Chapter 7, we will discuss the positivity problem of the Markovian Redfield equation in a more detailed fashion.

In Section 4.2, we have generalized the Haken-Strobl-Reineker (HSR) model for a system of n spins, and derived a generalized HSR equation of motion that describes

the dissipative dynamics of the n-spin system [Eq. (4.4)]. Furthermore, we stated that because of the δ-function correlation time assumed in the model, the resulting propagator satisfies complete positivity, unlike methods based on the Bloch-Redfield formalism. This property is important for the range of applicability of the generalized HSR model, however, we did not provide a proof in Section 4.2. In this Appendix, we show that the generalized HSR equation of motion indeed satisfy the positive condition by transforming it into the Lindblad form of a generator of quantum dynamical semigroups [36].

Recall that in the derivation of the generalized HSR equation of motion, we consider the N-dimensional Hilbert space representing a system of n spins ($N = 2^n$), and start from an effective Hamiltonian with time independent and time dependent parts:

$$\begin{aligned} \mathbf{H}(t) &= \mathbf{H}_0 + \mathbf{h}(t) \\ &= \sum_{i,j=1}^{N} \left[H_{ij} + h_{ij}(t)\right] c_i^\dagger c_j \\ &= \mathbf{H}_0 + \sum_{i=1}^{N} h_{ii}(t) \cdot c_i^\dagger c_i + \sum_{i<j} h_{ij}(t) \left[c_i^\dagger c_j + c_j^\dagger c_i\right], \end{aligned} \tag{4.9}$$

where $c_i^\dagger$ and c_i are the creation and annihilation operators for the i-th state of the basis set. Notice that in the last line of Eq. (4.9), there are totally $N(N+1)/2$ time dependent terms; we can renumber these terms and case the Hamiltonian into the following form:

$$\mathbf{H}(t) = \mathbf{H}_0 + \sum_{\alpha=1}^{N(N+1)/2} f_\alpha(t) \cdot V_\alpha, \tag{4.10}$$

where $f_\alpha(t)$ are the time dependent matrix elements, and V_α are corresponding system operators. Also notice that by definition, V_α are Hermitian operators. Following Haken and Strobl , we consider the time dependent $f_\alpha(t)$ as random Gaussian Markov processes with zero mean and δ-function correlation times:

$$\begin{aligned} \langle f_\alpha(t) \rangle &= 0 \\ \langle f_\alpha(t) f_\beta(t') \rangle &= C_{\alpha\beta} \cdot \delta(t - t') \end{aligned} \tag{4.11}$$

Here the brackets $\langle\rangle$ represents the thermal average over all bath degrees of freedom, and the time independent correlation matrix element $C_{\alpha\beta}$ is a real number describing the correlations between $f_\alpha(t)$ and $f_\beta(t')$. All $C_{\alpha\beta}$ elements form a $N(N+1)/2$-dimensional correlation matrix $\mathbf{C}$. Because we assume δ-function correlation time and classical nature of the correlation functions, $\mathbf{C}$ is a real symmetric matrix. In addition, the correlation matrix $\mathbf{C}$ is positive semidefinite. It is easy to check the positive semidefiniteness; for any $N(N+1)/2$-dimensional real vector $\mathbf{z} = (z_1, z_2, ..., z_{N(N+1)/2})$, we have

$$\begin{aligned} \mathbf{z}\mathbf{C}\mathbf{z}^t &= \sum_{\alpha,\beta=1}^{N(N+1)/2} z_\alpha C_{\alpha\beta} z_\beta \\ &= \left\langle \sum_\alpha z_\alpha f_\alpha(t) \sum_\beta z_\beta f_\beta(t) \right\rangle \\ &= \left\langle \left| \sum_\alpha z_\alpha f_\alpha(t) \right|^2 \right\rangle \geq 0. \end{aligned}$$

The positive semidefiniteness of the correlation matrix is an important property that is required for the generalized HSR equation of motion to satisfy the positivity condition.

The dynamics of the system is described by the stochastic Liouville equation ($\hbar = 1$)

$$\dot{\rho}(t) = -i[\mathbf{H}(t), \rho(t)],$$

where $\rho(t)$ is the density matrix of the system at time t. Using the operator form of the Hamiltonian [Eq. (4.10)], and applying the second order generalized cumulant expansion method, the exact equation of motion for the averaged density matrix of the system can be written as:

$$\frac{d}{dt}\tilde{\rho} = -i[\mathbf{H}_0, \tilde{\rho}] + \sum_{\alpha,\beta} C_{\alpha\beta}\left[V_\alpha \tilde{\rho} V_\beta^\dagger - \tfrac{1}{2}(V_\alpha^\dagger V_\beta \tilde{\rho} + \tilde{\rho} V_\alpha^\dagger V_\beta)\right], \tag{4.12}$$

where we have used the statistical properties of $f_\alpha(t)$ [Eq. (4.11)], the property that $\mathbf{C}$ is a real symmetric matrix, and the property that V_α matrices are Hermitian. Since the correlation matrix $\mathbf{C}$ is real and symmetric, we can diagonalize it with a unitary transformation $\mathbf{S}$, and define a diagonal matrix $\mathbf{\Gamma} = \mathbf{SCS}^\dagger$. We then introduce a new set of operators A_k using

$$V_\alpha = \sum_k S_{k\alpha} A_k. \tag{4.13}$$

Rewrite Eq. (4.12) in terms of A_k, we obtain

$$\frac{d}{dt}\tilde{\rho} = -i[\mathbf{H}_0, \tilde{\rho}] + \sum_k \Gamma_k\left[A_k \tilde{\rho} A_k^\dagger - \tfrac{1}{2}(A_k^\dagger A_k \tilde{\rho} + \tilde{\rho} A_k^\dagger A_k)\right], \tag{4.14}$$

where Γ_k is the k-th eigenvalue of the correlation matrix $\mathbf{C}$. Recall that the correlation matrix $\mathbf{C}$ is positive semidefinite, hence, all matrix elements Γ_k are nonnegative, $\Gamma_k \geq 0$. Equation (4.14) is clearly of the Lindblad form, thus, it preserves the complete positivity of the dynamics [36]. In a finite-dimensional Hilbert space, the Lindblad form is the most general form for the generator of Markovian quantum dynamics that preserves the complete positivity and trace of the density matrix [36]. Therefore, we prove that the generalized HSR equation of motion in Eq. (4.4) does respect the positivity of the dynamics.

Gaspard and Nagaoka have shown that the Redfield master equation for δ-correlated bath, a equivalent condition to our generalized HSR equation of motion, reduces to a equation of motion with the Lindblad form [9]. However, they did not prove the positivity of their $\mathbf{D}$ matrix (equivalent to the correlation matrix $\mathbf{C}$ here). Therefore, their proof is incomplete. Note that we use the property that $\mathbf{C}$ is a real symmetric matrix to transform the equation of motion into the Lindblad form. This property is a consequence of the δ-function correlation time assumption, and is not true for general finite-temperature correlation matrices.

Bibliography

[1] R. Silbey and R. A. Harris. Variational calculation of the dynamics of a 2 level system interacting with a bath. *J. Chem. Phys.*, 80(6):2615 – 2617, 1984.

[2] R. A. Harris and R. Silbey. Variational calculation of the tunneling system interacting with a heat bath .2. dynamics of an asymmetric tunneling system. *J. Chem. Phys.*, 83(3):1069 – 1074, 1985.

[3] A. J. Leggett, S. Chakravarty, A. T. Dorsey, M. P. A. Fisher, A. Garg, and W. Zwerger. Dynamics of the dissipative 2-state system. *Rev. Mod. Phys.*, 59(1):1 – 85, 1987.

[4] U. Weiss. *Quantum Dissipative Systems.* World Scientific, Singapore, 2001.

[5] H. P. Breuer and F. Petruccione. *The Theory of Open Quantum Systems.* Oxford University Press, Oxford, 2002.

[6] A. G. Redfield. The theory of relaxation processes. *Adv. Mag. Res.*, 1:1, 1965.

[7] R. Dümcke and H. Spohn. The proper form of the generator in the weak coupling limit. *Z. Phys. B*, 34:419, 1979.

[8] A. Suárez, R. Silbey, and I. Oppenheim. Memory effects in the relaxation of quantum open systems. *J. Chem. Phys.*, 97(7):5101 – 5107, 1992.

[9] P. Gaspard and M. Nagaoka. Slippage of initial conditions for the Redfield master equation. *J. Chem. Phys.*, 111(13):5668 – 5675, 1999.

[10] D. Loss and D. P. DiVincenzo. Quantum computation with quantum dots. *Phys. Rev. A*, 57(1):120 – 126, 1998.

[11] M. Thorwart and P. Hänggi. Decoherence and dissipation during a quantum XOR gate operation. *Phys. Rev. A*, 65(1):012309, 2002.

[12] P. N. Argyres and P. L. Kelley. Theory of spin resonance and relaxation. *Phys. Rev.*, 134:A98, 1964.

[13] C. P. Slichter. *Principles of Magnetic Resonance.* Springer Verlag, 1996.

[14] R. Kubo. Stochastic liouville equations. *J. Math. Phys.*, 4:174 – 183, 1963.

[15] G. L. Sewell. Model of thermally activated hopping motion in solids. *Phys. Rev.*, 129:597 – 608, 1963.

[16] H Haken and G. Strobl. An exactly solvable model for coherent and incoherent exciton motion. *Z. Physik*, 262:135, 1973.

[17] H. Haken and P. Reineker. The coupled coherent and incoherent motion of excitons and its influence on the line shape of optical absorption. *Z. Physik*, 249:253, 1972.

[18] P. Reineker. *Exciton Dynamics in Molecular Crystals and Aggregates.* Springer-Verlag, Berlin, 1982.

[19] W. G. Unruh. Maintaining coherence in quantum computers. *Phys. Rev. A*, 51(2):992 – 997, 1995.

[20] G. M. Palma, K.-A. Suominen, and A. K. Ekert. Quantum computers and dissipation. *Proc. R. Soc. Lond. A.*, 452:567, 1996.

[21] R. J. Silbey. Electronic energy transfer in molecular crystals. *Ann. Rev. Phys. Chem.*, 27:203, 1976.

[22] M. A. Nielsen and I. L. Chuang. *Quantum Computation and Quantum Information.* Cambridge University Press, 2000.

[23] C. Miquel, J. P. Paz, and W. H. Zurek. Quantum computation with phase drift errors. *Phys. Rev. Lett.*, 78(20):3971 – 3974, 1997.

[24] P. L. Knight, M. B. Plenio, and V. Vedral. Decoherence and quantum error correction. *Philos. Trans. R. Soc. Lond. Ser. A-Math. Phys. Eng. Sci.*, 355(1733):2381 – 2385, 1997.

[25] S. Rackovsky and R. Silbey. Electronic-energy transfer in impure solids .1. 2 molecules embedded in a lattice. *Mol. Phys.*, 25(1):61, 1973.

[26] V. Čápek. Haken-strobl-reineker model - its limits of validity and a possible extension. *Chem. Phys.*, 171(1-2):79 – 88, 1993.

[27] M. J. Storcz and F. K. Wilhelm. Decoherence and gate performance of coupled solid-state qubits. *Phys. Rev. A*, 67(4):042319, 2003.

[28] C. Warns, I. Barvik, and P. Reineker. Energy transport and optical line shapes in dimers: Analytical description of the influence of colored noise. *Phys. Rev. E*, 57(4):3928 – 3936, 1998.

[29] V. Kraus and P. Reineker. Exact treatment of the transport of a quantum particle in a dimer under the influence of dichotomic colored noise. *Phys. Rev. A*, 43(8):4182 – 4191, 1991.

[30] M. A. Palenberg, R. J. Silbey, and W. Pfluegl. Coherent and incoherent motion in a one-dimensional lattice. *Phys. Rev. B*, 62(6):3744 – 3750, 2000.

[31] M. A. Palenberg, R. J. Silbey, C. Warns, and P. Reineker. Local and nonlocal approximation for a simple quantum system. *J. Chem. Phys.*, 114(10):4386 – 4389, 2001.

[32] L. Accardi, S. V. Kozyrev, and I. V. Volovich. Dynamics of dissipative two-level systems in the stochastic approximation. *Phys. Rev. A*, 56(4):2557 – 2562, 1997.

[33] Y. E. Kuzovlev. Quantum interactions in a stochastic representation and two-level systems. *Jetp Lett.*, 78(2):92 – 96, 2003.

[34] N. G. van Kampen. *Stochastic Processes in Physics and Chemistry.* North-Holland, Amsterdam, 2001.

[35] N. G. van Kampen. A soluble model for quantum mechanical dissipation. *J. Stat. Phys.*, 78(1-2):299 – 310, 1995.

[36] G. Lindblad. On the generators of quantum dynamical semigroups. *Comm. Math. Phys.*, 48:110, 1976.

Chapter 5

The Effect of Noise in Quantum Computations

Part of the content in this chapter has been published in the following papers:
Y.C. Cheng and R.J. Silbey. Stochastic Liouville equation approach for the effect of noise in quantum computations. *Physical Review A*, 69:052325, 2004.
Y.C. Cheng and R.J. Silbey. Microscopic quantum dynamics study on the noise threshold of fault-tolerant quantum error correction. *Physical Review A*, 72:012320, 2005.

5.1 Introduction

In Chapter 4, we derived a generalized HSR equation of motion from a stochastic Liouville equation approach that is capable of describing the relaxation and decoherence of multi-spin quantum systems. Starting from a effective system Hamiltonian that incorporates stochastic fluctuating terms to describe the effect of system-bath interactions, this model describes the dissipative dynamics of a many-spin system using realistic device conditions. In this chapter, the generalized HSR equation of motion is applied to study the effect of noise in quantum computations.

Quantum information processing is of much current interest [1, 2, 3, 4, 5, 6, 7, 8]. Since the discovery of the quantum factoring algorithm by Peter Shor in 1994 [9],

quantum computing, or more broadly, quantum information theory, has grown into an active interdisciplinary field involving physics, computer science, and mathematics. Given the rapid advancement in quantum computation, it is impossible to present an adequate overview of the subject here. Therefore, interested readers should consult recent review papers [1, 2, 3, 4, 5] and textbooks [6, 7, 8] for an overview of quantum computation.

In this chapter, we focus on modeling the dissipative dynamics of a quantum computer. A quantum computer can be modeled as an array of two-level systems (qubits)[1] evolving according to a sequence of prescribed unitary operations (also called quantum gate operations) that is designed to achieve the desired outcome state; these sequences of quantum operations are often called quantum algorithms. The realization of quantum algorithms using nuclear magnetic resonance (NMR) [10, 11, 12, 13] and ion-trap [14] techniques has shown that quantum computing is realizable in principle. More recent efforts for building quantum computers have focused on techniques based on solid-state devices that are believed to be more scalable [15, 16, 17]. However, such solid-state devices usually require sophisticated manufacturing techniques, and the inevitable interactions between a qubit and its surrounding environment ("bath") introduce noise into the quantum system, resulting in the degradation of the quantum superposition state. A quantum algorithm usually requires applications of a long series of quantum gate operations sequentially. For example, factorizing a 130 digit number ($\sim$430 bits)[2] using Shor's algorithm would require $\sim$ 2200 qubits and of order $\sim 10^9$ quantum gate operations [18]. To obtain the correct outcome, all these operations need to be performed precisely, and at the same time the quantum superposition state of all qubits has to be preserved. Thus, the extra degrees of freedom of a solid-state system and the inherent system-bath interactions pose a

[1]Deriving from "bits" used in classical computations, qubit is a term coined by the quantum computing community to represent a quantum two-level system. A qubit can be an intrinsic two-level system such as a spin-1/2 particle, or an effective two-level system such as a double-well tunneling system. Throughout this thesis, we will use the two terms, "qubit" and "quantum two-level system", interchangeably.

[2]Factoring a number of this size would take several months on a current computer cluster using the best known classical algorithm. The size of this problem is considered as the boundary where the quantum factoring algorithm would start to outperform all classical algorithms.

great challenge for quantum computing with such devices. The decoherence problem is the main obstacle towards the realization of a universal quantum computer, and a sound theoretical framework for the description of the decoherence and population relaxation of qubit systems is necessary [19, 20, 5, 21].

Because the ability to compute and predict the behavior of a quantum computer under the influence of noise is crucial, a model that can describe errors from the system-bath interactions could be extremely useful. Such a model will also be useful in the study of quantum error-correcting and error-preventing schemes, as well as provide informative guidelines for the design of quantum computers. However, describing the non-equilibrium decoherence and population relaxation of a many-qubit system is non-trivial. No general model exists for this purpose. Classical noise models and microscopic noise models have yielded some success, but these formulations do not provide a general solution framework for a many-qubit system. Axiomatic approaches based on the semigroup Lindblad formalism has been successful in phenomenological descriptions of the dissipative dynamics of qubit systems [22, 21]. However, the Lindblad dissipation operators required in the Lindblad equation are not constructed from microscopic properties of the system, hence, for general physical systems how to realistically include the physical properties of the system in the Lindblad formalism is not always clear.

Microscopic noise models based on the spin-boson Hamiltonian that explicitly include the linear couplings between the system and the bath degrees of freedom have provided valuable insights about decoherence effects [23, 19, 20]. Recently, the decoherence and gate performance of a quantum controlled-NOT gate operation for several different physical realizations has been studied based on such spin-boson type Hamiltonians [24, 25, 26, 27]. A number of different techniques has been developed to solve dynamics of microscopic Hamiltonians [28]. However, these methods are often complicated, and difficult to generalize for systems with more than two qubits. In addition, in many cases the exact form of the system-bath interactions is unknown, or the parameters are difficult to obtain experimentally, thus the microscopic models are difficult to use in these cases.

The generalized HSR equation of motion derived in Chapter 4 provides an efficiently way to simulate a quantum computer and obtain full dynamics of the qubit system. Since a quantum computer always operates in the weak system-bath coupling regime and its state is never close to the thermal equilibrium, the shortcomings of the white noise assumption in the model are avoided (see Section 4.4). Therefore, the applicability of the generalized HSR equation of motion to the decoherence problem in quantum computing is well justified.

In this chapter, we will study the effect of noise on quantum teleportation and a generic controlled-NOT gate operation, and then compare our results with previous work by other group. We show that the generalized HSR model can reproduce the main results obtained previously by using microscopic model Hamiltonians. Finally, we apply the noise model to study the most important quantum algorithm, namely, the algorithm for fault-tolerant quantum computation, and evaluate the noise threshold of fault-tolerant quantum computing using the generalized HSR equation of motion. We will also study how the efficiency of fault-tolerant quantum error-correction depends on the physical conditions of the quantum computer.

5.2 Dissipation in Quantum Teleportation

By exploiting the entangled nature of an Einstein-Podolsky-Rosen (EPR) pair, the quantum teleportation protocol enables a sender to transmit the quantum state of a qubit to a receiver, without physically transferring the qubit through space [29]. Quantum teleportation is the backbone of all quantum communication techniques [3, 30], and can be used to implement efficient quantum gates [31]. A more detailed discussion of the quantum teleportation protocol is given in Appendix 5.A. In this section, we focus on the study of the effect of noise on quantum teleportation using the stochastic Liouville equation approach.

5.2.1 Quantum teleportation

We consider the scenario of teleporting one qubit from Alice to Bob. Suppose Alice and Bob share a EPR pair, labeled as qubit a and b, emitted from an EPR pair source, and Alice wants to teleport qubit c in state $|\psi\rangle = c_0|0\rangle + c_1|1\rangle$ to Bob. The EPR pair source emits two entangled qubits in one of the four Bell states [see Eq.(5.3)] at time $t = 0$, and then the two qubits are sent through separate quantum channels C_a and C_b to Alice and Bob, respectively. After receiving qubit a, Alice performs a Bell-state measurement on her qubits (a and c), and sends the outcome of her measurement to Bob through a classical channel. Alice's measurement projects qubit b onto one of the four corresponding states, i.e. $\mathbf{I}\cdot(c_0|0\rangle_b + c_1|1\rangle_b)$, $\sigma_z\cdot(c_0|0\rangle_b + c_1|1\rangle_b)$, $\sigma_x\cdot(c_0|0\rangle_b + c_1|1\rangle_b)$, and $i\sigma_y\cdot(c_0|0\rangle_b + c_1|1\rangle_b)$. Bob then applies the corresponding inverse transformation ($\mathbf{I}$, σ_z, σ_x, and $-i\sigma_y$, respectively) to recover his qubit in the state $|\psi\rangle$.

In practice, errors can happen during the quantum teleportation from several origins: (1) the degradation of qubit c after the preparation, (2) the noise in the quantum channels C_a and C_b, (3) the imperfect Bell-state measurement performed by Alice, (4) the further degradation of qubit b when transmitting the result of Bell-state measurement through the classical channel, (5) the imperfect unitary transformations performed by Bob. Here, we only consider situation (2) where channel C_a and C_b are noisy, and focus on the errors due to the degradation of entanglement. We assume all other operations are done perfectly. This means that result obtained in the following represents a lower bound on the errors in the quantum teleportation.

5.2.2 Effect of noise on a pair of entangled qubits

To apply the generalized HSR equation of motion, we first define the zeroth order Hamiltonian of the system and the correlation functions that describe the source of noises. To this end, we consider the following effective Hamiltonian for two uncorrelated qubits a and b:

$$
\begin{aligned}
\mathbf{H} &= \mathbf{H_a} + \mathbf{H}_b \\
&= \sum_{n=a,b} \varepsilon_n(t) \cdot \sigma_z^{(n)} + \sum_{n=a,b} J_n(t) \cdot \sigma_x^{(n)} \\
&= \sum_{n=a,b} [\varepsilon_n + \delta\varepsilon_n(t)] \cdot \sigma_z^{(n)} + \sum_{n=a,b} [J_n + \delta J_n(t)] \cdot \sigma_x^{(n)},
\end{aligned}
\tag{5.1}
$$

where $\sigma_z^{(n)}$ and $\sigma_x^{(n)}$, $n = a, b$ are Pauli spin operators on qubit a and b; $2\varepsilon_a$ ($2\varepsilon_b$) is the averaged energy splitting between the $|0\rangle$ and $|1\rangle$ states of qubit a (b); J_a (J_b) is the averaged off-diagonal matrix element for qubit a (b); $\delta\varepsilon_a(t)$ ($\delta\varepsilon_b(t)$) is the time-dependent fluctuating part of the diagonal energy for qubit a (b); $\delta J_a(t)$ ($\delta J_b(t)$) is the time-dependent fluctuating part of the off-diagonal matrix element for qubit a (b). Following the assumption made in Section 4.2, we regard $\delta\varepsilon_n(t)$ and $\delta J_n(t)$, $n = a, b$ as Gaussian Markov processes fully described by their first two moments:

$$
\begin{aligned}
\langle \delta\varepsilon_n(t) \rangle &= \langle \delta J_n(t) \rangle = 0, \\
\langle \delta\varepsilon_n(t) \delta\varepsilon_m(t') \rangle &= \gamma_0^n \cdot \delta_{nm} \delta(t - t'), \\
\langle \delta J_n(t) \delta J_m(t') \rangle &= \gamma_1^n \cdot \delta_{nm} \delta(t - t'), \\
\langle \delta\varepsilon_n(t) \delta J_m(t') \rangle &= 0,
\end{aligned}
\tag{5.2}
$$

where γ_0^a (γ_0^b) describes the strength of the diagonal energy fluctuations of qubit a (b); γ_1^a (γ_1^b) describes the strength of the off-diagonal matrix element fluctuations of qubit a (b). Clearly, γ_0^a and γ_0^b are related to the system-bath interactions involving σ_z system operators, and γ_1^a and γ_1^b are related to the interactions involving σ_x system operators. These phenomenological parameters can be estimated experimentally [32, 33]. Notice that we treat the correlation between qubit a and b independently, because in quantum teleportation, the two EPR qubits are sent through different channels to two distantly separated places, thus the two qubits are coupled to distinct baths. In addition, we assume the diagonal and off-diagonal fluctuations are not correlated.

To simplify our computations, we choose to study the dynamics of the system in the Bell-state basis. The four Bell states are defined as

$$
\begin{aligned}
|B_1\rangle &= \tfrac{1}{\sqrt{2}}(|0\rangle_a|0\rangle_b + |1\rangle_a|1\rangle_b), \\
|B_2\rangle &= \tfrac{1}{\sqrt{2}}(|0\rangle_a|0\rangle_b - |1\rangle_a|1\rangle_b), \\
|B_3\rangle &= \tfrac{1}{\sqrt{2}}(|0\rangle_a|1\rangle_b + |1\rangle_a|0\rangle_b), \\
|B_4\rangle &= \tfrac{1}{\sqrt{2}}(|0\rangle_a|1\rangle_b - |1\rangle_a|0\rangle_b),
\end{aligned}
\tag{5.3}
$$

where subscript a, b labels the state of different qubits. For convenience, hereafter we will use the notation that use the first digit to denote the state of qubit a, and the second digit to denote the state of qubit b, i.e. $|1\rangle_a|1\rangle_b \equiv |11\rangle$. Note that these states are fully entangled states, meaning that they are not representable by a product state of the two qubits. In addition, the four Bell states form a complete basis for the two-qubit Hilbert space. The Hamiltonian for the two qubit system [Eq. (5.1)] in the Bell-state basis is

$$
\mathbf{H} = \begin{bmatrix}
0 & \varepsilon_a + \varepsilon_b + h_{12}(t) & J_a + J_b + h_{13}(t) & 0 \\
\varepsilon_a + \varepsilon_b + h_{21}(t) & 0 & 0 & J_b - J_a + h_{24}(t) \\
J_a + J_b + h_{31}(t) & 0 & 0 & \varepsilon_a - \varepsilon_b + h_{34}(t) \\
0 & J_b - J_a + h_{42}(t) & \varepsilon_a - \varepsilon_b + h_{43}(t) & 0
\end{bmatrix},
\tag{5.4}
$$

where the nonzero transformed time-dependent matrix elements are:

$$
\begin{aligned}
h_{12}(t) &= h_{21}(t) &&= \delta\varepsilon_a(t) + \delta\varepsilon_b(t), \\
h_{13}(t) &= h_{31}(t) &&= \delta J_a(t) + \delta J_b(t), \\
h_{24}(t) &= h_{42}(t) &&= \delta J_b(t) - \delta J_a(t), \\
h_{34}(t) &= h_{43}(t) &&= \delta\varepsilon_a(t) - \delta\varepsilon_b(t).
\end{aligned}
\tag{5.5}
$$

From Eq. (5.2) and Eq. (5.5), we can easily compute the correlation matrix $\mathbf{R}$ of the system [Eq. (4.2)]. In this case, $\mathbf{R}$ has only 32 nonzero elements that can be represented by the following 6 irreducible elements:

$$
\begin{aligned}
R_{12;12} &= \gamma_0^a + \gamma_0^b, \\
R_{12;34} &= \gamma_0^a - \gamma_0^b, \\
R_{13;13} &= \gamma_1^a + \gamma_1^b, \\
R_{13;23} &= \gamma_1^b - \gamma_1^a, \\
R_{24;24} &= \gamma_1^a + \gamma_1^b, \\
R_{34;34} &= \gamma_0^a + \gamma_0^b.
\end{aligned}
\tag{5.6}
$$

Other nonzero elements of $\mathbf{R}$ can be obtained using the symmetry property of $\mathbf{R}$ [Eq. (4.3)]. Plugging the correlation matrix elements [Eq. (5.4)] and the time-independent Hamiltonian matrix elements [Eq. (5.6)] into the generalized HSR equation [Eq. (4.4)], we obtain the equation of motion for the averaged density matrix of the system, $\tilde{\rho}(t)$.

In the limit of zero averaged Hamiltonian matrix elements, $\varepsilon_n = J_n = 0$, the equation of motion for the diagonal density matrix elements are decoupled from those for the off-diagonal density matrix elements. Therefore, the dynamics of a system initially in one of the four Bell states (i.e. the initial density matrix has only non-zero diagonal elements) can be fully described by the equations for the diagonal density matrix elements:

$$
\begin{aligned}
\tfrac{d}{dt}\tilde{\rho}_{11}(t) &= \Gamma_0 \cdot [\tilde{\rho}_{22}(t) - \tilde{\rho}_{11}(t)] + \Gamma_1 \cdot [\tilde{\rho}_{33}(t) - \tilde{\rho}_{11}(t)], \\
\tfrac{d}{dt}\tilde{\rho}_{22}(t) &= \Gamma_0 \cdot [\tilde{\rho}_{11}(t) - \tilde{\rho}_{22}(t)] + \Gamma_1 \cdot [\tilde{\rho}_{44}(t) - \tilde{\rho}_{22}(t)], \\
\tfrac{d}{dt}\tilde{\rho}_{33}(t) &= \Gamma_0 \cdot [\tilde{\rho}_{44}(t) - \tilde{\rho}_{33}(t)] + \Gamma_1 \cdot [\tilde{\rho}_{11}(t) - \tilde{\rho}_{33}(t)], \\
\tfrac{d}{dt}\tilde{\rho}_{44}(t) &= \Gamma_0 \cdot [\tilde{\rho}_{33}(t) - \tilde{\rho}_{44}(t)] + \Gamma_1 \cdot [\tilde{\rho}_{22}(t) - \tilde{\rho}_{44}(t)],
\end{aligned}
\tag{5.7}
$$

where we have defined $\Gamma_0 = (\gamma_0^a + \gamma_0^b)$, and $\Gamma_1 = (\gamma_1^a + \gamma_1^b)$. These equations have the form of a system of kinetic equations involving four states, and, clearly, Γ_0 and Γ_1 have the meaning of the degradation rate constants. The symmetric form of Eq. (5.7) suggests that all four states are equivalent dynamically, hence we expect the degradation rates of the systems initially in any of the four Bell states are equal. In this limit, the results of the teleportation based on different Bell-state channels are the same. Later we will show that this is only true when $\varepsilon_n = J_n = 0$ and the two

qubits are coupled to distinct baths.

Eq. (5.7) also shows that a system of two qubits initially in one of the maximumly entangled states degrades into a statistical mixture of the four Bell states. Assuming that the system is initially in the state $|B_1\rangle$ and stays in the noisy quantum channels for a time period t, the density matrix for the entangled qubits Alice and Bob obtained can be represented as the statistical mixture

$$\tilde{\rho}(t) = \tilde{\rho}_{11}(t) \cdot |B_1\rangle\langle B_1| + \tilde{\rho}_{22}(t) \cdot |B_2\rangle\langle B_2| + \tilde{\rho}_{33}(t) \cdot |B_3\rangle\langle B_3| + \tilde{\rho}_{44}(t) \cdot |B_4\rangle\langle B_4|. \quad (5.8)$$

The populations can be obtained by solving Eq. (5.7) with the initial condition $\rho_0 = |B_1\rangle\langle B_1|$:

$$\begin{aligned}
\tilde{\rho}_{11}(t) &= \tfrac{1}{4} + \tfrac{1}{4}e^{-2\Gamma_0 t} + \tfrac{1}{4}e^{-2\Gamma_1 t} + \tfrac{1}{4}e^{-2(\Gamma_0+\Gamma_1)t}, \\
\tilde{\rho}_{22}(t) &= \tfrac{1}{4} - \tfrac{1}{4}e^{-2\Gamma_0 t} + \tfrac{1}{4}e^{-2\Gamma_1 t} - \tfrac{1}{4}e^{-2(\Gamma_0+\Gamma_1)t}, \\
\tilde{\rho}_{33}(t) &= \tfrac{1}{4} + \tfrac{1}{4}e^{-2\Gamma_0 t} - \tfrac{1}{4}e^{-2\Gamma_1 t} - \tfrac{1}{4}e^{-2(\Gamma_0+\Gamma_1)t}, \\
\tilde{\rho}_{44}(t) &= \tfrac{1}{4} - \tfrac{1}{4}e^{-2\Gamma_0 t} - \tfrac{1}{4}e^{-2\Gamma_1 t} + \tfrac{1}{4}e^{-2(\Gamma_0+\Gamma_1)t}.
\end{aligned} \quad (5.9)$$

From Eq. (5.9), the fidelity of the entangled pair, defined as the overlap between the initial density matrix ρ_0 and the density matrix at time t, can be calculated:

$$F_e(t) = \mathbf{Tr}\rho_0\tilde{\rho}(t) = \frac{1}{4} + \frac{1}{4}e^{-2\Gamma_0 t} + \frac{1}{4}e^{-2\Gamma_1 t} + \frac{1}{4}e^{-2(\Gamma_0+\Gamma_1)t}. \quad (5.10)$$

Eq. (5.10) shows that when Γ_0 and Γ_1 are both non-zero, the fidelity $F_e(\infty) = \frac{1}{4}$ in the long time limit. When either Γ_0 or Γ_1 is zero, $F_e(\infty) = \frac{1}{2}$. This result indicates that if we can somehow transform the system and minimize either the diagonal energy fluctuations or the off-diagonal matrix element fluctuations, the original quantum state can be better preserved. In addition, Eq. (5.10) can be used to compute a critical time scale beyond which the degraded entanglement can not be purified by any entanglement purification method [34]. The fidelity required by a successful entanglement purification process, $F_e(t) > 0.5$, corresponds to a critical time t_c where $F_e(t_c) = \frac{1}{2}$. For any high-fidelity quantum teleportation to be possible, the EPR pair should not be allowed to stay in the noisy channels for a time period longer than t_c.

t_c also defines the critical distance for possible high-fidelity quantum teleportation, given the noise of the channels described by the parameters Γ_0 and Γ_1.

5.2.3 Outcome of teleportation

Now we can use the result in the previous section to study the outcome of teleporting a qubit c in state $|\psi\rangle = c_0|0\rangle + c_1|1\rangle$ from Alice to Bob. We assume the traveling time that the EPR pair spends in the noisy channels is t, and the averaged energy ε_n and off-diagonal matrix elements J_n for both qubits are very small so that the limit of $\varepsilon_n = J_n = 0$, $n = a, b$ can be applied. After receiving the degraded EPR pair described by Eq. (5.8), Alice and Bob then perform the Bell-state measurement and corresponding unitary transformation to complete the teleportation. Assuming that all measurements and unitary transformations are carried out perfectly and do not introduce more error, the teleportation outcome that Bob obtains is

$$\rho'(t) = \begin{bmatrix} \frac{1}{2} + \frac{1}{2}(|c_0|^2 - |c_1|^2) \cdot e^{-2\Gamma_1 t} & \frac{c_0 c_1^* + c_0^* c_1}{2} \cdot e^{-2\Gamma_0 t} + \frac{c_0 c_1^* - c_0^* c_1}{2} \cdot e^{-2(\Gamma_0+\Gamma_1)t} \\ \frac{c_0 c_1^* + c_0^* c_1}{2} \cdot e^{-2\Gamma_0 t} + \frac{c_0^* c_1 - c_0 c_1^*}{2} \cdot e^{-2(\Gamma_0+\Gamma_1)t} & \frac{1}{2} + \frac{1}{2}(|c_1|^2 - |c_0|^2) \cdot e^{-2\Gamma_1 t} \end{bmatrix}. \tag{5.11}$$

This result is similar to the result for the dissipation of a two level system in the HSR model (Section 4.3) [32, 33]. Notice that the decoherence depends on the total diagonal fluctuations, $\Gamma_0 = \gamma_0^a + \gamma_0^b$, and the population relaxation depends on the total off-diagonal fluctuations, $\Gamma_1 = \gamma_1^a + \gamma_1^b$. Clearly, noise in both channels affect the teleportation outcome additively. In fact, the outcome is exactly the same as if the teleported qubit is transfered physically from Alice to Bob through the noisy channel C_a and C_b, although the qubit Bob receives has never traveled through channel C_a physically.

The fidelity of teleportation as a function of the traveling time t is

$$F_{tele}(t) = \frac{1}{2} + \frac{1}{2}(c_0^* c_1 + c_0 c_1^*)^2 e^{-2\Gamma_0 t} + \frac{1}{2}(|c_0|^2 - |c_1|^2)^2 e^{-2\Gamma_1 t} - \frac{1}{2}(c_0^* c_1 - c_0 c_1^*)^2 e^{-2(\Gamma_0+\Gamma_1)t}. \tag{5.12}$$

The fidelity of teleportation decreases monotonically from 1 to $\frac{1}{2}$ as the traveling time t increases. At the long time limit, the fidelity approaches $\frac{1}{2}$, which means the result of the quantum teleportation is a half-half mixture of $|0\rangle$ and $|1\rangle$ states, i.e. information about $|\psi\rangle$ is totally lost. This result is in agreement with recent studies on the effect of noise on quantum teleportation [35].

Eq. (5.12) provides a simple interpretation for the phenomenological parameter Γ_0 and Γ_1: Γ_0 is the total decay rate for the real part of the coherence, and Γ_1 is the total population relaxation rate. Recall that γ_0^n, $n = a, b$ is defined using the second moment of the diagonal energy fluctuation $\delta\varepsilon_n(t)$, $n = a, b$ (coupling involving σ_z) and γ_1^n, $n = a, b$ is defined using the second moment of the off-diagonal matrix element fluctuation $\delta J_n(t)$, $n = a, b$ (coupling involving σ_x). We see clearly the effects of different types of noise: the diagonal fluctuations introduce phase shifts that only affect the coherence of the qubit; the off-diagonal fluctuations introduce coupling between the two states and result in population transfer. Note that the decay of the imaginary part of the coherence depends on both diagonal and off-diagonal fluctuations. In the terminology of quantum computing, phase-shift errors are caused by the diagonal energy fluctuations, bit-flip errors are caused by the off-diagonal matrix element fluctuations, and the change in the σ_y component are due to both types of fluctuations. Previous studies on the dissipation of qubits using spin-boson types of Hamiltonian give similar results for the effects of different types of system-bath interactions [23, 19, 20]. Our model gives direct relationships between the phenomenological parameters describing the strength of the fluctuations and the dissipation rates. In addition, our model can take into account the effects of both types of fluctuations *simultaneously*, which is different from most error models used previously.

5.2.4 Nonzero averaged matrix elements

When the time-independent part of the Hamiltonian contains nonzero matrix elements, i.e. $\varepsilon_n \neq 0$ or $J_n \neq 0$, $n = a, b$, the exact analytical expression for $\tilde{\rho}(t)$ is not generally available. In addition, the effect of diagonal energy fluctuations no longer can be clearly distinguished from the effect of off-diagonal matrix element fluctuations, both population relaxation and decoherence depend on γ_0^n and γ_1^n, $n = a, b$. More importantly, the four Bell states no longer decay at the same rate, and we can see the effect of the coherent dynamics depending on the value of the averaged energy and off-diagonal matrix elements. In the weakly-damped regime where the averaged Hamiltonian matrix elements are larger than the strength of the noise, the dynamics of a pair of entangled qubits exhibits coherent oscillating behavior. These oscillations can lead to errors of the quantum teleportation. Figure 5-1 shows the fidelity of the four Bell states as a function of traveling time at $\varepsilon_a = \varepsilon_b = 1$, $J_a = J_b = 0.5$, $\gamma_0^a = \gamma_0^b = 0.1$, and $\gamma_1^a = \gamma_1^b = 0.1$. The different oscillating behavior of the Bell states can be understood by considering the time-independent part of the Hamiltonian. From Eq. (5.1), all the nonzero time-independent matrix elements are

$$\begin{aligned}
\langle B_1|\mathbf{H}_0|B_2\rangle &= \langle B_2|\mathbf{H}_0|B_1\rangle &&= \varepsilon_a + \varepsilon_b, \\
\langle B_1|\mathbf{H}_0|B_3\rangle &= \langle B_3|\mathbf{H}_0|B_1\rangle &&= J_a + J_b, \\
\langle B_2|\mathbf{H}_0|B_4\rangle &= \langle B_4|\mathbf{H}_0|B_2\rangle &&= J_b - J_a, \\
\langle B_3|\mathbf{H}_0|B_4\rangle &= \langle B_4|\mathbf{H}_0|B_3\rangle &&= \varepsilon_a - \varepsilon_b.
\end{aligned}$$

These matrix elements govern the coherent transition between the Bell states, and result in the oscillating behavior of the dynamics. In Fig. 5-1, the fidelity of the $|B_4\rangle$ state decays monotonically as t increases, because both matrix elements couple this state to the other states, $J_b - J_a$ and $\varepsilon_a - \varepsilon_b$, are zero for the parameters used. This also explains why the fidelity of the $|B_4\rangle$ state provides an upper bound on the fidelity of other Bell states in Fig. 5-1. The state that is coupled most weakly to other states decay most slowly.

In the regime where the averaged Hamiltonian matrix elements are smaller than

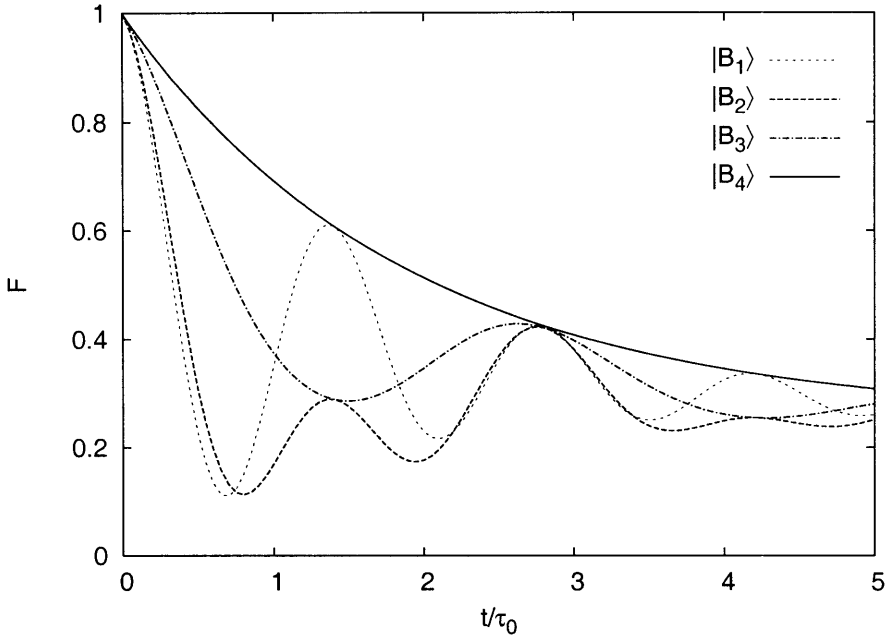

Figure 5-1: Fidelity as a function of the traveling time for the Bell states in the coherent regime: $\varepsilon_a = \varepsilon_b = 1$, $J_a = J_b = 0.5$, $\gamma_0^a = \gamma_0^b = 0.1$, and $\gamma_1^a = \gamma_1^b = 0.1$. The characteristic time scale $\tau_0 = 1/\varepsilon_a$.

the strength of the noise, the system is overdamped and no oscillating behavior can be observed. Figure 5-2 shows the fidelity of the four Bell states at $\varepsilon_a = \varepsilon_b = 0.1$, $J_a = J_b = 0.05$, $\gamma_0^a = \gamma_0^b = 0.1$, and $\gamma_1^a = \gamma_1^b = 0.1$. In this regime, all Bell states degrade monotonically as the traveling time increases.

The fidelity of the EPR pair used in the quantum teleportation is directly related to the fidelity of teleportation. Therefore, the above discussion can be directly applied to the fidelity of teleportation performed using different Bell states. When $\varepsilon_n \neq 0$ or $J_n \neq 0$, $n = a, b$, the fidelity of the teleportation behaves differently when different Bell states are used. To achieve the best result for the teleportation, we have to choose the Bell state that is coupled most weakly to other states. In general, $\varepsilon_n > 0$, $n = a, b$ and J_a and J_b have the same sign, thus $|B_4\rangle$ state will have the weakest coupling. The singlet $|B_4\rangle$ state is the preferred EPR state for the quantum teleportation.

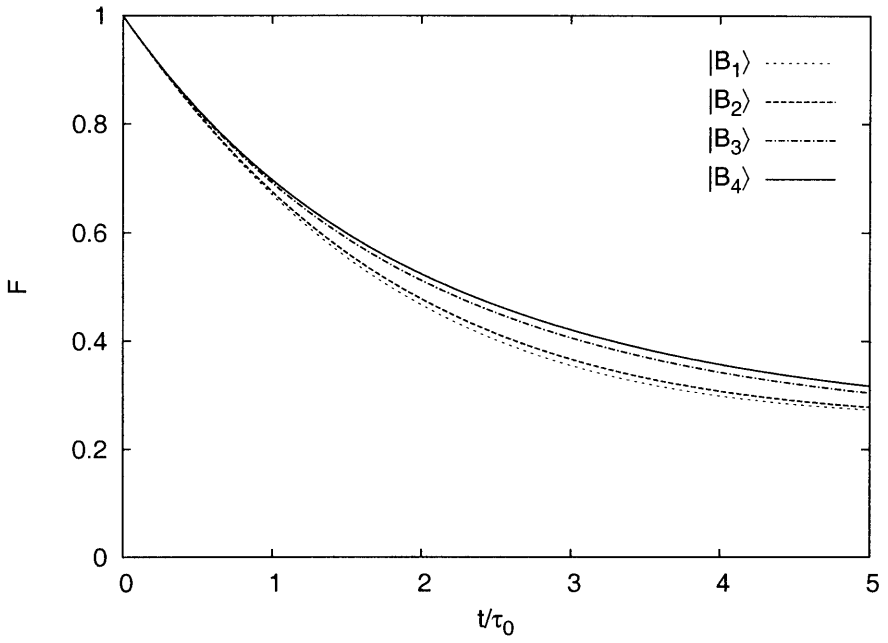

Figure 5-2: Fidelity as a function of the traveling time for the Bell states in the over-damped regime: $\varepsilon_a = \varepsilon_b = 0.1$, $J_a = J_b = 0.05$, $\gamma_0^a = \gamma_0^b = 0.1$, and $\gamma_1^a = \gamma_1^b = 0.1$. The characteristic time scale $\tau_0 = 0.1/\varepsilon_a$.

5.2.5 Effect of collective bath

We have studied the dissipation of two entangled qubits each coupled to a distinct bath, which is the typical situation relevant for the quantum teleportation. Another interesting case is when the two qubits are coupled to a common bath. In this case, we use the Hamiltonian of Eq. (5.1); the difference in the state of the bath is reflected by different correlation functions for the stochastic processes. When the two qubits are coupled to a common bath, the first two moments can be represented as

$$\begin{aligned} \langle \delta\varepsilon_n(t) \rangle &= \langle \delta J_n(t) \rangle = 0, \\ \langle \delta\varepsilon_n(t)\delta\varepsilon_m(t') \rangle &= \gamma_0 \cdot \delta(t-t'), \\ \langle \delta J_n(t)\delta J_m(t') \rangle &= \gamma_1 \cdot \delta(t-t'), \\ \langle \delta\varepsilon_n(t)\delta J_m(t') \rangle &= 0, \end{aligned} \tag{5.13}$$

where γ_0 describes the strength of the diagonal fluctuations; γ_1 describes the strength of the off-diagonal fluctuations. Note that because the qubits are coupled to a common

bath, the fluctuations on different qubits are correlated. From Eq. (5.5) and Eq. (5.13), we can derive the correlation matrix $\mathbf{R}$ for the system in the Bell-state basis. In this collective bath limit, $\mathbf{R}$ has only 8 nonzero elements that can be represented by the following 2 irreducible elements:

$$\begin{aligned} R_{12;12} &= 4\gamma_0, \\ R_{13;13} &= 4\gamma_1. \end{aligned} \tag{5.14}$$

Using Eq. (5.14), we can derive the equation of motion for the dynamics of two qubits coupled to a common bath. In the limit of zero averaged Hamiltonian matrix elements ($\varepsilon_n = J_n = 0$, $n = a, b$), we obtain a simple result for the populations in the four Bell states:

$$\begin{aligned} \tfrac{d}{dt}\tilde{\rho}_{11}(t) &= 4\gamma_0 \cdot [\tilde{\rho}_{22}(t) - \tilde{\rho}_{11}(t)] + 4\gamma_1 \cdot [\tilde{\rho}_{33}(t) - \tilde{\rho}_{11}(t)], \\ \tfrac{d}{dt}\tilde{\rho}_{22}(t) &= 4\gamma_0 \cdot [\tilde{\rho}_{11}(t) - \tilde{\rho}_{22}(t)], \\ \tfrac{d}{dt}\tilde{\rho}_{33}(t) &= 4\gamma_1 \cdot [\tilde{\rho}_{11}(t) - \tilde{\rho}_{33}(t)], \\ \tfrac{d}{dt}\tilde{\rho}_{44}(t) &= 0. \end{aligned} \tag{5.15}$$

Eq. (5.15) describes the dynamics for a system of two qubits coupled to a common bath in the Bell-state basis. Interestingly, the symmetry that exists in the distinct bath case [Eq. (5.7)] no longer holds, and the population in the $|B_4\rangle$ state, $\tilde{\rho}_{44}(t)$, is invariant in time. In addition, when only diagonal energy fluctuations exist ($\gamma_1 = 0$), the population in the $|B_3\rangle$ state is also invariant; when only off-diagonal matrix element fluctuations exist ($\gamma_1 = 0$), the population in the $|B_2\rangle$ state is invariant. Compared to the result of two qubits coupled to distinct baths [see Eq.(5.7)], Eq. (5.15) shows that the fluctuations interfere constructively for the $|B_1\rangle$ state leading to a faster decay rate, but destructively for the $|B_4\rangle$ state. This result can be understood easily in our stochastic model. In our model, the effect of environment on the system is represented by a fluctuating field, and the interaction Hamiltonian for the two qubits is $\mathbf{H}_{int} = \sigma_i^{(a)} \cdot V_a(t) + \sigma_i^{(b)} \cdot V_b(t)$ ($i = x, z$; a and b are labels for different qubits). When the two qubits are coupled to a common bath, $V_a(t) = V_b(t)$, we can factorize the interaction into the form $\mathbf{H}_{int} = (\sigma_i^{(a)} + \sigma_i^{(b)}) \cdot V_a(t)$. Therefore, any

state $|\phi\rangle$ that satisfies $\langle\phi|\sigma_i^{(a)} + \sigma_i^{(b)}|\phi\rangle = 0$ does not interact with the fluctuating field, and is invariant to the noise. We can see that $\langle B_3|\sigma_z^{(a)} + \sigma_z^{(b)}|B_3\rangle = 0$ and $\langle B_4|\sigma_z^{(a)} + \sigma_z^{(b)}|B_4\rangle = 0$, thus both the $|B_3\rangle$ and $|B_4\rangle$ states are not affected by phase-shifting noise; $\langle B_2|\sigma_x^{(a)} + \sigma_x^{(b)}|B_2\rangle = 0$ and $\langle B_4|\sigma_x^{(a)} + \sigma_x^{(b)}|B_4\rangle = 0$, thus both the $|B_2\rangle$ and $|B_4\rangle$ states are not affected by bit-flipping noise.

The effect of the collective bath has been verified experimentally [36], and studied in theoretical works related to the ideas of "quantum error-avoiding codes" [37, 38] and "decoherence-free subspaces" [39, 40]. Duan and Guo have shown similar result using a Hamiltonian that explicitly includes the linear coupling terms between the system and the boson bath [41, 38]. The agreement indicates that our simple stochastic model can handle both the independent and the collective bath properly.

Recently, Kumar and Pandey have studied the effect of noise on quantum teleportation [35]. They applied two different models, a stochastic model and a spin-boson type model, to this problem, and studied the relative teleportation efficiencies of the Bell states. Their main result is that for the simple stochastic model, the four Bell states are equivalent, but for the second model in which the effect of environment is considered explicitly, the $|B_4\rangle$ state is least affected by the noise. We obtain a similar conclusion using the stochastic Liouville equation approach. Based on our result, we understand that the $|B_4\rangle$ state is the least affected state because of the assumption of a collective bath, not because the effect of bath is considered microscopically. Like spin-boson type models, a simple stochastic model when treated correctly can provide the same result, and gives a simple picture for the effect of a collective bath versus a localized bath.

5.3 Errors in a Quantum controlled-NOT Gate

Qubits and quantum gates are the basic elements of quantum computing. A quantum circuit[3] that performs a particular quantum operation can be expressed as a network

[3]Quantum algorithms are usually described schematically by a quantum circuit, in which a horizontal line represents a qubit, and blocks that shown above represent quantum gate operations. The computation is done by applying corresponding quantum gates from left to right sequentially.

of elementary quantum gates [42, 43]. In fact, quantum circuits can be constructed using one- and two-qubit gates as basic building blocks. For example, the quantum controlled-NOT gate together with all one-qubit quantum gates form such a set of universal quantum gates [42, 44]. In reality, quantum computations are performed by subjecting an array of qubits under a sequence of control fields that control the Hamiltonian of the qubit system and result in specific quantum gate operations. Therefore, we consider the process of quantum computation as preparing the qubit system in the initial state, then performing programmed control fields on the qubits in a sequence of time steps, and finally measuring the output in the working basis.

To understand the effect of noise on general quantum computations and help the implementation of quantum computers, we need a model that can be used to describe the decoherence and population relaxation for a system of qubits subjected to external control fields. The decoherence and gate performance of a controlled-NOT gate on various types of physical realizations have been studied in Refs. [24, 25, 27, 26, 45]. In particular, Thorwart and Hänggi investigated the decoherence and dissipation for a generic controlled-NOT gate operation using the numerical *ab initio* technique of the quasiadiabatic-propagator path integral (QUAPI). They demonstrated that this numerical method is capable of describing the full time-resolved dynamics of the two-qubit system in the presence of noise. To our knowledge, so far, the QUAPI method is the most sophisticated method that has been applied to study the decoherence during a controlled-NOT gate operation. In this section, we apply the stochastic Liouville equation approach to study the same generic controlled-NOT operation investigated by Thorwart and Hänggi, and show that our model yields similar results. In general, our model is easier to extend to many qubit systems than the QUAPI method, and can incorporate the effects of noise from different sources at the same time.

Usually, the measurement in the working basis is performed in the end of computation to read the outcome. We will see examples of quantum circuits later in this chapter (for example, see Fig. 5-10).

5.3.1 A generic model for 2-qubit quantum gates

In a physical implementation of a quantum computer, a quantum gate can be expressed by a Hamiltonian with terms representing the control fields that result in the gate operation. Consider a elementary step in a quantum gate operation where the control Hamiltonian is switched on, a generic Hamiltonian describing the constant external fields and the time-dependent fluctuations (noise) for a two-qubit system can be written as

$$\begin{aligned} \mathbf{H}(t) &= \sum_{n=a,b} [\varepsilon_n + \delta\varepsilon_n(t)] \cdot \sigma_z^{(n)} + \sum_{n=a,b} [J_n + \delta J_n(t)] \cdot \sigma_x^{(n)} \\ &\quad + [g + \delta g(t)] \cdot (\sigma_+^{(a)}\sigma_-^{(b)} + \sigma_-^{(a)}\sigma_+^{(b)}), \\ &\equiv \mathbf{H}_0 + \mathbf{h}(t) \end{aligned} \tag{5.16}$$

where the two qubits are labeled as qubit a and qubit b; the first two terms comprise the Hamiltonian for two non-interacting qubits considered in Eq. (5.1); the last term represents the inter-qubit interaction with $\sigma_\pm^{(n)} = (\sigma_x^{(n)} \mp i\sigma_y^{(n)})$, $n = a, b$; g and $\delta g(t)$ are the time-independent and time-dependent fluctuating part of the inter-qubit coupling. The controllable fields are represented by the values of ε_n, J_n, $n = a, b$, and g. Quantum gates can be implemented by switching these fields on and off in a controlled manner. For simplicity, we assume throughout this work that the external control fields are switched on and off instantaneously, and the interactions introduced by the external control fields are constant in time; this corresponds to a rectangular pulse. More realistic pulse shapes can be incorporated into our treatment without too much additional work, and considering only constant external control fields does not affect the generality of this model. In addition, a sequence of different rectangular pulses can be divided into time periods with a constant external field in each of them, and then treated separately using a different time independent $\mathbf{H}_0$ for each time period. Note that because the generalized HSR equation of motion satisfies the positivity condition required for the dynamics of physically admissible density matrices, propagators computed for simple one- and two-qubit gates can be directly assembled to study the dissipative dynamics of more complicated quantum

circuits. This property is important for the application of the generalized HSR model to simulate quantum circuits.

The XY type of coupling is adopted in our model Hamiltonian. This interaction is just an illustrative example, and does not account for all the possible interactions in a specific realization of solid-state devices. The real form of the inter-qubit interaction term depends on the controllable interactions available for each individual physical implementation. Nevertheless, our model can handle the other types of interactions as well, and we expect that the model Hamiltonian we use here can reproduce the same general physical behavior as other two-qubit Hamiltonians.

From Eq. (5.16), we can write down the time-independent part of the Hamiltonian in the standard basis $\{|00\rangle, |01\rangle, |10\rangle, |11\rangle\}$:

$$\mathbf{H}_0 = \begin{bmatrix} \varepsilon_a + \varepsilon_b & J_b & J_a & 0 \\ J_b & \varepsilon_a - \varepsilon_b & g & J_a \\ J_a & g & \varepsilon_b - \varepsilon_a & J_b \\ 0 & J_a & J_b & -\varepsilon_a - \varepsilon_b \end{bmatrix}, \tag{5.17}$$

and the time-dependent part of the Hamiltonian is

$$\mathbf{h}(t) = \begin{bmatrix} \delta\varepsilon_a(t) + \delta\varepsilon_b(t) & \delta J_b(t) & \delta J_a(t) & 0 \\ \delta J_b(t) & \delta\varepsilon_a(t) - \delta\varepsilon_b(t) & \delta g(t) & \delta J_a(t) \\ \delta J_a(t) & \delta g(t) & \delta\varepsilon_b(t) - \delta\varepsilon_a(t) & \delta J_b(t) \\ 0 & \delta J_a(t) & \delta J_b(t) & -\delta\varepsilon_a(t) - \delta\varepsilon_b(t) \end{bmatrix}. \tag{5.18}$$

Furthermore, we assume the two qubits are close to each other in space, therefore, we consider the correlation functions suitable for two qubits coupled to a common bath. Again, we assume the fluctuations have zero mean and δ-function correlation times. The nonzero second moments are

$$\begin{aligned} \langle \delta\varepsilon_n(t)\delta\varepsilon_m(t')\rangle &= \gamma_0 \cdot \delta(t-t'), \\ \langle \delta J_n(t)\delta J_m(t')\rangle &= \gamma_1 \cdot \delta(t-t'), \\ \langle \delta g(t)\delta g(t')\rangle &= \gamma_2 \cdot \delta(t-t'), \end{aligned} \tag{5.19}$$

where γ_0 describes the strength of the diagonal energy fluctuations; γ_1 describes the strength of the off-diagonal matrix element fluctuations; γ_2 describes the strength of the fluctuations of the inter-qubit interactions. As we have shown in the previous section, these phenomenological parameters are related to the kinetic rate of each separate dissipative process, and can be easily measured experimentally. Also note that we directly include the inter-qubit coupling fluctuations, which corresponds to two-qubit flip-flop errors that are difficult to treat in the microscopic spin-boson type Hamiltonians.

Eq. (5.19) can be used to compute the elements of the correlation matrix $\mathbf{R}$. Using $\mathbf{R}$ together with the averaged Hamiltonian matrix elements in Eq. (5.17), we can obtain the equation of motion describing the dynamics of the two-qubit system subjected to arbitrary one- and two-qubit control fields. As a result, we can study the dissipative dynamics of the qubit system during arbitrary gate operations. Although we only consider an operation done by a set of constant external fields, the behavior of more complicated gates that involve more than one step can be studied by combining the result for each elementary operations. In our model, the results for a set of universal quantum gates can be assembled to compute the results for a general quantum circuit.

5.3.2 The quantum controlled-NOT gate

The quantum controlled-NOT gate plays a central role in the quantum computation, because, as we noted above, the set of all one-qubit gates together with the controlled-NOT gate is universal [44]. In the standard basis $\{|00\rangle, |01\rangle, |10\rangle, |11\rangle\}$, the ideal controlled-$NOT$ gate is represented as

$$U_{CNOT}^{ideal} = \begin{bmatrix} 1 & 0 & 0 & 0 \\ 0 & 1 & 0 & 0 \\ 0 & 0 & 0 & 1 \\ 0 & 0 & 1 & 0 \end{bmatrix},$$

where we have used the first qubit as the control qubit. This gate operates on two qubits, and inverts the state of the second qubit (i.e. perform logical NOT operation on the second qubit) if the first qubit is in the state $|1\rangle$, thus the name "controlled-NOT". The controlled-NOT gate cannot be constructed in one step using our model Hamiltonian. Instead, we must construct the controlled-NOT gate using multiple elementary one- and two-qubit gates.

To begin with, we define the following one-qubit rotations on qubit a and b:

$$U_{nz}(\alpha) = e^{i\frac{\alpha}{2}\sigma_z^{(n)}}, \quad n = a, b,$$

$$U_{nx}(\alpha) = e^{i\frac{\alpha}{2}\sigma_x^{(n)}}, \quad n = a, b,$$

and the two-qubit operation:

$$U_j(\alpha) = e^{i\alpha(\sigma_+^{(a)}\sigma_-^{(b)} + \sigma_-^{(a)}\sigma_+^{(b)})}.$$

All these operations can be easily implemented using our model Hamiltonian [Eq. (5.16)] (with all control fields set to zero initially): $U_{nz}(\alpha)$, $n = a, b$, can be done by switching on $\varepsilon_n = -\varepsilon_0 \cdot \mathrm{Sign}(\alpha)$ for a time period of $\tau = \frac{\alpha}{2\varepsilon_0}$; $U_{nx}(\alpha)$, $n = a, b$, can be done by switching on $J_n = -J_0 \cdot \mathrm{Sign}(\alpha)$ for a time period of $\tau = \frac{\alpha}{2J_0}$; $U_j(\alpha)$ can be done by switching on $g = -g_0 \cdot \mathrm{Sign}(\alpha)$ for a time period of $\tau = \frac{\alpha}{g_0}$; where the sign function $\mathrm{Sign}(\alpha)$ returns -1 when $\alpha < 0$, and 1 when $\alpha > 0$. Using the corresponding averaged Hamiltonian $\mathbf{H}_0$ for each operations and the correlation matrix presented

in the previous section, the equation of motion describing the dynamics of the two-qubit system subjected to any of these operations can be easily obtained. Actually, for arbitrary initial conditions, the analytical solution for the time-dependent two-qubit density matrix $\rho(t)$ during $U_{nx}(\alpha)$, $U_{nz}(\alpha)$, $n = a, b$, and $U_j(\alpha)$ operations are available in the Laplace domain, and can be used to study arbitrary quantum circuits composed by these three elementary operations.

The controlled-NOT gate can be expressed by the following sequence of one- and two-qubit gate operations [17]:

$$U_{CNOT} = U_{bx}(\frac{\pi}{2})U_{bz}(\frac{-\pi}{2})U_{bx}(-\pi)U_j(\frac{-\pi}{2})U_{ax}(\frac{-\pi}{2})U_j(\frac{\pi}{2})U_{bz}(\frac{-\pi}{2})U_{az}(\frac{-\pi}{2}). \quad (5.20)$$

Table 5.1 lists the required control fields and time span to implement each step using our model Hamiltonian. In Table 5.1, we use ε_0, J_0, and g_0 to denote the strength of the controllable single-qubit bias, intra-qubit coupling, and inter-qubit XY interaction, respectively. In addition, we assume that the controllable field strengths and noise (defined by parameters γ_0, γ_1, and γ_2 as mentioned in the previous section) for the two qubits are identical. The value of these parameters should depend on the specific physical realization of the qubit systems. The total time required to perform the controlled-NOT gate is $\tau_{cnot} = \pi/2\varepsilon_0 + \pi/J_0 + \pi/g_0$. For a typical energy scale of 1 meV (suitable for quantum dot qubits), the operation time is on the picosecond time scale.

Using the parameters listed in Table 5.1, we can calculate the time-dependent two-qubit density matrix $\rho(t)$ during controlled-NOT operations under different noise conditions defined by γ_0, γ_1, and γ_2. Figure 5-3 shows the time-resolved controlled-NOT operation for two qubits initially in the $|11\rangle$ state. We set the strengths of the control fields equal to 1, i.e. $\varepsilon_0 = J_0 = g_0 = 1$. The ideal operation (solid line) starts at population 1 in the $|11\rangle$ state, and ends its total population in the $|10\rangle$ state, showing a successful controlled-NOT operation. Three different noisy operations are shown in Fig. 5-3: (1) operation with the strength of the diagonal energy fluctuations

Table 5.1: Parameters of the model Hamiltonians used to perform the controlled-*NOT* gate in 7 steps. The required control fields and time span for each step are listed. Note that we only list the nonzero field parameters.

No.	Operation	Control Fields	Time
1	$U_{bz}(\frac{-\pi}{2})U_{az}(\frac{-\pi}{2})$	$\varepsilon_a = \varepsilon_0$, $\varepsilon_b = \varepsilon_0$	$\tau_1 = \frac{\pi}{4\varepsilon_0}$
2	$U_j(\frac{\pi}{2})$	$g = -g_0$	$\tau_2 = \tau_1 + \frac{\pi}{2g_0}$
3	$U_{ax}(\frac{-\pi}{2})$	$J_a = J_0$	$\tau_3 = \tau_2 + \frac{\pi}{4J_0}$
4	$U_j(\frac{-\pi}{2})$	$g = g_0$	$\tau_4 = \tau_3 + \frac{\pi}{2g_0}$
5	$U_{bx}(-\pi)$	$J_b = J_0$	$\tau_5 = \tau_4 + \frac{\pi}{2J_0}$
6	$U_{bz}(\frac{-\pi}{2})$	$\varepsilon_b = \varepsilon_0$	$\tau_6 = \tau_5 + \frac{\pi}{4\varepsilon_0}$
7	$U_{bx}(\frac{\pi}{2})$	$J_b = -J_0$	$\tau_7 = \tau_6 + \frac{\pi}{4J_0}$

$\gamma_0 = 0.05$ (dashed line), (2) operation with the strength of the off-diagonal matrix element fluctuations $\gamma_1 = 0.05$ (dash-dotted line), (3) operation with the strength of the inter-qubit coupling fluctuations $\gamma_2 = 0.05$ (dotted line). The effect of noise on the controlled-*NOT* operation can be clearly seen. In previous work, Thorwart and Hänggi derived the same time-resolved controlled-*NOT* operation result [25]. Our result is very close to their numerical *ab initio* QUAPI result. The agreement between our time-resolved result to the QUAPI result gives us confidence that our model captures the correct physics.

5.3.3 Dependence on the noise strength

We use gate fidelity and gate purity to characterize the performance of the controlled-*NOT* gate. Other gate quantifiers including the quantum degree and entanglement capability are also calculated [46], but we do not show the results here because they follow the same trend as the gate fidelity and gate purity. In our formalism, the density matrix for the two qubits after the noisy controlled-*NOT* operation, $\rho(\tau_{cnot})=U_{CNOT}\rho_0 U_{CNOT}^{\dagger}$, can be calculated for any initial density matrix ρ_0. Following Thorwart and Hänggi , we average the gate fidelity and gate purity over 16 initial states to account for the general performance of the controlled-*NOT* gate. The 16 unentangled input states $|\psi_0^{ij}\rangle$, $i,j = 1,2,3,4$ are defined as $|\psi_0^{ij}\rangle = |\phi_i\rangle_a \otimes |\phi_j\rangle_b$

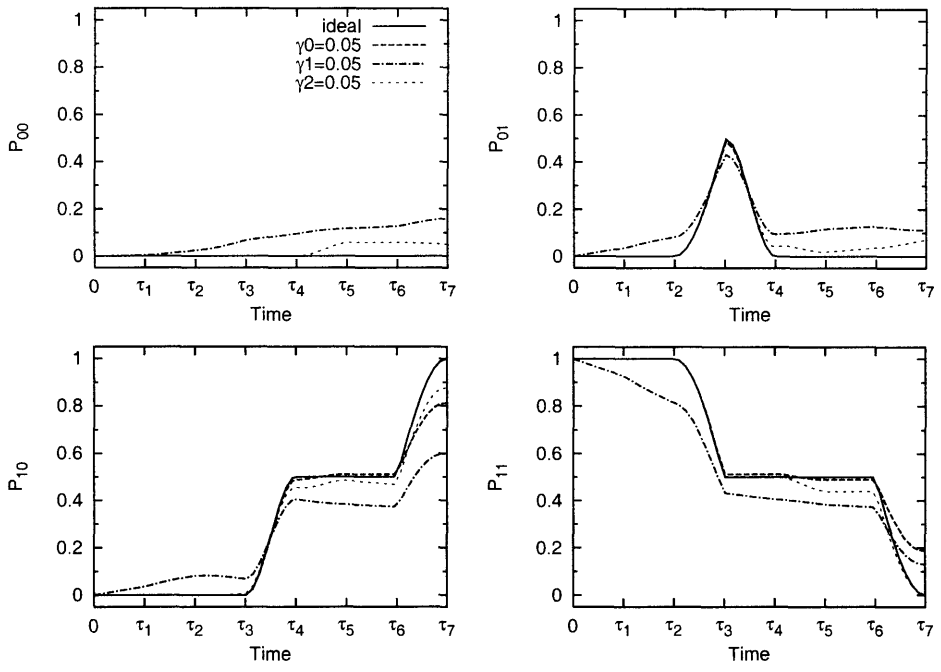

Figure 5-3: Time-resolved controlled-NOT gate operation on the $|11\rangle$ input state. Shown are the populations in the four basis states $\mathbf{P}_{ij}(t) = \langle ij|\rho(t)|ij\rangle$ as a function of time. The strengths of all the fields are set to 1 in the calculation, i.e. $\varepsilon_0 = J_0 = g_0 = 1$, and the corresponding time steps are defined in Table (5.1). We show the results for four different controlled-NOT gate operations: (1) ideal operation without any noise (solid line), (2) operation with the strength of the diagonal fluctuations $\gamma_0 = 0.05$ (dashed line), (3) operation with the strength of the off-diagonal fluctuations $\gamma_1 = 0.05$ (dash-dotted line), (4) operation with the strength of the inter-qubit coupling fluctuations $\gamma_2 = 0.05$ (dotted line).

with $|\phi_1\rangle = |0\rangle$, $|\phi_2\rangle = |1\rangle$, $|\phi_3\rangle = (|0\rangle + |1\rangle)/\sqrt{2}$, $|\phi_3\rangle = (|0\rangle + |1\rangle)/\sqrt{2}$, $|\phi_4\rangle = (|0\rangle + i|1\rangle)/\sqrt{2}$, and a, b denoting the state for different qubits. These states span the Hilbert space for the two-qubit operations, and should give a reasonable result for the averaged effect [46, 25].

The gate fidelity is defined as the overlap between the ideal output and the output of the real gate operation. Using the 16 initial states, the averaged fidelity can be written as

$$F = \frac{1}{16} \sum_{i,j=1}^{4} \langle \psi_{out}^{ij} | \rho_{CNOT}^{ij} | \psi_{out}^{ij} \rangle,$$

where we have defined the ideal controlled-NOT output $|\psi_{out}^{ij}\rangle = U_{CNOT}^{ideal} |\psi_0^{ij}\rangle$, and the output of the real controlled-NOT operation $\rho_{CNOT}^{ij} = U_{CNOT} |\psi_0^{ij}\rangle \langle \psi_0^{ij}| U_{CNOT}^{\dagger}$. The gate fidelity is a measure of how close the real operation is compared to the ideal operation. For a perfect gate operation, the gate fidelity should be 1.

Similarly, the averaged gate purity is defined as

$$P = \frac{1}{16} \sum_{i,j=1}^{4} \mathrm{Tr}((\rho_{CNOT}^{ij})^2).$$

The gate purity quantifies the effect of decoherence. For a perfect gate operation, the gate purity should be 1.

The results of the averaged gate fidelity and gate purity as a function of the strength of each individual type of noise are shown in Fig. 5-4. For our generic study, we again set the strengths of all the control fields to 1, i.e. $\varepsilon_0 = J_0 = g_0 = 1$. Clearly, different types of noise cause different amount of errors. However, they all follow the same trend. The deviations of the gate fidelity and gate purity from the ideal values, i.e. $1 - F$ and $1 - P$, are sensitive to the strength of the noise, and saturate to 0.75 in the strong noise limit; the value 0.75 corresponds to a fully mixed state. In the weak noise regime, both $1 - F$ and $1 - P$ depend linearly on the noise strength, as expected [25, 26]. The proportionality constant in this case is ~ 10. In fact, the proportionality constant depends on the strengths of the control fields, and reflects

the total operation time required to complete the controlled-NOT gate operation. As the strength of the control field increases, the total operation time decreases, and the qubits have less time to undergo the dissipative processes, resulting in less degradation. To minimize the effect of noise, we need to reduce the proportionality constant, therefore, we will want to operate the device at the highest control fields possible. However, the situation will be different if increasing the strengths of the control fields will also introduce more noise. We will explicitly discuss the effect of the control-field strength in the next subsection.

From our results for $\varepsilon_0 = J_0 = g_0 = 1$, to achieve the threshold accuracy of the 0.999 99 level needed for arbitrary long quantum computations [47, 48, 49], one needs to keep the noise strength below the 10^{-6} level. Assuming a characteristic energy scale of 1 meV, this value corresponds to a decoherence time γ^{-1} in the μs scale, which provides a serious challenge for experimentalists working on the realization of solid-state quantum computers.

The linear dependence of $1-F$ and $1-P$ on the noise strengths also indicates that the effect of *the same* type of noise is additive in the weak noise regime. To study the additivity of *different* types of noise, we calculate the averaged controlled-NOT gate fidelity when different types of noise coexist at the same time. We define the total error of the controlled-NOT gate operation E as the deviation of the gate fidelity from the ideal value:

$$E(\gamma_0, \gamma_1, \gamma_2) = 1 - F(\gamma_0, \gamma_1, \gamma_2), \tag{5.21}$$

where we have explicitly expressed the total error E as a function of the three different types of noise strengths:γ_0, γ_1, and γ_2. In Fig. 5-5, we show the errors of the controlled-NOT gate operation where the different types of noise coexist, and compare them to the total errors obtained by adding up the errors caused by the individual type of noise. Clearly, for all four situations considered, these two lines collapse in the weak noise regime. The results indicate that errors caused by different types of noise are additive in the small noise regime. In other words, the following identity

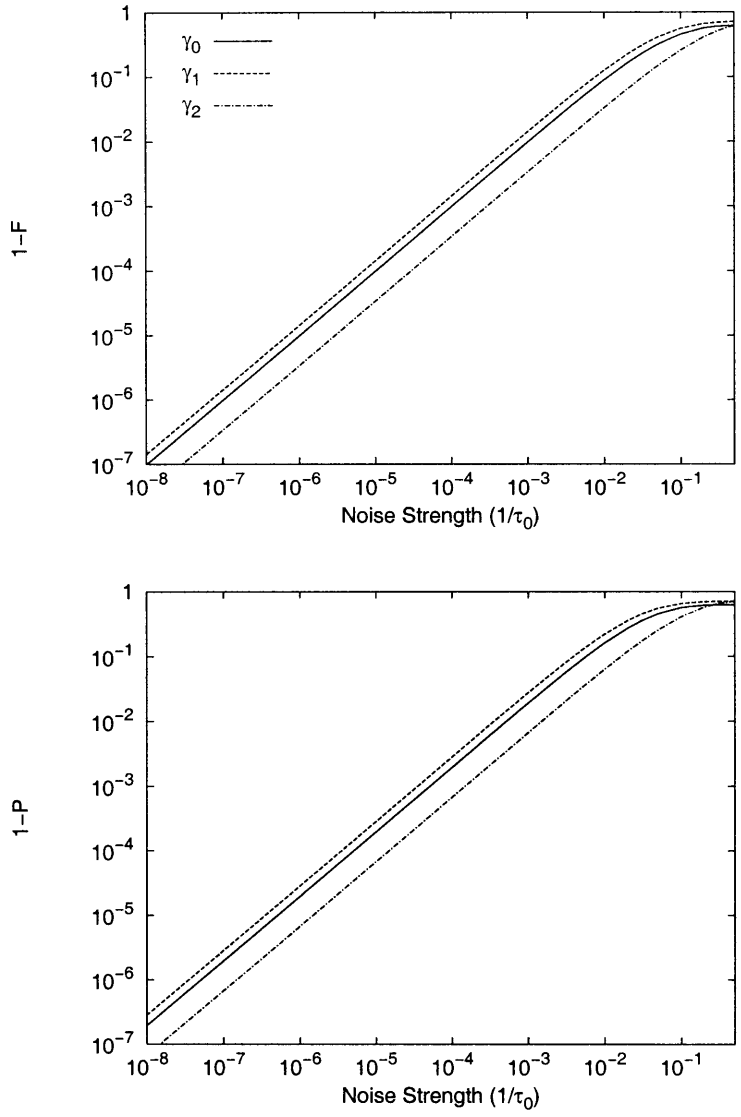

Figure 5-4: Dependence of the errors in the controlled-NOT gate operation on the noise strength. The deviations of the gate fidelity (upper panel) and gate purity (lower panel) from the ideal values are shown, i.e. $1-F$ and $1-P$. The effects of three types of noise are shown in both plots: (1) diagonal fluctuations represented by γ_0 (solid line), (2) off-diagonal fluctuations represented by γ_1 (dashed line), (3) inter-qubit fluctuations represented by γ_2 (dash-dotted line). The control-field strengths are set to $\varepsilon_0 = J_0 = g_0 = 1$. The unit of noise strength is set to $1/\tau_0$, with characteristic time scale $\tau_0 = 1/\varepsilon_0$.

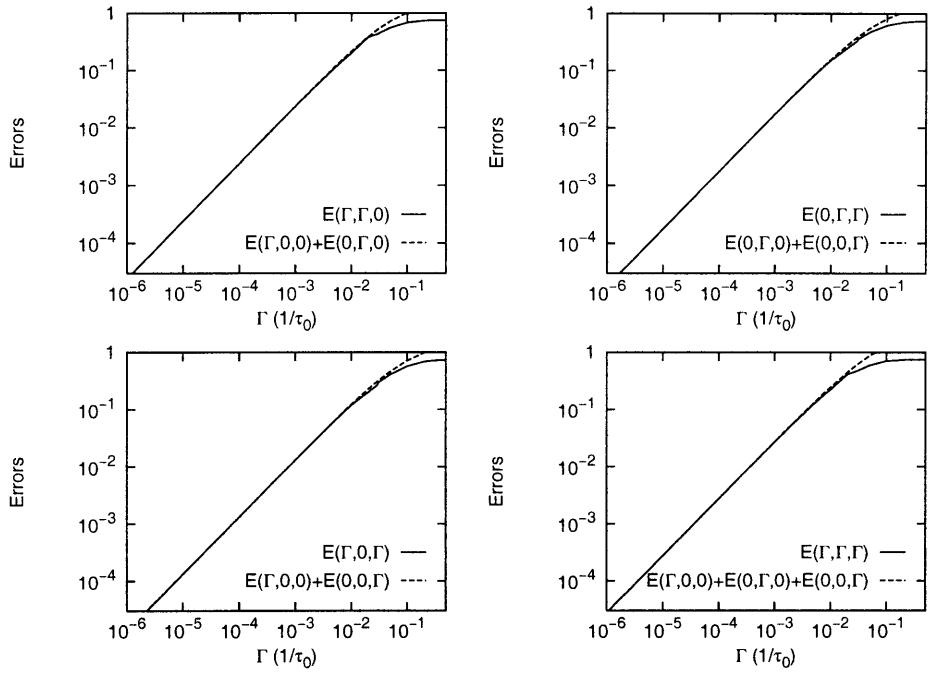

Figure 5-5: We show the error functions $E(\gamma_0, \gamma_1, \gamma_2)$ of the controlled-NOT gate operation in situations where the different types of noise coexist (solid lines). For each case, the corresponding total errors obtained by adding up the errors caused by the individual types of noise is also shown (dotted lines). Four different combinations are compared: upper-left: $E(\Gamma, \Gamma, 0)$ *vs.* $E(\Gamma, 0, 0)$+$E(0, \Gamma, 0)$ (γ_0 and γ_1); upper-right: $E(0, \Gamma, \Gamma)$ *vs.* $E(0, \Gamma, 0)$+$E(0, 0, \Gamma)$ (γ_1 and γ_2); lower-left: $E(\Gamma, 0, \Gamma)$ *vs.* $E(\Gamma, 0, 0)$+$E(0, 0, \Gamma)$ (γ_0 and γ_2); lower-right: $E(\Gamma, \Gamma, \Gamma)$ *vs.* $E(\Gamma, 0, 0)$+$E(0, \Gamma, 0)$+$E(0, 0, \Gamma)$ (all types of noise). The strengths of all the control fields are set to 1, i.e. $\varepsilon_0 = J_0 = g_0 = 1$. The characteristic time scale $\tau_0 = 1/\varepsilon_0$. We can clearly see that errors caused by different types of noise are additive in the small noise regime.

holds in the small noise regime:

$$E(\gamma_0, \gamma_1, \gamma_2) = E(\gamma_0, 0, 0) + E(0, \gamma_1, 0) + E(0, 0, \gamma_2). \tag{5.22}$$

Eq. (5.22) justifies previous studies where different types of system-bath interactions are treated independently [25, 26].

5.3.4 Dependence on the strength of the inter-qubit coupling

The time required to finish a quantum gate operation is inverse proportional to the strength of the control field used, and longer operation time results in more errors. Therefore, the quality of gate operations also depend on the strength of the control field. In this subsection, we analyze the dependence of the quality of the quantum controlled-NOT gate operation on the strength of the inter-qubit coupling g_0.

If the strength of the inter-qubit coupling g_0 can be increased without introducing any extra disturbance on the system, then we expect operating the device in the strongest g_0 achievable will give the best result. However, physically, applying a stronger field also means introducing stronger noise due to the imperfectness of the field. In our model, this means stronger fluctuations on the inter-qubit XY interaction. The extra noise can be expressed in the value of the γ_2 term. To incorporate this effect, we allow γ_2 to depend on the strength of the inter-qubit coupling g_0. Figure 5-6 shows the errors of the controlled-NOT gate operation as a function of g_0 at $\gamma_0 = 0.001$, $\gamma_1 = 0.001$, $\varepsilon_0 = 1$, and $J_0 = 1$. Three different noise strength dependences are shown: (1) constant $\gamma_2 = 0.001$ (solid curve), (2) linear $\gamma_2 = 0.001 \cdot (1 + g_0)$ (dashed curve), and (3) quadratic $\gamma_2 = 0.001 \cdot (1 + g_0^2)$ (dash-dotted curve). The three curves show the same behavior in the small g_0 regime, in which the operation takes too much time and the system is fully degraded. As the strength of the coupling g_0 increases, the errors decrease due to the shorter operation time. When the strength of the coupling g_0 approaches the strengths of other control fields ($\varepsilon_0 = J_0 = 1$ in this case), the three curves start to show different behavior. For both constant and linear γ_2, the errors generated by other operations ($U_{nz}(\alpha)$ and $U_{nx}(\alpha)$) dominate the errors of the controlled-NOT gate operation, therefore, increasing g_0 gains nothing and the curve saturates. Our result for the constant γ_2 case is in agreement with the result obtained previously using the QUAPI method [25]. The situation is different when the strength of the noise depends on g_0 quadratically. For this case, the errors start to increase after $g_0 > 1$, because increasing the inter-qubit coupling g_0 introduces stronger noise that cannot be compensated by shorter operation times. Therefore, in

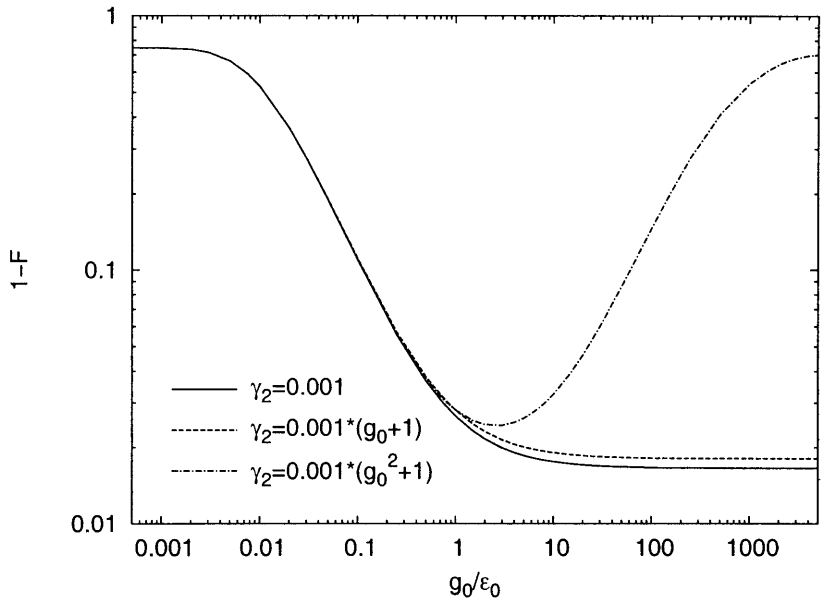

Figure 5-6: Dependence of the errors in the controlled-NOT gate operation on the strength of the inter-qubit coupling g_0. Shown are the deviations of the gate fidelity from the ideal value for three types of γ_2: (i) constant $\gamma_2 = 0.001$ (solid curve), (ii) linear $\gamma_2 = 0.001 \cdot (1 + g_0)$ (dashed curve), and (iii) quadratic $\gamma_2 = 0.001 \cdot (1 + g_0^2)$ (dash-dotted curve). Other parameters are set to $\gamma_0 = 0.001$, $\gamma_1 = 0.001$, $\varepsilon_0 = 1$, and $J_0 = 1$.

the quadratic case, there exists an optimal g_0 for the gate operation.

Finally, we emphasize that the noise model presented in this work can be used to study the dissipative dynamics of a many-qubit system with direct inter-qubit coupling, imperfectness of the control field, and other many-qubit effects. In addition, because of the δ-function correlation time assumed in the model, the resulting propagator satisfies complete positivity, therefore no additional time period has to be inserted between switching events, as will be necessary for methods based on the Bloch-Redfield formalism. As a result, propagators computed for simple one- and two-qubit gates can be directly assembled to study the dissipative dynamics of more complicated quantum circuits. We expect this method to be applied to evaluate the quality of quantum circuits under realistic device conditions. Such theoretical studies will be useful for the design and implementation of quantum computers.

5.4 Noise Threshold of Fault-tolerant Quantum Error Correction

Recent developments in the theory of quantum computation have generated significant interest in utilizing quantum mechanics to achieve new computational capability [6]. However, the intrinsic sensitivity of a quantum superposition state to imperfect operations and interactions with its surrounding environment prohibits the realization of a scalable quantum computer. To combat the inevitable errors and decoherence of quantum states during the process of computation, quantum error correction (QEC) and fault-tolerant methods of quantum computation have to be applied in the construction of large-scale quantum computers. It has become clear that the future of robustly storing and manipulating quantum information relies upon the success of fault-tolerant quantum error correction [50, 51, 52].

Fault-tolerant methods combined with concatenated coding yield the threshold result, that states if the noise level per elementary operation is below a threshold value, then arbitrarily long quantum computation can be achieved using faulty components [53, 47, 48, 49, 54]. Using a t-error correcting code, fault-tolerant circuits constructed from faulty gates with error rate ϵ can achieve a logical error rate of $O(\epsilon^{t+1})$ per logical gate. This fact together with the concept of concatenated coding provides a method for possible large-scale quantum computation, and can lead to the realization of a scalable quantum computer. Therefore, it is important to study fault-tolerant methods and estimate the noise threshold values. In addition, the noise threshold indicates the tolerable noise level in a certain quantum circuit, and provides a benchmark for the efficiency of QEC circuits.

A number of theoretical estimates of noise threshold and improvements for the efficiency of QEC circuits have been proposed [53, 47, 48, 49, 55, 56, 57]. In general, these analyses all based on the following *standard assumptions in QEC*: (1) uncorrelated and stochastic errors, (2) depolarizing noise channel, (3) maximal parallelism, (4) low noise level in storing qubits, (5) no leakage errors, (6) fresh supply of ancilla qubits, (7) no overhead for performing gates acting on distant pair of qubits. Realis-

tically, these assumptions are not usually applicable, and the power of fault-tolerant QEC under realistic physical conditions is still unclear (see Ref. [49] for a through examination on these assumptions). In particular, assumptions 3 and 4 are unlikely to be fulfilled in real physical systems, and these ad-hoc classical stochastic noise models all neglect device details. Classical noise models that describe the decoherence and population relaxation as exponential decays of the off-diagonal and diagonal components of the density matrix are widely used for the estimate of the error rates during quantum computation [58, 20], but generally these models lack quantum features that are important for quantum computing, such as the quantum interference effect. We emphasize that noise threshold values are of little use if limitations of the physical implementation and realistic noise sources are not considered in the estimation. Therefore, it is of importance to study fault-tolerant QEC circuits using a noise model that reflects realistic device conditions.

In this section, the generalized HSR equation of motion is applied to investigate the performance of fault-tolerant QEC circuits implementing three qubit bit-flip code and five-qubit code. Relatively small codes are studied because we perform a systematic investigation on several variables that can affect the performance of fault-tolerant QEC circuits. In section 5.4.1 we first present the model Hamiltonian we used to implement quantum gates, and briefly review the noise model we proposed. The stochastic Liouville equation approach we used allows us to use a more realistic noise model and avoid standard assumptions 2, 3, and 4. We then introduce the fault-tolerant QEC circuits studied in this work in section 5.4.3, and show our estimates of noise threshold in section 5.4.4. Finally, we go beyond standard QEC and perform a systematic study on how factors like imperfect measurement, collective bath, repetition protocol, and level of parallelism affect the performance of fault-tolerant QEC in section 5.4.5. This theoretical study will be useful for the design and implementation of fault-tolerant QEC circuits.

5.4.1 Interactions and Noise Model

We study the performance of fault-tolerant QEC circuits using the stochastic Liouville equation described in Chapter 4 [59]. In this model, a n-qubit system is described by a Hamiltonian with a controlled part and a time dependent stochastic part. The general Hamiltonian of the qubit system can be written as ($\hbar = 1$)

$$\mathbf{H}(t) \;=\; \mathbf{H}_0(t) + \mathbf{h}(t), \tag{5.23}$$

where the controlled Hamiltonian $\mathbf{H}_0(t)$ describes the interactions between qubits, and the stochastic part $\mathbf{h}(t)$ describes the fluctuations of the interactions due to the coupling to the environment. During the process of quantum computation, $\mathbf{H}_0(t)$ is controlled to implement gate operations, whereas $\mathbf{h}(t)$ is stochastic and results in the decoherence of the quantum system.

We choose to simulate fault-tolerant QEC circuits using a model control Hamiltonian with single-qubit X, Z and two-qubit ZZ interactions:

$$\mathbf{H}_0(t) = \sum_{i=1}^{n} \varepsilon_i(t) Z_i + \sum_{i=1}^{n} J_i(t) X_i + \sum_{i=1, j<i}^{n} g_{ij}(t) Z_i Z_j, \tag{5.24}$$

where Z_i and X_i are Pauli operators acting on the i-th qubit, and $\varepsilon_i(t)$, $J_i(t)$, and $g_{ij}(t)$ are controllable parameters that can be turned on and off to implement desired gate operations. For simplicity, all gate operations are simulated using step function pulses with field strengths set to 1 (uniform field strengths), and the "on-time" of each pulses are controlled to obtain the desired unitary transformations. Note that by doing so we adopt a dimensionless system in which a unit time scale Δt is defined by the field strength ε, i.e. $\Delta t = 1/\varepsilon$. We consider fault-tolerant QEC circuits composed of single-qubit bit-flip (X), phase-flip (Z), Hadamard (H) gates, two-qubit controlled-Z and controlled-NOT gates, plus measurement of a single qubit in the computational basis. All these operations can be easily implemented using the model Hamiltonian in Eq. (5.24). Figure 5-7 shows the gate symbols and corresponding unitary transformations used in our simulations. More complicated transformations

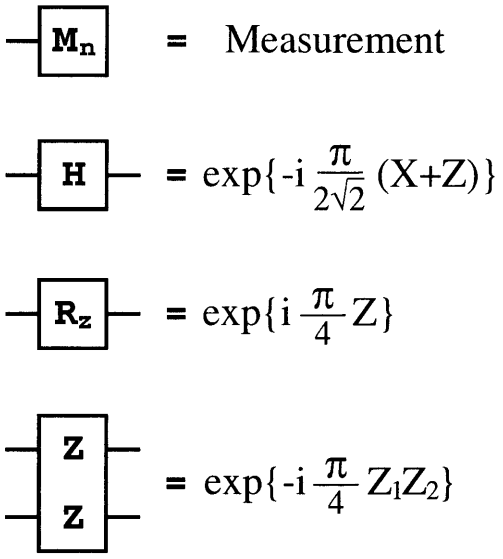

Figure 5-7: Quantum gate symbols used to denote unitary transformations implemented with single-qubit X, Z and two-qubit ZZ interactions. Here, physical qubits are depicted by horizontal solid lines, and quantum gates are represented by boxes.

such as controlled-Z and controlled-NOT gates can be trivially constructed using these elementary gates, see Figure 5-8.

Note that the set of quantum gates we use is not sufficient for universal quantum computation. To address the noise threshold of universal quantum computation, implementations of more complicated quantum gates such as the logical Toffoli gate (controlled-controlled-NOT) or the logical $\pi/8$ gate ($\pi/4$ rotation about the Z-axis) have to be considered [52, 31]. However, quantum circuits implementing these non-trivial gates are more complicated and do not directly relate to QEC. In addition, analysis on the noise threshold of the fault-tolerant Toffoli gate has shown that with proper arrangement of QEC blocks, the presence of Toffoli gates only causes minor reduction in the threshold value [54]. Therefore, to demonstrate our methodology and the effect of fault-tolerant QEC, we will focus on quantum circuits performing fault-tolerant QEC and calculate the noise threshold for quantum memory and logical X gate in this paper. All the fault-tolerant QEC circuits studied in this section can be implemented using the set of quantum gates shown in Figure 5-7.

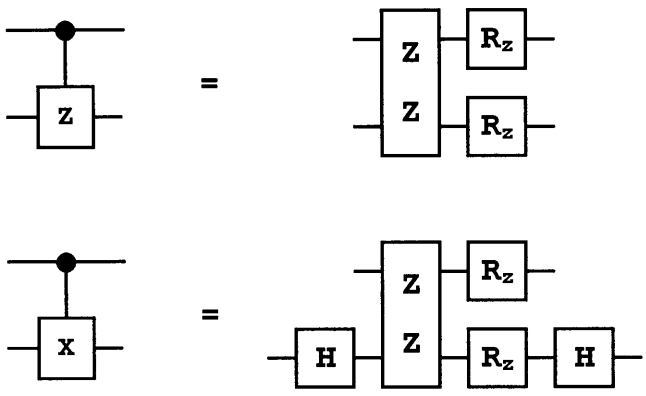

Figure 5-8: Constructions used to implement controlled-Z (upper one) and controlled-NOT (bottom one) gates. The definitions of elementary gates are shown in Figure 5-7.

We adopt the ZZ type two-qubit coupling in our model Hamiltonian for an illustrative purpose. Although, Hamiltonian in this form can be implemented in many solid-state systems [15, 17], the real form of the inter-qubit interaction depends on the controllable interactions available for each individual physical implementations. Nevertheless, our model can handle the other types of interactions as well, and we expect that the model Hamiltonian we use here can reproduce the same general physical behavior as other two-qubit Hamiltonians.

The dissipative dynamics of the system is governed by the stochastic part $\mathbf{h}(t)$. We consider the fluctuations as random Gaussian Markov processes with zero mean and δ-function correlation times:

$$\begin{aligned} \langle h_{ij}(t) \rangle &= 0, \\ \langle h_{ij}(t) h_{kl}(t') \rangle &= R_{ij;kl} \cdot \delta(t - t'), \end{aligned} \tag{5.25}$$

where bracket $\langle\rangle$ means averaging over the stochastic variables, and the time independent correlation matrix element $R_{ij;kl}$ describes the correlations between $h_{ij}(t)$ and $h_{kl}(t')$. In this section, we consider the following form of fluctuations:

$$\mathbf{h}(t) = \sum_i \delta\varepsilon_i(t) Z_i + \sum_i \delta J_i(t) X_i, \tag{5.26}$$

where $\delta\varepsilon_i(t)$ and $\delta J_i(t)$ describe the time-dependent diagonal and off-diagonal fluctuations on the i-th qubit, respectively. This corresponds to stochastic single-qubit phase (Z) and bit-flip (X) errors on each individual qubit. In addition, we consider the fluctuations described by the following set of equations:

$$\begin{aligned} \langle \delta\varepsilon_i(t) \rangle &= \langle \delta J_i(t) \rangle = 0, \\ \langle \delta\varepsilon_i(t)\delta\varepsilon_j(t') \rangle &= \gamma_0 \cdot \delta_{ij}\delta(t-t'), \\ \langle \delta J_i(t)\delta J_j(t') \rangle &= \gamma_1 \cdot \delta_{ij}\delta(t-t'), \\ \langle \delta\varepsilon_i(t)\delta J_j(t') \rangle &= 0, \end{aligned} \tag{5.27}$$

where γ_0 and γ_1 describe the strength of the diagonal energy fluctuations and off-diagonal matrix element fluctuations, respectively. For a free single-qubit system ($\varepsilon = J = 0$), γ_0 and γ_1 are well-defined physical quantities, i.e. γ_0 and γ_1 are population relaxation rate and pure dephasing rate, respectively [59]. Note that noise strengths γ_0 and γ_1 should be interpreted as the error rate per unit time scale $\Delta t = 1/\varepsilon$, where ε is the strength of the control fields. Also notice that we treat the correlation between different qubits independently, which means each qubit in the system is coupled to a distinct environment (bath). Later we will remove this constraint and examine the effect of a collective bath on the noise threshold value. We also assume that the diagonal and off-diagonal fluctuations are not correlated. Using the generalized HSR equation [Eq. (4.4)], the time evolution of the qubit system can be obtained by numerically propagating the density matrix of the system using the equations of motion. In our numerical simulation, the density matrix of a system with up to twelve qubits can be easily propagated (bound by the size of physical memory on a personal computer). This method provides an efficiently way to simulate quantum circuits and obtain full dynamics of the qubit system.

For simplicity, we assume that the noise strengths are uniform, i.e. γ_0 and γ_1 are constants. The noise strength is set to be the same on all qubits at all times, therefore, we do not distinguish storage and gate errors. By assuming that the storage and gate errors are at the same level, the uniform noise assumption overestimates the errors in the system. At the same time it also avoids the weak storage noise assumption

usually made in standard QEC. This uniform noise assumption also partly addresses the standard QEC assumption of no overhead for gates acting on distant pair of qubits. Realistically, to perform a quantum gate between two distant qubits in a large-scale quantum circuit, multiple quantum swap gates must be employed to shuffle quantum states around [60]. Our uniform noise assumption reflects the physical condition in this scenario. Note that the assumption of uniform noise strengths is not required in our model; more complex setups, in which control field and noise strengths are different for each individual qubits, can be studied with exactly the same method.

Although our noise model also assumes uncorrelated and stochastic fluctuations, it is different from classical noise models usually used in standard QEC analyses. The generalized HSR equation treats coherent evolution and incoherent dynamics at the same time, thus includes interference effect between different noise channels and the controlled Hamiltonian $\mathbf{H}_0(t)$. These effects do not exist in classical noise models applied in standard QEC analyses. In addition, our numerical simulation propagates the full density matrix of the system in time, hence the effect of noise is naturally followed by studying the continuous time evolution of the system. Therefore, our method takes into account the state dependent dissipation and dephasing rates as well as correct propagation of errors in quantum circuits. In standard QEC analyses, state dependent properties are usually ignored, and the propagation of errors is usually included using calculations that requires additional approximations [53, 47, 48, 49, 55, 56, 57]. As a result, our noise model not only provides a greater flexibility for including device conditions, but is also a more realistic description than classical noise models.

5.4.2 Quantum Error-correcting Codes

The discovery of quantum error-correcting codes enables us to protect quantum information by encoding [61, 62, 63, 54]. We choose to investigate fault-tolerant QEC circuits implementing the three qubit bit-flip code and five qubit code, because they are relatively small and allow us to perform systematic studies. Previous studies on the fault-tolerant QEC have been mainly focused on Calderbank-Shor-Steane (CSS)

codes, especially the CSS [[7,1,3]] code [62, 63, 55]. Because fault-tolerant encoded operations on CSS codes are easy to implement, CSS codes are expected to be more useful for quantum computation than the three qubit bit-flip code and five qubit code. Nevertheless, since we focus on variables affecting the performance of fault-tolerant QEC circuits, we expect that results gained in our study can be applied to more general codes. We first introduce these two quantum error-correcting codes in this subsection.

5.4.2.1 Three qubit bit-flip code

The three qubit bit-flip code encodes a logical qubit in three physical qubits using the following logical states:

$$\begin{aligned} |0_L\rangle &= |000\rangle, \\ |1_L\rangle &= |111\rangle. \end{aligned}$$

This code is a stabilizer code with two stabilizer operators $g_1 = ZZI$ and $g_2 = IZZ$. It is easy to verify that any encoded state $|\psi\rangle = c_0|0_L\rangle + c_1|1_L\rangle$ is an eigenstate of both g_1 and g_2 with $+1$ eigenvalue, i.e. $g_n|\psi\rangle = |\psi\rangle$. The $|0_L\rangle$ and $|1_L\rangle$ basis span the encoding subspace, and the two stabilizers can be used to check whether a state is in the encoding subspace or not.

The three qubit bit-flip code corrects single bit-flip error on any of the three encoding qubits. This code does not correct phase errors, therefore it is only useful when the degradation of the quantum state is dominated by bit-flip errors. However, we believe insights gained by studying this code can be applied to more general quantum error-correcting codes.

Figure 5-9 shows a quantum error-correcting circuit for the three qubit bit-flip code. In this circuit, physical qubits are represented by horizontal solid lines, and quantum gates are represented by boxes. The first three qubits from the bottom are data qubits that take a encoded state as the input, and the fourth and fifth qubits are ancilla qubits that are used to measure the syndromes. The circuit can be divided into a syndrome detection part and a recovery part. The syndrome detection part uses

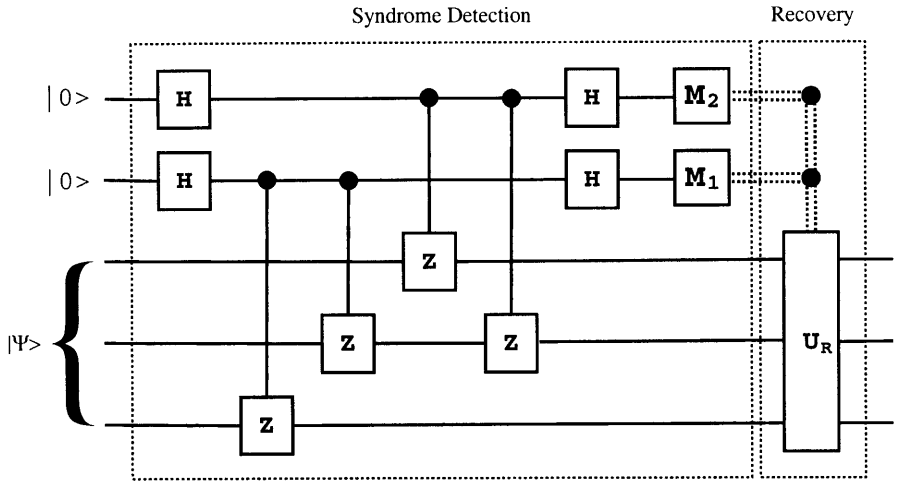

Figure 5-9: A quantum error-correcting circuit for the three qubit bit-flip code. The codewords are $|0_L\rangle = |000\rangle$ and $|1_L\rangle = |111\rangle$. Two stabilizer operators are $g_1 = ZZI$ and $g_2 = IZZ$.

several controlled-stabilizer gates to transfer the information about the errors to the ancilla qubits: the first two controlled-Z gates implement a controlled-g_1 gate, and the following two controlled-Z gates implement a controlled-g_2 gate. The controlled-stabilizer gates effectively perform parity check on the data qubits, and measurements M_1 and M_2 reveal the parity check results against the stabilizer $g_1$and g_2, respectively. The outcome of M_1 and M_2 indicates the error syndrome on the data qubits, and the recovery part can then apply the corresponding action to correct the error. Table 5.2 lists the syndrome and the corresponding recovery actions for the three qubit bit-flip code.

5.4.2.2 The five-qubit code

The five-qubit code is the smallest quantum code that corrects all single-qubit errors [64, 65]. This code encodes a logical qubit in five physical qubits using the following logical states:

Table 5.2: Measurement results and the corresponding actions required to correct the error in the data qubit for the three qubit bit-flip code.

Syndrome		Action[a]
M_1	M_2	U_R
0	0	I
0	1	X_3
1	0	X_1
1	1	X_2

[a]The subscript denotes the qubit to be corrected.

$$
\begin{aligned}
|0_L\rangle &= \frac{1}{4}\{|00000\rangle + |10010\rangle + |01001\rangle + |10100\rangle \\
&\quad +|01010\rangle - |11011\rangle - |00110\rangle - |11000\rangle \\
&\quad -|11101\rangle - |00011\rangle - |11110\rangle - |01111\rangle \\
&\quad -|10001\rangle - |01100\rangle - |10111\rangle + |00101\rangle\}, \\
|1_L\rangle &= \frac{1}{4}\{|11111\rangle + |01101\rangle + |10110\rangle + |01011\rangle \\
&\quad +|10101\rangle - |00100\rangle - |11001\rangle - |00111\rangle \\
&\quad -|00010\rangle - |11100\rangle - |00001\rangle - |10000\rangle \\
&\quad -|01110\rangle - |10011\rangle - |01000\rangle + |11010\rangle\}.
\end{aligned}
$$

The four stabilizers of the five qubit code is listed in Table 5.3 along with the logical bit-flip ($\bar{X}$) and phase ($\bar{Z}$) gates. It is easy to verify that the logical $\bar{X}$ operator flips the logical state, $\bar{X}|0_L\rangle = |1_L\rangle$, and the logical $\bar{Z}$ operator changes the phase of $|1_L\rangle$ while leaving $|0_L\rangle$ intact. The QEC circuit for the five-qubit code can be easily constructed from the stabilizers [6]. Table 5.4 shows the syndromes and recovery actions for the five qubit code.

Table 5.3: Stabilizers and logical bit-flip ($\bar{X}$) and phase ($\bar{Z}$) operators for the five qubit code

Name	Operators
g_1	XZZXI
g_2	IXZZX
g_3	XIXZZ
g_4	ZXIXZ
logical $\bar{X}$	XXXXX
logical $\bar{Z}$	ZZZZZ

Table 5.4: Syndromes and the corresponding actions required to correct the error in the data qubit for the five qubit code.

Syndrome				Action
g_1	g_2	g_3	g_4	U_R
0	0	0	0	I
0	0	0	1	X_1
0	0	1	0	Z_3
0	0	1	1	X_5
0	1	0	0	Z_5
0	1	0	1	Z_2
0	1	1	0	X_4
0	1	1	1	Y_5
1	0	0	0	X_2
1	0	0	1	Z_4
1	0	1	0	Z_1
1	0	1	1	Y_1
1	1	0	0	X_3
1	1	0	1	Y_2
1	1	1	0	Y_3
1	1	1	1	Y_4

5.4.3 Fault-Tolerant QEC Circuit

Although quantum error-correcting codes can correct errors that occur during the storage of qubits, they are unable to protect against errors due to faulty quantum gate operations because multiple-qubit gates can propagate errors and result in uncorrectable erroneous states. For example, imagine that an error happens in the first ancilla qubit in Fig. 5-9 before the ancilla qubit interacts with the data qubits. Because the same ancilla is used twice, the error will propagate to two data qubits through the controlled-Z gates, and render both data qubits erroneous. As a result, a single qubit error, which is correctable under the QEC code, propagates and generates uncorrectable multiple qubit errors. Simple quantum error-correction is helpless against errors in quantum computation.

A significant achievement in the theory of quantum computation is the discovery of fault-tolerant methods [51]. In the framework of fault-tolerant quantum computation, a quantum error-correcting code is used to encode the quantum information in its logical states (data qubits), and quantum computation is performed directly on the encoded level without decoding. In addition, quantum gates have to be implemented *fault-tolerantly,* meaning that a single error happening during a fault-tolerant operation will not lead to more than one error in the outgoing data qubits. Therefore, with high probability errors due to faulty gate operations can be corrected in the subsequent QEC step. By constantly applying fault-tolerant QEC to the data qubits, the accumulation of errors can be decreased. A good introduction to the principle of fault-tolerant QEC can be found in Ref. [49] and [54]. In this subsection, we present the general scheme and the constructions of the quantum circuit that we apply to perform fault-tolerant QEC. For readers from outside the field, a discussion about the idea of fault-tolerance is given in the Appendix 5.B.

5.4.3.1 Fault-tolerant QEC scheme

We adopt the fault-tolerant QEC scheme proposed by DiVincenzo and Shor [51]. Their protocol utilizes cat states[4] and transversal controlled-X/Z gates to detect error syndromes and achieve fault-tolerance. The use of cat states and transversal gates ensures that the same physical ancilla qubit is never used twice, thus the propagation of uncorrectable errors can be controlled. The fault-tolerant QEC procedure is divided into three different stage: (1) ancilla preparation and verification, (2) syndrome detection, and (3) recovery.

Entangled states are required to detect syndrome fault-tolerantly. To ensure fault-tolerance, ancilla cat states are used to perform transversal controlled-X/Z operations to transfer information about the errors from the data qubits to the ancilla qubits. After decoding the ancilla state, projective measurement is then applied to obtain error syndromes. Because there are more gates in the circuits than the number of measurements, it is reasonable to assume that measurement has smaller effect on the threshold result. Therefore, we assume perfect measurement at first. Later we will study the effect of imperfect measurements.

To ensure that we do not accept a wrong syndrome and mistakenly apply bit-flip or phase-flip gates on the data qubits, we must repeat syndrome detection and take a majority vote. Following Shor's protocol [51], the following repetition scheme is used:

[4]The cat states are maximally entangled states with the form $|\psi\rangle = \frac{1}{\sqrt{2}}(|00...0\rangle + |11...1\rangle)$.

Repetition Protocol A (three majority vote):

1. Perform the syndrome detection twice. If the same measurement results are obtained, the syndrome is accepted and data qubits are corrected.

2. Otherwise, perform one more syndrome detection. If any two of the three measurement results are the same, the syndrome is accepted and data qubits are corrected.

3. If all three measurement results are different, no further action is taken.

This protocol is basically a simple majority vote in three trials. Note that the choice of the repetition protocol is not unique. In fact, later we will compare protocol A to another protocol, and show that we can improve the repetition protocol to increase the efficiency of the fault-tolerant QEC procedure. After a syndrome is detected and confirmed by the repetition protocol, a final recovery operation is carried out to correct the detected error in the data qubit. This completes a fault-tolerant QEC step.

The DiVincenzo-Shor protocol ensures that a single error during the fault-tolerant procedure only leads to a single-qubit error in the outgoing data qubits. As a result, all multiple-qubit errors in the outgoing data qubits must be due to multiple error events during the QEC procedure; these multiple error events are less possible to happen. For example, if the fault-tolerant circuit is constructed from faulty gates with error probability ϵ, the probability of generating a two-qubit error, i.e. a two-error event, is of order ϵ^2. In fault-tolerant quantum computation, we constantly perform the fault-tolerant QEC on the data qubits. As a consequence, single-qubit errors in earlier computation and QEC steps will be corrected in later QEC steps with high probability (suppose a single-error correcting code is used). Therefore, single-qubit errors would not accumulate during the process of computation; only multiple-qubit errors will accumulate at a rate of $O(\epsilon^2)$. In consequences, we can achieve longer computation when ϵ is small.

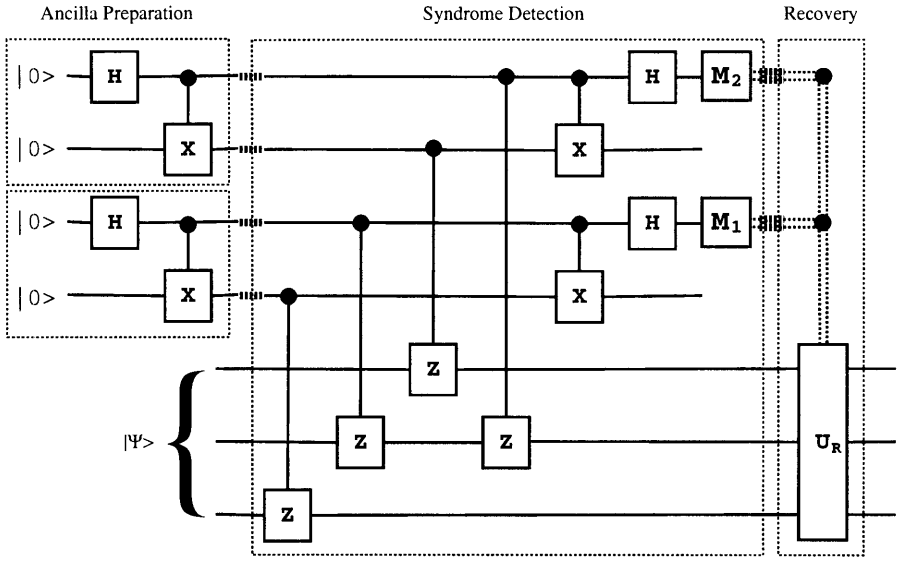

Figure 5-10: The fault-tolerant circuit for a QEC step using the three qubit bit-flip code. Note that to ensure the fault-tolerant condition, the syndrome detection have to be repeated for several times, and then take the result of a majority vote. Also notice that the ancilla preparation and verification of the ancilla states can be done off-line.

5.4.3.2 Three qubit bit-flip code

Figure 5-10 shows the fault-tolerant QEC circuit for the three qubit bit-flip code. Compared to the circuit in Fig. 5-9, the fault-tolerant version utilizes entangled ancilla states and transversal gate operations to achieve fault-tolerance. The quantum circuit includes two pairs of ancilla qubits that will be prepared in the Bell state $\frac{1}{\sqrt{2}}(|00\rangle + |11\rangle)$ and used to measure the syndromes. Note that the Bell state is invariant under correlated bit-flip errors (i.e. XX), therefore no ancilla verification step is needed.

Figure 5-11 shows the syndrome detection circuit in detail. We want to point out that only limited ability to perform operations in parallel is assumed in constructing this circuit. In addition, by arranging two-qubit ZZ gate in front of single-qubit R_z gate, the circuit minimizes error propagation from the ancilla qubits to the data qubits. At the end of the circuit, two measurements, M_1 and M_2, are performed

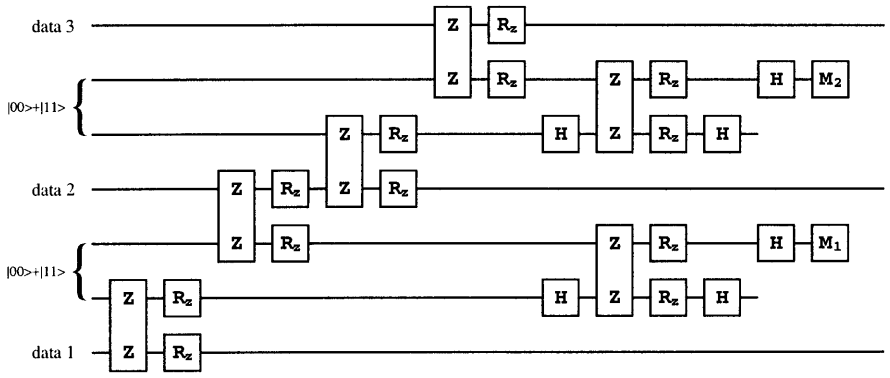

Figure 5-11: A circuit implementing the fault-tolerant syndrome detection for the three qubit bit-flip code.

to obtain the error syndrome. After the syndrome is confirmed according to the repetition protocol A, we then apply the corresponding recovery action to correct the detected error according to Table 5.2.

Because the three qubit bit-flip code only corrects bit-flip errors, we only consider off-diagonal fluctuations on each qubit when dealing with this code ($\gamma_0 = 0$). Note that the circuit does not protect against Z errors, nor can it prevent the generation of Z errors. To access its performance on controlling X errors on the data qubits, we study the fault-tolerant QEC procedure only when the data qubits are initially in the logical $|0_L\rangle$ state. In our model, using the logical $|1_L\rangle$ state as the initial state will give the same result. This selection of initial state is unrealistic, but it allows us to avoid uncorrectable Z errors that will ruin the QEC procedure.

5.4.3.3 The five-qubit code

A scheme for fault-tolerant quantum computation using five-qubit code is presented by Gottesman in Ref. [52]. In this work, we adopt the representation and fault-tolerant QEC circuit presented by DiVincenzo and Shor in Ref. [51]. Their implementation uses a nine-qubit system with five data qubits and four ancilla qubits, which utilizes four-qubit cat state $\frac{1}{\sqrt{2}}(|0000\rangle + |1111\rangle)$ for syndrome detection. Moreover, four syndromes are detected by operator-measuring the four stabilizers sequentially. It is

straightforward to simulate the syndrome detection circuit presented in their paper using our choice of model Hamiltonian (Eq. 5.23-5.27). More details about the fault-tolerant quantum circuit we used to prepare the four-qubit cat state is presented in Appendix 5.C.

Ideally, multiple input states have to be studied to obtain averaged performance of the QEC procedure. To avoid such tedious computations, we use a logical qubit initially in the following pure state density matrix (in the $\{|0_L\rangle, |1_L\rangle\}$ basis):

$$\rho_0 = \frac{1}{2}(I + \frac{1}{\sqrt{3}}X + \frac{1}{\sqrt{3}}Y + \frac{1}{\sqrt{3}}Z).$$

This state provides an averaged measure for all possible logical states, thus should give us a reasonable estimate of the averaged circuit performance.

The quantum circuit implementing the decoding, error-correction, and decoding of the five-qubit code has been studied experimentally using a NMR quantum computer with five qubits [66]. Note that our setup simulates a minimal circuit for the fault-tolerant QEC using five-qubit code with limited physical resources. We expect such nine-qubit system can be realized on a liquid-state NMR quantum computer using available technologies. An experimental study on such minimal fault-tolerant QEC circuit will be an excellent test for our noise model, and can also provide us invaluable information that is essential for the design of large-scale quantum computers.

5.4.4 Estimate of Noise Threshold

To estimate the noise threshold for a logical operation, we simulate a computation in which fault-tolerant QEC is performed after each logical operation on the encoded qubits, and compare the magnitude of logical errors to the magnitude of errors generated by the same operation on a bare physical qubit without QEC. We use the crash probability P_c to describe the amount of logical errors in an encoded state [56]. The crash probability is defined as the probability of having an uncorrectable error in the data qubits, and can be obtained from the fidelity of the state *after a perfect QEC process*. For the single-error correcting codes used in this section, the crash

probability P_c equals to the probability of having more than one error in the data qubits.

We define a computational step as a logical gate followed by a fault-tolerant QEC step. If the same computational step is applied repeatedly on the data qubits n times, we can describe the crash probability as a function of n, i.e. $P_c = P_c(n)$. In general, $P_c(n)$ satisfies an exponential form:

$$P_c(n) = \frac{1}{2}(1 - e^{-2\Gamma_n n}). \tag{5.28}$$

We can perform simulation and compute crash probability at each step, $P_c(n)$. By fitting our simulation result to the functional form in Eq. (5.28), we obtain the crash rate constant per computational step $\Gamma_n = \left.\frac{dP_c(n)}{dn}\right|_{n=0}$. In addition, we also define the crash rate constant per unit time $\Gamma_t = \left.\frac{dP_c(t)}{dt}\right|_{t=0} = \Gamma_n/\tau$, where τ is the time period required to complete a computational step. Note again that the unit time scale Δt is defined by the strength of control fields ε, $\Delta t = 1/\varepsilon$.

We compute noise threshold for a quantum memory, where repeated fault-tolerant QEC is applied on the data qubits to stabilize quantum information; and logical X gate, where a logical X gate followed by a fault-tolerant QEC step are applied on the data qubits. Figure 5-12 shows the crash rate constants as a function of noise strength for the three qubit bit-flip code, as well as the results for the five-qubit code. In Fig. 5-12, we clearly see that in the weak noise regime, the crash rate constant is proportional to the square of the noise strength. This is the standard result of fault-tolerant QEC using single-error correcting codes, and reflects the power of the fault-tolerant QEC procedures. The noise threshold can be obtained from the critical value at which the crash rate constant for encoded computation crosses over with the error rate of a bare physical qubit. At noise strength below the threshold value, the errors in the encoded state accumulated slower than for the bare physical qubit. At noise strength above the threshold value, the fault-tolerant QEC provides no benefit. For the three qubit bit-flip code, the noise threshold is about 2×10^{-2} for quantum memory, and about 1×10^{-3} for the logical X gate.

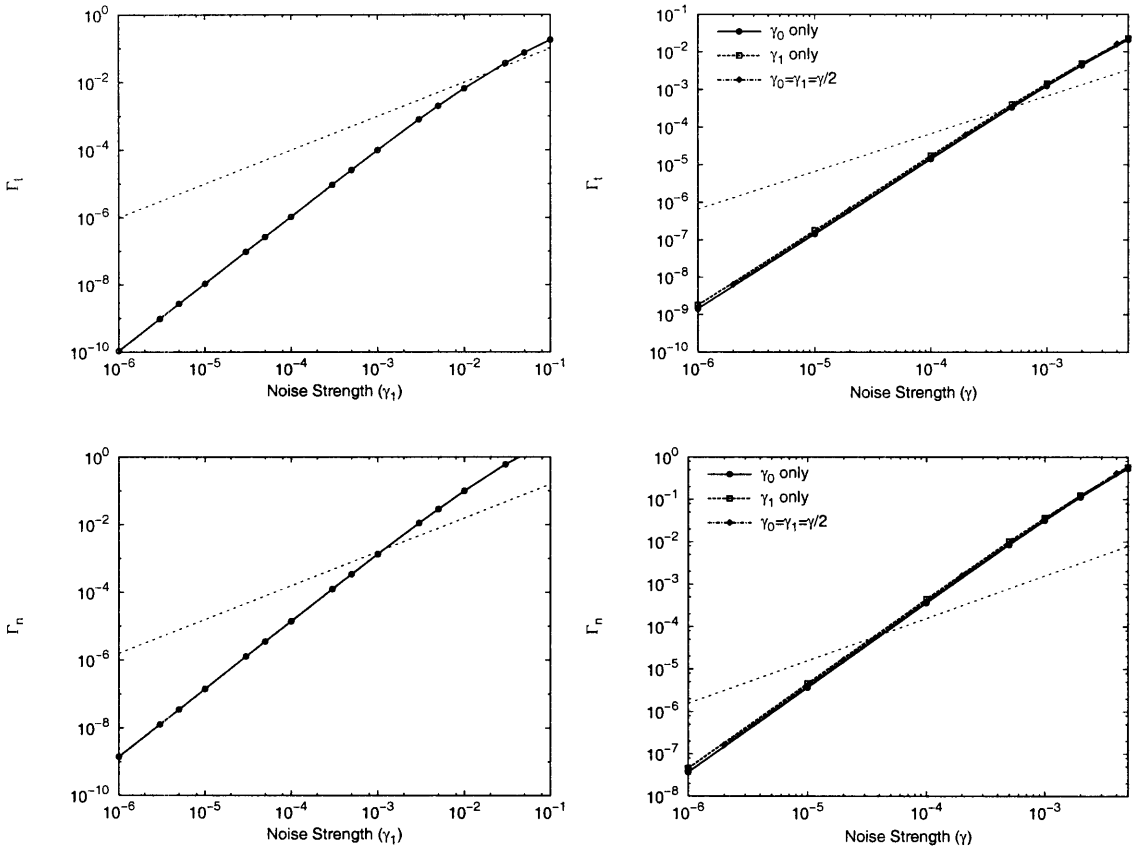

Figure 5-12: Crash rate constants as a function of the noise strength. We show crash rate constants for a quantum memory using the three qubit bit-flip code (upper-left) and five-qubit code (upper-right), and for a logical X gate on the three qubit bit-flip code (bottom-left) and on the five-qubit code (bottom-right). For the five-qubit code circuits, curves for different types of noise are presented. To show the threshold result, we also present curves for the error rate of a single physical qubit (dotted line). The noise threshold values are summarized in Table 5.5.

We also perform calculations on five-qubit code. Table 5.5 summarizes threshold values for three qubit bit-flip code and five-qubit code. The five-qubit code corrects all single-qubit errors, so we can compute the threshold for different types of noise. Clearly, there exist minor differences between noise thresholds for different types of noise. This result indicates that correcting different types of errors requires different amount of resources, and suggests that by choosing different computational basis, one can minimize the effect of noise and the required amount of resources for error-correcting.

In addition, the noise threshold of a quantum memory is about an order of magnitude higher than the threshold of a logical $\bar{X}$ gate. A closer look indicates that the difference is mainly due to the different basis of comparison. For the quantum memory, we must compare crash rate constant per unit time Γ_t to the decay rate of a free physical qubit; however, for the X gate, we need to use the crash rate constant per computational step Γ_n. The extra logical $\bar{X}$ operation has little effect on the crash rate per computational step because the fault-tolerant QEC circuit is much larger than the circuit for the logical $\bar{X}$ gate. This observation suggests that other encoded single-qubit operations and transversal encoded two-qubit operations should have similar threshold values. Note that noise thresholds of quantum memory and logical $\bar{X}$ gate calculated in this section is only an upper bound to the noise threshold of universal quantum computations, which is probably determined by the implementations of non-trivial gates.

For the five-qubit code, our estimate of the noise threshold is about 4×10^{-5} for the logical $\bar{X}$ gate. Previous threshold calculations have all adopted CSS codes. For comparison, we have followed Gottesman's analysis in Ref. [54] and calculated thresholds of the three qubit bit-flip code and the five-qubit code. Following Gottesman's model, we estimated for the five-qubit code a threshold of 10^{-3} when storage errors are negligible, and 2×10^{-4} when the strength of storage errors are equal to gate errors. These values cannot be compared directly to our threshold estimates because the definitions of unit time and error rates are different. Nevertheless, we can draw useful observations from the comparison. Clearly, the limited parallelism

Table 5.5: Summary of noise threshold values. The noise strengths (γ_0 and γ_1) should be interpreted as the error rate per unit time scale $\Delta t = 1/\varepsilon$, where ε is the strength of the control fields. For comparison, thresholds obtained from a classical noise model are listed in the parentheses. These numbers are obtained by following Gottesman's analysis in Ref. [54], and all standard QEC assumptions mentioned on page 175 are applied.

	three qubit bit-flip code		five-qubit code	
	memory	X gate	memory	X gate
X errors (γ_1)	2.1×10^{-2}	1.2×10^{-3} (5.8×10^{-3})	4.2×10^{-4}	3.5×10^{-5}
Z errors (γ_0)	-	-	5.1×10^{-4}	4.3×10^{-5}
Both X and Z errors	-	-	4.7×10^{-4}	3.9×10^{-5} (1×10^{-3})

in the circuits and the uniform noise assumption that treats gate errors and storage errors on the same footing are responsible for the significantly lower threshold we have obtained for the five-qubit code. Previous calculations have indicated that including storage errors would decrease the threshold value by almost an order of magnitude. Our result implies that without maximal parallelism, there is an order of magnitude reduction on the threshold.

We summarize the assumptions we made for these calculations: (1) stochastic and uncorrelated X and Z noises, (2) each qubit coupled to a distinct bath, (3) uniform noise strength, (4) perfect physical $|0\rangle$ states as initial states, (5) no leakage errors, (6) no overhead for performing gates acting on distant pair of qubits, (7) perfect instantaneous projective measurement. Compared to the standard assumptions in QEC, we do not assume maximal parallelism and weak storage errors. In addition, our calculations include real construction of quantum gates. Note that up to this point we have basically reproduced the standard results of fault-tolerant QEC using a more realistic noise model. In the next section we will study factors that are usually overlooked in standard QEC analyses, and examine how these factors affect the performance of fault-tolerant QEC.

5.4.5 Efficiency of Fault-tolerant QEC Circuits

In this subsection, we study several variables that can affect the efficiency of the fault-tolerant QEC scheme. The effects of these variables are usually overlooked in standard noise threshold analyses. We perform a systematic investigation on the performance of quantum memories stabilized by fault-tolerant QEC and aim to generate a generic picture on how these variables quantitatively change the efficiency of fault-tolerant QEC circuits. Because our noise model can provide a quantitative description of the efficiency of fault-tolerant QEC circuits including realistic device conditions, the method applied here can be used to benchmark different quantum circuits and search for optimal circuit design for real physical implementations.

5.4.5.1 Effect of imperfect measurement

Previous studies on the noise threshold of fault-tolerant QEC typically treat the measurements as simple one qubit operations [53, 48, 49, 55]. Recently, Steane has studied the effect of measurement time and found that long measurement time can significantly reduce the noise threshold [56]. Here we test another type of errors due to measurement, namely projecting to an incorrect state due to imperfect measurement. We assume the measurement is instantaneous, and use the following POVM (positive operator-valued measure) to describe an imperfect projective measurement on a single qubit:

$$\begin{aligned} M_0 &= (1-\eta)|0\rangle\langle 0| + \eta|1\rangle\langle 1|, \\ M_1 &= (1-\eta)|1\rangle\langle 1| + \eta|0\rangle\langle 0|, \end{aligned}$$

where M_0 (M_1) describes events in which basis state $|0\rangle$ ($|1\rangle$) is measured, and η is the probability of measurement error, i.e. a projection onto the wrong basis state. Figure 5-13 shows curves for the crash rate constant per unit time Γ_t at different probabilities of measurement errors for a quantum memory implementing the three qubit bit-flip code. Clearly, Γ_t is insensitive to the measurement errors even when the probability of measurement errors is significantly higher than the noise strength γ_1. The probability of the measurement error as high as 5% has only minor effect on the threshold value. This result suggests that a short and less accurate measurement is preferable to a long one.

5.4.5.2 Effect of a collective bath

A distinct feature of our noise model is the ability to describe the effect of a collective bath, in which all qubits are coupled to the same environment. Such an environment is relevant in physical implementations such as trapped-ion quantum computers, where qubits are coupled to the same collective phonon modes [67, 68]. The effect of a collective bath on the fault-tolerant QEC is an interesting topic. Because a collective bath seems to contradict the idea of uncorrelated and stochastic errors that is

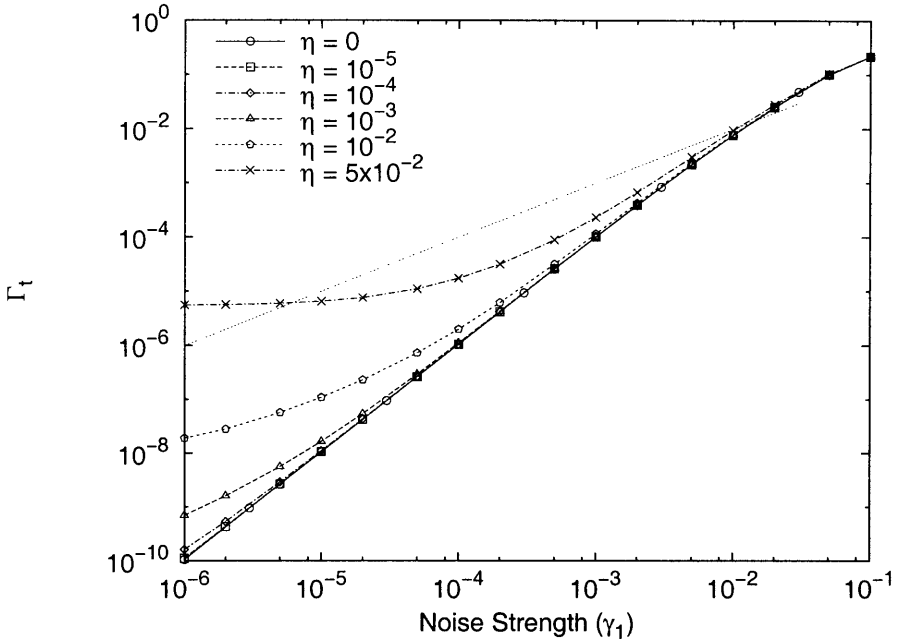

Figure 5-13: Γ_t as a function of noise strength for the fault-tolerant QEC circuit using three qubit bit-flip code at different level of measurement errors. The error rate of a single physical qubit is also shown (dotted line). The measurement error has little effect on the threshold value.

the foundation of fault-tolerant QEC, several authors have suggested that collective decoherence has to be avoided for fault-tolerant quantum computing [49, 69]. Also, in a collective bath the effects of noise on different qubits add coherently; as a result, superdecoherence states exist, and might affect the efficiency of fault-tolerant QEC [20].

To address this question, we simulate the fault-tolerant QEC circuit for the three qubit bit-flip code using a noise model in which all qubits are coupled to a common bath. The following forms of correlation functions for the stochastic process are used:

$$\begin{aligned} \langle \delta\varepsilon_i(t) \rangle &= \langle \delta J_i(t) \rangle = 0, \\ \langle \delta\varepsilon_i(t)\delta\varepsilon_j(t') \rangle &= \gamma_0 \cdot \delta(t-t'), \\ \langle \delta J_i(t)\delta J_j(t') \rangle &= \gamma_1 \cdot \delta(t-t'), \\ \langle \delta\varepsilon_i(t)\delta J_j(t') \rangle &= 0, \end{aligned} \tag{5.29}$$

Notice that in Eq. (5.29), fluctuations on different qubits are fully correlated; this

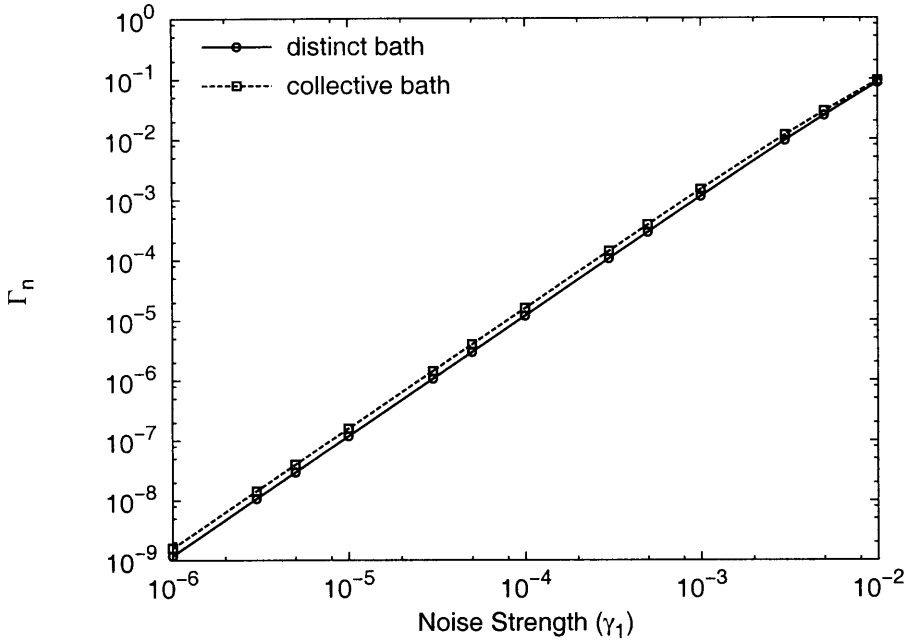

Figure 5-14: The crash rate per computational step Γ_n for the three qubit bit-flip code as a function of the noise strength. Curves for the distinct bath system (solid line) and collective bath system (dotted line) are shown. The result for the collective bath is close to the result for localized baths. This result suggests that collective bath has minor effect on the efficiency of fault-tolerant QEC.

reflects the result of coupling to a common bath. Figure 5-14 shows the crash rate constant Γ_n for quantum memories using the three qubit bit-flip code with two different types of baths. The crash rate curve for the collective bath case is only slightly higher than the curve for the localized bath, and there is no significant difference between these two lines. This result suggests that a collective Markovian bath, which exhibits spatial but not temporal correlation, has little effect on the efficiency of fault-tolerant QEC. Although superdecoherence states do exist when the system is coupled to a collective bath, they have little effect on the dynamics of the system, because those states represent only a small fraction in the whole Hilbert space. The fault-tolerant QEC circuit using the five-qubit code was also studied, and similar results were obtained.

Fault-tolerant QEC methods might not be the best way to deal with collective decoherence in quantum computation. In a collective bath setup, there exist states

that are robust against collective decoherence. These states form a subspace called decoherence-free subspace (DFS) [39, 40]. The existence of DFSs has been verified experimentally [36, 70, 71, 72]. In addition, by encoding quantum information in the DFSs and performing quantum gates that are strictly inside the DFSs, universal fault-tolerant quantum computation can be achieved without the extensive space and time overheads required for QEC [73, 74, 75]. Other proposals that utilize the properties of a collective bath include concatenation of DFS and quantum error-correcting codes [76] and supercoherent qubits [77]. These passive error preventing schemes are preferable for fault-tolerant quantum computation in collectively decoherent environments. Although our focus in this section is on QEC methods, it is worth noting that our stochastic Liouville equation approach can be used to study these collective decoherence models. In fact, in Section 5.2.1 we have theoretically demonstrated a decoherence-free state in a two-qubit system using the same approach. Moreover, in a realistic physical device such as solid state qubits, the correlation between noise on different qubits is likely to be a function of the distance between the qubits. For example, the correlations of the diagonal fluctuations might exponentially decay in space:

$$\langle \delta\varepsilon_i(t)\delta\varepsilon_j(t')\rangle = \gamma_0 e^{-|i-j|/L} \cdot \delta(t-t').$$

where L is a characteristic coherence length of the system. Our stochastic Liouville equation approach can easily model such partially collective baths, and it will be interesting to apply our approach to study DFS methods in these realistic bath conditions.

5.4.5.3 Repetition protocol

Our simulation propagates the density matrix of the system in the process of computation, therefore, we obtain the full information about the time evolution of the system. The ability to obtain the full trajectory of the qubit system is another important advantage of our simulation method. By examining the trajectory of the system

during the fault-tolerant QEC process, we find the following repetition protocol yields the best performance:

Repetition Protocol B (conditional generation):

1. Perform the syndrome detection once. If this syndrome is zero, do nothing.

2. Otherwise, perform the syndrome detection again. If the same syndrome is obtained, accept the syndrome and correct data qubits accordingly.

3. Otherwise, no further action is taken.

Figure 5-15 shows the crash rate constant Γ_n for quantum memories implementing three qubit bit-flip code using different repetition protocols. Because the majority of the measured syndromes will be zero in the weak noise regime, protocol B reduces the amount of time required for a fault-tolerant QEC step by a factor of two. As a result, the crash rate constant per computational step Γ_n decreases by a factor of two when protocol B is used. Similar improvements on the fault-tolerant QEC protocol have been suggested by other groups [78, 56, 57]. The idea behind protocol B is that the syndrome detection circuit is complicated and generates extra errors on the data qubits, therefore minimizing the number of syndrome detection and accepting a syndrome only when two consecutive detections agree on the same syndrome improve the efficiency of the fault-tolerant QEC procedure.

5.4.5.4 Level of parallelism

An important factor related to the efficiency of a QEC circuit is the level of parallelism in the circuit. The level of parallelism available is determined by the computing device, but previous threshold calculations typically ignore this issue. The syndrome detection circuit shown in Fig. 5-11 assumes a restricted level of parallelism. In fact, for a reasonable physical implementation, gate operations on different qubits might

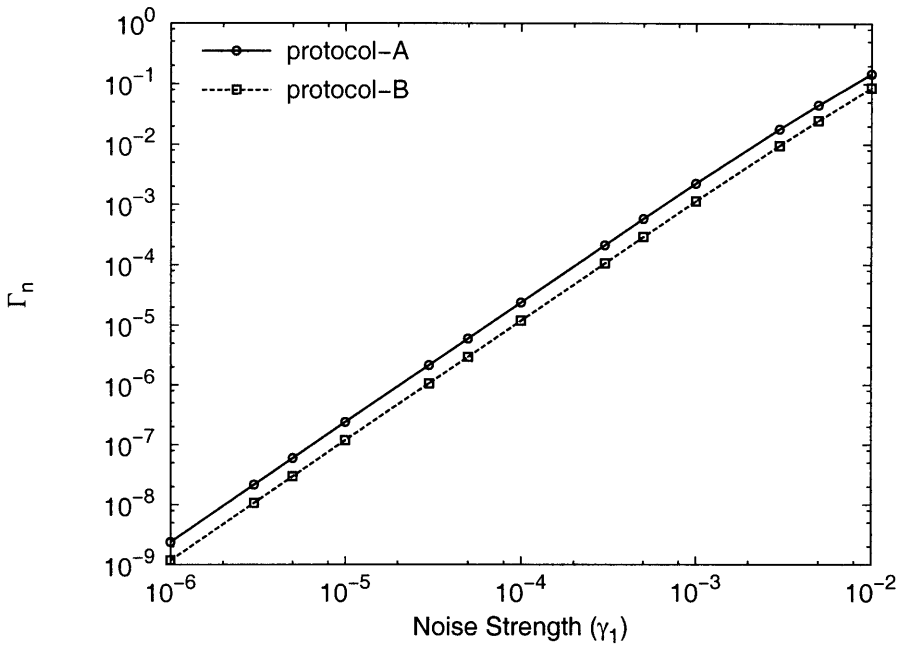

Figure 5-15: The crash rate constant per step Γ_n as a function of the noise strength for the two different repetition protocols for a quantum memory using three qubit bit-flip code. Using protocol B reduces the crash rate constant by a factor of two.

actually be operated in parallel to reduce the operation time. For example, a quantum computer implementing Kane architecture is capable of performing controlled-Z gates in parallel on different pairs of qubits [15]. Figure 5-16 shows a compressed version of the syndrome detection circuit that has increased level of parallelism.

Furthermore, because the interactions used to implement the controlled-Z gate commute with each other (Z_i and Z_1Z_2 commute), in principle the controlled-Z gate can be made in one step:

$$controlled - Z = e^{-i\pi Z_1 Z_2/4} e^{i\pi(Z_1+Z_2)/4} = e^{-i\pi(Z_1Z_2-Z_1-Z_2)/4}.$$

This makes it possible to perform a controlled-Z operation in a single pulse. This maximal parallelism design is a theoretical model used to benchmark the maximal gain available from the increase of parallelism. This design does not correspond to any physical implementation, and is a special case for our choice of model interactions (ZZ coupling).

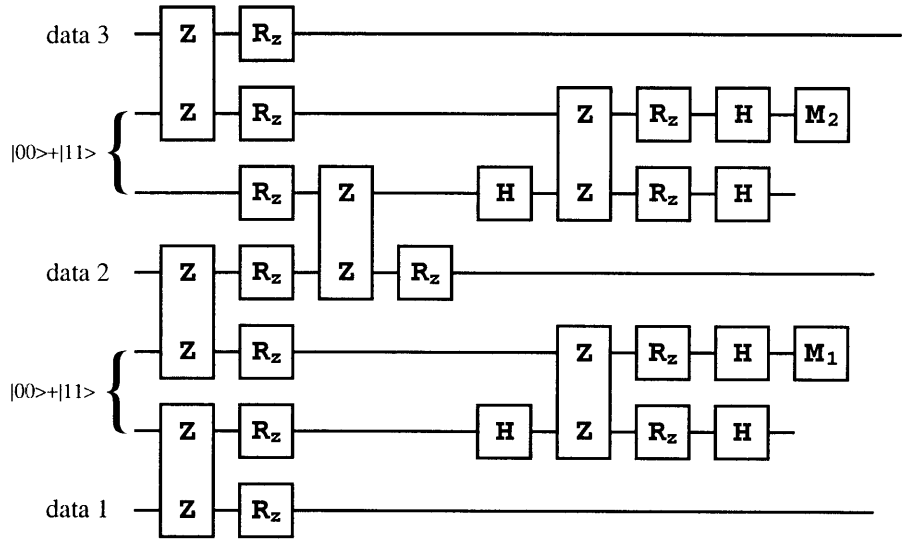

Figure 5-16: A circuit implementing the fault-tolerant syndrome detection for the three qubit bit-flip code. In this circuit, we assume the quantum computer can perform quantum gates on different qubits in parallel.

Figure 5-17 shows the crash rate constant per unit time Γ_t for quantum memories implementing the three qubit bit-flip code. Results for three syndrome detection circuits with different levels of parallelism are shown. The noise thresholds for the original circuit (Fig. 5-11), increased parallelism circuit (5-16), and maximal parallelism circuit are approximately 1.5×10^{-2}, 2.3×10^{-2}, and 4.6×10^{-2}, respectively. The results indicate that by increasing the level of parallelism, the noise threshold can be significantly improved. Note that the reduction of the operation time in higher level of parallelism cannot account for all of the improvement on the threshold values; because the crash rate constant per unit time Γ_t has been scaled by the amount of time needed to complete a fault-tolerant QEC step ($\Gamma_t = \Gamma_n/\tau$), any difference in Γ_t is from sources other than difference in τ. The improvement on the threshold value is because when the level of parallelism is increased, the number of pathways that generate uncorrectable errors decreases. Finally, we emphasize that our method can access the real threshold value reflecting the limitations of an individual computing device.

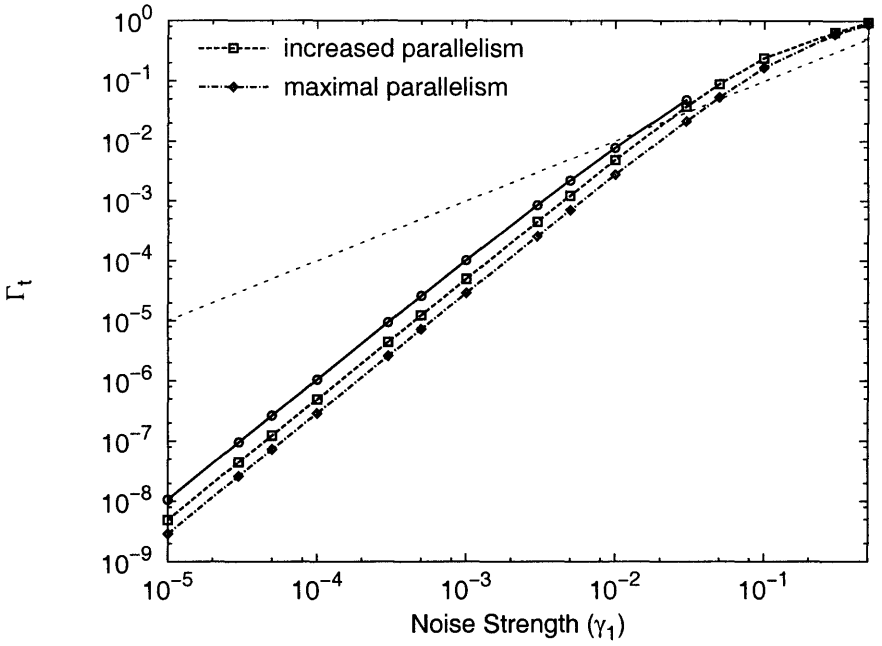

Figure 5-17: The crash rate constant per unit time Γ_t as a function of the noise strength for quantum memories using three qubit bit-flip code. Curves for three syndrome detection circuits different in the level of parallelism are shown. The solid line is for the circuit shown in Fig. 5-11, the dashed line is the increased parallelism circuit shown in Fig. 5-16, and the dash-dotted line is the maximal parallelism circuit that finishes all controlled-Z operations in a single pulse. We see dramatic improvement on the noise threshold values when the level of parallelism is increased. The result indicates that by increasing the level of parallelism, the threshold value can be significantly improved.

5.5 Conclusion

In this chapter, we have applied the stochastic Liouville equation approach described in Chapter 4 to study the effect of noise in systems that are relevant to quantum computations. The model includes realistic physical interactions for the implementations of quantum gates, and describes the effect of system-bath interactions by including stochastic fluctuating terms in the system Hamiltonian. As a noise model for quantum computers, our approach provides a great flexibility for including device conditions and a realistic description that takes into account the state dependent dissipation and dephasing rates as well as correct propagation of errors in quantum circuits. Thus, we have presented a noise model that can simulate quantum circuits in a reasonable size under realistic physical conditions and gives us a full description of the dissipative dynamics of the quantum computer.

We have applied the noise model to study the dissipative dynamics of a system of two independent qubits that mimics the EPR pair used in the quantum teleportation, and showed that the phenomenological parameters used in our model, i.e. γ_0 and γ_1, correspond to the decoherence and population relaxation rate, respectively. To study the effect of noise on quantum teleportation, we have calculated the fidelity of quantum teleportation. We found the effect of noise in the quantum channels are additive, and the teleportation fidelity depends on the state of the teleported qubit. When the two EPR qubits are degenerate and have no intra-qubit coupling, the relative efficiencies of teleportation for the four Bell states are the same; otherwise, the singlet state $|B_4\rangle$ is the most efficient one. When the two qubits are coupled to the same bath (collective decoherence case), the $|B_1\rangle$ state is superdecoherent, while the $|B_4\rangle$ state is decoherence-free.

Furthermore, we have studied a generic two-qubit Hamiltonian containing XY type inter-qubit interaction. The dissipative dynamics of a set of one- and two-qubit quantum gates were studied, and the results were then combined to calculate the averaged gate fidelity and gate purity for the quantum controlled-NOT gate operation. The dependence of the quality of the quantum controlled-NOT gate operation on

the noise strength and the strength of the inter-qubit coupling were investigated. We found that the quality of the controlled-NOT gate operation is sensitive to the noise strength and the strengths of the control fields. In addition, the effect of noise is additive regardless of its origin. We compared our results to Thorwart and Hänggi's results obtained by the numerical *ab initio* QUAPI technique. In general, our results are in good agreement with those obtained by the numerical QUAPI method.

Finally, we have applied the noise model to study the effect of noise on the performance of fault-tolerant QEC circuits. Fault-tolerant QEC circuits implementing either the three qubit bit-flip code or the five-qubit code were investigated, and the noise threshold for quantum memory and logical X gate were calculated by comparing the logical crash rate to the error rate of a bare physical qubit. The noise threshold of quantum memories using the three qubit bit-flip code and five qubit code is about 2×10^{-2} and 5×10^{-4}, respectively. The noise threshold of logical X gates using the three qubit bit-flip code and five qubit code is about 1×10^{-3} and 4×10^{-5}, respectively. Note that in our dimensionless system, these noise strength values should be interpreted as the error rate per unit time scale $\Delta t = 1/\varepsilon$, where ε is the strength of the control fields. These threshold values are obtained from an uniform noise model where magnitudes of storage errors and gate errors are the same. This result indicates that fault-tolerant quantum computing is possible in systems with strong storage errors. A possible scenario for such system is the linear nearest-neighbor architecture, where only nearest-neighbor interactions are available for two-qubit gates, and excess amount of quantum swap gates have to be added to the circuit to perform two-qubit gates between qubits distant in space.

We have also carried out a systematic study on several variables that can affect the performance of the fault-tolerant QEC procedure for the three qubit bit-flip code. Our results show that both collective bath and imperfect projective measurement have minor effects on the threshold value. However, changing the repetition protocol and level of parallelism can significantly change the performance of the fault-tolerant QEC procedure. Our density matrix results indicate that accepting a syndrome only when two consecutive syndrome detections agree (protocol B), which reduces the number of

required syndrome detection steps, is the optimal repetition protocol. Compared to the simple majority vote algorithm (protocol A), protocol B increases the efficiency of fault-tolerant QEC at least by a factor of two. Regarding the level of parallelism in the syndrome detection circuit, in general, a higher level of parallelism results in a more efficient fault-tolerant QEC circuit. The improvement can not be fully explained by the shorter operational time for a more parallelized circuit; we suggest the major contribution for the improvement comes from the reduction of possible pathways for error propagation. Since the level of parallelism is actually limited by available physical resources in reality, it will be interesting to examine and simulate this factor according to a specific physical implementation of quantum computer (such as ion-trap or NMR).

Finally, we emphasize that without specifying the specific noise model and physical device conditions, noise threshold values are of little use. Our noise model is based on well defined parameters that reflect realistic device conditions, and provides a full description for the dissipative dynamics of the quantum computer. As a result, this noise model enables us to access the real performance of fault-tolerant QEC for individual physical implementations. We believe that such information can be useful for the design and optimization of quantum computers.

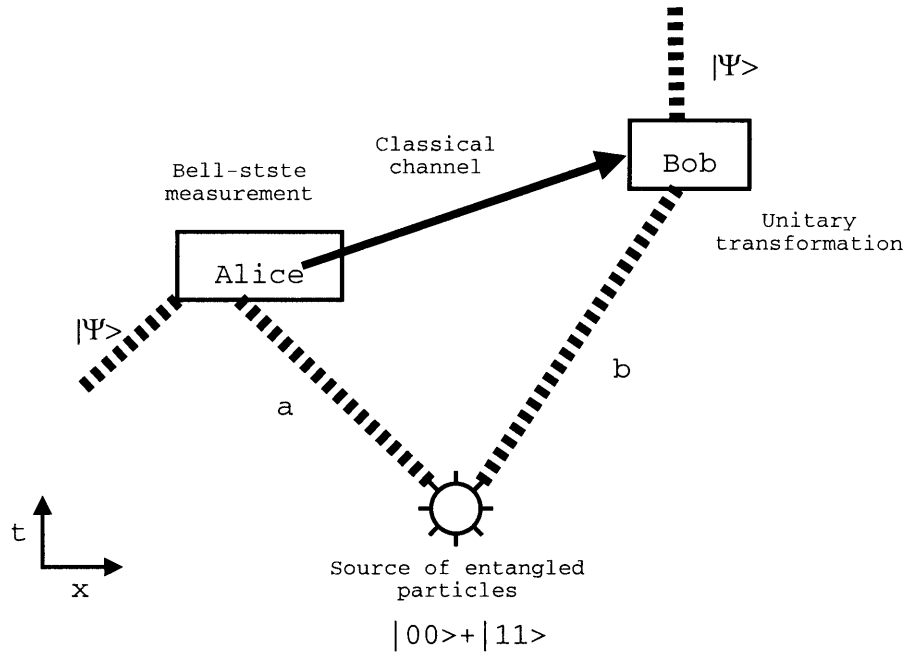

Figure 5-18: A schematic representation for the quantum teleportation protocol.

Appendix 5.A Bennett's Quantum Teleportation Protocol

Since first proposed by Bennett *et al.* in 1993 [29], the concept of "quantum teleportation" has received much attention. In addition, using quantum teleportation to securely exchange keys has potentially important impact on quantum communication and cryptography. Recently, the experimental realization of long-distance teleportation of qubits [79, 80, 81, 82] and entanglement purification [83] has provided clear evidence for the applicability of the quantum teleportation idea. The goal of quantum teleportation is to transfer the exact quantum state of a system over space to another location, without either moving the system physically nor knowing the exact state of the system (which is impossible in quantum mechanics). One can achieve such operation by exploiting the entangled nature of Einstein-Podolsky-Rosen (EPR) pairs.

Consider the teleportation scheme shown in Fig. 5-18, where we have a sender, a receiver, and an entangled particle generator that generates EPR pairs. Following

the tradition in information theory, we will call the sender Alice and the receiver Bob hereafter. Consider the scenario of teleporting one qubit from Alice to Bob. Alice has a qubit in state $|\Psi\rangle_a = \alpha|0\rangle_a + \beta|1\rangle_a$, where the subscript a denotes that the qubit belongs to Alice, and she wants to transfer the information about the state to Bob (i.e. α and β). In addition, the EPR pair source emits two entangled qubits, one to Alice and one to Bob, in the following maximal entangled state:

$$\frac{1}{\sqrt{2}}(|0\rangle_a|0\rangle_b + |1\rangle_a|1\rangle_b)$$

Note that we use the subscript a to denote qubits owned by Alice, and use b to denote qubits owned by Bob. The total state of the three qubits is the tensor product of $|\Psi\rangle_a$ and EPR state:

$$(\alpha|0\rangle_a + \beta|1\rangle_a) \otimes \frac{1}{\sqrt{2}}(|0\rangle_a|0\rangle_b + |1\rangle_a|1\rangle_b) \tag{5.30}$$

After the two EPR qubits have been received by Alice and Bob, respectively, Alice holds two qubits, and Bob holds one qubit. We can rewrite the two qubits at Alice's hands in the Bell-state representation, and obtain four different possible entanglement of the system. The total three qubits system can be represented as

$$\begin{aligned}
&\tfrac{1}{\sqrt{8}}[(|0\rangle_a|0\rangle_a + |1\rangle_a|1\rangle_a) \cdot (\alpha|0\rangle_b + \beta|1\rangle_b) \\
&+(|0\rangle_a|0\rangle_a - |1\rangle_a|1\rangle_a) \cdot (\alpha|0\rangle_b - \beta|1\rangle_b) \\
&+(|1\rangle_a|0\rangle_a + |0\rangle_a|1\rangle_a) \cdot (\beta|0\rangle_b + \alpha|1\rangle_b) \\
&+(|1\rangle_a|0\rangle_a - |0\rangle_a|1\rangle_a) \cdot (\beta|0\rangle_b - \alpha|1\rangle_b)]
\end{aligned} \tag{5.31}$$

It is trivial to expand the tensor product and confirm that Eq. (5.30) and Eq. (5.31) are the same. Also, notice that the part involve Bob's qubit can actually be written using a Pauli matrix representation ($\mathbf{I}$, σ_z, σ_x, and $i\sigma_y$, respectively).

In Eq. (5.31), the left column are qubits owned by Alice, therefore Alice can perform Bell-state measurement on these two qubits, and project the partial system onto one of the four Bell eigenstates [one of the lines in (5.31)]. The consequence of this measurement is that the qubit at Bob's place will also be projected onto

corresponding states, i.e. $\mathbf{I} \cdot (\alpha|0\rangle_b + \beta|1\rangle_b)$, $\sigma_z \cdot (\alpha|0\rangle_b + \beta|1\rangle_b)$, $\sigma_x \cdot (\alpha|0\rangle_b + \beta|1\rangle_b)$, and $i\sigma_y \cdot (\alpha|0\rangle_b + \beta|1\rangle_b)$, respectively. Now, if Bob can know the result of Alice's measurement, he can apply the corresponding inverse transformation ($\mathbf{I}$, σ_z, σ_x, and $-i\sigma_y$) to recover his qubit to the original state $|\Psi\rangle$. However, since Alice can not know the result of her measurement before she has performed the measurement, an additional channel is required to transmit this information to Bob. Therefore, two bits containing the result of the measurement have to be transmitted to Bob classically, then Bob can perform the encoded unitary transformation to recover his qubit to the state $\alpha|0\rangle_b + \beta|1\rangle_b$. Note that in the quantum teleportation protocol, a classical channel is required to transfer two bits of classical information. As a result, the transmission of information is not faster than the speed of light.

The end result is using a shared EPR pair and two classical bits to transmit one quantum qubit, without even knowing the state of the qubit (knowledge about α, and β never appears in this protocol), from Alice to Bob. Note that energy and matter can not be teleported in this manner, only the quantum state (i.e. quantum information) is transmitted. In addition, although a continuous qubit (infinite degree of freedom) is transmitted using two classical bits (four degree of freedom), this process can not be used to increase the capacity of classical channel. Holevo's theorem states that one qubit can only be used to transport at most one classical bit. There is another protocol called "quantum superdense coding", where we reverse the protocol to use one shared EPR pair and one qubit to encode two classical bits [84, 85, 86]. Another side-effect of the teleportation protocol is that while the two bits sent through the classical channel can be intercepted by a third party, the information is totally useless without Bob's entangled copy of the qubit. Therefore, this is an absolutely secure way to transmit information, and has been suggested as an ideal way for crypt key distribution, i.e. quantum cryptography [30].

Appendix 5.B The Idea of Fault-tolerance

In this appendix, we use the fault-tolerant QEC circuit for the three qubit bit-flip code shown in Fig. 5-10 to elaborate the main ideas behind fault-tolerant quantum error-correction. In essence, the fault-tolerant method is *a procedure that controls the propagation of errors* in quantum circuits. Figure 5-10 shows the fault-tolerant QEC circuit for the three qubit bit-flip code. The fault-tolerant circuit implements several main elements: (1) entangled ancilla states, (2) transversal gate operations, (3) repetition.

Entanglement is an indispensable resource for quantum computing. Entangled states are required to detect error syndrome fault-tolerantly, therefore, ancilla qubits have to be prepared in appropriate entangled states. In addition, the prepared ancilla qubits must be verified to ensure that the possibility of having correlated multi-qubit errors, which are uncorrectable errors, is low. Sometimes ancilla qubits need to go through multiple verification steps to ensure that uncorrectable error in the entangled state is small (see also Appendix 5.C). Because the ancilla qubits cab be prepared off-line, we can generate multiple copies of the entangled states and only use the genuine ones that pass multiple verification steps. If the probability of error in a gate operation is ϵ, we can ensure that probability of multi-qubit error in the prepared ancilla states is of order ϵ^2 by only accepting states that pass the verification step.

Transversal gate operations are required in a fault-tolerant quantum circuit in order to ensure that errors do not propagate in an uncontrolled manner. Notice that in Fig. 5-10, any ancilla qubits interacts only once with a data qubit, therefore any error in an ancilla qubit does not infect multiple data qubits, and error in a data qubit does not propagate to other data qubits. Requirement for transversal gates is the reason that we need many ancilla qubits and entangled ancilla states.

In addition, repetition is required to ensure that we detect the correct error syndrome. An error during the syndrome detection can result in a wrong syndrome, hence an incorrect recovery action that causes further damage in the data. Therefore, the whole syndrome detection in Fig. 5-10 has to be repeated for several times

and take a majority vote. For example, if we repeat the syndrome detection for three times and accept the syndrome only when two of the three outcomes indicate the same syndrome, then we can assure that the probability of detecting a wrong syndrome is of order ϵ^2.

Combining all these elements, namely using verification to ensure the quality of input states, interacting each ancilla qubit strictly with only one data qubit to control the propagation of errors, and utilizing repetition to reduce the possibility of making errors, we can ensure that the probability of generating a two-qubit error is of order ϵ^2, and avoid the catastrophic propagation of uncorrectable errors. In a quantum computation using a single error correcting code such as the three qubit bit-flip code and the five qubit code, we can perform the fault-tolerant QEC after each gate operations. In consequence, single-qubit errors generated in earlier computation and QEC steps will be corrected in later QEC steps. Therefore, only two-qubit errors will be accumulated in a rate of order ϵ^2. As a result, we can achieve longer computation when ϵ is small. Note that the sample principle can be applied to general quantum error-correcting code. Using a t-error correcting code, with high probability all errors that involve no more than t-qubits would be corrected, provided that the errors occur in ancilla preparation and syndrome detection are small.

Appendix 5.C Fault-tolerant Preparation of Ancilla States

To fault-tolerantly detect error syndrome, we need ancilla qubits to be prepared in maximally entangled cat states and go through multiple verification steps to ensure that magnitudes of correlated multiple-qubit errors are small. This procedure requires many quantum resources, and could be time-consuming. Fortunately, the ancilla states can be prepared off-line, and efficient methods for ancilla preparation and verification do exist [87]. In practice, ancilla preparation requires large amount of physical resources, and might be the bottleneck for the scale-up of implementations

of quantum computers. Nevertheless, because high-quality ancilla qubits can be prepared off-line, the difficulty of ancilla preparation does not affect the threshold result as long as we can have an ancilla factory that prepares high-quality ancilla states in parallel.

Entangled states are required to detect syndrome fault-tolerantly, therefore, ancilla qubits have to be prepared in appropriate entangled states. For example, the four-qubit cat state $\frac{1}{\sqrt{2}}(|0000\rangle + |1111\rangle)$ is necessary for the fault-tolerant QEC of the five-qubit code. Figure 5-19 shows the circuit we used to prepare and verify four-qubit cat states [49]. An extra qubit is used to detect correlated X errors in the cat state; after the measurement, only states with measurement result equals to zero are accepted. This verification step ensures that a single error in the circuit causes at most a single-qubit error in the final cat state, therefore the circuit fulfills the fault-tolerant condition. Compared to other fault-tolerant cat state preparation circuits [6, 87], an important feature in the circuit in Fig. 5-19 is that only a projective measurement is required to verify the cat state fault-tolerantly. This is possible because the circuit takes into account the error propagation pattern in the preparation step. General n-qubit cat states can be generated using a quantum circuit with similar construction.

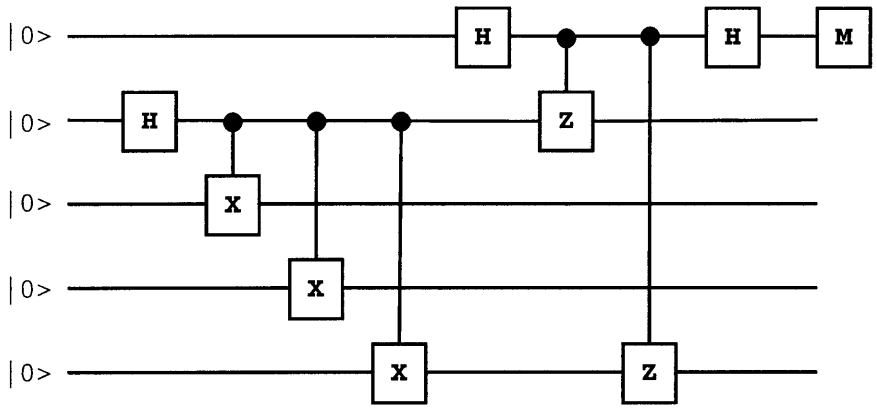

Figure 5-19: The fault-tolerant circuit for the preparation and verification of the four-qubit cat state. Note that the final result is conditioned by the outcome of the measurement at the end of the circuit. If the measurement outcome is zero, we accept the state; otherwise, the state is discarded and the circuit is started over again. The verification step ensures that a single error in the circuit causes at most a single-qubit error in the outcome.

Bibliography

[1] C. H. Bennett and P. W. Shor. Quantum information theory. *IEEE Trans. Inf. Theory*, 44(6):2724 – 2742, 1998.

[2] A. Steane. Quantum computing. *Rep. Prog. Phys.*, 61(2):117 – 173, 1998.

[3] C. H. Bennett and D. P. DiVincenzo. Quantum information and computation. *Nature*, 404(6775):247 – 255, 2000.

[4] D. P. DiVincenzo. Quantum computation. *Science*, 270(5234):255 – 261, 1995.

[5] H. E. Brandt. Qubit devices and the issue of quantum decoherence. *Prog. Quantum Electron.*, 22(5-6):257 – 370, 1998.

[6] M. A. Nielsen and I. L. Chuang. *Quantum Computation and Quantum Information.* Cambridge University Press, 2000.

[7] M. Hirvensalo. *Quantum Computing.* Springer-Verlag, Berlin; New York, 2004.

[8] D. Bouwmeester, Ekert. A., and A. Zeilinger. *The Physics of Quantum Information : Quantum Cryptography, Quantum Teleportation, Quantum Computation.* Springer-Verlag, Berlin; New York, 2000.

[9] P. W. Shor. Algorithms for quantum computation: Discrete logarithms and factoring. In *Proceedings of the Symposium on the Foundations of Computer Science, 1994, Los Alamitos, California*, pages 124 – 134. IEEE Computer Society Press, New York, 1994.

[10] I. L. Chuang, L. M. K. Vandersypen, X. L. Zhou, D. W. Leung, and S. Lloyd. Experimental realization of a quantum algorithm. *Nature*, 393(6681):143 – 146, 1998.

[11] I. L. Chuang, N. Gershenfeld, and M. Kubinec. Experimental implementation of fast quantum searching. *Phys. Rev. Lett.*, 80(15):3408 – 3411, 1998.

[12] L. M. K. Vandersypen, M. Steffen, G. Breyta, C. S. Yannoni, R. Cleve, and I. L. Chuang. Experimental realization of an order-finding algorithm with an NMR quantum computer. *Phys. Rev. Lett.*, 85(25):5452 – 5455, 2000.

[13] L. M. K. Vandersypen, M. Steffen, G. Breyta, C. S. Yannoni, M. H. Sherwood, and I. L. Chuang. Experimental realization of Shor's quantum factoring algorithm using nuclear magnetic resonance. *Nature*, 414(6866):883 – 887, 2001.

[14] S. Gulde, M. Riebe, G. P. T. Lancaster, C. Becher, J. Eschner, H. Haffner, F. Schmidt-Kaler, I. L. Chuang, and R. Blatt. Implementation of the Deutsch-Jozsa algorithm on an ion-trap quantum computer. *Nature*, 421(6918):48 – 50, 2003.

[15] B. E. Kane. A silicon-based nuclear spin quantum computer. *Nature*, 393(6681):133 – 137, 1998.

[16] A. Imamoglu, D. D. Awschalom, G. Burkard, D. P. DiVincenzo, D. Loss, M. Sherwin, and A. Small. Quantum information processing using quantum dot spins and cavity QED. *Phys. Rev. Lett.*, 83(20):4204 – 4207, 1999.

[17] Y. Makhlin, G. Schon, and A. Shnirman. Quantum-state engineering with Josephson-junction devices. *Rev. Mod. Phys.*, 73(2):357 – 400, 2001.

[18] D. Beckman, A. N. Chari, S. Devabhaktuni, and J. Preskill. Efficient networks for quantum factoring. *Phys. Rev. A*, 54(2):1034 – 1063, AUG 1996.

[19] W. G. Unruh. Maintaining coherence in quantum computers. *Phys. Rev. A*, 51(2):992 – 997, 1995.

[20] G. M. Palma, K.-A. Suominen, and A. K. Ekert. Quantum computers and dissipation. *Proc. R. Soc. Lond. A.*, 452:567, 1996.

[21] G. G. Carlo, G. Benenti, G. Casati, and C. Mejia-Monasterio. Simulating noisy quantum protocols with quantum trajectories. *Phys. Rev. A*, 69(6), 2004.

[22] A. M. Childs, E. Farhi, and J. Preskill. Robustness of adiabatic quantum computation. *Phys. Rev. A*, 65(1), 2002.

[23] D. F. Walls and G. J. Milburn. Effect of dissipation on quantum coherence. *Phys. Rev. A*, 31:2403, 1985.

[24] D. Loss and D. P. DiVincenzo. Quantum computation with quantum dots. *Phys. Rev. A*, 57(1):120 – 126, 1998.

[25] M. Thorwart and P. Hänggi. Decoherence and dissipation during a quantum XOR gate operation. *Phys. Rev. A*, 65(1):012309, 2002.

[26] M. J. Storcz and F. K. Wilhelm. Decoherence and gate performance of coupled solid-state qubits. *Phys. Rev. A*, 67(4):042319, 2003.

[27] M. Governale, M. Grifoni, and G. Schon. Decoherence and dephasing in coupled Josephson-junction qubits. *Chem. Phys.*, 268(1-3):273 – 283, 2001.

[28] A. J. Leggett, S. Chakravarty, A. T. Dorsey, M. P. A. Fisher, A. Garg, and W. Zwerger. Dynamics of the dissipative 2-state system. *Rev. Mod. Phys.*, 59(1):1 – 85, 1987.

[29] C. H. Bennett, G. Brassard, C. Crepeau, R. Jozsa, A. Peres, and W. K. Wootters. Teleporting an unknown quantum state via dual classical and Einstein-Podolsky-Rosen channels. *Phys. Rev. Lett.*, 70(13):1895 – 1899, 1993.

[30] N. Gisin, G. G. Ribordy, W. Tittel, and H. Zbinden. Quantum cryptography. *Rev. Mod. Phys.*, 74(1):145 – 195, 2002.

[31] D. Gottesman and I. L. Chuang. Demonstrating the viability of universal quantum computation using teleportation and single-qubit operations. *Nature*, 402(6760):390 – 393, 1999.

[32] R. J. Silbey. Electronic energy transfer in molecular crystals. *Ann. Rev. Phys. Chem.*, 27:203, 1976.

[33] P. Reineker. *Exciton Dynamics in Molecular Crystals and Aggregates.* Springer-Verlag, Berlin, 1982.

[34] C. H. Bennett, G. Brassard, S. Popescu, B. Schumacher, J. A. Smolin, and W. K. Wootters. Purification of noisy entanglement and faithful teleportation via noisy channels. *Phys. Rev. Lett.*, 76(5):722 – 725, 1996.

[35] D. Kumar and P. N. Pandey. Effect of noise on quantum teleportation. *Phys. Rev. A*, 68(1):012317, 2003.

[36] P. G. Kwiat, A. J. Berglund, J. B. Altepeter, and A. G. White. Experimental verification of decoherence-free subspaces. *Science*, 290(5491):498 – 501, 2000.

[37] P. Zanardi and M. Rasetti. Noiseless quantum codes. *Phys. Rev. Lett.*, 79(17):3306 – 3309, 1997.

[38] L. M. Duan and G. C. Guo. Preserving coherence in quantum computation by pairing quantum bits. *Phys. Rev. Lett.*, 79(10):1953 – 1956, 1997.

[39] D. A. Lidar, I. L. Chuang, and K. B. Whaley. Decoherence-free subspaces for quantum computation. *Phys. Rev. Lett.*, 81(12):2594 – 2597, 1998.

[40] D. Bacon, D. A. Lidar, and K. B. Whaley. Robustness of decoherence-free subspaces for quantum computation. *Phys. Rev. A*, 60(3):1944 – 1955, 1999.

[41] L. M. Duan and G. C. Guo. Reducing decoherence in quantum-computer memory with all quantum bits coupling to the same environment. *Phys. Rev. A*, 57(2):737 – 741, 1998.

[42] D. P. DiVincenzo. 2-bit gates are universal for quantum computation. *Phys. Rev. A*, 51(2):1015, 1995.

[43] D. P. DiVincenzo. Quantum gates and circuits. *Proc. R. Soc. London Ser. A-Math. Phys. Eng. Sci.*, 454(1969):261 – 276, 1998.

[44] A. Barenco, C. H. Bennett, R. Cleve, D. P. DiVincenzo, N. Margolus, P. Shor, T. Sleator, J. A. Smolin, and H. Weinfurter. Elementary gates for quantum computation. *Phys. Rev. A*, 52(5):3457 – 3467, 1995.

[45] A. G. Fowler, C. J. Wellard, and L. C. L. Hollenberg. Error rate of the Kane quantum computer controlled-NOT gate in the presence of dephasing. *Phys. Rev. A*, 67(1):012301, 2003.

[46] J. F. Poyatos, J. I. Cirac, and P. Zoller. Complete characterization of a quantum process: The two-bit quantum gate. *Phys. Rev. Lett.*, 78(2):390 – 393, 1997.

[47] D. Aharonov and M. Ben-Or. Fault-tolerant quantum computation with constant error. In *Proceedings of the twenty-ninth annual ACM symposium on Theory of computing*, pages 176–188. ACM Press, 1997.

[48] E. Knill, R. Laflamme, and W. H. Zurek. Resilient quantum computation: error models and thresholds. *Proc. R. Soc. London A*, 454(1969):365 – 384, 1998.

[49] J. Preskill. Reliable quantum computers. *Proc. R. Soc. London A*, 454(1969):385 – 410, 1998.

[50] P. W. Shor. Fault-tolerant quantum computation. In *Proceedings of the 37th Symposium on Foundations of Computer Science*, page 56. IEEE Computer Society Press, Los Alamitos, CA, 1996.

[51] D. P. DiVincenzo and P. W. Shor. Fault-tolerant error correction with efficient quantum codes. *Phys. Rev. Lett.*, 77(15):3260 – 3263, 1996.

[52] D. Gottesman. Theory of fault-tolerant quantum computation. *Phys. Rev. A*, 57(1):127 – 137, 1998.

[53] C. Zalka. Threshold Estimate for Fault Tolerant Quantum Computation. *e-print quant-ph/9612028*, 1996.

[54] D. Gottesman. Stabilizer Codes and Quantum Error Correction. *e-print quant-ph/9705052*, 1997.

[55] A. M. Steane. Efficient fault-tolerant quantum computing. *Nature*, 399(6732):124 – 126, 1999.

[56] A. M. Steane. Overhead and noise threshold of fault-tolerant quantum error correction. *Phys. Rev. A*, 68(4):042322, 2003.

[57] B. W. Reichardt. Improved ancilla preparation scheme increases fault-tolerant threshold. *e-print quant-ph/0406025*, 2004.

[58] P. L. Knight, M. B. Plenio, and V. Vedral. Decoherence and quantum error correction. *Philos. Trans. R. Soc. Lond. Ser. A-Math. Phys. Eng. Sci.*, 355(1733):2381 – 2385, 1997.

[59] Y. C. Cheng and R. J. Silbey. Stochastic Liouville equation approach for the effect of noise in quantum computations. *Phys. Rev. A*, 69(5):052325, 2004.

[60] A. G. Fowler, C. D. Hill, and L. C. L. Hollenberg. Quantum-error correction on linear-nearest-neighbor qubit arrays. *Phys. Rev. A*, 69(4):042314, 2004.

[61] P. W. Shor. Scheme for reducing decoherence in quantum computer memory. *Phys. Rev. A*, 52(4):R2493 – R2496, 1995.

[62] A. R. Calderbank and P. W. Shor. Good quantum error-correcting codes exist. *Phys. Rev. A*, 54(2):1098 – 1105, 1996.

[63] A. M. Steane. Error correcting codes in quantum theory. *Phys. Rev. Lett.*, 77(5):793 – 797, 1996.

[64] C. H. Bennett, D. P. DiVincenzo, J. A. Smolin, and W. K. Wootters. Mixed-state entanglement and quantum error correction. *Phys. Rev. A*, 54(5):3824 – 3851, 1996.

[65] R. Laflamme, C. Miquel, J. P. Paz, and W. H. Zurek. Perfect quantum error correcting code. *Phys. Rev. Lett.*, 77(1):198, 1996.

[66] E. Knill, R. Laflamme, R. Martinez, and C. Negrevergne. Benchmarking quantum computers: The five-qubit error correcting code. *Phys. Rev. Lett.*, 86(25):5811, 2001.

[67] J. I. Cirac and P. Zoller. Quantum computations with cold trapped ions. *Phys. Rev. Lett.*, 74(20):4091, 1995.

[68] D. J. Wineland, M. Barrett, J. Britton, J. Chiaverini, B. DeMarco, W. M. Itano, B. Jelenkovic, C. Langer, D. Leibfried, V. Meyer, T. Rosenband, and T. Schatz. Quantum information processing with trapped ions. *Philos. Trans. R. Soc. Lond. Ser. A-Math. Phys. Eng. Sci.*, 361(1808):1349 – 1361, 2003.

[69] A. M. Steane. Space, time, parallelism and noise requirements for reliable quantum computing. *Fortschritte Phys.-Prog. Phys.*, 46(4-5):443 – 457, 1998.

[70] L. Viola, E. M. Fortunato, M. A. Pravia, E. Knill, R. Laflamme, and D. G. Cory. Experimental realization of noiseless subsystems for quantum information processing. *Science*, 293(5537):2059 – 2063, 2001.

[71] M. Bourennane, M. Eibl, S. Gaertner, C. Kurtsiefer, A. Cabello, and H. Weinfurter. Decoherence-free quantum information processing with four-photon entangled states. *Phys. Rev. Lett.*, 92(10):107901, 2004.

[72] J. B. Altepeter, P. G. Hadley, S. M. Wendelken, A. J. Berglund, and P. G. Kwiat. Experimental investigation of a two-qubit decoherence-free subspace. *Phys. Rev. Lett.*, 92(14):147901, 2004.

[73] D. Bacon, J. Kempe, D. A. Lidar, and K. B. Whaley. Universal fault-tolerant quantum computation on decoherence-free subspaces. *Phys. Rev. Lett.*, 85(8):1758 – 1761, 2000.

[74] D. P. DiVincenzo, D. Bacon, J. Kempe, G. Burkard, and K. B. Whaley. Universal quantum computation with the exchange interaction. *Nature*, 408(6810):339 – 342, 2000.

[75] J. Kempe, D. Bacon, D. A. Lidar, and K. B. Whaley. Theory of decoherence-free fault-tolerant universal quantum computation. *Phys. Rev. A*, 63:042307, 2001.

[76] D. A. Lidar, D. Bacon, and K. B. Whaley. Concatenating decoherence-free subspaces with quantum error correcting codes. *Phys. Rev. Lett.*, 82(22):4556 – 4559, 1999.

[77] D. Bacon, K. R. Brown, and K. B. Whaley. Coherence-preserving quantum bits. *Phys. Rev. Lett.*, 87:247902, 2001.

[78] M. B. Plenio, V. Vedral, and P. L. Knight. Conditional generation of error syndromes in fault-tolerant error correction. *Phys. Rev. A*, 55(6):4593 – 4596, 1997.

[79] D. Bouwmeester, J. W. Pan, K. Mattle, M. Eibl, H. Weinfurter, and A. Zeilinger. Experimental quantum teleportation. *Nature*, 390(6660):575 – 579, 1997.

[80] J. W. Pan, M. Daniell, S. Gasparoni, G. Weihs, and A. Zeilinger. Experimental demonstration of four-photon entanglement and high-fidelity teleportation. *Phys. Rev. Lett.*, 86(20):4435 – 4438, 2001.

[81] I. Marcikic, H. de Riedmatten, W. Tittel, H. Zbinden, and N. Gisin. Long-distance teleportation of qubits at telecommunication wavelengths. *Nature*, 421(6922):509 – 513, 2003.

[82] J. W. Pan, S. Gasparoni, M. Aspelmeyer, T. Jennewein, and A. Zeilinger. Experimental realization of freely propagating teleported qubits. *Nature*, 421(6924):721 – 725, 2003.

[83] J. Pan, S. Gasparoni, R. Ursin, G. Weihs, and A. Zeilinger. Experimental entanglement purification of arbitrary unknow states. *Nature*, 423:417, 2003.

[84] A. Barenco and A. K. Ekert. Dense coding based on quantum entanglement. *J. Mod. Optic.*, 42(6):1253 – 1259, JUN 1995.

[85] K. Mattle, H. Weinfurter, P. G. Kwiat, and A. Zeilinger. Dense coding in experimental quantum communication. *Phys. Rev. Lett.*, 76(25):4656 – 4659, 1996.

[86] R. F. Werner. All teleportation and dense coding schemes. *J. Phys. A Math. Gen.*, 34(35):7081 – 7094, 2001.

[87] A. M. Steane. Fast fault-tolerant filtering of quantum codewords. *e-print quant-ph/0202036*, 2004.

Chapter 6

Coherence Effect and the Dynamics of Excitation Energy Transfer in a Single LH2 Complex

Part of the content in this chapter has been published in the following paper:
Y.C. Cheng and R.J. Silbey. Coherence in the B800 ring of purple bacteria LH2. *Physical Review Letters*, 96:028103, 2006.

6.1 Introduction

In the previous chapters, we have studied the dynamics of a quantum system under the influence of an external bath in the limit that the fluctuations induced by the system-bath interactions are much faster than the time scale of interest, which is a reasonable assumption for ultra-pure molecular crystals and models for quantum computers. However, in many interesting systems, such as in molecular aggregates, slow fluctuations that results in energetic disorders in the system can have dominating effect on the dynamics of the system. In this chapter, we study the nature of the excitations and the dynamics of excitation energy transfer (EET) in this "static disorder" limit.

The optical properties of nanoscale molecular aggregates have drawn consider-

able attention both experimentally and theoretically due to their important role in biological processes and synthetic molecular devices. One of the most studied molecular assemblies is the photo-synthetic unit of purple bacteria [1, 2, 3], in which light-harvesting antenna systems capture solar energy and transfer the excitation energy to the reaction center (RC) to drive the photosynthetic reaction. These light-harvesting complexes store and transfer excitation energy with astonishingly high efficiency (above 95%); thus, understanding the underlying design principles of photo-synthetic light-harvesting systems can lead to improvements of the design of synthetic antenna devices.

Most purple bacteria contain two types of light-harvesting complexes in their photosynthetic unit. The light-harvesting complex 1 (LH1) is known to directly surround the RC, and the light-harvesting complex 2 (LH2) is arranged around the LH1 complexes. LH2 complexes is not in direct contact with the RC, they transfer energy to RC via LH1 complexes. The high-resolution X-ray structures of the LH2 complexes of purple bacteria revealed remarkable symmetry in the arrangement of bacteriochlorophylls (BChls) in the pigment-protein complexes and have motivated extensive studies on those systems [4, 5]. For example, the LH2 complex of *Rhodopseudomonas acidophila* carries a cyclic 9-mer of $\alpha\beta$-polypeptide heterodimers; each structural unit consists of two transmembrane polypeptides called the α and β units, one or two carotenoids, and three BChl a molecules. The 27 BChl a molecules form two highly symmetric rings (C_9 symmetry); 9 of them form the so called B800 ring which absorbs maximally at 800 nm, and the other 18 form the B850 ring which absorbs maximally at 850 nm. The B850 ring contains nine heterodimers whose two monomers are inequivalent BChl a molecules. In Fig. 6-1, we show the geometrical arrangement of the 27 BChl a molecules. The Mg-Mg distance between adjacent B800 BChl a molecules is 21 Å, which results in weak nearest-neighbor electronic couplings (~ -25 cm^{-1}) in the B800 ring [6, 7]. The Mg-Mg distance between the nearest BChl a pigments in a B850 BChl a heterodimer is 9.6 Å, and the nearest Mg-Mg distance between adjacent B850 heterodimers is 8.9 Å. The short BChl a-BChl a distance in the B850 ring leads to strong nearest-neighbor coupling of ~ -300 cm^{-1} [8]. In addition, the nearest-

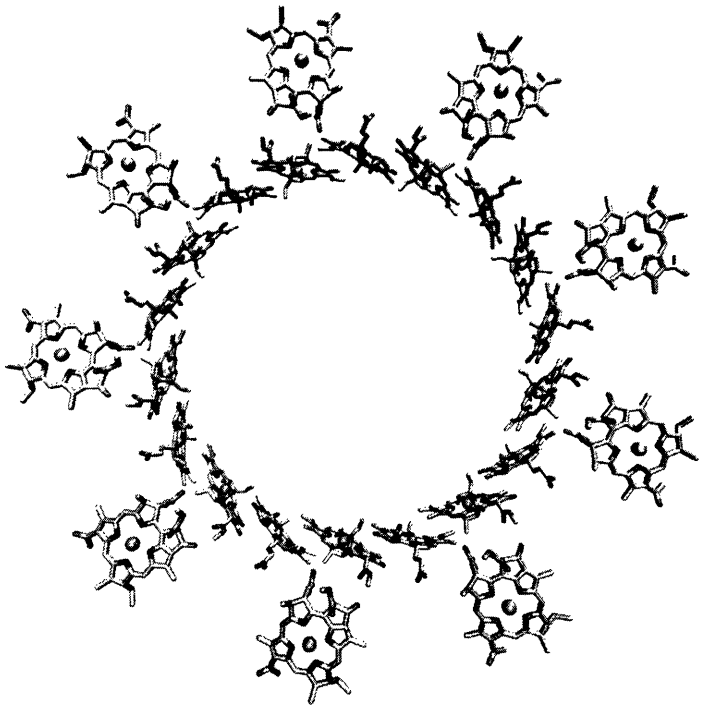

Figure 6-1: Arrangement of the pigments in the LH2 complex of *Rps. acidophila.* This is a top view showing the 9 B800 BChl *a* molecules (the outer ring) and the 18 B850 BChl *a* molecules (the inner ring). The X-ray data have been taken from the RCSB Protein Data Bank (PDB ID: 1kzu).

neighbor distance between B800 and B850 rings is 17.6 Å, results in a B800-B850 coupling of about 30 cm-1.

In order to understand the nature of excitations and dynamics of excitation energy transfer (EET) in the LH2 complexes of purple bacteria, a molecular-level description is essential. Spectroscopic studies, especially recent single-molecule (SM) experiments, have significantly advanced our knowledge about these processes; however, a detailed understanding is still not at hand, mainly due to the difficulty of characterizing the quasi-static disorder due to the slow fluctuations of local protein environments and pigment structures in LH2. These fluctuations can lead to disorder in the excitation energies of the BChl molecules in a single LH2 complex (intra-complex energy disorder). In addition, both ensemble[9] and SM[10] spectroscopy show that there is also inter-complex disorder that changes the average excitation energy in each LH2

complexes.

The magnitude of energetic disorders characterize the energy transfer dynamics and spectroscopic properties of the LH2 complex; for example, the extent to which the excitations are delocalized depends on the relative magnitude of the spread in site energies disorders (Δ) to the electronic coupling (J). It has been clearly established that quantum coherence in the B850 ring of LH2 plays a crucial role in light-energy harvesting, storage, and transfer [11, 12, 13]. Because the electronic coupling between B850 BChls is sufficiently large [1, 14, 3], a delocalized Frenkel exciton description is required for B850 excited states. In contrast, for the B800 ring, excitations are usually considered to be localized on individual pigments because the couplings between B800 BChls are smaller than the energetic inhomogeneities in the system [10, 9]. Although SM studies using polarization-dependent spectroscopic techniques have provided strong evidence that excitations in the B800 band are delocalized on two or three pigments [15, 16], the effect of the B800 coherence is usually not considered. In this chapter, we focus on the B800 ring of *Rps. acidophila* and demonstrate that, contrary to conventional wisdom, quantum coherence in the B800 ring cannot be neglected. We show that the type and degree of disorder in the B800 ring can be extracted from the ensemble spectrum, and that the effect of coherence in the B800 ring subtly changes both the spectrum and EET dynamics in the LH2.

6.2 Theoretical Methods

To describe excitations on a B800 ring, we consider a system of N pigments arranged in a circular geometry and described by the following exciton Hamiltonian:

$$H = \sum_{n=1}^{N} E_n |n\rangle\langle n| + \sum_{n \neq m} J_{nm} |n\rangle\langle m|, \tag{6.1}$$

where $|n\rangle$ denotes a BChl Q_y excited state localized at site n, E_n is the excitation energy of $|n\rangle$, and J_{nm} is the electronic coupling between $|n\rangle$ and $|m\rangle$. For the B800 ring,

the couplings between the next-nearest-neighbor BChl molecules are weak, therefore we consider only the nearest-neighbor couplings $J_{n,n\pm1}$ (note that for the ring structure, $n = N + 1$ denotes the $n = 1$ site). A reasonable model for B800 excitations should include intercomplex energy disorder and intracomplex energy disorder (diagonal disorder). In addition, due to slow fluctuations of pigment orientations and positions, disorder in the nearest-neighbor couplings (off-diagonal disorder) must be considered too. Therefore, to model static disorder, we treat E_n and $J_{n,n+1}$ as having random components:

$$\begin{aligned} E_n &= E(0) + \delta E_I + \delta E_D(n), \\ J_{n,n+1} &= J(0) + \delta J(n). \end{aligned} \tag{6.2}$$

where $E(0)$ and $J(0)$ are ensemble average values of the site-energy and the electronic coupling, respectively; δE_I is the intercomplex energy disorder for the ring, $\delta E_D(n)$ is the intracomplex disorder (diagonal disorder) at site n, and $\delta J(n)$ is the off-diagonal disorder between nearest-neighbor sites n and $n + 1$. For simplicity, we assume a phenomenological disorder model and treat δE_I, $\delta E_D(n)$, and $\delta J(n)$ as independent Gaussian random variables with zero mean and standard deviations σ_I, σ_D, and σ_J, respectively. Figure 6-2 illustrates the different types of disorders.

Sampling over the distribution of static disorders is done by performing Monte Carlo simulations. Given σ_I, σ_D, and σ_J, we numerically generate and diagonalize H to obtain eigenstates,

$$H|\phi_\alpha\rangle = \varepsilon_\alpha|\phi_\alpha\rangle,$$

where ε_α is the excitation energy of the the α-*th* exciton state, and the eigenfunction $|\phi_\alpha\rangle$ can be written as a superposition of the site-localized states:

$$|\phi_\alpha\rangle = \sum_n c_n^\alpha |n\rangle.$$

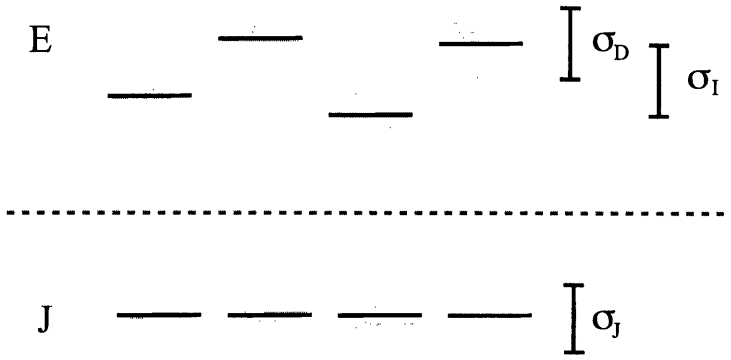

Figure 6-2: A schematic representation of different types of static disorders. In this work, we consider static disorder as Gaussian random variables with zero mean. The degrees of intercomplex energy disorder, intracomplex energy disorder (diagonal disorder), and disorder in the nearest-neighbor couplings (off-diagonal disorder) are represented by standard deviations σ_I, σ_D, and σ_J, respectively.

If the transition-dipole moment of $|n\rangle$ is denoted as $\vec{\mu}_n$, the transition-dipole moment of the α-*th* exciton state $\vec{M}_\alpha$ is

$$\vec{M}_\alpha = \sum_n c_n^\alpha \vec{\mu}_n.$$

Therefore, the ensemble absorption spectral lineshape due to inhomogeneous broadening can be represented as a sum of sticks,

$$I(\omega) = \langle \sum_\alpha |\vec{M}_\alpha|^2 \delta(\omega - \varepsilon_\alpha) \rangle_s, \tag{6.3}$$

where the bracket $\langle \ldots \rangle_s$ represents the ensemble average over static disorders. Monte Carlo simulations are carried out to sample disorders and compute transition-dipole moments $\vec{M}_\alpha$ and ensemble absorption spectrum $I(\omega)$. Typically, a simulation averages over 100,000 realizations of disordered Hamiltonian, each with a randomly generated site energies and couplings according to Eq. (6.2). Note that we only consider static disorder at this stage; electron-phonon coupling and other dynamical effects are neglected. Because the B800 BChls are weakly coupled to phonon modes and the observed homogeneous linewidth is much smaller than the inhomogeneities in the B800 band, at low temperatures static disorder dominates the lineshape and

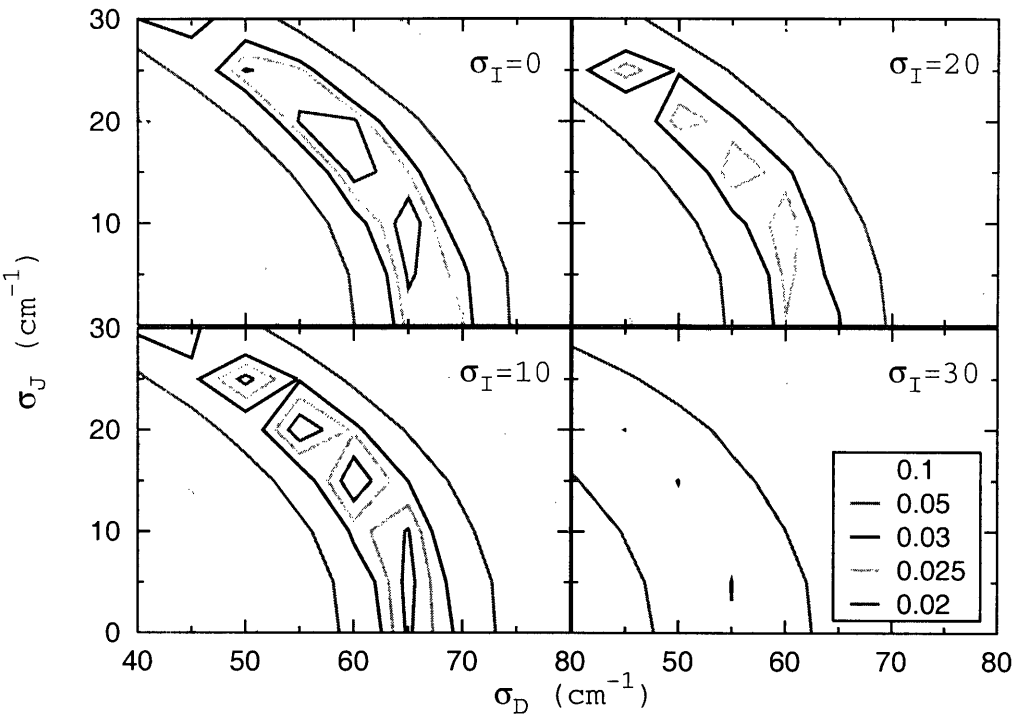

Figure 6-3: Root-mean-square deviation (RMSD) map for simulated ensemble B800 absorption spectra. The contour maps show the RMSD values obtained by comparing the simulated spectrum using a particular set of disorder parameters (σ_I, σ_D, and σ_J) to a low-temperature ensemble spectrum of *Rps. acidophila* from the Köhler group.

dynamical effects are negligible [15, 17].

6.3 B800 Absorption Spectrum

We examine the B800 ring of *Rps. acidophila* for which $N = 9$ and $J(0) = -27$ cm^{-1} [7]. In addition, we assume $|\vec{\mu}_n| = \mu_0$ with dipole orientations taken from the B800 BChl NB to ND directions in the X-ray data [4]. Spectra with a broad range of σ_I, σ_D, and σ_J are simulated and compared to a low-temperature ensemble spectrum of *Rps. acidophila*. The B800-only spectrum is obtained by subtracting a simulated B850 spectrum from an LH2 absorption spectrum at 6K from the Köhler group. The B850 spectrum is generated using the lineshape theory developed in Ref. [18]. To fit the B850 part of the LH2 spectrum, we chose for B850 BChl molecules a Gaussian energy disorder and dipole orientation disorder with σ equals to 220 cm^{-1}

and 10°, respectively. More details about our model of the B850 ring is described in the Appendix.

Our model enables us to extract detailed information regarding the degree of static disorder (σ_I, σ_D, and σ_J) from the ensemble spectrum. In Fig. 6-3, we show contour maps of the root-mean-square deviation (RMSD) calculated by comparing the simulated spectrum to the low-temperature ensemble spectrum. Note that a smaller RMSD value indicates a better fit to the experimental spectrum. We find reasonable fits located at $\sigma_I = 10 \pm 5$ cm^{-1}, $\sigma_D = 60 \pm 10$ cm^{-1}, and $\sigma_J = 15 \pm 5$ cm^{-1}. From these RMSD maps, we conclude that for the B800 ring of *Rps. acidophila* at low temperature, the inter-complex inhomogeneity is minor ($\sigma_I < 20$ cm^{-1}), the diagonal disorder σ_D is around 60 cm^{-1}, and the off-diagonal disorder σ_J is around 15 cm^{-1}. Note that no region with small RMSD value can be found around the $\sigma_J = 0$ line, thus, our fit also indicates that the off-diagonal disorder *cannot* be ignored. In addition, our estimate of σ_D is in excellent agreement with SM experiments [10], providing an independent confirmation to the interpretation of the SM experiments, and demonstrating the possibility of extracting the degree of disorder and coherence from ensemble measurements.

Figure 6-4(a) shows the simulated density of states and the spectral lineshape for an ensemble of B800 rings with $\sigma_I = 10$ cm^{-1}, $\sigma_D = 60$ cm^{-1}, and $\sigma_J = 15$ cm^{-1}. While the density of states is a symmetric function, the spectral lineshape is asymmetric. The maximum of the spectral lineshape is red-shifted from the average energy, and a pronounced tail in the blue side of the band can be clearly seen. The blue tail agrees with ensemble measurements. In Fig. 6-4(b), we compare the simulated spectrum to the low-temperature B800-only ensemble spectrum. The excellent agreement indicates that although the B800 lineshape is dominated by inhomogeneous line broadening, as expected, the effect of coherence exists and results in the blue tail.

Since the absorption spectrum is modeled as the density of states weighted by the transition dipole strength $|\vec{M}_\alpha|^2$ [Eq. (6.3)], the asymmetric lineshape indicates an asymmetric distribution in transition dipole strengths. Figure 6-4(c) shows the distribution of transition dipole moments for 100 realizations of B800 rings and the

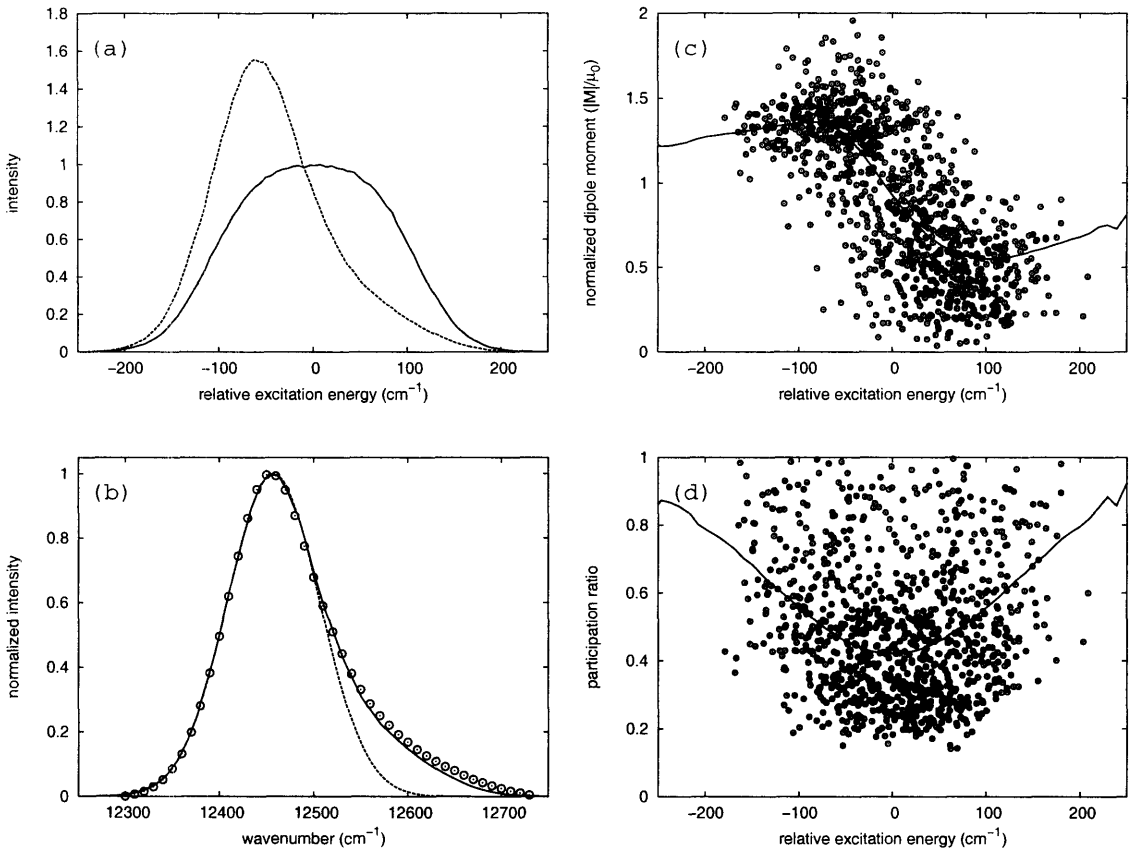

Figure 6-4: Simulation results for an ensemble of the B800 rings from *Rps. acidophila* using $\sigma_I = 10$ cm^{-1}, $\sigma_D = 60$ cm^{-1}, and $\sigma_J = 15$ cm^{-1}. (a) the simulated density of states (solid line) and the inhomogeneous spectral lineshape (dashed line). (b) a comparison of the simulated spectrum (solid line) with the ensemble absorption spectrum (open circle). The small discrepancy close to the blue edge of the band can be explained by vibrational origins. A Gaussian fit to the red side of the simulated spectrum (dashed line) is also presented to emphasize the long tail at the blue side of the band. (c) scatter plot of participation ratio and (d) amplitude of dipole moment as a function of excitation energy for exciton states in the B800 ring. The solid lines are average values as a function of the excitation energies.

average dipole moment as a function of the excitation energies. Clearly, the distribution exhibits an anti-correlated behavior around the center of the band; the states in the red side of the band has stronger dipole strengths than the states in the blue side of the band. For excitations in both edges of the band, the transition dipole moment is close to 1. The redistribution of dipole moments in the B800 band indicates that the B800 excitations are coherently delocalized to some extent.

To characterize the nature of the B800 excitations, we compute the participation ratio $P_\alpha = \sum_n |c_n^\alpha|^4$ [19] for the B800 exciton states. The participation ratio comes in as the fourth power because it measures the spatial overlap of the probability densities of the exciton state. Note that the inverse of P_α is a measure of the delocalization length for the excited state. Figure 6-4(d) shows the distribution of the participation ratio. The average participation ratio ranges from 0.4 in the center to about 0.9 in both edges of the band, indicating that exciton states at the edges of the band are more localized, as expected. In addition, we see a broad distribution for the participation ratios across the band, and a majority of the states have participation ratio in a range from 0.25 to 0.6, corresponding to delocalized excitons on 2-4 pigments.

For the set of disorder parameters that reproduces the low-temperature ensemble spectrum of the B800 ring of *Rps. acidophila*, our calculation clearly shows that the coherence in the B800 ring cannot be neglected, and the blue tail in the ensemble spectrum is actually a signature of the quantum coherence. In Ref. [20], Matsuzaki *et al.* studied an LH2 complex of *Rps. acidophila* containing only one B800 BChl molecule, with no possible coherence. The B800-deficient absorption spectrum they measured clearly shows a more Gaussian-like profile, a strong evidence supporting our results. Note that a pronounced blue tail is also observed in the B800 absorption spectrum at room temperatures, suggesting that the dynamical localization effect at room temperatures does not fully destroy the coherence in the B800 ring.

Since the average participation ratio is close to 0.5 in a broad range of the B800 band, a reasonable zeroth-order description for the B800 excited states is a coherent excitation delocalized on nearest-neighbor dimers. We have simulated the B800 spectrum using a dimer Hamiltonian with diagonal and off-diagonal static disorder,

and the result successfully captures the important spectral signatures. In the following, we will apply the dimer picture to examine the effect of B800 coherence on the dynamics of B800 intra-band and B800→B850 inter-band EET.

6.4 Effect of Coherence on the Dynamics of EET in Single LH2

6.4.1 Dynamics of B800 intraband transfer

Spectroscopic experiments have identified a fast decay channel with wavelength dependent rates in the blue side of the B800 band [21, 22, 10, 23]. This extra decay channel has been attributed to B800 intraband EET [23, 24], and its dynamics has been described either as incoherent hopping of excitations between monomers [9, 24, 25] or coherent relaxation in the exciton manifold [10]. However, so far no theoretical model can quantitatively explain the wavelength dependent rates measured in hole-burning experiments.

In this section, we apply a simplified dimer exciton-bath to describe the B800 intraband transfer. Based on Eq. (6.1) and (6.2), we consider a disordered exciton Hamiltonian for a pair of B800 BChl molecules. The total Hamiltonian including baths is $H = H_0 + H_b + V$, where H_0 is the dimer exciton Hamiltonian, H_b is the bath Hamiltonian, and V describes the system-bath interactions. Based on Eq. (6.1), we consider a disordered dimer exciton Hamiltonian

$$H_0 = E_1|1\rangle\langle 1| + E_2|2\rangle\langle 2| + J_{12}(|1\rangle\langle 2| + |2\rangle\langle 1|),$$

where the site energies E_1 and E_2 and electronic coupling J_{12} are treated as random variables according to Eq. (6.2). The two exciton states of H_0 will be denoted as $|\phi_+\rangle$ and $|\phi_-\rangle$, which satisfy

$$H_0|\phi_\pm\rangle = E_\pm|\phi_\pm\rangle,$$

where the exciton energies $E_\pm = (E_1 + E_2)/2 \pm \sqrt{(E_1 - E_2)^2/4 + J^2}$. For H_b and V, we consider independent harmonic baths ($\hbar = 1$)

$$H_b = \sum_n \omega_n (b_n^\dagger b_n + 1/2),$$

and a general linear coupling term

$$V = B_1|1\rangle\langle 1| + B_2|2\rangle\langle 2|) + B_j(|1\rangle\langle 2| + |2\rangle\langle 1|),$$

where $B_\alpha = \sum_n g_{n\alpha}(b_n^\dagger + b_n)$ for $\alpha = 1, 2, j$. Note that B_1 and B_2 represent diagonal linear coupling to phonon modes that modulate site-energies of pigment 1 and 2, respectively; and B_j represents off-diagonal linear coupling to phonon modes that modulate electronic couplings between these two pigments. The electron-phonon coupling term in the excitonic basis ($|\phi_\pm\rangle$ basis) reads

$$\begin{aligned}
\tilde{V} \;=\; & \tfrac{1}{2}(B_1 + B_2)(|\phi_+\rangle\langle\phi_+| + |\phi_-\rangle\langle\phi_-|) \\
& + \tfrac{1}{2\sqrt{E^2+J^2}} \left[|J| \cdot (B_1 - B_2) - 2E\tfrac{|J|}{J} \cdot B_j \right] (|\phi_+\rangle\langle\phi_-| + |\phi_-\rangle\langle\phi_+|) \\
& + \tfrac{1}{2\sqrt{E^2+J^2}} \left[E \cdot (B_1 - B_2) + J \cdot B_j \right] (|\phi_+\rangle\langle\phi_+| - |\phi_-\rangle\langle\phi_-|),
\end{aligned}$$

where we have defined $E = (E_1 - E_2)/2$, and $J = J_{12}$. To calculate the downward ($|\phi_+\rangle \rightarrow |\phi_-\rangle$) relaxation rates, we assume the initial condition of the total system is

$$\rho(0) = |\phi_+\rangle\langle\phi_+| \otimes \rho_b^{eq},$$

where

$$\rho_b^{eq} = \frac{\exp(-\beta H_b)}{\mathrm{Tr}_b\{\exp(-\beta H_b)\}},$$

and Tr_b means "trace over the bath degrees of freedom". For weak electron-phonon couplings appropriate for BChl molecules, we neglect the back reaction (justified at low temperature) and apply the first-order time-dependent perturbation theory to

calculate the probability of finding the excitation at the $|\phi_-\rangle$ state at time t:

$$\begin{aligned} P_-(t) &= \mathrm{Tr}_b\left\{\langle\phi_-|\rho(t)|\phi_-\rangle\right\} \\ &= \int_0^t dt_1 \int_0^t dt_2 \langle A_X(t_1)A_X(t_2)\rangle_{eq} \cdot e^{2iE_+(t_1-t_2)}, \end{aligned} \tag{6.4}$$

where the bath operator

$$A_X(\tau) = \frac{1}{2\sqrt{E^2+J^2}}\left\{|J|\cdot[B_1(\tau)-B_2(\tau)] - 2E\frac{|J|}{J}\cdot B_j(\tau)\right\},$$

and $\langle ...\rangle_{eq}$ means thermal average of over the equilibrium bath states. Taking the derivative of Eq. (6.4) and applying the equilibrium property of the correlation function, we obtain the non-equilibrium downward transition rate

$$k(t) = \frac{dP_-(t)}{dt} = 2Re\int_0^t d\tau \langle A_X(\tau)A_X\rangle_{eq}\cdot e^{2iE_+\tau} \tag{6.5}$$

For simplicity, we assume a short relaxation time for the bath, therefore, the steady-state rate $k(\infty)$ can be used. In addition, we assume that B_1, B_2, and B_j are not correlated, i.e. $[B_\alpha, B_\beta] = 0$ for $\alpha, \beta = 1, 2, j$. Therefore, the bath correlation function factorizes and the rate $k(\infty)$ can be divided into contributions from the diagonal and off-diagonal electron-phonon couplings, $k(\infty) = \Gamma_d + \Gamma_j$, where

$$\Gamma_d = \frac{J^2}{2(E^2+J^2)} Re\int_0^\infty e^{i(E_+-E_-)\tau}[C_1(\tau)+C_2(\tau)]d\tau, \tag{6.6}$$

$$\Gamma_j = \frac{E^2}{2(E^2+J^2)} Re\int_0^\infty e^{i(E_+-E_-)\tau} C_j(\tau)d\tau, \tag{6.7}$$

Γ_d and Γ_j are relaxation rates due to diagonal and off-diagonal electron-phonon couplings, respectively. In Eq. (6.6) and (6.7), we have defined auto-correlation functions $C_\alpha(\tau) = \langle B_\alpha(\tau)B_\alpha(0)\rangle_{eq}$. The correlation functions can be calculated from a spectral function characterizing the bath. For simplicity, we use the following spectral function:

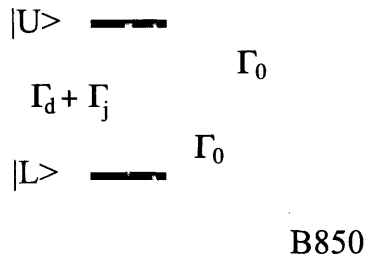

Figure 6-5: Transition pathways included in the calculation of the homogeneous linewidth of B800 excitations.

$$D_\alpha(\omega) = \sum_n g_{n\alpha}^2 \delta(\omega - \omega_n) = \gamma_\alpha (0.5\omega + 0.58\frac{\omega^2}{\omega_c}) e^{-\omega/\omega_c}, \tag{6.8}$$

where γ_α represents relative coupling strengths to the phonon modes, and ω_c is a cut-off frequency. $\omega_c = 100$ cm^{-1} is used in our calculations. The algebraic-exponential form of the spectral function is justified because it reproduces the BChl absorption spectrum [26, 18]. To calculate the homogeneous linewidth of B800 excitations, we assume the lifetime of B800 excitations is determined exclusively by the B800 downward relaxation and B800→B850 EET, as shown in Fig. 6-5. At low temperatures, the back reactions can be neglected and the homogeneously broaden lineshape for each B800 exciton state is a Lorentzian. The linewidths for the blue state and red state are $\Gamma_B = \Gamma_0 + \Gamma_d + \Gamma_j$, and $\Gamma_R = \Gamma_0$, respectively, where we have assumed a constant B800→B850 rate Γ_0.

Using the degrees of disorders that reproduces the B800 ensemble spectrum, $\sigma_I = 10$ cm^{-1}, $\sigma_D = 60$ cm^{-1}, and $\sigma_J = 15$ cm^{-1}, we calculate the average linewidth across the B800 band at zero-temperature. The contributions due to the diagonal and off-diagonal coupling are treated separately, and the low-temperature B800→B850 transfer rate $\Gamma_0 = 1.7$ cm^{-1} is used [10, 27]. In Fig. 6-6, we show two theoretical curves, one with only diagonal electron-phonon coupling (Γ_d-only) and the other with only off-diagonal electron-phonon coupling (Γ_j-only), and compare them with the homogeneous linewidths measured in low-temperature SM experiments [10]. For the

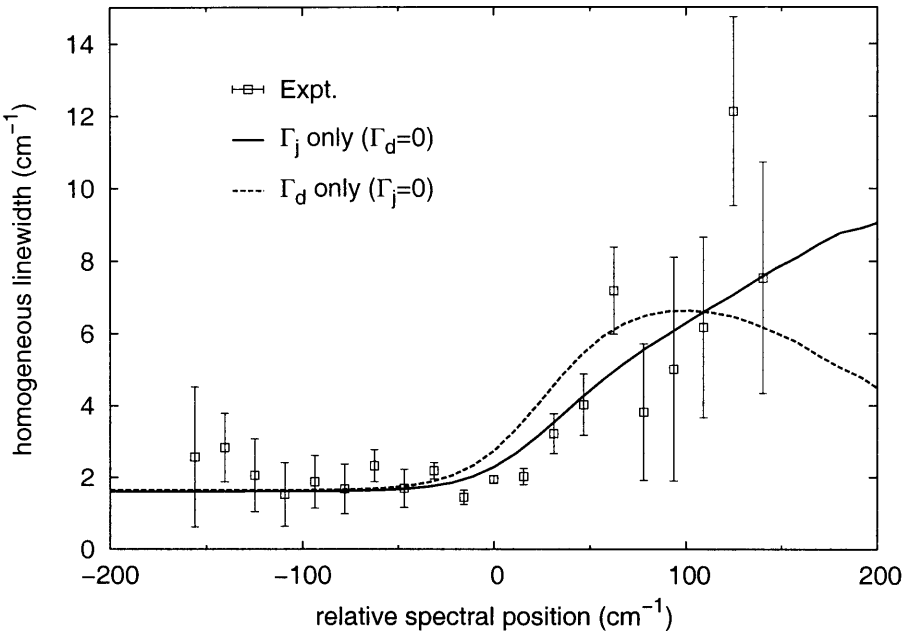

Figure 6-6: Comparison of the theoretical homogeneous linewidth with the single-molecule measurements in Ref. [10]. The relative spectral position is the position of the absorption lines with respect to the spectral mean of a single B800 ring.

Γ_j-only case, we use $\gamma_j = 0.04$ to obtain the best fit to the experiment. For the Γ_d-only case, $\gamma_1 = \gamma_2 = 0.1$ is used. Both models give reasonable e-ph coupling strengths and are in qualitative agreement with experiment. Note that the Γ_j-only model describes the wavelength dependence and the activation of the relaxation channel semi-quantitatively, and is also consistent with hole-burning experiments [21, 24].

In conclusion, the dimer model captures the activation of the B800 intraband transfer and the trend that the EET rate increases towards the blue side of the band. Our result suggests that B800 intraband EET is due to phonon induced relaxation in the exciton manifold, and that the phonon induced fluctuations in J play a major role in the process. A similar notion has been proposed to explain B800 intraband EET [10, 24, 28]; our analysis is the first quantitative model that explains the wavelength dependence and the activation of the relaxation channel. Note that our dimer model includes hopping between nearest-neighbor sites in the $E \gg J$ limit, in which the two exciton states are highly localized.

6.4.2 Dynamics of the B800→B850 transfer

Much effort has been focused on the calculation of the B800→B850 EET rate within a single LH2 [11, 12, 29, 28, 13]. However, while the coherence in the B850 ring has been proved to be crucial for the efficient B800→B850 EET, the B800 coherence was generally neglected. To study the effect of the B800 coherence on the dynamics of B800→B850 EET, we consider theoretical B800→B850 rates for two simplified models for the B800 ring: a B800 BChl monomer, and a B800 BChl dimer. Note that while the monomer model neglects coherence effect in the B800 ring, the dimer model includes the coherence between nearest-neighbor pigments. Therefore, by comparing the theoretical results calculated from these two models, we can access how quantum coherence in the B800 ring alters the dynamics of B800→B850 EET.

To describe the B800 BChls, we use an effective Hamilton with independent harmonic baths and linear diagonal electron-phonon coupling. The average excitation energy of B800 BChls is set to be 515 cm^{-1} higher than that of B850 BChls, and the spectral function in Eq. (6.8) with $\gamma = 0.7$ is employed for the B800 BChl molecules. For the B800 dimer model, the nearest-neighbor coupling is -27 cm^{-1}. To compute the B800→B850 EET rate, we also need a model for the B850 excitations. For the B850 ring, we assume the B850 effective Hamiltonian in Ref. [8] and the e-ph coupling in Ref. [18]. The interactions between B800 and B850 BChls in Ref. [7] are employed. We also consider energetic disorder that reproduce the ensemble spectrum of the LH2 from *Rps. acidophila*. For the static disorder of the B800 ring, Gaussian energetic disorders with the standard deviations 10 cm^{-1} and 65 cm^{-1} are employed for the intercomplex disorder and diagonal disorder, respectively. For the B850 ring, Gaussian energetic disorders with the standard deviations 50 cm^{-1} and 200 cm^{-1} are used for the intercomplex disorder and diagonal disorder, respectively. More than 100000 realizations of disorder are used for the ensemble average. A more detailed account for the model for the B850 ring is presented in Appendix 6.A.

B800→B850 EET rates at $k_BT = 10$ cm^{-1} are calculated using Jang, Newton, and Silbey's multichromophoric Förster resonance energy transfer (MC-FRET) theory

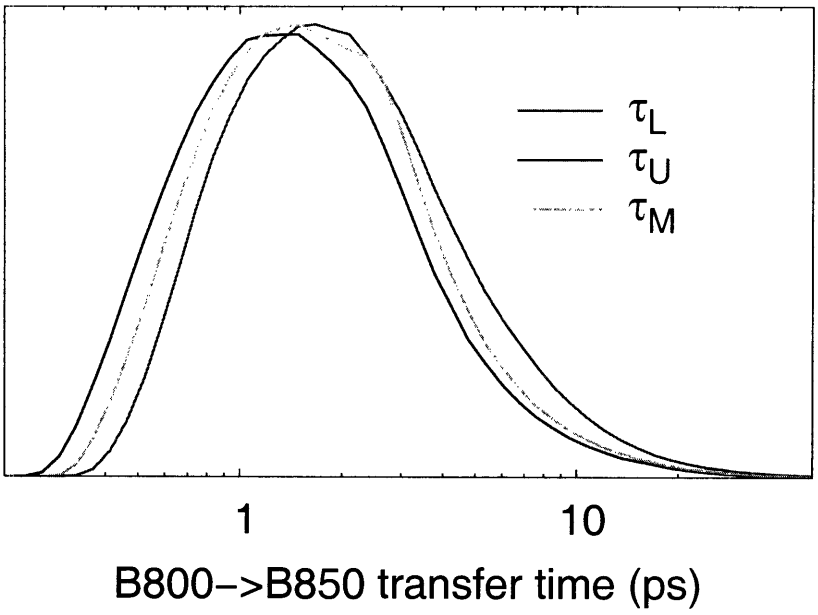

Figure 6-7: The distribution of the B800→B850 EET time at $k_BT = 10$ cm^{-1} calculated from the MC-FRET theory.

[13]. We calculated B800→B850 EET times for the monomer model (τ_M), and for the lower levels (τ_L) and the upper levels (τ_U) of the dimer model. Figure 6-7 shows the distributions of the theoretical B800→B850 EET times. The ensemble average values of τ_M, τ_L, and τ_U are 1.3 ps, 1.6 ps, and 1.2 ps, respectively. At low temperatures, the equilibrium B800→B850 rate is given by τ_L. The theoretical value of 1.6 ps is in agreement with experimental transfer time of 1.6 ± 0.2 ps determined by femtosecond pump-probe spectroscopy [22]. The distributions in Fig. 6-7 shows that most upper levels have faster B800→B850 EET rates than the lower levels. This difference is due to the B800 coherence.

In Fig. 6-7, we show the average rate as a function of the B800 excitation energy for both monomer and dimer models. The monomer model gives a relatively weak energy dependence for the B800→B850 EET rate, a result that is consistent with the measurement made on B800-deficient LH2 [20]. The weak energy dependence can be attributed to the strong site-energy disorder of the B850 BChl molecules, which results in a broad B850 band and almost uniform spectral overlaps between the B800

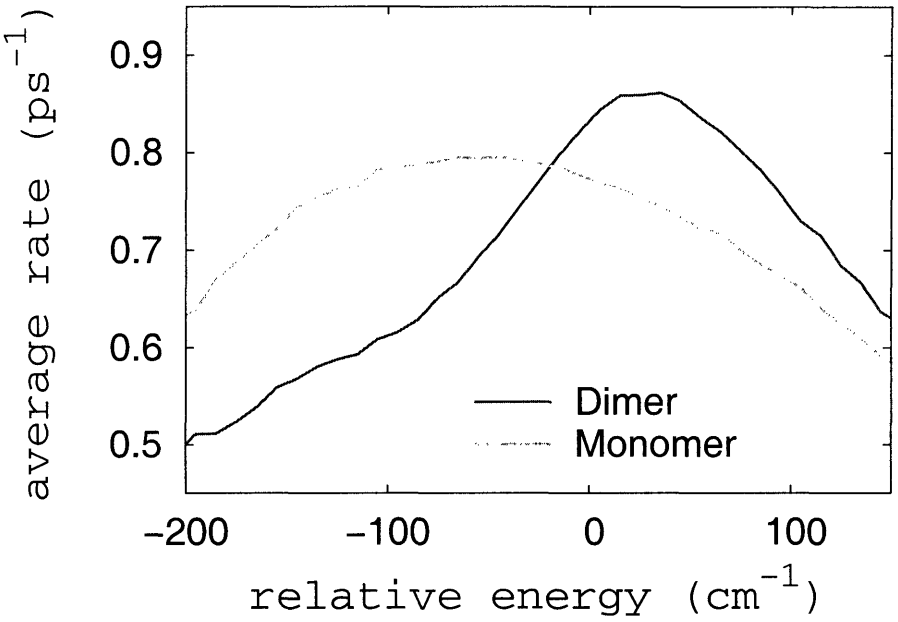

Figure 6-8: The average B800→B850 rate as a function of the energy relative to the average B800 excitation energy.

and upper B850 levels. The dimer model, however, gives a more dramatic energy dependence for the B800→B850 EET rate; the rate is higher in the blue side of the band and lower in the red side of the band. This trend is contrary to the prediction of simple Förster theory, which would give faster rate for states in the red side of the band because of their stronger dipole strengths [see Fig. 6-4(c)]. Our results demonstrate the importance of the B800 coherence and multichromophoric effects for the light-harvesting in LH2.

With this particular B850 model Hamiltonian, our calculations suggest that the B800 coherence reduces the B800→B850 EET rate at low temperatures. At room temperature, however, the rapid B800 intraband EET allows the upper levels to dominate the B800→B850 dynamics, because both upper and lower levels can now transfer energy to the B850 ring. Thus the efficient B800 intraband EET, due to the B800 coherence, is likely to assist the B800→B850 EET at room temperature. To demonstrate the effect, we calculate the B800→B850 EET time for the dimer model at high T, $\tau_E = 2\tau_L\tau_U/(\tau_L + \tau_U)$. In Fig. 6-9, the distribution of τ_E is significantly

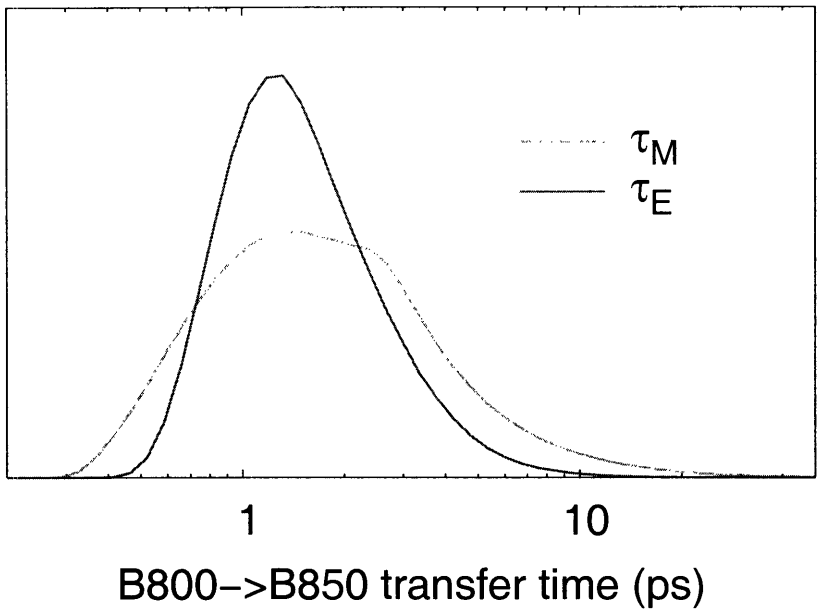

Figure 6-9: A comparison of the distribution of the average dimer B800→B850 EET time τ_E to the distribution of the monomer B800→B850 EET time τ_M. The theoretical B800→B850 EET time is calculated from the MC-FRET theory.

narrower then the distribution of τ_M, indicating that the B800 coherence makes the B800→B850 EET process more uniform and hence more robust.

We have also performed similar calculations using other B850 model Hamiltonians, and found that while the values and profiles in Fig. 6-7 are sensitive to the electronic couplings between B850 BChls, the distribution of τ_E is narrow regardless of the B850 Hamiltonians used. Thus, the coherence in the B800 ring creates more uniform pathways for B800→B850 EET, and increases the rate of EET at room temperature. Finally, we point out that compared to the SM measurements shown in Fig. 6-6, our theoretical result overestimates the B800→B850 rate in the red side of the band by about a factor of 2. While this disagreement does not alter our conclusion about the B800 intraband EET because the absolute value is small compared to the B800 intraband EET rate, we believe it indicates that the B850 Hamiltonian needs improvement. Methods presented in this chapter can be applied to characterize B850 electronic couplings and provide a consistent theoretical model that consistently describes the whole LH2 complex.

6.5 Conclusion

In this chapter, we have demonstrated that the coherence in the B800 ring of the purple bacterium *Rps. acidophila* cannot be neglected, and the long blue tail observed in the B800 band is a signature of the B800 coherence. Our calculation suggests that the B800 intraband transfer is described by energy relaxation in the exciton manifold, and the B800 coherence significantly changes the dynamics of the B800→B850 EET. The results are applicable to light-harvesting complexes from other species and other molecular aggregates. We have largely neglected temperature effects and focused on low temperature data; at finite temperatures, the ideal lineshape theory of Jang and Silbey can be used to incorporate the effect of quasi-static and dynamical disorders [30, 18]. Additional calculations on *Rs. Molischianum* indicate that B800 coherence also plays a similar role in that structure.

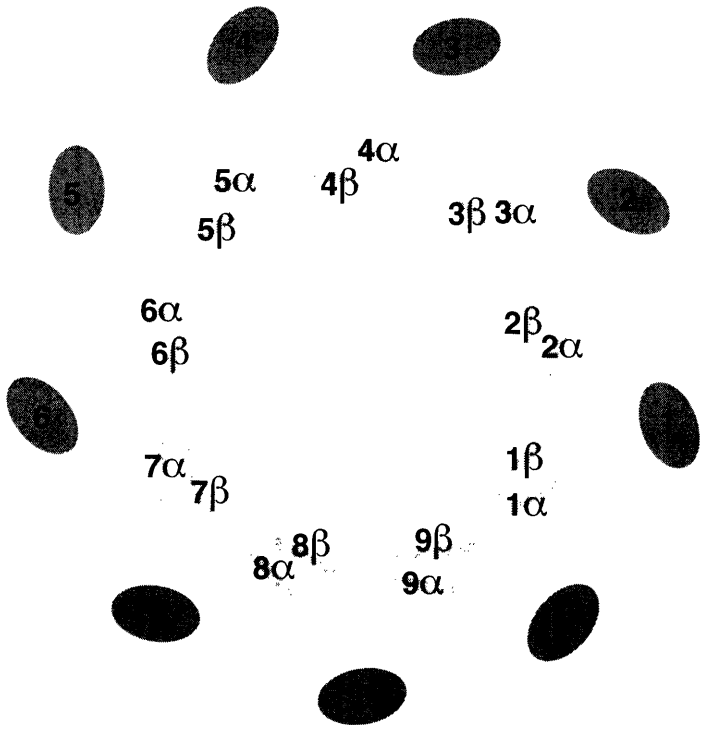

Figure 6-10: A graphical illustration showing the arrangement and labeling of pigments in the LH2 complex of *Rps. acidophila*. The outer ring represents the B800 unit, and the inner ring represents the B850 unit.

Appendix 6.A A Model for the B850 System

To study the B800→B850 EET, we need a model Hamiltonian that describes the B850 excitations. In addition, we need to obtain the disorder parameters for the B850 ring at low temperatures. In this appendix, we describe the model Hamiltonian and the lineshape theory that we used to compute the ensemble spectrum of the B850 ring in the LH2 complex from *Rps. acidophila*. We then fit the simulated spectrum to the B850 part of a low-temperature LH2 ensemble spectrum to obtain the suitable disorder parameters. As a result, we obtain a model for the B850 system that includes both electronic couplings and static disorders, and reproduces the observed ensemble spectrum at low temperatures.

The B850 ring of *Rps. acidophila* consists of 9 $\alpha\beta$ heterodimer of BChl a molecules (see Fig. 6-10). Similar to the B800 ring, the Q_y excitations in the B850 ring can be described by the disordered exciton Hamiltonian shown in Eq. (6.1) and Eq. (6.2).

However, the couplings between B850 BChl molecules are stronger than the B800 couplings, therefore, including only nearest-neighbor interactions is insufficient, and a complete effective Hamiltonian for B850 interactions is required. Over the past few years, several effective Hamiltonian for the B850 ring of *Rps. acidophila* have been purposed [8, 29, 14, 3, 28]. In this work, we adopted the nearest-neighbor and next-nearest-neighbor interactions from the parameterization of Scholes *et al.* [8], because their effective Hamiltonian is known to produce results that are in good agreement with nonlinear spectroscopic experiments [12]. To calculate electronic couplings, they applied a super-molecule approach similar to the one we used to calculate the transfer integrals of polyacene crystals in Chapter 1 [31, 32]. Their *ab initio* molecular orbital calculations employed Hartree-Fock theory with single-excitation configuration-interaction (HF-CIS) to describe the Q_y excited states using the 3-21G* basis set. For the B00-B850 inter-ring couplings, we used the values calculated in Ref. [12]. The B850 model Hamiltonian and the B800-B850 couplings used in this work are listed in Table 6.1. Note that all other interactions not listed in Table 6.1 can be obtained by applying the 9-fold rotational symmetry of the LH2 complex,

We use the following Hamiltonian to describe B850 excitations:

$$\begin{aligned} H_0 &= -\varepsilon_g|g\rangle\langle g| + \sum_n E_n|n\rangle\langle n| + \sum_{n\neq m} J_{nm}|n\rangle\langle m| \\ &\equiv -\varepsilon_g|g\rangle\langle g| + H_e \end{aligned}$$

where $|g\rangle$ denotes the groundstate of the B850 system, $|n\rangle$ denotes a BChl Q_y excited state localized at site n, ε_g is the average gap between the groundstate and the BChl Q_y excited state, E_n is the excitation energy of $|n\rangle$, and J_{nm} is the electronic coupling between $|n\rangle$ and $|m\rangle$. Note that the average matrix elements for H_e are listed in Table 6.1. To include static disorder, we consider intercomplex energy disorder and diagonal disorder for the site-energies $E_n = E_0(n) + \delta E_I + \delta E_D(n)$ [see Eq.(6.2)].

Similar to the exciton-bath Hamiltonian adopted for the B800 BChls in Section 6.4.1, we consider a total Hamiltonian including B850 electronic states and baths $H =$

Table 6.1: B850 Model Hamiltonian and B800-B850 Interactions

Matrix elements of the model B850 Hamiltonian H_e (cm^{-1}):[a]

	1α	1β	2α	2β	3α	3β	4α	4β	5α	5β	6α	6β	7α	7β	8α	8β	9α	9β
1α	390	320	-48	13	-6	3	-2	1	-1	1	-1	1	-2	2	-6	11	-48	255
1β	320	0	255	-37	11	-4	2	-1	1	-1	1	-1	1	-1	3	-4	13	-37

B800-B850 interactions (cm^{-1}):[b]

	1α	1β	2α	2β	3α	3β	4α	4β	5α	5β	6α	6β	7α	7β	8α	8β	9α	9β
B800 BChl 1	-13	5	27	3	-4	5	-3	2	-2	1	-1	1	-1	1	-2	2	-4	7

[a] The nearest-neighbor and next nearest-neighbor interactions are taken from Ref. [8]; all other interactions are calculated assuming dipole-dipole interactions.

[b] The B800-B850 interactions are taken from Ref. [7].

$H_0 + H_b + V$. We consider independent harmonic baths ($\hbar = 1$) $H_b = \sum_\alpha \omega_\alpha (b_\alpha^\dagger b_\alpha + 1/2)$, and a diagonal linear coupling term

$$V = \sum_{n,\alpha} g_{n\alpha} |n\rangle\langle n| \cdot (b_\alpha^\dagger + b_\alpha).$$

In contrast to the B800 spectrum, the homogeneous line broadening in the B850 absorption spectrum is not negligible even at low temperatures, because of the strong electronic couplings in the B850 ring. Therefore, a lineshape theory that describes the homogeneous broadening is needed. Assuming an isotropic electromagnetic field, we apply the expression derived by Jang and Silbey [30] for the single molecule lineshape of a multichromophoric system:

$$I(\omega) \approx -\frac{1}{\pi} Im \mathrm{Tr}_e \left\{ \frac{\sum_{n,m} \vec{\mu}_n \cdot \vec{\mu}_m |n\rangle\langle m|}{\omega + (\varepsilon_g - H_e) + i\mathcal{K}(\omega)} \right\}, \tag{6.9}$$

where $\mathrm{Tr}_e\{...\}$ means "trace over the electronic degrees of freedom", $\mathcal{K}(\omega)$ is the dissipation kernel, and $\vec{\mu}_n$ is the transition-dipole moment of $|n\rangle$, which we use the orientations taken from the B800 BChl NB to ND directions in the X-ray data [4]. The dissipation kernel $\mathcal{K}(\omega)$ is calculated using an expression which is valid up to the second order of the electron-phonon coupling V:

$$\mathcal{K}(\omega) \approx \int_0^\infty dt e^{i\omega t} \mathrm{Tr}_b \left\{ e^{iH_b t} V e^{-iH_b t} e^{-iH_e t} V \rho_b^{eq} \right\}. \tag{6.10}$$

Here, we compute the dissipation kernel $\mathcal{K}(\omega)$ in Eq. (6.10) using the spectral function in Eq. (6.8) with $\gamma = 1$.

Equation 6.9 enables us to calculate the "ideal lineshape" of a single B850 system. To obtain the ensemble spectrum, we use Monte-Carlo simulations to sample and average over static disorder. Figure 6-11 shows a simulated spectrum that includes intercomplex energy disorder with $\sigma_I = 50$ cm^{-1} and diagonal disorder with $\sigma_D = 200$ cm^{-1}. The excellent fit in the B850 part of the spectrum justifies the model B850 Hamiltonian and disorder parameters that we adopted in this chapter.

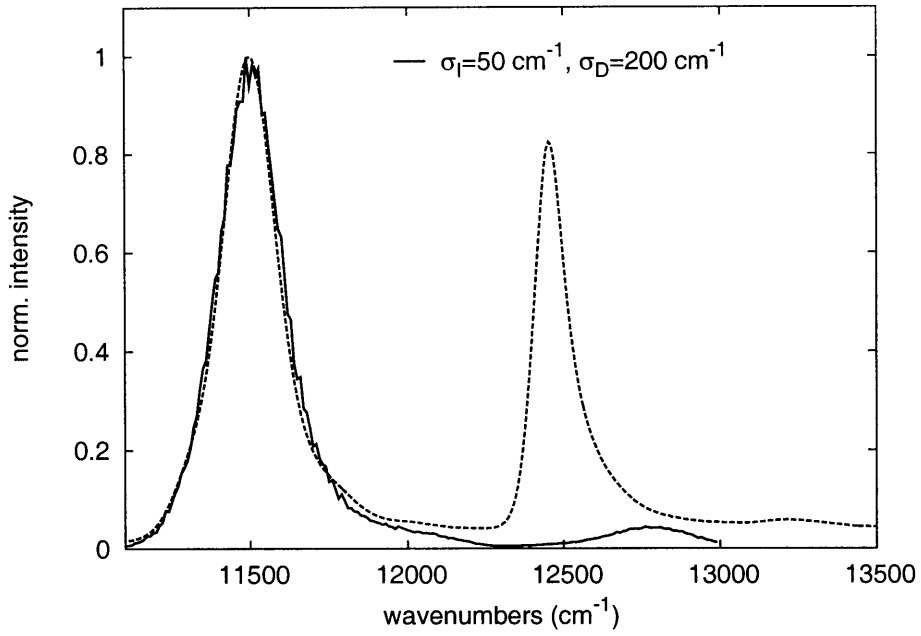

Figure 6-11: A comparison of the simulated B850 absorption spectrum using $\sigma_I = 50$ cm^{-1} and $\sigma_D = 200$ cm^{-1} (solid line) with a ensemble spectrum of the LH2 from *Rps. acidophila* at 6K from the Köhler group (dashed line). The agreement in the B850 part of the spectrum justifies the disorder parameters and spectral function used in this chapter.

Bibliography

[1] V. Sundstrom, T. Pullerits, and R. van Grondelle. Photosynthetic light-harvesting: Reconciling dynamics and structure of purple bacterial LH2 reveals function of photosynthetic unit. *J. Phys. Chem. B*, 103(13):2327 – 2346, 1999.

[2] T. Renger, V. May, and O. Kuhn. Ultrafast excitation energy transfer dynamics in photosynthetic pigment-protein complexes. *Phys. Rep.*, 343(3):138 – 254, 2001.

[3] X. C. Hu, T. Ritz, A. Damjanovic, F. Autenrieth, and K. Schulten. Photosynthetic apparatus of purple bacteria. *Quart. Rev. Biophys.*, 35(1):1 – 62, 2002.

[4] G. McDemott, S. M. Prince, A. A. Freer, A. M. Hawthornthwaite-Lawless, M. Z. Papiz, R. J. Cogdell, and N. W. Isaacs. Crystal-structure of an integral membrane light-harvesting complex from photosynthetic bacteria. *Nature*, 374(6522):517 – 521, 1995.

[5] J. Koepke, X. C. Hu, C. Muenke, K. Schulten, and H. Michel. The crystal structure of the light-harvesting complex II (B800-850) from Rhodospirillum molischianum. *Structure*, 4(5):581 – 597, 1996.

[6] K. Sauer, R. J. Cogdell, S. M. Prince, A. Freer, N. W. Isaacs, and H. Scheer. Structure-based calculations of the optical spectra of the LH2 bacteriochlorophyll-protein complex from Rhodopseudomonas acidophila. *Photochem. Photobiol.*, 64(3):564 – 576, 1996.

[7] B. P. Krueger, G. D. Scholes, and G. R. Fleming. Calculation of couplings and energy-transfer pathways between the pigments of LH2 by the ab initio transition density cube method. *J. Phys. Chem. B*, 102(27):5378 – 5386, 1998.

[8] G. D. Scholes, I. R. Gould, R. J. Cogdell, and G. R. Fleming. Ab initio molecular orbital calculations of electronic couplings in the LH2 bacterial light-harvesting complex of Rps-acidophila. *J. Phys. Chem. B*, 103(13):2543 – 2553, 1999.

[9] R. Agarwal, M. Yang, Q. H. Xu, and G. R. Fleming. Three pulse photon echo peak shift study of the B800 band of the LH2 complex of Rps. acidophila at room temperature: A coupled master equation and nonlinear optical response function approach. *J. Phys. Chem. B*, 105(9):1887 – 1894, 2001.

[10] A. M. van Oijen, M. Ketelaars, J. Kohler, T. J. Aartsma, and J. Schmidt. Spectroscopy of individual light-harvesting 2 complexes of Rhodopseudomonas acidophila: Diagonal disorder, intercomplex heterogeneity, spectral diffusion, and energy transfer in the B800 band. *Biophys. J.*, 78(3):1570 – 1577, 2000.

[11] K. Mukai, S. Abe, and H. Sumi. Theory of rapid excitation-energy transfer from B800 to optically-forbidden exciton states of B850 in the antenna system LH2 of photosynthetic purple bacteria. *J. Phys. Chem. B*, 103(29):6096 - 6102, 1999.

[12] G. D. Scholes and G. R Fleming. On the mechanism of light harvesting in photosynthetic purple bacteria: B800 to B850 energy transfer. *J. Phys. Chem. B*, 104(8):1854 – 1868, 2000.

[13] S. J. Jang, M. D. Newton, and R. J. Silbey. Multichromophoric Forster resonance energy transfer. *Phys. Rev. Lett.*, 92(21):218301, 2004.

[14] M. Ketelaars, A. M. van Oijen, M. Matsushita, J. Kohler, J. Schmidt, and T. J. Aartsma. Spectroscopy on the B850 band of individual light-harvesting 2 complexes of Rhodopseudomonas acidophila I. Experiments and Monte Carlo simulations. *Biophys. J.*, 80(3):1591 – 1603, 2001.

[15] A. M. van Oijen, M. Ketelaars, J. Kohler, T. J. Aartsma, and J. Schmidt. Spectroscopy of individual LH2 complexes of Rhodopseudomonas acidophila: localized excitations in the B800 band. *Chem. Phys.*, 247(1):53 – 60, 1999.

[16] C. Hofmann, M. Ketelaars, M. Matsushita, H. Michel, T. J. Aartsma, and J. Kohler. Single-molecule study of the electronic couplings in a circular array of molecules: Light-harvesting-2 complex from Rhodospirillum molischianum. *Phys. Rev. Lett.*, 90(1):013004, 2003.

[17] C. Hofmann, H. Michel, M. van Heel, and J. Kohler. Multivariate analysis of single-molecule spectra: Surpassing spectral diffusion. *Phys. Rev. Lett.*, 94(19):195501, 2005.

[18] S. J. Jang and R. J. Silbey. Single complex line shapes of the B850 band of LH2. *J. Chem. Phys.*, 118(20):9324 – 9336, 2003.

[19] D. J. Thouless. Electrons in disordered systems and the theory of localization. *Phys. Rep.*, 13(3):93, 1974.

[20] S. Matsuzaki, V. Zazubovich, N. J. Fraser, R. J. Cogdell, and G. J. Small. Energy transfer dynamics in LH2 complexes of Rhodopseudomonas acidophila containing only one B800 molecule. *J. Phys. Chem. B*, 105(29):7049 – 7056, 2001.

[21] C. De Caro, R. W. Visschers, R. van Grondelle, and S. Volker. Interband and intraband energy-transfer in LH2-antenna complexes of purple bacteria - a fluorescence line-narrowing and hole-burning study. *J. Phys. Chem.*, 98(41):10584 – 10590, 1994.

[22] H. M. Wu, S. Savikhin, N. R. S. Reddy, R. Jankowiak, R. J. Cogdell, W. S. Struve, and G. J. Small. Femtosecond and hole-burning studies of B800's excitation energy relaxation dynamics in the LH2 antenna complex of Rhodopseudomonas acidophila (strain 10050). *J. Phys. Chem.*, 100(29):12022 – 12033, 1996.

[23] J. M. Salverda, F. van Mourik, G. van der Zwan, and R. van Grondelle. Energy transfer in the B800 rings of the peripheral bacterial light-harvesting complexes of Rhodopseudomonas acidophila and Rhodospirillum molischianum studied with photon echo techniques. *J. Phys. Chem. B*, 104(47):11395 – 11408, 2000.

[24] V. Zazubovich, R. Jankowiak, and G. J. Small. On B800 -> B800 energy transfer in the LH2 complex of purple bacteria. *J. Luminesc.*, 98(1-4):123 – 129, 2002.

[25] D. Abramavicius, L. Valkunas, and R. van Grondelle. Exciton dynamics in ring-like photosynthetic light-harvesting complexes: a hopping model. *Phys. Chem. Chem. Phys.*, 6(12):3097 – 3105, 2004.

[26] T. Renger and R. A. Marcus. On the relation of protein dynamics and exciton relaxation in pigment-protein complexes: An estimation of the spectral density and a theory for the calculation of optical spectra. *J. Chem. Phys.*, 116(22):9997 – 10019, 2002.

[27] M. Wendling, F. van Mourik, I. H. M. van Stokkurn, J. M. Salverda, H. Michel, and R. van Grondelle. Low-intensity pump-probe measurements on the B800 band of Rhodospirillum molischianum. *Biophys. J.*, 84(1):440 – 449, 2003.

[28] V. Novoderezhkin, M. Wendling, and R. van Grondelle. Intra- and interband transfers in the B800-B850 antenna of Rhodospirillum molischianum: Redfield theory modeling of polarized pump-probe kinetics. *J. Phys. Chem. B*, 107(41):11534 – 11548, 2003.

[29] S. Tretiak, C. Middleton, V. Chernyak, and S. Mukamel. Exciton Hamiltonian for the bacteriochlorophyll system in the LH2 antenna complex of purple bacteria. *J. Phys. Chem. B*, 104(18):4519 – 4528, 2000.

[30] S. J. Jang and R. J. Silbey. Theory of single molecule line shapes of multichromophoric macromolecules. *J. Chem. Phys.*, 118(20):9312 – 9323, 2003.

[31] J. Cornil, J. Ph. Calbert, D. Beljonne, R. Silbey, and J. L. Brédas. Charge transport versus optical properties in semiconducting crystalline organic thin films. *Adv. Mater.*, 12(13):978, 2000.

[32] J. Cornil, J. Ph. Calbert, and J. L. Brédas. Electronic structure of the pentacene single crystal: Relation to transport properties. *J. Am. Chem. Soc.*, 123(6):1250, 2001.

Chapter 7

Markovian Approximation in the Relaxation of Quantum Open Systems

Part of the content in this chapter has been published in the following paper:
Y.C. Cheng and R.J. Silbey. Markovian Approximation in the Relaxation of Open Quantum Systems. *The Journal of Physical Chemistry B*, 109:21399-21405, 2005.

7.1 Introduction

Dissipative dynamics of a quantum system embedded in a complex environment has been of great interest in recent years. Because of its important role in physics and chemistry, numerous works have been devoted to theoretical models for open quantum systems[1, 2]. However, in contrast to classical dissipative processes, that can be satisfactorily described by classical Langevin or Fokker-Planck equations [3], a general theory for quantum dissipation is still considered an unsolved issue.

Despite the difficulty of formulating a general theory, adequate results can be obtained in many limiting cases. We have shown successful applications dealing with electron-phonon coupling and decoherence in quantum computing in this Thesis. As a general theoretical framework, the celebrated reduced dynamics description derived

from projection operator or cumulant expansion techniques has generated promising results over the past few decades. By partitioning the total system into a "system" part and a "bath" part, one can reformulate the exact quantum Liouville equation and perform a mathematically rigorous expansion in the weak-coupling limit. As a result, time-convolution or time-convolutionless quantum master equations describing the dynamics of the reduced system can be derived by following either a chronological ordering prescription (COP) or partial ordering prescription (POP), respectively [4, 5, 6]. These equations are usually non-Markovian and difficult to treat analytically. Therefore, a separation of time scales is usually postulated and the memory effects in the dynamics are then neglected for times greater than the bath relaxation time τ_b. This approximation allows us to derive Markovian master equations (Redfield equations [7]) for the reduced dynamics of the quantum system. All applications covered in the previous chapters of this Thesis are based on dynamical equations of the Markovian nature, i.e. the dynamics of the system does not depend on its memory of the previous history of the trajectory. In this chapter, we will study the applicability of the Markovian approximation in condensed phases.

The applicability of the Markovian approximation has long been criticized in the literature [8, 9]. In addition to the assumption of the short bath relaxation time, it is well known that the Markovian master equations do not always preserve the positivity of the reduced density matrix of the system, thus resulting in physically inconsistent outcomes. Suarez *et al.* have shown that the problem of non-positivity is due to the transient memory effects in a short time scale, and can be repaired by a modification of the initial conditions (slippage) [10]. Gaspard and Nagaoka adopted the slippage idea and developed a slippage superoperator method that can determine the slippage of initial conditions in a consistent way, but the range of applicability of their slippage superoperator has not been fully tested [11]. Despite these stringent conditions and obvious inconsistencies, Markovian master equations have been applied successfully to a broad range of physical and chemical problems. Although non-Markovian approaches have grown in interest recently, Markovian approaches are favored due to their simplicity and computational efficiency [12, 13]. Therefore, a scheme that can

ensure the positivity of the reduced system dynamics in the framework of quantum Markovian equations is desirable.

In this chapter, we examine two problems concerning the applicability of the Markovian approximation, and propose a simple scheme for applying Markovian master equations that is capable of reproducing results from the non-Markovian master equations over a wide range of parameters. In Section 7.2 we shall briefly review the derivation of the Markovian master equation. In Section 7.3 the physical requirements for the Markovian approximation will be examined in detail, and the factors defining the time scale for the non-Markovian dynamics will be clarified. In Section 7.4, we will then formulate a concatenation scheme that avoids using slippage initial conditions and absorbs the transient memory effects in a natural manner. In addition, we show that Gaspard and Nagaoka's slippage superoperator method is not successful of preserving positivity in all cases. Finally, in Section 7.5 we will examine the concatenation scheme by applying it to study the spin-boson problem.

7.2 The Quantum Master Equation

Consider a system S governed by the system Hamiltonian H_S and coupled to a bath B of harmonic oscillators through an interaction linear in the oscillator coordinates ($\hbar = 1$) [3, 14]:

$$\begin{aligned} H &= H_S + H_B + \lambda H_{SB} \\ &= H_S + \textstyle\sum_\alpha \omega_\alpha a_\alpha^\dagger a_\alpha + \lambda S \cdot \sum_\alpha g_\alpha (a_\alpha^\dagger + a_\alpha), \end{aligned}$$

where $a_\alpha^\dagger$ and a_α are the creation and annihilation operators of the α-th bath mode, ω_α is the mode frequency, S is an operator referring to the system degrees of freedom only, and g_α is the coupling constant. The dynamics of the total system can be described by a time-dependent density matrix $\rho(t)$, and follows the Liouville equation

$$\dot{\rho}(t) = -i[H, \rho(t)].$$

To obtain the reduced description for the system, we define the following projection operator $\mathcal{P}$:

$$\mathcal{P}\rho = \rho_b^{eq} \mathrm{Tr}_B \rho, \tag{7.1}$$

where

$$\rho_b^{eq} = \frac{\exp(-\beta H_B)}{\mathrm{Tr}_B\{\exp(-\beta H_B)\}}, \tag{7.2}$$

and Tr_B means "trace over the bath degrees of freedom". The choice of projection operator corresponds to a factorized initial condition for the total system,

$$\rho(0) = \sigma(0) \otimes \rho_b^{eq}, \tag{7.3}$$

where $\sigma(0)$ is an arbitrary state for the system. The reduced density matrix for the system is then defined as

$$\sigma(t) = \mathrm{Tr}_B \rho(t).$$

Following the standard projection operator technique and neglecting all terms of higher order than λ^2,[15] we obtain the differential-integral equation for the reduced density matrix for the system,

$$\begin{aligned} \dot{\sigma}(t) &= -i[H_S, \sigma(t)] + i\lambda^2 \int_0^t \Gamma_i(\tau) \cdot [S, [S_0(-\tau), \sigma(t)]_+] d\tau \\ &\quad -\lambda^2 \int_0^t \Gamma_r(\tau) \cdot [S, [S_0(-\tau), \sigma(t)]] d\tau, \end{aligned} \tag{7.4}$$

where $[...]_+$ denotes the anticommutator, $S_0(\tau) = e^{iH_S\tau} S e^{-iH_S\tau}$, and memory kernels $\Gamma_r(\tau)$ and $\Gamma_i(\tau)$ are the real part and imaginary part of the bath correlation function, respectively (see details in Appendix 7.A). In this linear coupling model, these memory kernels can be explicitly written as

$$\begin{aligned}\Gamma_r(\tau) &= \textstyle\sum_\alpha g_\alpha^2 \cos(\omega_\alpha \tau) \cdot \coth(\beta\omega_\alpha/2), \\ \Gamma_i(\tau) &= \textstyle\sum_\alpha g_\alpha^2 \sin(\omega_\alpha \tau).\end{aligned}$$

Equation (7.4) is the quantum master equation that describes the dynamics of the reduced quantum system. To derive this equation, we have assumed that the system-bath coupling is small, so that we can neglect terms of higher order than λ^2 and replace the evolution kernel in the integrals by the zeroth-order one. Note that in Eq. (7.4) we have adopted the POP approximation and derive the time-convolutionless form of the master equation by replacing $\sigma(t-\tau)$ with $e^{iH_S\tau}\sigma(t)e^{-iH_S\tau}$; in the weak-coupling limit, the COP and POP approximations are equivalent. A formal derivation of Eq. (7.4) using the projection operator technique is given in Appendix 7.A.

Equation (7.4) is not yet a Markovian master equation because the integrals still refer to the initial time. If the bath correlation functions $\Gamma_r(\tau)$ and $\Gamma_i(\tau)$ decay to zero within a finite bath relaxation time τ_b, then for long times $t \gg \tau_b$, we can extend the integrations over τ to infinity and obtain the Markovian master equation:

$$\begin{aligned}\dot{\sigma}(t) &= -i[H_S, \sigma(t)] + i\lambda^2 \int_0^\infty \Gamma_i(\tau) \cdot [S, [S_0(-\tau), \sigma(t)]_+] d\tau \\ &\quad -\lambda^2 \int_0^\infty \Gamma_r(\tau) \cdot [S, [S_0(-\tau), \sigma(t)]] d\tau.\end{aligned} \tag{7.5}$$

This step is the Markovian approximation. The resulting Markovian master equation (Redfield equation) has been studied in innumerable papers in the literature. However, to the best of our knowledge, concrete criteria for the applicability of the Markovian approximation are still unclear. In the next two sections, we will study the applicability of the Markovian approximation, and provide a simple scheme that absorbs the transient memory effects in a straightforward manner.

7.3 The Markovian Approximation

It is convenient to define a spectral strength function for the bath, $J(\omega) = \sum_\alpha g_\alpha^2 \delta(\omega_\alpha - \omega)$, and rewrite memory kernels $\Gamma_r(\tau)$ and $\Gamma_i(\tau)$ as integrals:

$$\begin{aligned} \Gamma_r(\tau) &= \int_0^\infty J(\omega)\cos(\omega\tau)\cdot\coth(\beta\omega/2)d\omega, \\ \Gamma_i(\tau) &= \int_0^\infty J(\omega)\sin(\omega\tau)d\omega. \end{aligned} \tag{7.6}$$

To avoid infrared and ultraviolet divergences in $\Gamma_r(\tau)$ and $\Gamma_i(\tau)$, we assume that $J(\omega)$ has the form ω^s with $s \geq 0$ at small ω, and decays to zero faster than ω^{-1} in the limit of $\omega \to \infty$. In addition, we assume that $J(\omega)$ does not depend on the temperature. These conditions are reasonable assumptions for many physical problems.[16] Also note that if the low frequency behavior of $J(\omega)$ is subohmic (of the form ω^s with $0 < s < 1$ at small ω), the memory kernel $\Gamma_r(\tau)$ would never decay to zero within a finite time scale. In this case, the low frequency modes of the bath dominate the dissipative processes, and Markovian dynamics is inapplicable.

At long times, the integrand in $\Gamma_i(\tau)$ is rapidly oscillating due to the $\sin(\omega\tau)$ term. Therefore, if the spectral function $J(\omega)$ can be treated as a continuous and fairly smooth function, then a time scale τ_b exists due to the cancellation of the rapidly oscillating integrand at large t. This means that the number of bath degrees of freedom must be large, the distribution of bath frequencies has to be dense and spread out, and the coupling strength must vary uniformly with frequency. For $J(\omega)$ with these properties, $\Gamma_i(\tau)$ decays to zero within a τ_b defined by the width of the spectral function $J(\omega)$. If the width of the spectral function is ω_d, then at times $t \gg 1/\omega_d$ the oscillating integrand cancels out and the integral tends to zero, i.e. $\tau_b \sim 1/\omega_d$.

The real part seems more difficult because of the temperature dependence, but we found the temperature has only a minor effect on the bath relaxation time τ_b, provided our assumptions on the properties of the bath are correct. Notice that $\coth(\beta\omega/2)$ is a smooth function that peaks at $\omega \approx 0$, and behaves like $2/\beta\omega$ in a range from $\omega = 0$ to $\omega = 2/\beta$. At low temperatures, this range is small and has little effect

on the shape of the integrand because of the ω^s factor in the spectral function. At high temperatures, this range can be broad, and the hyperbolic cotangent function can be replaced with $2/\beta\omega$. Therefore, the bath relaxation time at high temperature is determined by the width of the function $J(\omega)/\beta\omega$. Since we assume the spectral function decays to zero faster than $1/\omega$, the extra $1/\omega$ frequency dependence has little effect on the width of the function. We argue that τ_b is only weakly dependent on the temperature of the bath, and is largely determined by the properties of the spectral function.

Figure 7-1 shows the normalized memory kernel $\Gamma_r(\tau)/\Gamma_r(0)$ for several form of spectral functions at different temperatures. The time τ_b at which $\Gamma_r(\tau)$ decays to zero depends strongly on the form of the spectral function, but only weakly on the temperature. For the Gaussian bath case, the function $\Gamma_r(\tau)/\Gamma_r(0)$ is almost temperature independent. We emphasize that such a weak dependence in temperature is in contrast to the widely accepted notion that the relaxation time of a general bath decreases when temperature increases. Figure 7-1 indicates that care must be taken when assuming the bath relaxation time is short at high temperatures. Note that the widths of spectral functions used in Fig. 7-1 are set to one; as a result, all memory kernels shown decay within a time scale of order ~ 1.

To summarize, if the spectral function $J(\omega)$ is fairly dense and smooth, and decays to zero reasonably fast in both $\omega \to 0$ and $\omega \to \infty$ limit, then a time-scale $\tau_b \sim 1/\omega_d$ exists. For times $t > \tau_b$, the memory kernels tends to zero and the Markovian approximation is applicable. In addition, for the present model, the bath relaxation time τ_b is solely determined by the properties of the spectral function, and is only weakly dependent on the temperature of the bath.

7.4 Positivity

It is well known that the Markovian master equations derived from the projection operator or cumulant expansion techniques destroy the general positivity of the reduced dynamics. This has been a major problem for the application of the Markovian master

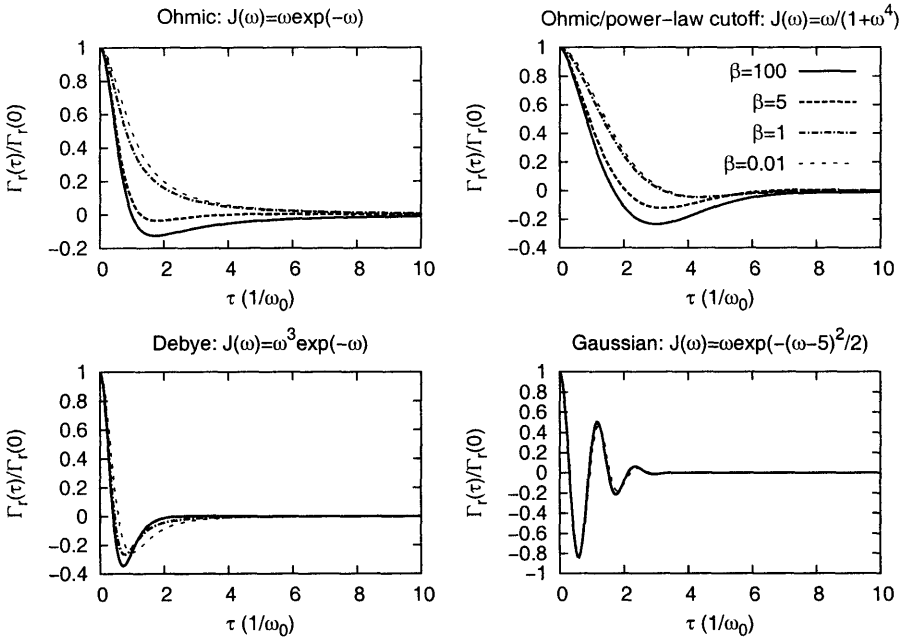

Figure 7-1: Normalized real-part of the bath correlation functions $[\Gamma_r(\tau)/\Gamma_r(0)]$ for baths with different forms of spectral functions at inverse temperatures $\beta = 0.01$ (thin dashed line), $\beta = 1$ (dashed-dotted line), $\beta = 5$ (dashed line), and $\beta = 100$ (solid line). The point where $\Gamma_r(\tau)$ decays to zero is dependent on the form of the spectral function, but only weakly dependent on the temperature. In addition, in general higher temperatures do not correspond to shorter bath relaxation times. The cutoff frequencies are set to 1, so the units of time and β are $1/\omega_0$.

equations. Suarez, Silbey, and Oppenheim have argued that the Markovian master equation is in fact correct, and the source of the inconsistency is due to transient memory effects in a short time scale. In this section, we will present a prescription that quantitatively incorporates the short time memory effects in the Markovian evolution.

The slippage scheme proposed by Suarez, Silbey, and Oppenheim (SSO slippage scheme) aligns the trajectories given by the Markovian evolution and second order perturbation theory (known to be correct at short times), and then extrapolates the Markovian evolution back to zero time to find a set of slipped initial condition. Using the slipped initial condition together with the Markovian master equation correctly produces the long time dynamics of the system, and solves the non-positivity problem. However, the amount of the slippage depends on the particular initial condition and can not be predicted quantitatively. This makes the slippage scheme difficult to implement.

As we pointed out above, Gaspard and Nagaoka suggested a slippage superoperator that can generate slipped initial conditions in a consistent way.[11] Based on the assumption that the dynamics of the Markovian master equation with slipped initial conditions can be approximately equal to that of the direct second-order perturbation theory for intermediate times $t \gg \tau_b$, they integrated the Markovian master equation up to second order in λ and compared the outcome to the result from second-order perturbation theory to obtain the slippage superoperator. Their formal result [Eq. (25) in Ref. 10] is rather complicated and difficult to apply to real systems, therefore they suggested using a short-time expansion to compute the simplified slippage superoperator. They also demonstrated that the simplified slippage superoperator indeed solved the non-positivity problem for a spin-boson system with Debye-like spectral function and gave excellent results. However, the applicability of their method for more general systems has not been tested. In fact, we find that their slippage superoperator does not always give results that satisfy the positivity condition. For example, if we replace the Debye-like spectral function of the spin-boson system studied in Ref. 10 with a Ohmic-like spectral function $J(\omega) = \omega e^{-\omega/\omega_c}$, the slippage superoperator

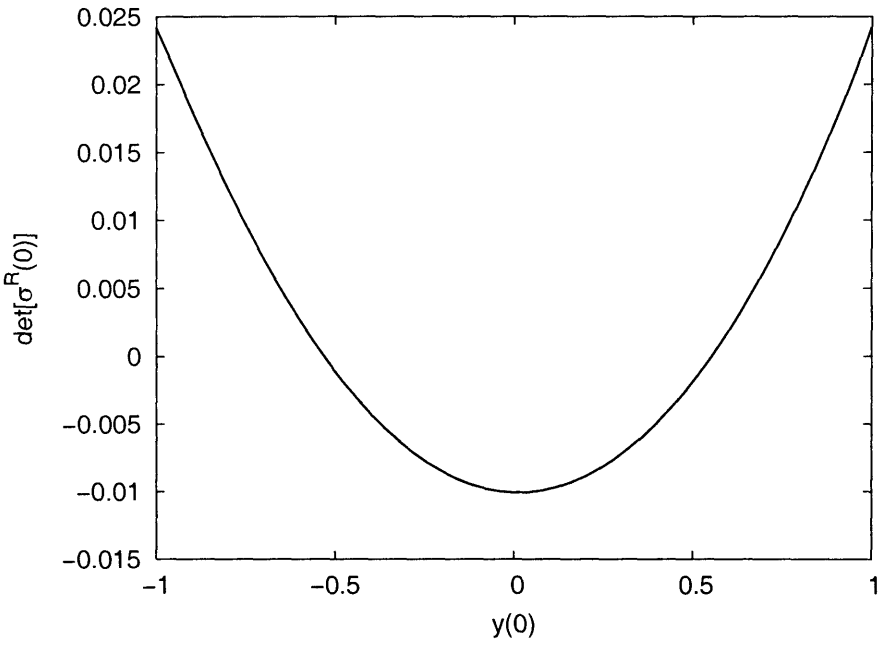

Figure 7-2: Violation of the positivity condition in the slippage superoperator method. We show the determinant of the slipped initial conditions for a spin-boson model with Ohmic-like bath as a function of $y(0)$, where $y(0)$ defines different non-slipped initial density matrix $\rho_s(0) = [I + \sqrt{1-y(0)^2}\sigma_x + y(0)\sigma_y]$. The results are calculated using Eq. (43)-(47) in Ref. 10 and an Ohmic-like spectral function $J(\omega) = \omega e^{-\omega/\omega_c}$. The parameters used are $\Delta = 0.1$, $\lambda = 0.1$, $\omega_c = 1$, and temperature $T = 0$. All notations used here are the same as defined in Ref. 10. The negative values of the determinant for $-0.55 < y(0) < 0.55$ indicate violations of the positivity condition.

gives nonpositive initial conditions in a broad range of parameters. Figure 7-2 shows the determinant of the slipped initial conditions calculated using Eq. (43)-(47) in Ref. 10 and spectral function $J(\omega) = \omega e^{-\omega/\omega_c}$. The negative determinant values shown in Fig. 7-2 clearly indicate that the slippage superoperator breaks down for the spin-boson model with Ohmic-like bath. Therefore, we conclude that the slippage superoperator method in its simplified form [Eq. (26) in Ref. 10] does not always give physically admissible slipped initial conditions. The applicability of the slippage superoperator in its formal form, which does not require the short-time expansion, is still untested.

We now turn to an extension of the SSO slippage scheme in order to increase its range of applicability. A natural and simple modification of the SSO slippage

scheme is to concatenate the second order perturbation theory with the Markovian master equation. The idea is to use second order perturbation theory to propagate the reduced dynamics at short times, and switch to using Markovian master equation at long times. We define a transient time τ_t at which the Markovian master equations are applied with the initial condition given by the second order perturbation theory at time τ_t. To this end, τ_t must be in the regime where both the second order perturbation theory and Markovian master equation are valid, i.e. the memory kernels already decay to zero and the second order perturbation theory is still correct. As we have mentioned in the previous section, the Markovian master equation is valid after times $t > \tau_b \sim 1/\omega_d$. In addition, for the second order perturbation theory to be correct, we need the temperature weighted parameter $J(\omega_0)\coth(\beta\omega_0/2)\tau_t \ll 1$, where ω_0 is the averaged frequency for modes that contribute strongly in the spectral function $J(\omega)$. Therefore we obtain the range of τ_t for the concatenation scheme to be valid:

$$\frac{1}{\omega_d} \ll \tau_t \ll \frac{1}{J(\omega_0)\coth(\beta\omega_0/2)}. \tag{7.7}$$

For simplicity, we choose τ_t as the midpoint between the upper-bound and lower-bound in the log scale:

$$\tau_t = \sqrt{\frac{\omega_d}{J(\omega_0)\coth(\beta\omega_0/2)}}. \tag{7.8}$$

Note that the expression of τ_t in Eq. (7.8) is just a convenient choice. Any choice of τ_t that satisfies Eq. (7.7) should be valid. When second order perturbation theory and Markovian master equation are both valid during intermediate times, the resulting dynamics will not be sensitive to the choice of τ_t and ω_0. Therefore, the requirement of specifying τ_t is not a weak point of the the concatenation scheme. In contrary, the choice of τ_t and Eq. (7.7) provide a measure for the quality of the concatenated dynamics.

There is a fundamental difference between the SSO slippage scheme and the concatenation scheme described here. The slippage scheme implicitly assumes that the

Markovian trajectory generated from an invalid initial condition is parallel to the trajectories from slipped initial conditions, while the concatenation scheme assumes that the new initial condition given by the second order perturbation at the time τ_t correctly absorbs the memory effects. In the next section, we will show that at high temperatures the SSO slippage scheme breaks down, while the concatenation scheme still gives correct description of the long time dynamics.

7.5 The Spin-boson Model

To illustrate the concatenation scheme, we study the spin-boson model in this section. Consider a nondegenerate two-level system coupled to its environment through the system σ_x operator:

$$H = -\frac{\Delta}{2}\sigma_z + \sum_\alpha \omega_\alpha a_\alpha^\dagger a_\alpha + \sigma_x \cdot \sum_\alpha g_\alpha (a_\alpha^\dagger + a_\alpha). \tag{7.9}$$

The model chosen for the bath is a Debye-like bath of independent harmonic oscillators described by the following spectral function:

$$J(\omega) = \eta(\omega^3/\omega_c^2)e^{-\omega/\omega_c}, \tag{7.10}$$

where η is a dimensionless friction constant of order λ^2, and ω_c is an appropriate cutoff frequency for the bath (for example, the Debye frequency of the crystal). Hereafter we will set $\omega_c = 1$, effectively using ω_c as the the unit for energy and $1/\omega_c$ as the unit for time. It is convenient to adopt the Bloch representation and describe the density matrix for the two-level system using a Bloch vector:

$$\sigma(t) = \frac{1}{2}[I + x(t) \cdot \sigma_x + y(t) \cdot \sigma_y + z(t) \cdot \sigma_z].$$

Using equations (7.4)-(7.6), we can easily obtain the non-Markovian master equations for the spin-boson model in the Bloch representation:

$$\begin{aligned}
\dot{x}(t) &= \Delta y(t), \\
\dot{y}(t) &= -[\Delta + 4f(t)]x(t) - 4g(t)y(t), \\
\dot{z}(t) &= -4g(t)z(t) + 4h(t),
\end{aligned} \tag{7.11}$$

where we have defined the following time-dependent functions

$$\begin{aligned}
f(t) &= \int_0^t \Gamma_r(\tau)\sin(\Delta\tau)d\tau, \\
g(t) &= \int_0^t \Gamma_r(\tau)\cos(\Delta\tau)d\tau, \\
h(t) &= \int_0^t \Gamma_i(\tau)\sin(\Delta\tau)d\tau.
\end{aligned} \tag{7.12}$$

The non-Markovian master equations Eq. (7.11) - Eq. (7.12) can not be solved analytically, therefore we propagate the solutions numerically using a 4-*th* order Runge-Kutta method. On the other hand, the Markovian master equations can be solved analytically, yielding

$$\begin{aligned}
x(t) &= \left\{x(0)\cosh(\nu t) - \tfrac{\sinh(\nu t)}{\nu}\left[\Delta y(0) + \gamma x(0)\right]\right\} e^{-\gamma t}, \\
y(t) &= \left\{y(0)\cosh(\nu t) - \tfrac{\sinh(\nu t)}{\nu}\left[\gamma y(0) + \Delta x(0) + 4f(\infty)x(0)\right]\right\} e^{-\gamma t}, \\
z(t) &= z_{eq} + \left[z(0) - z_{eq}\right] e^{-2\gamma t},
\end{aligned} \tag{7.13}$$

where we have used $\gamma = 2g(\infty)$, $z_{eq} = h(\infty)/g(\infty)$, and $\nu = \sqrt{\gamma^2 - \Delta^2 - 4\Delta f(\infty)}$.

Figure 7-3 shows the non-Markovian [Eq. (7.11)] and Markovian [Eq. (7.13)] evolution of the determinant of the reduced density matrix, with initial condition $x(0) = 0$, $y(0) = \sqrt{3}/2$, and $z(0) = 0.5$. The parameters used are $\Delta = 0.1$ and $\eta = 0.01$, and $\beta = 0.5$. We observe that although the Markovian evolution reaches correct thermal equilibrium at long times, and it is negative during a short time period at the beginning, indicating at least one of the two eigenvalues are outside the [0,1] range. Note that at this high temperature regime, the amount by which the positivity is broken can be greater than η, because of the thermal population of the phonon modes. In contrast to the Markovian evolution, the non-Markovian evolution preserves the positivity of the reduced dynamics at all times. This result confirms that the source of the non-positivity problem is the short time memory effects. Numerical

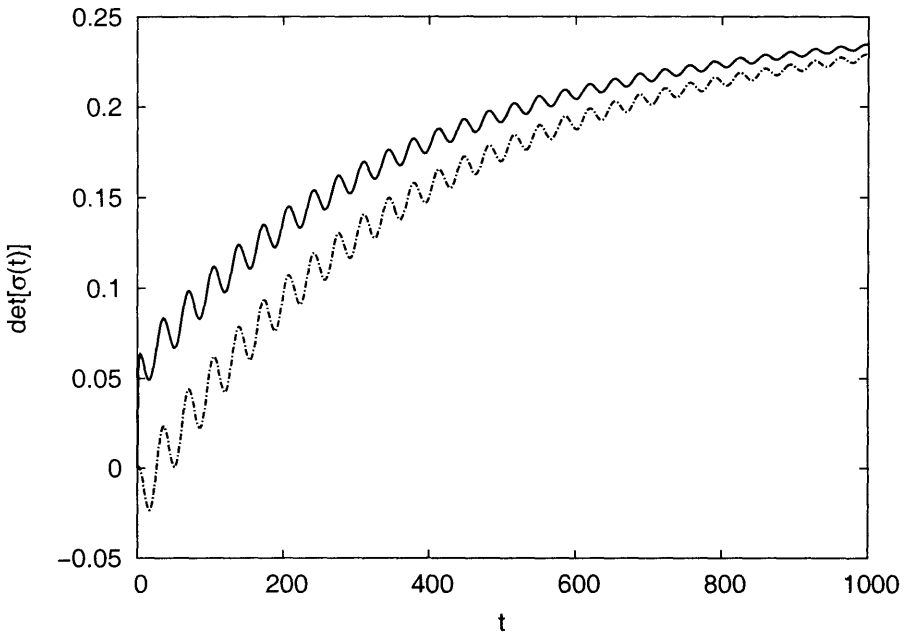

Figure 7-3: Non-Markovian (solid line) and Markovian (dashed-dotted line) dynamics of $\det[\sigma(t)]$. The Debye-like spectral function in Eq. (7.10) is used. The parameters used are $\Delta = 0.1$ and $\eta = 0.01$, and $\beta = 0.5$; the initial condition is $x(0) = 0$, $y(0) = \sqrt{3}/2$, and $z(0) = 0.5$.

studies on non-Markovian quantum master equations have indicated that they provide reasonable results in a wide parameter range.[17, 18, 19, 20] In this weak-coupling case, the non-Markovian master equation correctly describes the dynamics of the open system at all times.

At short times, the second order perturbation theory can provide correct dynamics. The results are

$$\begin{aligned} x_p(t) &= [\cos(\Delta t) - I_1(t)]\, x(0) + [\sin(\Delta t) - I_2(t)]\, y(0), \\ y_p(t) &= [\cos(\Delta t) - I_3(t)]\, y(0) - [\sin(\Delta t) - I_2(t)]\, x(0), \\ z_p(t) &= [1 - I_4(t)]\, z(0) + I_5(t), \end{aligned} \tag{7.14}$$

where we use subscript p to denote the results obtained from the second order perturbation theory; the integrals $I_n(t)$ are

$$
\begin{aligned}
I_1(t) &= 2\int_0^t \Gamma_r(\tau)\left\{(t-\tau)\cos[\Delta(t-\tau)] - \tfrac{1}{\Delta}\sin[\Delta(t-\tau)]\right\}d\tau, \\
I_2(t) &= 2\int_0^t \Gamma_r(\tau)(t-\tau)\sin[\Delta(t-\tau)]d\tau, \\
I_3(t) &= 2\int_0^t \Gamma_r(\tau)\left\{(t-\tau)\cos[\Delta(t-\tau)] + \tfrac{1}{\Delta}\sin[\Delta(t-\tau)]\right\}d\tau, \\
I_4(t) &= 4\int_0^t \Gamma_r(\tau)(t-\tau)\cos(\Delta\tau)d\tau, \\
I_5(t) &= 4\int_0^t \Gamma_i(\tau)(t-\tau)\sin(\Delta\tau)d\tau.
\end{aligned}
\tag{7.15}
$$

Figure 7-4 compares the short time dynamics obtained from the non-Markovian master equation, second order perturbation theory [Eq. (7.14)], and Markovian master equation at three different temperatures. The same parameters and initial condition as in Fig. 7-3 are used. In order to compare the dynamics, the Markovian evolution shown in Fig. 7-4 has been shifted to be aligned with the second order perturbation result. Notice that the amount of slippage and violation of positivity in the Markovian dynamics increases as the temperature increases, and so does the deviation between the second order perturbation theory and the non-Markovian master equation. These trends can be explained by the temperature dependence of the phonon-mode thermal populations. As the temperature increases, the population in phonon modes increases, and the effective system-bath interaction also increases. As a result, the range that the second order perturbation theory is applicable reduces when the temperature increases. Also note that at high temperatures the Markovian dynamics is totally off and can not be aligned with the results calculated from the second order perturbation theory. This indicates that the Markovian dynamics is not necessarily parallel to the correct dynamics of the reduced system (can be seen clearer in Fig. 7-3), especially at high temperatures. In the high temperature regime the SSO slipped initial condition is not well defined and the SSO slippage scheme will be difficult to apply.

We also applied the concatenation scheme to this problem. The temperature dependent transient time τ_t can be estimated from the cutoff frequency ω_c, yielding

$$
\tau_t \approx \sqrt{\frac{\omega_c}{J(\omega_c)\coth(\beta\omega_c/2)}}.
$$

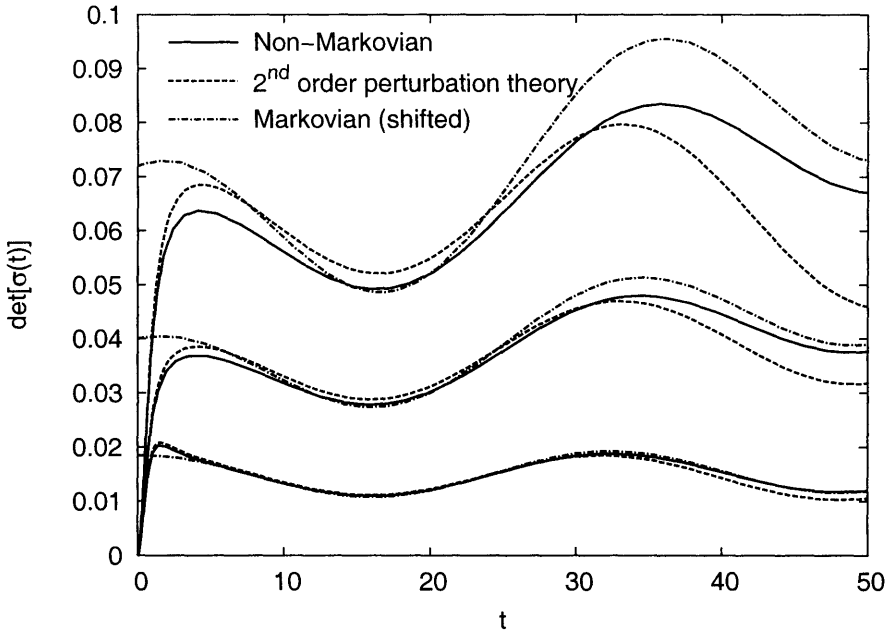

Figure 7-4: Short time dynamics of $\det[\sigma(t)]$ at different temperatures (from bottom to top: $\beta = 10$, $\beta = 1$, and $\beta = 0.5$). Dynamics obtained from the non-Markovian master equation (solid lines), second order perturbation theory (dashed lines), and Markovian master equation (dashed-dotted lines) are shown for each temperatures. The Debye-like spectral function in Eq. (7.10) is used. The parameters used are $\Delta = 0.1$ and $\eta = 0.01$, and the initial condition is $x(0) = 0$, $y(0) = \sqrt{3}/2$, and $z(0) = 0.5$.

For $t < \tau_t$, the second-order perturbation theory [Eq. (7.14)] is used. For $t > \tau_t$, the second-order perturbation theory to compute the initial condition at $t = \tau_t$ for the Markovian dynamics. Using Eq. (7.13)-(7.15), we obtain the concatenation result for $t > \tau_t$ explicitly:

$$\begin{aligned}
x(t) &= \left\{ x_p(\tau_t)\cosh[\nu(t-\tau_t)] - \tfrac{\sinh[\nu(t-\tau_t)]}{\nu}\left[\Delta y_p(\tau_t) + \gamma x_p(\tau_t)\right] \right\} e^{-\gamma(t-\tau_t)}, \\
y(t) &= \left\{ y_p(\tau_t)\cosh[\nu(t-\tau_t)] - \tfrac{\sinh[\nu(t-\tau_t)]}{\nu}\left[\gamma y_p(\tau_t) + \Delta x_p(\tau_t) + 4f(\infty)x_p(\tau_t)\right] \right\} e^{-\gamma(t-\tau_t)}, \\
z(t) &= z_{eq} + \left[z_p(\tau_t) - z_{eq}\right] e^{-2\gamma(t-\tau_t)}.
\end{aligned} \tag{7.16}$$

Note that there is no adjustable parameters in this scheme. Comparing to Eq. (7.13), we can see that simple slipped initial conditions in the Markovian master equation cannot reproduce the concatenation result in Eq. (7.16). This indicates the fundamental difference between the SSO slippage scheme and the concatenation scheme proposed here. Figure 7-5 shows the short time dynamics obtained form the concatenation scheme together with the dynamics from non-Markovian master equation. The same dynamics at a longer time period is shown in Fig. 7-6. Compared to the Markovian dynamics shown in Fig. 7-3, the simple concatenation scheme gives dramatic improvement. Clearly, the concatenation scheme adequately reproduces the correct dynamics at both short and long times. At high temperatures, small deviations from the non-Markovian results exist at short times. The deviations can be ascribed to the errors in the second order perturbation theory, and do not change the long time dynamics. In fact, Fig. 7-6 shows that the concatenation scheme gives results that are in excellent agreement with the non-Markovian master equation even at high temperatures.

We have also applied the concatenation scheme to a similar spin-boson model with an Ohmic-like spectral function $J(\omega) = \omega e^{-\omega/\omega_c}$. In this case, the concatenation scheme produces results that satisfy the positivity condition at all times in all parameter and initial condition range examined. Given the simplicity and the clear background of the concatenation scheme, we expect that it is generally applicable in

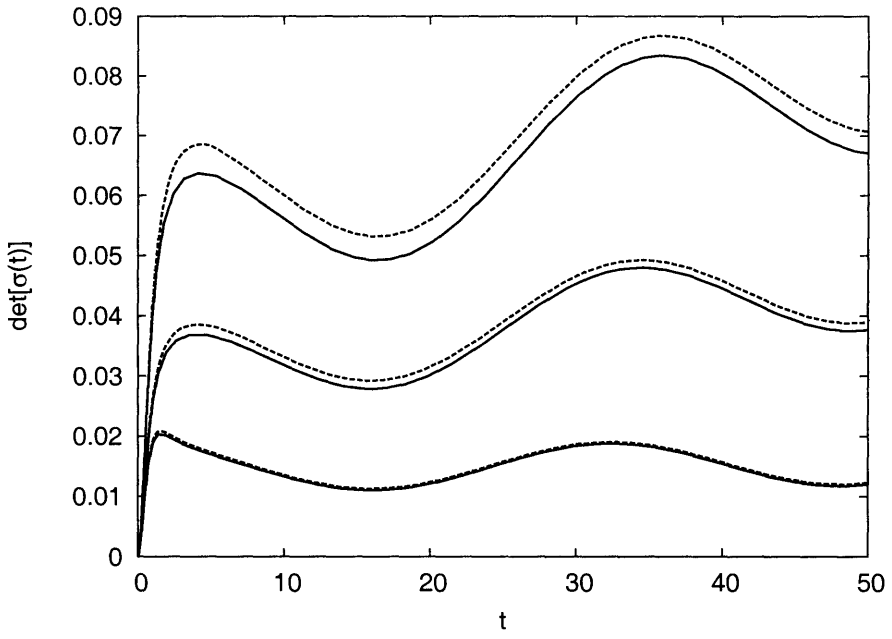

Figure 7-5: Short time dynamics of $\det[\sigma(t)]$ at different temperatures (from bottom to top: $\beta = 10$, $\beta = 1$, and $\beta = 0.5$). Dynamics obtained from the non-Markovian master equation (solid lines) and the concatenation scheme (dashed lines) are shown for each temperatures. The Debye-like spectral function in Eq. (7.10) is used. The parameters used are $\Delta = 0.1$ and $\eta = 0.01$, and the initial condition is $x(0) = 0$, $y(0) = \sqrt{3}/2$, and $z(0) = 0.5$.

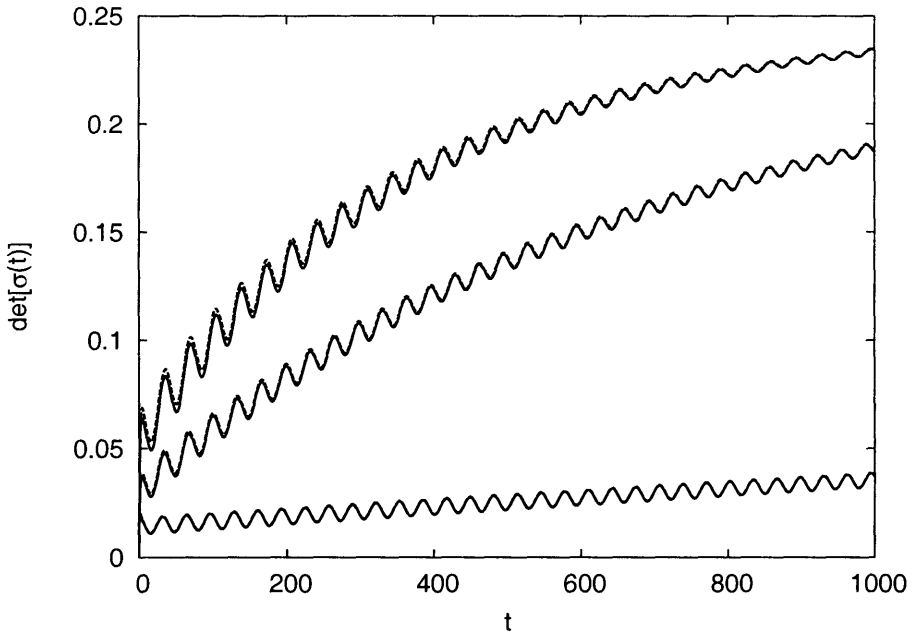

Figure 7-6: Dynamics of $\det[\sigma(t)]$ at a longer time period at three different temperatures (from bottom to top: $\beta = 10$, $\beta = 1$, and $\beta = 0.5$). Dynamics obtained from the non-Markovian master equation (solid lines) and the concatenation scheme (dashed lines) are shown for each temperatures. Damping of the oscillations at high temperatures can be clearly seen. The Debye-like spectral function in Eq. (7.10) is used. The parameters used are $\Delta = 0.1$ and $\eta = 0.01$, and the initial condition is $x(0) = 0$, $y(0) = \sqrt{3}/2$, and $z(0) = 0.5$.

systems with weak system-bath couplings.

7.6 Conclusion

In this chapter, we have examined the validity of the Markovian approximation based on a generic model with system-bath interaction linear in the oscillator coordinates. We argued that if the spectral function $J(\omega)$ of the bath is fairly dense and smoothly spread out, then a time-scale τ_b exists for bath relaxations. For times $t > \tau_b$, the memory kernels tends to zero and the Markovian approximation is applicable. In addition, if $J(\omega)$ decays to zero reasonably fast in both the $\omega \to 0$ and $\omega \to \infty$ limit, the bath relaxation time τ_b is determined by the width of the spectral function, $\tau_b \sim 1/\omega_d$, and is only weakly dependent on the temperature of the bath. We emphasize that in this context the width of the spectral function should be determined by the physical conditions of the system, and can not be choose arbitrarily by an imposed cutoff frequency. Although all our discussions are based on the linear form of the coupling, we believe that the random phase argument is generic and can be applied to other forms of interactions.

Moreover, we have proposed a concatenation scheme that absorbs the transient memory effects in a natural manner and fixes the non-positivity problem. The concatenation scheme applies second-order perturbation theory at short times and uses Markovian master equations for long time dynamics, therefore it in fact describes both the short-time and long-time dynamics. Applications of the concatenation scheme on the spin-boson problem show excellent agreements with the results obtained from the non-Markovian master equation at all temperature range studied. Our results indicate that with proper adjustments, the Markovian master equations are applicable in the weak-coupling limit. Although we have only studied the concatenation scheme on the simple spin-boson model, we expect it can be easily applied to multilevel systems. It will be interesting to study the performance of the concatenation scheme on more complicated multilevel problems. Because of its simplicity, the concatenation scheme can provide an efficient way to apply multilevel Markovian master equations, while

avoiding the non-positivity problem.

All our results in this chapter are based on the assumption that the system-bath interactions are weak and neglecting higher order terms in the memory kernels is valid. This weak-coupling condition seems to be a stringent limitation for quantum master equations Eq. (7.4)-(7.5). However, in many physical scenarios the system is strongly coupled to only a few bath modes. Therefore, the system-bath boundary can be redefined to include strongly coupled modes into the system, and the weak coupling approximation can still be adequate. In addition, sometimes a similarity transformation that transforms the total Hamiltonian and recovers the weak-coupling regime can be found [21, 22]. In these systems, the similarity transformation creates a new set of "dressed" states that are only weakly coupled to the bath, thus the weak-coupling approximation is still applicable. Our unified theory for exciton transportation presented in Chapter 3, where the Merrifield transformation is applied to the Holstein model to generate partially-dressed polaron states, is a demonstration of such an approach.

Appendix 7.A Derivation of the Quantum Master Equation

It is instructive to formally derive the quantum master equation [Eq. (7.4)] and see how the irreversible dynamics of the reduced system emerges from the reversible dynamics generated by the Hamiltonian of a macroscopic total system. In this appendix, we provide such a derivation and explicitly show the approximations involved in deriving the quantum master equation.

We start from the quantum Liouville equation ($\hbar = 1$) that describes the density matrix $\rho(t)$ of a total system with Hamiltonian H

$$\begin{aligned} \dot{\rho}(t) &= -i[H, \rho(t)] \\ &= -i\mathcal{L}\rho(t), \end{aligned} \tag{7.17}$$

where we have defined the Liouville superoperator as the commutator of the Hamiltonian with an arbitrary operator $\mathcal{O}$, $\mathcal{L}\mathcal{O} = [H, \mathcal{O}]$. In the Laplace space ($t \to s$), the Liouville equation is

$$s\tilde{\rho}(s) = \rho(0) - i\mathcal{L}\tilde{\rho}(s), \tag{7.18}$$

where $\tilde{\rho}(s)$ is the Laplace transform of $\rho(t)$, and $\rho(0)$ is the initial condition of the total system. Equation (7.18) provides the formal solution of the Liouville equation in the Laplace space, $\tilde{\rho}(s) = \frac{1}{s+i\mathcal{L}}\rho(0)$. Note that $\frac{1}{s+i\mathcal{L}}$ is a superoperator and should be interpreted as the inverse of $(s + i\mathcal{L})$.

In most physical applications, we are only interested in properties that are determined by states in a subspace of the total Hilbert space. Using a projection operator $\mathcal{P}$, we divide the density matrix of the total system into a relevant part $\rho_1(t) = \mathcal{P}\rho(t)$, and an irrelevant part $\rho_2(t) = (1 - \mathcal{P})\rho(t) \equiv \mathcal{Q}\rho(t)$, so that $\rho(t) = \rho_1(t) + \rho_2(t)$. Note

that by definition, projectors $\mathcal{P}$ and $\mathcal{Q}$ must satisfy $\mathcal{P}\mathcal{P}\ldots\mathcal{P}=\mathcal{P}$, $\mathcal{Q}\mathcal{Q}\ldots\mathcal{Q}=\mathcal{Q}$, and $\mathcal{P}\mathcal{Q}=\mathcal{Q}\mathcal{P}=0$. Applying $\mathcal{P}$ and $\mathcal{Q}$ to both sides of Eq. (7.18), we obtain two coupled linear equations:

$$\begin{aligned} s\tilde{\rho}_1(s)-\rho_1(0) &= -i\mathcal{P}\mathcal{L}[\tilde{\rho}_1(s)+\tilde{\rho}_2(s)], \\ s\tilde{\rho}_2(s)-\rho_2(0) &= -i\mathcal{Q}\mathcal{L}[\tilde{\rho}_1(s)+\tilde{\rho}_2(s)]. \end{aligned}$$

These equations can be solved to obtain the formal solution for the relevant part of the density matrix in the Laplace space,

$$s\tilde{\rho}_s(s)-\rho_s(0)=-i\mathcal{P}\mathcal{L}\tilde{\rho}_s(s)-i\mathcal{P}\mathcal{L}\frac{1}{s+i\mathcal{Q}\mathcal{L}}\rho_b(0)-\mathcal{P}\mathcal{L}\frac{1}{s+i\mathcal{Q}\mathcal{L}}\mathcal{Q}\mathcal{L}\tilde{\rho}_s(s)]. \quad (7.19)$$

The inverse Laplace transform of Eq. (7.19) yields the following differential-integral equation that describes the time evolution of $\rho_1(t)$:

$$\dot{\rho}_1(t)=-i\mathcal{P}\mathcal{L}e^{-i\mathcal{Q}\mathcal{L}t}\rho_2(0)-i\mathcal{P}\mathcal{L}\rho_1(t)-\int_0^t d\tau\mathcal{K}(\tau)\rho_1(t-\tau), \quad (7.20)$$

where we have defined the memory kernel

$$\mathcal{K}(\tau)=\mathcal{P}\mathcal{L}e^{-i\mathcal{Q}\mathcal{L}\tau}\mathcal{Q}\mathcal{L}. \quad (7.21)$$

The first term in the right hand side of Eq. (7.20) explicitly depends on the initial condition of the irrelevant part of the total system $\rho_2(0)$. However, by choosing an initial condition so that $\mathcal{P}\rho(0)=\rho(0)$, we can make $\rho_2(0)=0$, and the $\rho_2(0)$ term will vanish identically. For example, the projection operator defined in Eq. (7.1) and the product state initial condition defined in Eq. (7.3) satisfy the this condition. Hence, by selecting a proper combination of projector and initial conditions, Eq. (7.20) can be simplified to

$$\dot{\rho}_1(t) = -i\mathcal{P}\mathcal{L}\rho_1(t) - \int_0^t d\tau \mathcal{K}(\tau)\rho_1(t-\tau). \tag{7.22}$$

Equation (7.22) has a non-Markovian memory kernel, and is in the form of a generalized Fokker-Planck equation. The first term in Eq. (7.22) represents the unitary evolution governed by the Hamiltonian of the system, and the second term represents the dissipative dynamics of the relevant part of the total system. Note that total system still undergoes unitary evolution [Eq. (7.17)], it is the reduced system degrees of freedom (after tracing out the environment degrees of freedom) that have to be described by a non-unitary evolution. Clearly, the non-unitary evolution is a result of the separation of the total system into the system part and the bath part.

To derive the dynamics of a reduced system, we separate the total Hamiltonian H into the system part H_S, the bath part H_B, and the system-bath interaction part λH_{SB}. We also require that H_S and H_B operate in two different Hilbert spaces, so that their commutator vanishes, $[H_S, H_B] = 0$. The corresponding Liouville operator can be decomposed accordingly:

$$\mathcal{L} \;=\; \mathcal{L}_S + \mathcal{L}_B + \lambda\mathcal{L}_{SB}. \tag{7.23}$$

In addition, we also define the projection operators $\mathcal{P}$ and $\mathcal{Q} = 1 - \mathcal{P}$ using

$$\mathcal{P}\rho = \rho_b^{eq}\mathrm{Tr}_B\rho. \tag{7.24}$$

Note that the projector in Eq. (7.24) not only defines the relevant part of the total system by tracing out the irrelevant part, it also provides a definition for the temperature of the system. Eq. (7.24) is a convenient choice of projector, but this form is not required. Other projection operators can be chosen [23, 24]. With the definition in Eq. (7.24), the projector $\mathcal{P}$ and the Liouville operators satisfy the equalities $\mathcal{L}_B\mathcal{P} = \mathcal{P}\mathcal{L}_B = 0$, $\mathcal{P}\mathcal{L}_S\mathcal{Q} = \mathcal{Q}\mathcal{L}_S\mathcal{P} = 0$, and $\mathcal{P}\mathcal{L}_{SB}\mathcal{P} = 0$. The last equality is true if the thermal average of H_{SB} over the equilibrium bath states is zero, $\langle H_{SB}\rangle_{eq} = 0$

(where $\langle ... \rangle_{eq}$ denotes $\mathrm{Tr}_B\{...\rho_b^{eq}\}$). Note that for any Hamiltonian with $\langle H_{SB}\rangle_{eq} \neq 0$, we can always absorb the average into H_S and obtain a new interaction term with vanishing average, $H'_{SB} = H_{SB} - \langle H_{SB}\rangle_{eq}$, therefore, the condition to establish the equality $\mathcal{P}\mathcal{L}_{SB}\mathcal{P} = 0$ can always be achieved. For simplicity, we assume $\langle H_{SB}\rangle_{eq} = 0$ hereafter. Plugging Eq. (7.23) into Eq. (7.22) and applying the equalities, we obtain the equation of motion for the reduced system after tracing out the irrelevant bath degrees of freedom:

$$\begin{aligned} \dot{\sigma}(t) &= \mathrm{Tr}_B \dot{\rho}_1(t) \\ &= -i\mathcal{L}_s\sigma(t) - \lambda^2 \int_0^t d\tau \mathrm{Tr}_B \left\{ \mathcal{L}_{SB} e^{-i\mathcal{Q}\mathcal{L}\tau} \mathcal{Q}\mathcal{L}_{SB}\rho_b^{eq} \right\} \sigma(t-\tau). \end{aligned} \tag{7.25}$$

Equation (7.25) describes the dynamics of the reduced system under the initial condition $\rho(0) = \sigma(0) \otimes \rho_b^{eq}$, and is often called the "generalized master equation" [3]. Note that Eq. (7.22) is still exact, provided that the proper projectors and equilibrium bath initial conditions are used. In fact, up to this point we did nothing but reformulating the Liouville equation. Equation (7.25) is of little use because solving the propagator $e^{-i\mathcal{Q}\mathcal{L}\tau}$ in the memory kernel is as difficult as solving the original Liouville equation, but this equation is a convenient starting point for the derivations of many useful quantum master equations.

To derive Eq. (7.4), we need to apply two approximations. The first one is to replace the full propagator $e^{-i\mathcal{Q}\mathcal{L}\tau}$ in the memory kernel with the zeroth order propagator $e^{-i\mathcal{Q}(\mathcal{L}_S+\mathcal{L}_B)\tau}$, which effectively neglects terms beyond second order in λ in $\mathcal{K}(\tau)$. This approximation is similar to the Born approximation usually used in the scattering theory. The second one is to replace $\sigma(t-\tau)$ in the integral with $e^{iH_S\tau}\sigma(t)e^{-iH_S\tau}$, which makes the integral time-convolutionless and is effectively the partial ordering prescription (POP) used in the generalized cumulant expansion methods [5, 6]. If the second approximation is not made, then the integral retains the time-convolution $\rho(t-\tau)$ term, which is sometimes called the chronological ordering prescription (COP) [4, 6]. Note that the two approximations both assume weak system-bath interactions,

i.e. $\lambda \ll 1$. In the $\lambda \ll 1$ limit, both approximations are valid and we obtain from Eq. (7.25)

$$\dot{\sigma}(t) = -i[H_S, \sigma(t)] - \lambda^2 \int_0^t d\tau \mathrm{Tr}_B \left\{[H_{SB}, [H_{SB}(-\tau), \sigma(t) \otimes \rho_b^{eq}]]\right\}. \tag{7.26}$$

To explicitly evaluate the trace over the bath degrees of freedoms, we consider a generic product form for H_{SB}:

$$H_{SB} = \sum_{n,\alpha} S_n \otimes B_\alpha,$$

where S_n are an system operators, and B_α are bath operators, so that $[S_n, B_\alpha] = 0$. Substitution of H_{SB} in Eq. (7.26) yields

$$\begin{aligned}
\dot{\sigma}(t) \;=\; & -i[H_S, \sigma(t)] \\
& -\frac{1}{2}\lambda^2 \int_0^t d\tau \sum_{n,n',\alpha,\alpha'} \Big\{ \left[\langle B_{\alpha'}(-\tau) B_\alpha \rangle_{eq} + \langle B_\alpha B_{\alpha'}(-\tau) \rangle_{eq}\right] [S_n, [e^{-iH_S\tau} S_{n'} e^{iH_S\tau}, \sigma(t)]] \\
& - \left[\langle B_{\alpha'}(-\tau) B_\alpha \rangle_{eq} - \langle B_\alpha B_{\alpha'}(-\tau) \rangle_{eq}\right] [S_n, [e^{-iH_S\tau} S_{n'} e^{iH_S\tau}, \sigma(t)]_+] \Big\}.
\end{aligned} \tag{7.27}$$

where $[...]_+$ denotes the anticommutator.

Finally, we define bath correlation functions

$$C_{\alpha'\alpha}(\tau) = \langle B_{\alpha'}(\tau) B_\alpha \rangle_{eq} = \Gamma_r^{\alpha'\alpha}(\tau) + i\Gamma_i^{\alpha'\alpha}(\tau), \tag{7.28}$$

where $\Gamma_r^{\alpha'\alpha}(\tau)$and $\Gamma_i^{\alpha'\alpha}(\tau)$ are real functions representing the real part and the imaginary part of the correlation functions, respectively. Using the definitions in Eq. (7.28) and the symmetry properties of quantum correlation functions,

$$\langle B_\alpha B_{\alpha'}(\tau) \rangle_{eq} \;=\; \langle B_{\alpha'}(\tau) B_\alpha \rangle_{eq}^* = \Gamma_r^{\alpha'\alpha}(\tau) - i\Gamma_i^{\alpha'\alpha}(\tau),$$

we obtain

$$\dot{\sigma}(t) = -i[H_S, \sigma(t)] - \lambda^2 \int_0^t d\tau \sum_{n,n',\alpha,\alpha'} \Big\{ \Gamma_r^{\alpha'\alpha}(-\tau)[S_n, [e^{-iH_S\tau} S_{n'} e^{iH_S\tau}, \sigma(t)]]$$
$$-i\Gamma_i^{\alpha'\alpha}(-\tau)[S_n, [e^{-iH_S\tau} S_{n'} e^{iH_S\tau}, \sigma(t)]_+] \Big\}, \qquad (7.29)$$

which is the non-Markovian quantum master equation shown in Eq. (7.4). This is an equation for $\sigma(t)$ along, and the influence of the bath on the system is formulated through the bath correlation functions. The bath correlation functions, which are equilibrium properties of the bath, determine the non-equilibrium dynamics of the system. Note that no fast bath relaxation time has been assumed yet; the only assumptions made in deriving Eq. (7.4) are the equilibrium bath at the initial time and the weak system-bath interaction.

Bibliography

[1] H. P. Breuer and F. Petruccione. *The Theory of Open Quantum Systems.* Oxford University Press, Oxford, 2002.

[2] U. Weiss. *Quantum Dissipative Systems.* World Scientific, Singapore, 2001.

[3] N. G. van Kampen. *Stochastic Processes in Physics and Chemistry.* North-Holland, Amsterdam, 2001.

[4] S. Mukamel, I. Oppenheim, and J. Ross. Statistical reduction for strongly driven simple quantum systems. *Phys. Rev. A*, 17(6):1988 – 1998, 1978.

[5] D. R. Reichman, F. L. H. Brown, and P. Neu. Cumulant expansions and the spin-boson problem. *Phys. Rev. E*, 55(3):2328 – 2337, 1997.

[6] M. A. Palenberg, R. J. Silbey, C. Warns, and P. Reineker. Local and nonlocal approximation for a simple quantum system. *J. Chem. Phys.*, 114(10):4386 – 4389, 2001.

[7] A. G. Redfield. The theory of relaxation processes. *Adv. Mag. Res.*, 1:1, 1965.

[8] R. Dümcke and H. Spohn. The proper form of the generator in the weak coupling limit. *Z. Phys. B*, 34:419, 1979.

[9] H. Spohn. Kinetic equations from hamiltonian dynamics. *Rev. Mod. Phys.*, 52:569, 1980.

[10] A. Suárez, R. Silbey, and I. Oppenheim. Memory effects in the relaxation of quantum open systems. *J. Chem. Phys.*, 97(7):5101 – 5107, 1992.

[11] P. Gaspard and M. Nagaoka. Slippage of initial conditions for the Redfield master equation. *J. Chem. Phys.*, 111(13):5668 – 5675, 1999.

[12] W. T. Pollard and R. A. Friesner. Solution of the redfield equation for the dissipative quantum dynamics of multilevel systems. *J. Chem. Phys.*, 100(7):5054 – 5065, 1994.

[13] I. Kondov, U. Kleinekathofer, and M. Schreiber. Efficiency of different numerical methods for solving Redfield equations. *J. Phys. Chem.*, 114(4):1497 – 1504, 2001.

[14] N. G. van Kampen and I. Oppenheim. Langevin and master equation in quantum mechanics. *J. Stat. Phys.*, 87(5-6):1325 – 1334, 1997.

[15] R. Zwanzig. Ensemble mathod in the theory of irreversibility. *J. Chem. Phys.*, 33:1338, 1960.

[16] A. J. Leggett, S. Chakravarty, A. T. Dorsey, M. P. A. Fisher, A. Garg, and W. Zwerger. Dynamics of the dissipative 2-state system. *Rev. Mod. Phys.*, 59(1):1 – 85, 1987.

[17] T. Mancal and V. May. Interplay of non-Markovian relaxation and ultrafast optical state preparation in molecular systems: The Laguerre polynomial method. *J. Chem. Phys.*, 114(4):1510 – 1523, 2001.

[18] M. Thoss, H. B. Wang, and W. H. Miller. Self-consistent hybrid approach for complex systems: Application to the spin-boson model with Debye spectral density. *J. Chem. Phys.*, 115(7):2991 – 3005, 2001.

[19] D. Egorova, M. Thoss, W. Domcke, and H. B. Wang. Modeling of ultrafast electron-transfer processes: Validity of multilevel Redfield theory. *J. Chem. Phys.*, 119(5):2761 – 2773, 2003.

[20] U. Kleinekathofer. Non-Markovian theories based on a decomposition of the spectral density. *J. Chem. Phys.*, 121(6):2505 – 2514, 2004.

[21] R. Silbey and R. A. Harris. Variational calculation of the dynamics of a 2 level system interacting with a bath. *J. Chem. Phys.*, 80(6):2615 – 2617, 1984.

[22] K. Ji and H. Zheng. A unitary transformation approach to the mutual quenching of structural and magnetic ordering in cooperative Jahn-Teller systems. *J. Phys.-Condes. Matter*, 13(5):1079 – 1091, 2001.

[23] V. Romero-Rochin and I. Oppenheim. Relaxation properties of 2-level systems in condensed phases. *Physica A*, 155(1):52 – 72, 1989.

[24] V. Romero-Rochin, A. Orsky, and I. Oppenheim. Theory of spin-relaxation processes. *Physica A*, 156(1):244 – 259, 1989.

Yuan-Chung Cheng

Massachusetts Institute of Technology
77 Massachusetts Avenue 6-228
Cambridge, MA 02139
(617) 253-1538
yccheng@mit.edu

Education

Ph. D. in Physical Chemistry, February 2006, Massachusetts Institute of Technology, Cambridge, MA.
M. S. in Chemistry, June 1997, National Taiwan University, Taipei, Taiwan.
B. S. in Chemistry, June 1995, National Taiwan University, Taipei, Taiwan.

Research

MIT Department of Chemistry, Cambridge, MA.
Advisor: Robert J. Silbey
Ph. D. thesis research on "Quantum Dynamics in Condensed Phases: Charge Carrier Mobility, Decoherence, and Excitation Energy Transfer." (September 2000 - February 2006).

NTU Department of Chemistry, Taipei, Taiwan.
Advisor: Jwu-Ting Chen and Bih-Yaw Jin
Applied QM/MM combined methods to study steric and electronic factors in Ni(II) diimine olefin polymerization catalysts. (June 1999 - June 2000).

NTU Department of Chemistry, Taipei, Taiwan.
Advisor: Jwu-Ting Chen
M. S. thesis research on "Mechanistic Investigation of Nucleophilic Addition of Amine and Water to Platinum(II) η^3-Propargyl/Allenyl Complex - A Density Functional Study." (September 1995 - June 1997).

Teaching

MIT Department of Chemistry, Cambridge, MA.
Intermediate Chemical Experimentation. Graduate Teaching Assistant. (February - June 2001).
Introductory Chemical Experimentation. Graduate Teaching Assistant. (September - December 2000).

Awards

Distinguished Scientific Youth Award (1998), Yen, Yun-Tsai Thesis Award (1997), The Ministry of Education Graduate Scholarship (1995-1997), Lee Yuan Tze Scholarship for Chemistry (1991-1995).

Presentations

Gordon Research Conference: Quantum Information Science, Ventura, CA., February 2005.
The Eighth Workshop on Quantum Information Processing, Boston, MA., January 2005.
Summer School on Quantum Logic and Communication, Cargese, Corsica, France, August 2004.
Gordon Research Conference: Quantum Information Science, Ventura, CA., February 2004.

Publications

Y.C. Cheng and R.J. Silbey, *Phys. Rev. Lett.* , **96**, 028103 (2006).
Y.C. Cheng and R.J. Silbey, *J. Phys. Chem. B*, **109**, 21399 (2005).
Y.C. Cheng and R.J. Silbey, *Phys. Rev. A*, **72**, 012320 (2005).
Y.C. Cheng and R.J. Silbey, *Phys. Rev. A*, **69**, 052325 (2004).
E. Barkai and Y.C. Cheng, *J. Chem. Phys.*, **118**, 6167 (2003).
Y.C. Cheng, R.J. Silbey, D.A. da Silva,J.P. Calbert, J. Cornil, and J.L. Bredas, *J. Chem. Phys*, **118**, 3764 (2003).